Technische Universität München

Max-Planck-Institut für Physik
(Werner-Heisenberg-Institut)

Aspects of SUSY Phenomenology at the LHC

Jonas M. R. Lindert

Vollständiger Abdruck der von der Fakultät für Physik
der Technischen Universität München zur Erlangung des akademischen Grades eines
Doktors der Naturwissenschaften (Dr. rer. nat.)
genehmigten Dissertation

Vorsitzender:		Univ.-Prof. Dr. L. Oberauer
Prüfer der Dissertation:	1.	Hon.-Prof. Dr. W. F. L. Hollik
	2.	Univ.-Prof. Dr. B. Garbrecht

Die Dissertation wurde am 12. Juni 2013
bei der Technische Universität München eingereicht und
durch die Fakultät für Physik am 8. Juli 2013 angenommen.

This thesis is based on the author's work conducted at the Max-Planck-Institut für Physik (Werner-Heisenberg-Institut) in Munich from October 2010 until May 2013. Parts of this work have already been published in [1–4]:

[1] J. M. Lindert, F. D. Steffen, and M. K. Trenkel,
"Direct stau production at hadron colliders in cosmologically motivated scenarios,"
JHEP **1108** (2011) 151, `arXiv:1106.4005 [hep-ph]`.

[2] J. M. Lindert, F. D. Steffen, and M. K. Trenkel,
"Direct stau production at the LHC,"
PoS **CORFU2011** (2011) 024, `arXiv:1204.2379 [hep-ph]`.

[3] W. Hollik, J. M. Lindert, and D. Pagani,
"NLO corrections to squark-squark production and decay at the LHC,"
JHEP **1303** (2013) 139, `arXiv:1207.1071 [hep-ph]`.

[4] W. Hollik, J. M. Lindert, and D. Pagani,
"On cascade decays of squarks at the LHC in NLO QCD,"
Eur.Phys.J. **C73** (2013) 2410 , `arXiv:1303.0186 [hep-ph]`.

Zusammenfassung

In dieser Arbeit untersuchen wir verschiedene Aspekte von Supersymmetrie Phänomenologie an Beschleunigerexperimenten.

Im ersten Teil wird der theoretische Rahmen erläutert: das Standardmodell der Elementarteilchenphysik, die Prinzipien von Supersymmetrie und das Minimale Supersymmetrische Standardmodell (MSSM). Als nächstes geben wir einen Überblick über die resultierende Phänomänologie an Beschleunigern und im frühen Univserum.

Im zweiten Teil präsentieren wir eine Präzisionsstudie zur Produktion und dem Zerfall von skalaren Quarks (Squarks) am Large Hadron Collider (LHC) im Rahmen des MSSM. Dabei werden Strahlungskorrekturen zur nächstführenden Ordnung berücksichtigt. Zunächst motivieren wir eine solche Rechnung und präsentieren neben technischen Konzepten einige Details der Rechnung. Als nächstes untersuchen wir die Konsequenzen der berechneten Korrekturen für die experimentelle Signatur $2j + \not{E}_T(+X)$. Dabei nehmen wir an, dass die produzierten Squark-Paare direkt in zwei leichteste, als stabil angenommene Neutralinos und Jets zerfallen. Dies ist einer der wichtigsten Kanäle für die Suche nach Supersymmetrie am LHC. Speziell berechnen wir differentielle Wirkungsquerschnitte und vergleichen, wie sich die Form dieser Verteilungen durch die zusätzlichen Quantenkorrekturen verändert. Zuletzt untersuchen wir eine weitere Signatur: $2j + 2l + \not{E}_T(+X)$. Hier wird angenommen, dass die produzierten Squarks in ein leichtestes und ein zweitleichtestes Neutralino zerfallen. Das zweitleichteste Neutralino zerfällt nun wiederum schrittweise über eine elektroschwache Zerfallskette. Für die sich ergebenden invarianten Massenverteilungen untersuchen wir erneut die dominanten Strahlungskorrekturen. Solche Verteilungen sind speziell für zukünftige Parameterbestimmung von großer Bedeutung.

Im dritten Teil der Arbeit untersuchen wir, erneut innerhalb des MSSM, die dominanten Beiträge zum Wirkungsquerschnitt hadronischer Paarproduktion von skalaren Taus (Staus). Wir berücksichtigen dabei speziell die auftretende links-rechts Mischung der Staumasseneigenzustände. Im Vergleich zu Vorhersagen, die ausschließlich Drell-Yan Paarerzeugung berücksichtigen, können zusätzliche, von uns eingeschlossene Beiträge diesen Wirkungsquerschnitt um mehr als eine Größenordnung erhöhen. Unter der Annahme, dass die produzierten Staus langlebig sind, untersuchen wir phänomenologische Implikationen unserer Rechnung, speziell in Parameterbereichen, die auf Grund von kosmologischen Überlegungen motiviert sind.

Abstract

In this thesis we investigate different aspects of supersymmetric collider phenomenology with an emphasis on precision predictions for supersymmetric particle production and decay.

In the first part, we introduce the theoretical framework: the Standard Model of particle physics, the concept of supersymmetry and the Minimal Supersymmetric Standard Model (MSSM). Next, resulting collider and early-Universe phenomenology is discussed.

In the second part, we present precision calculations for combined scalar quark (squark) production and decay in next-to-leading order (NLO) QCD at the Large Hadron Collider (LHC) within the MSSM. First, the motivation and theoretical approach including computational details of such a combined calculation is presented. Second, an analysis of the signature $2j + \not{E}_T(+X)$ via squark–squark production and direct decays into the lightest neutralino, which is assumed to be the lightest supersymmetric particle and hence stable, is presented. Resulting differential distributions are compared with leading order (LO) approximations rescaled by a flat K-factor and a possible impact on cut-and-count searches for supersymmetry at the LHC is examined. Third, the signature $2j + 2l + \not{E}_T(+X)$ from squark–squark production and decay into a lightest and a second lightest neutralino, with a subsequent electroweak decay chain via an on-shell slepton, is investigated. The impact of NLO corrections on resulting invariant mass distributions is highlighted. Such distributions can be important for future determination of supersymmetry parameters.

In the third part, we present a calculation of the dominant cross section contributions for hadronic scalar tau (stau) pair-production within the MSSM, taking into account left-right mixing of the stau eigenstates. We find that b-quark annihilation and gluon fusion can enhance the cross sections by more than one order of magnitude with respect to the Drell-Yan predictions. For long-lived staus, we investigate phenomenological implications of our calculation, in particular for parameter regions favored by cosmology due to the appearance of exceptionally small stau yields.

Contents

Chapter 1

Introduction

Supersymmetry (SUSY) [5–11] is a hypothetical additional symmetry of nature which can solve several experimental and theoretical shortcomings of the Standard Model (SM) of particle physics. Actually, supersymmetry is the only non-trivial extension of the Poincaré group of space-time symmetries [12], the SM is based on. Indeed, despite the great success of the SM explaining the electromagnetic, weak, and strong interactions of all known elementary particles in a consistent renormalizable quantum field theory based on gauge symmetries [13–22] and predicting a new scalar degree of freedom – the Higgs boson [23–26], several unresolved issues remain. Amongst others, for a Higgs mass of $125 - 126$ GeV, as spectacularly observed recently by the experiments at the Large Hadron Collider (LHC) [27, 28], the electroweak (EW) vacuum of the SM cannot be absolutely stable [29] and an unnatural amount of fine-tuning is necessary to explain such a light Higgs [30]. Furthermore, within the SM gauge couplings do not unify at some higher scale, there is no possible explanation for the observed dark matter in the Universe and the SM does not incorporate gravity – the fourth known force of nature. These issues indicate that the SM should only be seen as an effective theory, i.e. it explains precisely all phenomena at currently testable energies but has to be embedded into a more fundamental theory at higher energy scales.

In a supersymmetric extension of the SM all of the aforementioned shortcomings can be solved rather naturally. In particular, within the Minimal Supersymmetric Standard Model (MSSM) and its (extended) two-Higgs-doublet Higgs-sectors [31, 32] the electroweak vacuum is stabilized as the Higgs self-coupling is not a free parameter anymore. Furthermore, no (or much smaller) fine-tuning is necessary as quadratic divergences are automatically canceled due to new degrees of freedom [33, 34]. In fact, under quite general assumptions the MSSM predicts a Higgs boson mass at $\lesssim 135$ GeV [35], in agreement with the recently observed state. In a SUSY theory all known particles of the SM get a partner with spin differing by one half; the SM fermions get scalar partners and the SM gauge and Higgs bosons get fermionic partners. In an exact supersymmetric Universe these partners would have the same mass as their SM counterparts. Therefore, if realized in nature, SUSY has to be broken. Still, for additional SUSY particles around the TeV scale renormalization group equations (RGEs) are altered in such a way that gauge couplings unify in one point [36, 37]. Furthermore, in many SUSY models the lightest new particle is stable due to an additional discrete symmetry called R-parity and often a viable dark matter candidate. Finally, in a local supersymmetric theory gravitational interactions can potentially be incorporated consistently.

Unfortunately, up to now no direct hints for SUSY particles have been observed. Still, the ongoing search for such particles is one of the prime goals of the current LHC physics program. Indeed, for the first time the TeV scale can directly be probed. Due to the mentioned properties of SUSY theories there are still high hopes to find direct evidence in the upcoming run of the LHC, or already in the currently available data. Eventually, a future linear collider will conclusively confirm or rule out TeV scale supersymmetry. A discovery would be a major breakthrough with far reaching consequences also for our understanding of cosmology and the early Universe. However, also a conclusive exclusion at the TeV scale would be a milestone in the search program for physics *beyond the Standard Model* (BSM) in general. Furthermore, given the LHC (or a future linear collider) observed evidence for BSM physics, nature and parameters of the new theory would have to be determined.

From a theoretical perspective all these endeavors require, on the one hand, precise and reliable theoretical predictions of production and decay processes of supersymmetric particles including higher-order corrections. In this way, experimental searches can be refined and uncertainties, both for exclusion limits and future parameter determination, can be reduced. On the other hand, due to the vast size of the SUSY parameter space, theoretical motivated parameter regions and resulting signatures have to be identified. Also new techniques for SUSY searches and for parameter determination have to be investigated. All of these goals are subject of this thesis, which we organize into three parts.

In **Part I** we introduce the theoretical framework of this thesis and give an overview over relevant SUSY phenomenology.

In chapter 2 we first introduce the SM and elaborate on its success and shortcomings. Second, we offer SUSY as a possible solution and introduce its concepts. Third, the MSSM and its particle spectrum is introduced together with the idea of R-parity. Also possible parametrizations are given. All calculations presented in the following parts of this work are performed within the MSSM. Forth, we raise the issues of supersymmetry breaking and supergravity. Here, unavoidably the gravitino is brought up as the supersymmetric partner of the graviton.

In chapter 3 various phenomenological consequences of SUSY are discussed – both at colliders and for the early Universe. First, the currently most powerful collider, the LHC, is presented. Second, an overview over possible signatures of SUSY at colliders is given. Here (and in the rest of the thesis), we assume the lightest supersymmetric particle (LSP) to be stable due to R-parity conservation and focus on two scenarios: 1) the LSP is assumed to be the lightest neutralino (a mixture of the SUSY partners of the neutral gauge and Higgs bosons of the Standard Model). This results in signatures with large missing transverse energy, as any produced SUSY particle eventually decays into a neutralino which in turn escapes the particle detectors unobserved. 2) The gravitino (or another additional particles with suppressed couplings outside the MSSM) is assumed to be the LSP, possibly rendering the next-to-LSP (NLSP) to be stable, with possibly striking consequences. Third, collider phenomenology of the colored, electroweak, Higgs and flavor sectors are discussed subsequently, with a focus on important issues for the following parts of this work. Fourth, implications of the different aforementioned LSPs as dark matter candidates and the early Universe are highlighted.

In **Part II** we present a calculation combining scalar quark (squark) pair production with subsequent decays in next-to-leading order (NLO) of (supersymmetric) QCD at the LHC.

First, in chapter 4 the motivation and theoretical approach for such a calculation including computational details of production and decay are presented. On the one hand, we present a general discussion of different approximations for the treatment of unstable particles at higher-orders of perturbation theory, where we focus on the narrow-width approximation (NWA) as a limit of the double-pole approximation. In NWA the intermediate SUSY particles are treated on-shell and the calculation of production and decay can be factorized. However, in this way only a part of the full NLO corrections can be calculated. Therefore, we present a discussion of the remaining so-called non-factorizable corrections. On the other hand, we present the factorized fully differential NLO calculation of squark–squark production and separate squark decay. Here, details on the treatment of occurring UV, soft and collinear divergences are given. Also the strategy to avoid a possible over-counting of real quark radiation contributions at NLO is discussed in detail. In our calculation of squark–squark production no assumptions on the particle spectrum are made. In particular, all flavor and chirality configurations are treated independently, as decays of squarks with different chiralities can have very different decays.

Second, in chapter 5 we apply the discussed approach to squark–squark production combined with two direct decays into a lightest neutralino, which is assumed to be the LSP and hence stable. Final state gluons and quarks are clustered into partonic jets and, thus, we investigate the experimental signature of 2 jets + missing transverse energy, $2j + \not{E}_T(+X)$, via squark–squark production at NLO in NWA, where we assume the gluino (the fermionic partners of the gluon) to be heavier than all light-flavor squarks. In our numerical evaluation for different benchmark scenarios we investigate various differential distributions relevant for current searches and future parameter determination. We demonstrate that at NLO scale uncertainties of the differential distributions are considerably reduced. Afterwards, we compare leading order approximations rescaled by a flat K-factor (defined as ratio between the NLO and LO integrated cross sections) with our fully differential treatment at NLO. In this way, we investigate corrections purely to the shapes of the differential distributions. The numerical effect of these corrections depend on the differential distribution and parameter point under consideration and typically are of the order of $10 - 40\%$, and thus larger than estimated before [38]. In the same way, we investigate a possible impact on cut-and-count searches for supersymmetry at the LHC. Here, differences between a flat K-factor and a fully differential treatment can be as large as 30% for an uncompressed spectrum. On the other hand, for a compressed spectrum the inclusion of initial state radiation is mandatory for a reliable prediction.

Third, in chapter 6 we again employ the same approach and we investigate the experimental signature of 2 jets + 2 leptons + missing transverse energy, $2j + 2l + \not{E}_T(+X)$, at NLO QCD via squark-left–squark-right production and decay in NWA. The right-handed squark is assumed to directly decay into a lightest neutralino, which is again assumed to be stable. The left-handed squark is assumed to decay into a second lightest neutralino, which subsequently decays via an on-shell lepton in an electroweak decay chain emitting two opposite-sign-same-flavor leptons and finally also a lightest neutralino. This decay chain is also known as the "golden" decay chain, as it can be very important for determination of masses and spins of

the intermediate SUSY particles from various invariant mass distributions. We highlight how such a determination can be performed and investigate the impact of NLO corrections on relevant invariant mass distributions for two benchmark scenarios. In particular, the issue of jet-combinatorics in the presence of more than one final-state jet can only be studied systematically at NLO. Additionally, we analyze the impact on predictions of inclusive rates and hence cut-and-count searches at the LHC using the $2j + 2l + \not{E}_T(+X)$ signature and appropriate experimental cuts. Here, differences between a flat K-factor (summed over all chirality combinations) and a fully differential treatment are smaller than 10% for the considered scenarios.

In this work we concentrate on the squark–squark channel. This should be understood as a first step towards a fully differential prediction for all sparticle production channels at NLO. It is, however, also of practical importance, since from recent searches at the LHC mass bounds for squarks and gluinos are generically pushed to higher values and here squark–squark production yields the dominant channel, as discussed in section 3.3.

In **Part III** we present theoretical predictions for direct scalar tau (stau) pair-production at the LHC focusing on scenarios with large left-right mixing.

First, in chapter 7 we present our calculation independently of a possible longevity of the produced staus. However, we highlight the relevance of parameter regions with large stau–stau–Higgs couplings, which are motivated either for a long-lived stau from cosmological consideration or for decaying staus to explain a possible enhancement in the branching ratio $\mathrm{BR}(h^0 \to \gamma\gamma)$ compared to the SM prediction. In our calculation we include Drell–Yan processes as well as b-quark annihilation and gluon fusion, where the latter two might become important in the mentioned parameter regions with large stau–stau–Higgs couplings. Special attention is given to mixing effects of the staus. In such a regime, the bottom–bottom–Higgs vertex might receive large radiative corrections, which requires appropriate resummation. We find in our numerical evaluation that b-quark annihilation and gluon fusion can enhance the cross sections by more than one order of magnitude with respect to the Drell–Yan predictions when the production proceeds via an on-shell heavy Higgs. In other regions the additional gluon-fusion and b-annihilation channels can still be of the same order or even larger than the Drell–Yan predictions.

Second, in chapter 8 we interpret our calculation for long-lived staus. We investigate the effect of relevant experimental cuts in the different production channels and propose new techniques for parameter determination. Within the constrained MSSM we compare direct production with production from cascade decays. Furthermore, we link regions motivated by cosmology due to an exceptionally small stau yield with distinct features at the LHC. Focusing on such regions we present prospects for ongoing searches at the LHC.

Finally, we summarize and draw our conclusions in chapter 9.

Furthermore, in Appendix A details and analytical results of the individual NLO calculations of squark–squark production and decay are given. In Appendix B relations for relevant invariant mass distributions used in chapter 6 are listed. In Appendix C constraints from the potential occurrence of charge or color breaking minima relevant for chapter 7 and 8 are explained.

Part I

From the Standard Model to SUSY phenomenology

Chapter 2

Theoretical framework

In this chapter we want to specify the theoretical framework of this thesis. In section 2.1 the Standard Model is summarized and its success explaining available empirical data is highlighted – together with an overview of several theoretical and experimental shortcomings. In section 2.2 a solution to several of these shortcomings is offered: the concept of supersymmetry. We sketch its general construction as an extension of the usual space-time symmetries and elaborate in more detail in section 2.3, where we introduce the Minimal Supersymmetric Standard Model. There, we introduce the particle spectrum of the MSSM at tree level and concentrate on the sectors and couplings most important in this thesis. As discussed below, supersymmetry cannot be an exact symmetry of nature – thus, it has to be broken. In section 2.4 we introduce the concept of supersymmetry breaking and sketch most relevant models. Detailed phenomenological implications of supersymmetric theories are discussed in the following chapter 3.

2.1 The Standard Model and its problems

The Standard Model [13–19] is a highly predictive, renormalizble [20–22] and successful [39] quantum field theory describing all known elementary particles and their strong, weak and electromagnetic (EM) interactions. It is based on the principles of global Poincaré space-time symmetry and local gauge invariance under the direct product $SU(3)_C \times SU(2)_L \times U(1)_Y$ of compact Lie groups. In the SM, matter particles – leptons and quarks – appear in three families. They are chiral spin-1/2 fermions with different charges under the gauge groups. Here, these fermions are described by left- and right-handed Weyl spinors, facilitating a supersymmetric extension. In the SM literature often instead an equivalent Dirac spinor notation is used. If charged, they transform in the fundamental representation of the corresponding group. All left(right)-handed fermions are doublets (singlets) under $SU(2)_L$; the charge Y (called *hypercharge*) of $U(1)_Y$ for all fermions is determined from validity of the Gell-Mann–Nishijima relation, $Q = I_3 + \frac{Y}{2}$. Here, Q is the electric charge and I_3 the third component of the *isospin* $\mathbf{I}$, the generator of $SU(2)_L$. In this way $SU(2)_L \times U(1)_Y$ unifies *quantum electrodynamics* (QED) with a weak theory into the *electroweak* Standard Model. Finally, all quarks are triplets under $SU(3)_C$, the gauge group of *quantum chromodynamics* (QCD).

As all the gauge symmetries are local symmetries, corresponding spin-1 bosonic vector

	field			spin	$SU(3)_C$	$SU(2)_L$	Y
quarks	$\begin{pmatrix} u \\ d \end{pmatrix}_L$	$\begin{pmatrix} c \\ s \end{pmatrix}_L$	$\begin{pmatrix} t \\ b \end{pmatrix}_L$	1/2	**3**	**2**	1/3
	u_R	c_R	t_R	1/2	**3**	**1**	4/3
	d_R	s_R	b_R	1/2	**3**	**1**	-2/3
leptons	$\begin{pmatrix} \nu_e \\ e \end{pmatrix}_L$	$\begin{pmatrix} \nu_\mu \\ \mu \end{pmatrix}_L$	$\begin{pmatrix} \nu_\tau \\ \tau \end{pmatrix}_L$	1/2	**1**	**2**	-1
	e_R	μ_R	τ_R	1/2	**1**	**1**	-2
Higgs-doublet	$\begin{pmatrix} \phi^+ \\ \phi^0 \end{pmatrix}_L$			0	**1**	**2**	1
gauge bosons	G^a_μ			1	**8**	**1**	0
	W^i_μ			1	**1**	**3**	0
	B_μ			1	**1**	**1**	0

Table 2.1: Field content of the Standard Model together with corresponding spin, representation under $SU(3)_C$, $SU(2)_L$ and hypercharge Y. Matter fields are shown in their $SU(2)$ representations.

fields have to be introduced. They transform in the adjoint representation of the respective gauge group. Thus, there is the octet G^a_μ of QCD, the isotriplet W^i_μ belonging to $SU(2)_L$ and the isosinglet B_μ of $U(1)_Y$. For these fields no gauge invariant mass terms can be formulated. Thus, only the G^a_μ can directly be identified with the physical gluons. The EW subgroup $SU(2)_L \times U(1)_Y$ has to be *spontaneously* broken to allow mass terms, as observed for the $W^\pm$ and Z^0 particles, in a gauge invariant way which thus does not spoil renormalizability. In the SM this is achieved in a minimal way via the Higgs mechanism [23–26]. Here, an additional spin-0 complex scalar $SU(2)_L$-doublet field Φ with hypercharge $Y = 1$ is introduced with a potential that spontaneously breaks

$$SU(2)_L \times U(1)_Y \to U(1)_{\mathrm{EM}}\,, \tag{2.1}$$

and in this way leaves the electromagnetic $U(1)_{\mathrm{EM}}$ with the photon A_μ as a gauge field as a symmetry of nature. All fields of the unbroken SM together with their spin and group representations are summarized in table 2.1. Here, the subscript L/R denotes left-/right-handed spinors. The left-handed lepton doublets are built out of left-handed electrons e_L, muons μ_L, taus τ_L and corresponding neutrinos ν_{iL}. There are no right-handed neutrinos in the SM. As already mentioned, also the quarks appear in three families: the up- u and down-type d quarks of the first generation, charm c and strange s of the second generation, and in the third generation top t and bottom b.

2.1.1 Standard Model Lagrangian

In the following we formulate the dynamics of the SM, based partly on [40].

Classical Lagrangian

The Lorentz-invariant Lagrange density of the unbroken SM at the classical level reads

$$\mathcal{L}_{\mathrm{SM}}^{\mathrm{classical}} = \mathcal{L}_{\mathrm{gauge}} + \mathcal{L}_{\mathrm{fermion}} + \mathcal{L}_{\mathrm{Higgs}} \,. \tag{2.2}$$

The kinetic term of the gauge fields $\mathcal{L}_{\mathrm{gauge}}$ is given by

$$\mathcal{L}_{\mathrm{gauge}} = -\frac{1}{4} G^{a\,\mu\nu} G^a_{\mu\nu} - \frac{1}{4} W^{i\,\mu\nu} W^i_{\mu\nu} - \frac{1}{4} B^{\mu\nu} B_{\mu\nu} \,, \tag{2.3}$$

with the field strength tensors

$$G^a_{\mu\nu} = \partial_\mu G^a_\nu - \partial_\nu G^a_\mu + g_s f^{abc} G^b_\mu G^c_\nu \,, \tag{2.4a}$$

$$W^i_{\mu\nu} = \partial_\mu W^i_\nu - \partial_\nu W^i_\mu + g_2 \epsilon^{ijk} W^j_\mu W^k_\nu \,, \tag{2.4b}$$

$$B_{\mu\nu} = \partial_\mu B_\nu - \partial_\nu B_\mu \,. \tag{2.4c}$$

Here, $g_s = g_3$ and g_2 are the coupling constants of the non-abelian $SU(3)_C$ and $SU(2)_L$; f_{abc} and ϵ_{ijk} are respectively the structure constants of the corresponding Lie algebras.

The kinetic terms and gauge interactions of the fermion fields $\mathcal{L}_{\mathrm{fermion}}$ on the other hand follow from minimal substitution of partial derivatives ∂_μ with gauge-covariant derivatives D_μ,

$$D_\mu = \partial_\mu + i g_s \mathbf{T}^a G^a_\mu + i g_2 \mathbf{I}^i W^i_\mu + i g_1 \frac{Y}{2} \mathbf{1} B_\mu \,, \tag{2.5}$$

and reads

$$\mathcal{L}_{\mathrm{fermion}} = \sum_{i=1}^{3} [q_L^{i\,\dagger} \bar{\sigma}^\mu D_\mu q_L^i \;+ u_R^{i\,\dagger} \sigma^\mu D_\mu u_R^i \;+ d_R^{i\,\dagger} \sigma^\mu D_\mu d_R^i \;+ l_L^{i\,\dagger} \bar{\sigma}^\mu D_\mu l_L^i \;+ e_R^{i\,\dagger} \sigma^\mu D_\mu e_R^i \;] \,. \tag{2.6}$$

Here, g_1 is the coupling constant of $U(1)_Y$, $\mathbf{T}^a$ and $\mathbf{I}^i$ are the generators of $SU(3)_C$ and $SU(2)_L$ respectively, and $\sigma^\mu, \bar{\sigma}^\mu$ are defined as $\sigma^\mu \equiv (\mathbf{1}_2, \sigma^i)$ and $\bar{\sigma}^\mu \equiv (\mathbf{1}_2, -\sigma^i)$, where σ^i are the usual 2×2 Pauli matrices. We sum over the three fermion generations. As already mentioned for the gauge bosons, also for the fermions there is no way to write down a gauge and Lorentz-invariant mass term for the fermions. As we will see in the following, in the SM also fermion masses are generated by the Higgs mechanism.

The Lagrange density of the Higgs sector in the SM reads

$$\mathcal{L}_{\mathrm{Higgs}} = (D^\mu \Phi)^\dagger (D_\mu \Phi) - V(\Phi) + \mathcal{L}_{\mathrm{Yukawa}} \,, \tag{2.7}$$

where again in the kinetic term the gauge interactions are determined by minimal substitution. The Higgs potential is crucial for spontaneous electroweak symmetry breaking and reads

$$V(\Phi) = -\mu^2 \Phi^\dagger \Phi + \frac{\lambda}{4} (\Phi^\dagger \Phi)^2 \,, \tag{2.8}$$

with $\mu^2, \lambda > 0$. Due to the negative quadratic term, minimization of the potential yields a non-vanishing vacuum expectation value (vev), $v = \frac{2\mu}{\sqrt{\lambda}}$, which results in the breaking (2.1) – *electroweak symmetry breaking* (EWSB). We can now expand the Higgs field $\Phi(x)$ around this vacuum expectation value:

$$\Phi(x) = \begin{pmatrix} \phi^+(x) \\ \frac{1}{\sqrt{2}}(v + h^0(x) + i\chi^0(x)) \end{pmatrix} . \tag{2.9}$$

The real fields $\chi^0(x)$ and $h^0(x)$ and the complex field $\phi^+(x)$ have vanishing vev's. Out of these the fields $\chi^0(x)$ and $\phi^+(x)$ are unphysical degrees of freedom (d.o.f) of the spontaneously broken theory – the would-be *Goldstone bosons* or Higgs ghosts. At the classical level they can be rotated away by a gauge transformation, the so-called unitarity gauge, and only the massive electrical neutral real scalar field $h^0(x)$ with mass $m_{h^0} = \sqrt{2}\mu = \frac{v\lambda}{2}$ remains – the *Higgs boson*. Applying the expansion (2.9) together with the unitarity gauge rotation to eq. (2.7), the gauge interactions give rise to mass terms for three of the four W^i_μ, B_μ fields. However, these mass terms are non-diagonal and particularly the unbroken fields are not eigenstates of the remaining $U(1)_{\mathrm{EM}}$. After diagonalization, we find as physical fields the massive $W^\pm_\mu$, Z^0_μ and the massless A_μ as linear combinations of the unbroken fields,

$$W^\pm_\mu = \frac{1}{2}(W^1_\mu \pm W^2_\mu) , \tag{2.10}$$

$$Z^0_\mu = \cos\theta_W W^3_\mu \; - \; \sin\theta_W B_\mu , \tag{2.11}$$

$$A_\mu = \sin\theta_W W^3_\mu \; + \; \cos\theta_W B_\mu , \tag{2.12}$$

where the weak mixing angle θ_W is defined by

$$\cos\theta_W = \frac{g_2}{\sqrt{g_1^2 + g_2^2}} = \frac{m_W}{m_Z} , \qquad \sin\theta_W = \frac{g_1}{\sqrt{g_1^2 + g_2^2}} , \tag{2.13}$$

and the masses of $W^\pm_\mu$ and Z^0_μ are given by $m_W = \frac{g_2 v}{2}$ and $m_Z = \frac{v}{2}\sqrt{g_1^2 + g_2^2}$ respectively. The electric elementary charge e is now related to the gauge couplings g_1 and g_2 via $e = \frac{g_1 g_2}{\sqrt{g_1^2 + g_2^2}}$.

Finally, Yukawa couplings are realized in the Yukawa part $\mathcal{L}_{\mathrm{Yukawa}}$ of (2.7), which emerges automatically in the most general ansatz of a renormalizable, gauge- and Lorentz-invariant theory including the SM fermions and the Higgs doublet,

$$\mathcal{L}_{\mathrm{Yukawa}} = -\sum_{i,j=1}^{3} \left[y^d_{ij} (q^i_L)^\dagger \Phi d^j_R \; + y^u_{ij} (q^i_L)^\dagger \Phi^c u^j_R \; + y^l_{ij} (l^i_L)^\dagger \Phi e^j_R \; + \mathrm{h.c.} \right] , \tag{2.14}$$

where y^f_{if} with $f = \{d, u, l\}$ are the Yukawa couplings and $\Phi^c \equiv i\sigma^2 \Phi^*$. After EWSB quadratic mass terms for the fermions arise, $m^f_{ij} = \frac{v}{\sqrt{2}} y^f_{ij}$. These can be diagonalized by a bi-unitary transformation with $U^{f,L}_{ik}$ for the left-handed and $U^{f,R}_{ik}$ for the right-handed fermions, yielding the physical masses

$$m_{f,i} = \frac{v}{\sqrt{2}} \sum_{k,m}^{3} U^{f,L}_{ik} y^f_{km} \left(U^{f,R}_{mi} \right)^\dagger \equiv \frac{v}{\sqrt{2}} \lambda^f_i , \tag{2.15}$$

with λ_i^f being the Yukawa couplings in the mass eigenbasis. The transformation matrices $U_{ik}^{f,L}$ and $U_{ik}^{f,R}$ enter also in fermion-gauge–boson interactions as fermion gauge eigenstates do not match mass eigenstates. However, due to their unitarity they drop out of interactions with neutral gauge bosons and at tree-level flavor-changing neutral currents (FCNC) remain absent in the Standard Model [41]. On the other hand, charged currents mediated by $W^{\pm}$-bosons connect up- and down-type fermions and a non-trivial mixing matrix, $V_{\mathrm{CKM}} = U^{u,L}(U^{d,L})^{\dagger}$, remains. This Cabibbo–Kobayashi–Maskawa (CKM) matrix can be parametrized by four parameters, three angles and one complex phase, violating charge-parity conservation (CP).

Lagrangian at the quantum level

For a systematic renormalizble treatment of the SM at the quantum level (including higher orders in perturbation theory) the classical Lagrange density $\mathcal{L}_{\mathrm{SM}}^{\mathrm{classical}}$ (2.2) has to be extended by gauge fixing and corresponding Faddeev-Popov ghost terms [42],

$$\mathcal{L}_{\mathrm{SM}} = \mathcal{L}_{\mathrm{SM}}^{\mathrm{classical}} + \mathcal{L}_{\mathrm{fix}} + \mathcal{L}_{\mathrm{ghost}}\,, \tag{2.16}$$

as the unitarity gauge becomes unfeasible at higher orders. Instead, we add gauge fixing terms à la 't Hooft via

$$\mathcal{L}_{\mathrm{fix}} = -\frac{1}{2}\left(F_A^2 + F_Z^2 + 2F_+F_- + F_{G^a}^2\right), \tag{2.17}$$

with

$$F_A = \frac{1}{\xi^A}\partial^\mu A_\mu\,, \qquad F_{G^a} = \frac{1}{\xi^G}\partial^\mu G_\mu^a\,, \tag{2.18}$$

$$F_Z = \frac{1}{\xi^Z}(\partial^\mu Z_\mu^0 - m_Z\xi^Z\chi^0)\,, \qquad F_\pm = \frac{1}{\xi^W}(\partial^\mu W_\mu^\pm \mp im_W\xi^W\phi^\pm)\,, \tag{2.19}$$

and arbitrary gauge fixing parameters $\xi^{A,G,Z,W}$. Conveniently, they can all be set to $\xi = 1$ (the 't Hooft-Feynman gauge). This also fixes the corresponding gauge boson propagators. When applying this kind of gauge fixing, at the same time we have to add Faddeev-Popov ghost terms to cancel unphysical degrees of freedom. These ghost terms read

$$\mathcal{L}_{\mathrm{ghost}} = \bar{u}^\alpha(x)\frac{\delta F^\alpha}{\delta\theta^\beta(x)}u^\beta(x)\,, \tag{2.20}$$

with the unphysical scalar ghost fields $u^{A,Z,W^\pm,G^a}$. The term $\delta F^\alpha/\delta\theta^\beta(x)$ denotes the change of the gauge fixing operators F^α under infinitesimal gauge transformations.

2.1.2 Success of the Standard Model

The Standard Model as sketched above is a very successful theory of elementary particle interactions which passes many stringent high-precision experimental tests [39]. Here we want to quickly summarize some of its key achievements:

- The electroweak standard model is the simplest renormalizable theory we know, that explains in a consistent way all experimentally measured charged- and neutral-current interactions in a unified framework with QED as low-energy limit.

- At the same time it predicted the massive $W^{\pm}$ and Z^0 gauge bosons before their observation in high-energy experiments at CERN [43–46].

- The QCD part of the Standard Model successfully explains *asymptotic freedom* in terms of the running of the strong coupling constant,

$$\alpha_s(\mu^2) \equiv g_s^2(\mu)/4\pi \approx \frac{1}{\beta_0 \ln(\mu^2/\Lambda^2_{\mathrm{QCD}})}\,, \tag{2.21}$$

  with the one-loop QCD β-function, which depends on the SM particle content and is given by $\beta_0 = -\frac{3}{12}(11 - \frac{2}{3}n_f)$, with n_f being the number of relevant fermions; Λ_{QCD} is the (scheme-dependent) scale of QCD. At the same time quarks are confined into hadrons within the parton model and thus form all known baryons and mesons. Various experimental tests at different energy scales of deep inelastic scattering (DIS), jet cross sections, and events shapes confirm this picture.

- Particularly at the Large Electron-Positron Collider (LEP) at CERN, but also at the Tevatron at Fermilab and the Stanford Linear Collider (SLC) at SLAC, many high-precision tests of *electroweak precision observables* (EWPO) were performed which are all in good agreement with higher-order predictions of the Standard Model, see ref. [47] and references therein.

- These EWPO observables allowed a robust prediction of the top-quark mass before its discovery at the Tevatron [48, 49].

- Also the mass of the SM Higgs boson was predicted to $m_{h^0} = 89^{+35}_{-26}$ GeV by EWPO's [47] and agrees nicely with the recently observed Higgs-like boson at the LHC with a mass at about ≈ 125 GeV [27, 28]. After the identification of this new particle with the SM Higgs boson all parameters of the SM are in principle determined.

- Precision experiments particularly in the B- and K-systems allow for various precision tests of the flavor sector and thus of the CKM structure of the SM. All experiments are in good agreement with SM predictions [50].

- In the standard picture of the history of the Universe, all light elements heavier than the lightest isotope of hydrogen (particularly ^{2}H, ^{2}He, ^{3}He, ^{6}Li, ^{7}Be and ^{7}Li) were formed in a process called *Big Bang nucleosynthesis* (BBN). This process started when the Universe had a temperature of about $T \approx 10$ MeV and ended at temperatures below $T \approx 100$ keV. Applying calculations within the SM, the theory of BBN yields precise predictions for the abundance of the light elements, which are in good agreement with experimental observations.

2.1.3 Shortcomings of the Standard Model

Despite the above mentioned success of the Standard Model, there are various shortcomings, both conceptually and experimentally. In the following we want to list the most striking ones. All of them point towards some kind of new physics *beyond the Standard Model* (BSM).

- Most evidently, the SM does not include gravitational interactions, which should become important at energies of about the Planck scale $\Lambda_{\text{Planck}} \simeq 10^{19}$ GeV. However, there is little hope that the standard theory of gravity, *General Relativity* (GR), can be promoted to a quantum field theory. Thus, completely new approaches seem to be necessary, *string theory* being the most promising one.

- Various cosmological observations point towards large amounts of non-baryonic, non-luminous and only weakly interacting cold (=non-relativistic) *dark matter* (DM) in the Universe, which cannot be explained within the SM. Amongst others, rotation curves of galaxies and clusters of galaxies, precision measurements of the *cosmic microwave background* (CMB), measurements of *baryonic acoustic oscillations* (BAO), multi-particle simulations of structure formation and gravitational lensing observations of the "bullet cluster" (1E 0657-558) give strong evidence for dark matter [39]. The Planck collaboration, measuring the CMB very precisely, recently stated the energy density of dark matter in terms of the squared Hubble constant, $H_0 = h \cdot 100 \, \frac{\text{km}}{\text{Mpc s}}$, as [51]

$$\Omega_{\text{DM}} h^2 = 0.1199 \pm 0.0027 \,. \tag{2.22}$$

- Besides dark matter, many cosmological observations, including the CMB and the observation of distant supernovae, indicate another unknown component of the Universe: dark energy, which is responsible for an accelerated expansion of the Universe. Despite its responsibility for about 70% of the energy density of the Universe [51], there is currently no compelling model of explaining dark energy.

- From the simple requirements of renormalizability and gauge invariance, the Lagrange density in eq. (2.3) can in principle be extended by an additional term

$$\mathcal{L}_{\not{CP}} \propto \frac{g_s^2}{32\pi^2} \, G^a_{\mu\nu} \tilde{G}^{a\,\mu\nu} \,, \tag{2.23}$$

  where $\tilde{G}^a_{\mu\nu} = \frac{1}{2}\epsilon_{\mu\nu\sigma\rho} G^{\sigma\rho}$ is the dual of the gluon field-strength tensor. The resulting theory breaks CP in the strong sector. Experimentally only a very small CP violation is observed, consistent with the complex phase in the CKM matrix. Additional dynamics, particularly an additional Peccei-Quinn axion field [52], could solve this *strong CP-problem*.

- As already mentioned above, in the SM mass terms for neutrinos are not allowed, as right-handed neutrinos are absent. However, in neutrino oscillation experiments a small finite mass for them has been observed [39]. Any model containing mass terms for neutrinos necessarily requires BSM physics. At the moment mass splittings between the different neutrinos are well established, the absolute scale remains unknown and only upper limits exist [39]. Experimentally even the very nature of the neutrinos is unknown: it is not clear if they are of Dirac-type or Majorana-type. In principle a sterile right-handed neutrino could be introduced in the Standard Model, generating mass terms for the neutrinos via Yukawa couplings with the Higgs field. However, it is quite unnatural that the neutrinos are so much lighter then all other fermions.

- The amount of CP-violation in the SM from the complex phase in the CKM matrix is by far too small to explain the matter–anti-matter asymmetry observed in the visible Universe. A sufficient amount of CP violation, for example due to new physics, is a necessary condition for such an asymmetry [53].

- The current observable Universe to a large extent appears to be flat, homogeneous, and isotropic. This fact can elegantly be explained by a phase of exponential expansion of the early Universe, called *inflation*, governed by a dynamical cosmological constant (the inflaton) [54]. At the same time the appearance of large scale structures is explained by the expansion of quantum fluctuations to macroscopic size by the very same process. After inflation the Universe enters the thermal Big Bang phase at a temperature T_R. The details of inflation are currently unknown, however, observations from the Planck satellite [51] are consistent with the most simple models of slow-roll [55] single field inflation. More complicated models can be distinguished, e.g., by the appearance of large non-Gaussianities in the CMB (see for example refs. [56, 57]).

- Above we mentioned the good agreement between SM predictions and experimental measurements, for example for EWPOs. However, there exist a few measurements with (slightly) significant discrepancies. Here, we only want to mention the discrepancy for the anomalous magnetic dipole moment of the muon $a_\mu^{\text{exp}} - a_\mu^{\text{theo}}$, which is above the 3-sigma level [58], and the too large top–anti-top forward-backward asymmetry measured at the Tevatron [59]. These anomalies could be a hint for new physics.

- As mentioned above, after the successful observation of a Higgs boson at the LHC [27, 28], all SM parameters are in principle measured. Now, via renormalization group equations, their (running) values at a much higher scale μ can be calculated. Including two-loop and leading three-loop corrections, the authors of reference [29] showed that at some scale $\mu \approx 10^8 - 10^{15}$ GeV the Higgs self coupling λ, defined in eq. (2.8), turns negative. Although subject to large parametric uncertainties (of m_t and α_s), this would dangerously destabilize the EW vacuum of the Standard Model while realizing a Higgs potential unbounded from below. Nevertheless, we could live in a metastable EW vacuum with a lifetime longer than the age of the Universe, as also shown in [29].

- Furthermore, also the running gauge couplings g_1, g_2 and g_s can be calculated at some higher scale μ. Within the Standard Model, these couplings do not meet at a common point. However, the unification of these couplings in one point (typically at a scale $\mu = \Lambda_{\text{GUT}} \approx 10^{16}$ GeV) is a necessary condition for many *Grand Unified Theories* (GUTs), where the SM gauge groups are a subgroup of a larger group like $SU(5)$ [60] or $SO(10)$ [61]. In such GUT theories the quantization of the electric charge can naturally be explained.

- Finally, the Standard Model is a renormalizable theory, which means that any dependance on an ultraviolet cut-off scale can in principle be renormalized and thus vanishes. However, all of the aforementioned shortcomings of the SM point towards new BSM physics at some higher scale and thus introduce a physical cut-off scale Λ_{UV}. Now, this *can* introduces a dependance on Λ_{UV} of all low scale parameters. This problem becomes most severe considering the renormalized mass of the Higgs boson m_h^2. Being

a scalar this dependance is quadratic (at most logarithmic for all other parameters) and becomes manifest when calculating higher-order corrections to the (squared) bare Higgs mass $(m_h^0)^2$. These read at the one-loop level

$$m_h^2 = (m_h^0)^2 + \frac{3\Lambda_{\mathrm{UV}}^2}{8\pi v^2}(m_h^2 + 2m_W^2 + m_Z^2 - 4m_t^2)\,. \tag{2.24}$$

Here, the loop-momenta in the dominant contributions due to Higgs–self-interactions, Higgs-couplings with massive gauge bosons and the (heavy) top-quark, are all cut-off at the scale Λ_{UV}. Clearly, a cut-off scale of the order of $\Lambda_{\mathrm{Planck}}$ or Λ_{GUT} either forces the Higgs mass and/or the EW scale to be of the same high scale (which is not observed), or requires an unnatural amount of *finetuning* of independent parameters at each order of perturbation theory. Due to the unnatural hierarchy between the EW scale and the Planck scale this problem is also known as the *hierarchy problem*.

Many different models have been proposed to solve a number of these shortcomings. In this thesis we want to concentrate on the framework of SUSY as a compelling solution to the problems of dark matter, vacuum stability, unification and the hierarchy problems. In the following we introduce the concept of SUSY and highlight these solutions.

2.2 Supersymmetry as a solution

In this section we first introduce the concept of supersymmetry and state its solutions to some of the problems of the Standard Model, raised in the previous section. Afterwards we discuses the MSSM and its particle spectrum. Finally, a short introduction to the unavoidable breaking of SUSY is given. In this section we avoid detailed theoretical discussions, where we refer to [62–64], on which this section is based on.

2.2.1 Motivation

From a theoretical point of view the concept of supersymmetry can be introduced in a very elegant way: it is the only symmetry extending the Poincaré group in a non-trivial way.

According to the Coleman-Mandula theorem [65], any combination of the space-time Poincaré group with an internal symmetry group can only be built out of direct products of commuting operators. However, this no-go theorem can be, according to the Haag-Lopuszański-Sohnius theorem [12], circumvented for symmetries with anti-commuting operators. The resulting fermionic operator Q_A and its conjugate $\bar{Q}^{\dot{A}}$ are the generators of *supersymmetry* transformations. They commute with any internal gauge group and in a two-component Weyl spinor notation [63] they obey the following algebra

$$\begin{aligned} \{Q_A, Q_B\} &= \{\bar{Q}^{\dot{A}}, \bar{Q}^{\dot{B}}\} = 0\,, \\ \{Q_A, \bar{Q}_{\dot{B}}\} &= 2(\sigma^\mu)_{A\dot{B}} P_\mu\,. \end{aligned} \tag{2.25}$$

Together with P_μ and $M_{\mu\nu}$, the generators of the Poincaré group, they form a super-Poincaré algebra,

$$[Q_A, P_\mu] = [\bar{Q}^{\dot{A}}, P_\mu] = 0\,, \tag{2.26}$$
$$[Q_A, M_{\mu\nu}] = -\frac{1}{2}(\sigma_{\mu\nu})_A{}^B\, Q_B\,, \qquad [\bar{Q}_{\dot{A}}, M_{\mu\nu}] = -\frac{1}{2}(\bar{\sigma}_{\mu\nu})_{\dot{A}}{}^{\dot{B}}\, \bar{Q}_{\dot{B}}\,.$$

Here, σ_μ are the Pauli matrices defined above and $\sigma_{\mu\nu} = \frac{i}{2}(\sigma_\mu\bar{\sigma}_\nu - \sigma_\nu\bar{\sigma}_\mu)$ are their tensorial extensions. The corresponding particle states form irreducible representations of this algebra, which are called *supermultiplets*. From the SUSY algebra it is easy to derive two important results: first, the number of fermionic and bosonic degrees of freedom have to match for each supermultiplet; second, particles in the same multiplet have equal eigenvalues of $-P^2$ and thus equal masses. Furthermore, the SUSY generators commute with any internal gauge symmetry groups, hence, components of a supermultiplet have to be in the same representation of these internal groups. In principle, it is possible to have N SUSY generators. However, in four dimensions chiral fermions are forbidden for $N > 1$; thus, here we restrict ourselves to the phenomenological relevant case $N = 1$.

At this point of our discussion these SUSY transformations are purely global and thus induce constant translations in Minkowski space. Promoting it to a local symmetry, gravity can be incorporated resulting in so-called *supergravity*. We will briefly discuss this in section 2.4.

Applying the concept of supersymmetry to particle physics, the main result is that SUSY transformations change the spin of a particle by 1/2. That means a boson is transformed into a fermion and vice versa, which symbolically reads

$$Q\,|\text{boson}\rangle = |\text{fermion}\rangle\,, \qquad Q\,|\text{fermion}\rangle = |\text{boson}\rangle\ , \tag{2.27}$$

and the particles related in this way form a supermultiplet. In $N = 1$ SUSY, there are two fundamental multiplets: first, the chiral supermultiplet, formed out of a chiral spin-1/2 Weyl fermion and a complex spin-0 scalar; second, the vector multiplet, formed out of a spin-1 massless vector and a spin-1/2 Weyl fermion. Embedding the Standard Model into a supersymmetric theory we observe one problem: every SM particle should have a SUSY (super-)partner with equal mass and spin different by 1/2. Such SUSY partners have not been observed. Thus, if realized in nature, SUSY has to be broken at some scale, resulting in different masses for the components of a supermultiplet.

Let us now come to the solution of some of the problems mentioned in section 2.1 offered by SUSY.

- First, as we will explicitly see in section 2.3, in the simplest phenomenologically relevant SUSY model, the MSSM, the Higgs mass is not a free parameter. Here, in contrast to the SM, the quartic coupling of the Higgs is related to the gauge couplings. This is the main reason why there is no vacuum stability problem in the MSSM.

- Second, the additional SUSY particles contribute to the RGE running of the gauge couplings. Assuming now that these particles enter around the TeV-scale, the running

is altered in such a way that all gauge couplings automatically meet in one point at a scale $\sim \Lambda_{\mathrm{GUT}}$.

- Third, many SUSY models can easily provide a *weakly interacting, massive particle* (WIMP) stable on cosmological timescales. Such a particle serves as a perfect dark matter candidate.

- Fourth, we want to discuss the solution of the hierarchy problem. For each contribution to the Higgs mass, shown in eq. (2.24), there is a contribution from the corresponding superpartner. Due to the opposite spin of the corresponding particles they contribute with opposite sign and thus, in unbroken SUSY they exactly cancel the SM contribution. In the phenomenologically relevant class of models with softly broken SUSY (as explained below), the resulting dependance on the cut-off scale Λ_{UV} remains logarithmic [33, 34]. In such models, at the one-loop level the divergent terms in the correction to the Higgs mass are proportional to

$$\Delta m_h^2 \propto (m_f^2 - m_b^2) \log \Lambda_{\mathrm{UV}} \tag{2.28}$$

and thus to the mass difference $m_f^2 - m_b^2$ of the fermionic and bosonic degrees in a supermultiplet. Therefore, a theory with superparticle masses up to a scale $\sim \mathcal{O}(1\ \mathrm{TeV})$ solves the hierarchy problem. Looking at eq. (2.24), this is necessary in particular for the masses of the superpartners of the Higgs, the massive gauge bosons and the top.

2.2.2 SUSY Lagrangian

The dynamics of a SUSY theory can most elegantly be derived in terms of superfield and superspace notation. Here we sketch how a general renormalizable supersymmetric Lagrange density of a chiral supermultiplet interacting with a non-abelian vector supermultiplet can be realized. For details we refer to [63]. In section 2.3, this is used to derive the dynamics of the MSSM.

Superspace and superfields

The idea of superspace extends the usual four-dimensional Minkowski space-time by two Grassmannian, i.e. anticommuting, auxiliary dimensions θ^A and $\bar{\theta}_{\dot{A}}$. In this way the number of bosonic and fermionic degrees of freedom is automatically preserved for every point in superspace. Now, a superfield is simply a field on superspace, $\Phi = \Phi(x, \theta, \bar{\theta})$, and can be expanded in the following way:

$$\begin{aligned}\Phi = \Phi(x,\theta,\bar{\theta}) = \phi(x) + \sqrt{2}\theta\psi(x) + \sqrt{2}\bar{\theta}\bar{\chi}(x) + \theta\theta\ F(x) + \bar{\theta}\bar{\theta}\ H(x) \\ + \theta\sigma^\mu\bar{\theta}\ A_\mu(x) + \theta\theta\ \bar{\theta}\bar{\lambda}(x) + (\bar{\theta}\bar{\theta})\ \theta\zeta(x) + \theta\theta(\bar{\theta}\bar{\theta})D(x)\,.\end{aligned} \tag{2.29}$$

Here, ϕ, F, H, D are complex scalar fields, A_μ is a complex vector field and $\psi, \bar{\chi}, \bar{\lambda}, \zeta$ are two-component complex Weyl spinors. Spinor indices are not written explicitly. Due to the Grassmannian nature of θ and $\bar{\theta}$, there are no higher order terms in these variables. Invariance under SUSY transformations yield relations between these component fields. Overall, a general superfield Φ has 16 bosonic and 16 fermionic degrees of freedom. Clearly, constraints

on such general superfields have to be imposed to yield irreducible representations. First, we define SUSY covariant derivatives on superspace

$$\mathrm{D}_A = i\partial_A + (\sigma^\mu\bar{\theta})_A\partial_\mu\,, \qquad \bar{\mathrm{D}}_{\dot{A}} = i\bar{\partial}_{\dot{A}} - (\theta\sigma^\mu)_{\dot{A}}\partial_\mu\,, \tag{2.30}$$

where $\partial_A = \partial/\partial\theta^A, \bar{\partial}_{\dot{A}} = \partial/\partial\bar{\theta}^{\dot{A}}$. These derivatives anti-commute with the SUSY generators and thus work in analogy with covariant derivatives of gauge theories in order to build SUSY invariant quantities.

Now left-handed and right-handed chiral superfields and vector superfields can be defined by

$$\bar{\mathrm{D}}_{\dot{A}}\Phi_L = 0 \ \text{(left chiral)}\,, \qquad \mathrm{D}_A\Phi_R = 0 \ \text{(right anti-chiral)}\,, \qquad \Phi_V = \Phi_V^\dagger \ \text{(vector)}\,. \tag{2.31}$$

The product of two chiral superfields is again a chiral superfield, whereas a chiral together with its conjugate field yield a vector superfield. Expanding as before, the left-chiral superfield defined in this same way we find

$$\begin{aligned}\Phi_L(x,\theta) = \phi(x) - i\theta\sigma^\mu\bar{\theta}\partial_\mu\phi(x) - \frac{1}{4}\theta\theta\ \bar{\theta}\bar{\theta}\partial^\mu\partial_\mu\phi(x) \\ + \sqrt{2}\theta\psi(x) + \frac{i}{\sqrt{2}}\theta\theta\ \partial_\mu\psi\sigma^\mu\bar{\theta} + \theta\theta F(x)\,.\end{aligned} \tag{2.32}$$

There are four fermionic ($\psi(x)$) and four bosonic ($\phi(x), F(x)$) d.o.f., which reduce on-shell to two fermionic and two bosonic ones, as the equations of motion of the (auxiliary) F-term field $F(x)$ are trivial, $F = F^* = 0$. For the vector superfield a similar expansion yields in the Wess-Zumino gauge [66]

$$\Phi_V = \theta\sigma^\mu\bar{\theta}A_\mu(x) + \theta\theta\ \bar{\theta}\bar{\lambda}(x) + \bar{\theta}\bar{\theta}\theta\lambda(x) + \frac{1}{2}\theta\theta\ \bar{\theta}\bar{\theta}D(x)\,. \tag{2.33}$$

Again, an auxiliary D-term field $D(x)$ is necessary to match the off-shell d.o.f and thus to preserve SUSY. Here we want to note that the F- and D-term fields always transform as total derivatives under SUSY transformations. This can be exploited to construct a SUSY invariant action, where surface terms can always be discarded.

SUSY Lagrange density

The most general combination of left-chiral superfields yielding a renormalizable and SUSY invariant Lagrangian is given by[1]

$$\mathcal{L}_{\text{chiral}} = \left[\Phi_{Li}^\dagger\Phi_{Li}\right]_D + \left[\mathcal{W} + \text{h.c.}\right]_F\,, \tag{2.34}$$

with the *superpotential* $\mathcal{W}$ defined by

$$\mathcal{W}(\{\Phi_{Li}\}) = h_i\Phi_{Li} + \frac{1}{2}m_{ij}\Phi_{Li}\Phi_{Lj} + \frac{1}{3!}f_{ijk}\Phi_{Li}\Phi_{Lj}\Phi_{Lk}\,. \tag{2.35}$$

[1] In the notation $[\ldots]_{F/D}$ only the F/D-term component is taken, i.e., $[\ldots]_F = \int d^2\theta\ldots$ and $[\ldots]_D = \int d^2\theta d^2\bar{\theta}\ldots$.

Here, m_{ij} and f_{ijk} are symmetric couplings and taking only the D- and F-term contributions ensures SUSY invariance.

In order to formulate a kinetic term for a non-abelian vector superfield we define a supersymmetric field-strength tensor

$$W_A = -\frac{1}{4}\bar{\mathrm{D}}_{\dot{A}}\bar{\mathrm{D}}^{\dot{A}}e^{-2gV}\mathrm{D}_A e^{2gV}\,, \tag{2.36}$$

where $V = \Phi_V^a T^a$ and g, T^a are the corresponding gauge coupling and gauge group generators respectively. This field-strength tensor itself is a chiral superfield. Thus, taking only F-term contributions, the SUSY invariant kinetic term for the vector superfield is given by

$$\mathcal{L}_{\text{gauge}} = \left[\frac{1}{16g^2}\mathrm{Tr}(W^A W_A) + \text{h.c.}\right]_F\,. \tag{2.37}$$

Now we have to reformulate the kinetic term (D-term) of $\mathcal{L}_{\text{chiral}}$ to ensure gauge invariance. Under SUSY gauge transformations chiral and vector superfields transform as

$$\Phi_{Li} \to \left(e^{-i2g\Lambda}\right)_{ij}\Phi_{Lj}, \qquad e^{2gV} \to e^{-i2g\Lambda^\dagger}e^{2gV}e^{i2g\Lambda}\,. \tag{2.38}$$

Here, $\Lambda = \Lambda^a T^a$ and Λ^a are chiral superfields defining the local gauge transformations. Hence, a gauge and SUSY invariant kinetic term for a chiral superfield is given by

$$\mathcal{L}_{\text{kinetic}} = \left[\Phi_{Li}^\dagger\left(e^{2gV}\right)_{ij}\Phi_{Lj}\right]_D\,, \tag{2.39}$$

where all derivatives in (2.32) are replaced by covariant derivatives. The most general renormalizable, SUSY and gauge invariant Lagrange density now reads

$$\mathcal{L}_{\text{SUSY}} = \mathcal{L}_{\text{kinetic}} + \mathcal{L}_{\text{gauge}} + [\mathcal{W} + \text{h.c.}]_F\,, \tag{2.40}$$

which can be expanded into component fields for further phenomenological analysis. In section 2.3 we state the explicit result for the MSSM.

2.3 The MSSM and its particle spectrum

The *minimal supersymmetric Standard Model* (MSSM) is the minimal realistic anomaly free supersymmetric theory including all SM fields and gauge groups. It is currently the most studied SUSY theory and due to its large number of parameters it offers a very rich phenomenology, while still being highly predictive. Furthermore, the MSSM is a renormalizable theory, thus high-precision predictions of direct and indirect observables are possible. In the following we study its building blocks and the concept of R-parity; based on the results of the previous section we state the full MSSM Lagrange density including necessary soft SUSY-breaking terms. Afterwards we investigate the tree-level particle and mass spectrum of the MSSM and finish this section with a discussion of possible parametrizations.

type	name	label	bosonic field spin=0,1	fermionic field spin=1/2	$SU(3)_C$	$SU(2)_L$	Y
Φ_L	(s)quarks	Q	$\tilde{q}_L = (\tilde{u}_L, \tilde{d}_L)$	$q_L = (u_L, d_L)$	**3**	**2**	1/3
	(3 families)	$\bar{U}$	$\tilde{u}_R^*$	$\bar{u}_L = u_R^c$	$\bar{\mathbf{3}}$	**1**	-4/3
		$\bar{D}$	$\tilde{d}_R^*$	$\bar{d}_L = d_R^c$	$\bar{\mathbf{3}}$	**1**	2/3
	(s)leptons	L	$\tilde{l}_L = (\tilde{\nu}_e, \tilde{e}_L)$	$l_L = (\nu_e, e_L)$	**1**	**2**	-1
	(3 families)	$\bar{E}$	$\tilde{e}_R^*$	$\bar{e}_L = e_R^c$	**1**	**1**	2
	Higgs(inos)	H_u	$h_u = (h_u^+, h_u^0)$	$\tilde{h}_u = (\tilde{h}_u^+, \tilde{h}_u^0)$	**1**	**2**	1
		H_d	$h_d = (h_d^0, h_d^-)$	$\tilde{h}_d = (\tilde{h}_d^0, \tilde{h}_d^-)$	**1**	**2**	-1
Φ_V	gluon/gluino	G	G_μ^a	$\tilde{g}^a$	**8**	**1**	0
	(W)ino	W	W_μ^i	$\tilde{W}^i$	**1**	**3**	0
	(B)ino	B	B_μ	$\tilde{B}$	**1**	**1**	0

Table 2.2: Superfield content of the MSSM together with corresponding bosonic and fermionic component fields and representation under $SU(3)_C$, $SU(2)_L$ and hypercharge Y. Superfields are labeled with capital letters and component fields of SUSY particles carry a tilde. Family and color indices for the chiral superfields have been suppressed.

2.3.1 Principles and field content

In table 2.2 we list the (super)field content of the MSSM. All SM fermionic matter fields sit in left-chiral supermultiplets and all SM bosonic vector fields sit in vector multiplets. The Higgs sector is a two Higgs doublet model (2HDM) of left-chiral superfields, as discussed below.

As physical d.o.f., a left-chiral supermultiplet contains a two-component left-chiral Weyl fermion and a complex scalar. Thus, both the left-handed and the right-handed component of the SM chiral fermions get scalar partners, the *sfermions* – scalar quarks (*squarks*) and scalar leptons (*sleptons*). These scalars are still denoted left- and right-handed, $\tilde{f}_{L/R}$, referring to their quantum number fixed by the chirality of the corresponding SM fermionic state. They are named with a prefix s- (for example the left-handed stop $\tilde{t}_L$ is the SUSY partner of the left-handed component of the SM top).

The physical d.o.f. of a vector multiplet are a massless vector field and a two-component Weyl fermion. Thus, all SM gauge-bosons (which are massless before EWSB) get a fermionic partner – the *gauginos*. They are named with a suffix -ino. The neutral gauginos (gluino $\tilde{g}$, bino $\tilde{B}$, neutral wino $\tilde{W}^3$) are Majorana fermions, while the charged ones (charged winos $\tilde{W}^{1,2}$) form Dirac fermions.

Within the MSSM, EWSB proceeds similar to the SM: a scalar field spontaneously acquires a non-zero vev and the would-be Goldstone d.o.f. give mass to the gauge bosons of the broken symmetry. Unlike the SM, the MSSM requires two Higgs doublets instead of just one because of two reasons. First, for any anomaly free theory the sum of the hypercharge of all fermions has to cancel [67, 68]. The SM fermions alone yield an anomaly free theory

and the gauginos have all $Y = 0$. However, a supersymmetric Higgs sector introduces new fermions with $Y \neq 0$. Hence, at least two doublets are needed. In the MSSM a hypercharge $Y = \pm 1$ is assigned to these. Second, the superpotential of a supersymmetric theory has to be an analytic function of chiral superfields. Hence, the second term in eq. (2.14) involving a Φ^c could not emerge. Therefore, two Higgs doublets h_u and h_d with individual vevs v_2, v_1 are necessary, one giving mass to up-type fermions, one to down-type fermions. The fermionic partners within the Higgs superfields are Majorana for the neutral and Dirac for the charged components and named *Higgsinos*. Non-minimal supersymmetric extensions of the SM often involve more complex Higgs sectors. For example the next-to MSSM (NMSSM) includes an additional gauge singlet Higgs superfield.

The Lagrange density of the MSSM follows from the considerations in section 2.2.2 and is given by

$$\mathcal{L}_{\text{MSSM}} = \mathcal{L}^{\text{MSSM}}_{\text{kinetic}} + \mathcal{L}^{\text{MSSM}}_{\text{gauge}} + \mathcal{L}^{\text{MSSM}}_{\text{int}} + \mathcal{L}^{\text{MSSM}}_{\text{soft}} \,. \tag{2.41}$$

The kinetic terms of the chiral superfields including the gauge interactions read

$$\begin{aligned} \mathcal{L}^{\text{MSSM}}_{\text{kinetic}} = \Big[& Q^\dagger e^{2(g_1 B + g_2 W + g_s G)} Q + \bar{U}^\dagger e^{2(g_1 B + g_s G)} \bar{U} + \bar{D}^\dagger e^{2(g_1 B + g_s G)} \bar{D} \\ & + L^\dagger e^{2(g_1 B + g_2 W)} L + \bar{E}^\dagger e^{2 g_1 B} \bar{E} \\ & + H_u e^{2(g_1 B + g_2 W)} H_u + H_d e^{2(g_1 B + g_2 W)} H_d \Big]_D \,. \end{aligned} \tag{2.42}$$

The kinetic terms of the vector superfields in terms of super-field-strength tensors read

$$\mathcal{L}^{\text{MSSM}}_{\text{gauge}} = \left[\frac{1}{16 g_s^2} \text{Tr}(W_G{}^A W_{GA}) + \frac{1}{16 g_2^2} \text{Tr}(W_W{}^A W_{WA}) + \frac{1}{16 g_1^2} \text{Tr}(W_B{}^A W_{BA}) \right]_F \,. \tag{2.43}$$

All other interactions follow from the superpotential,

$$\mathcal{L}^{\text{MSSM}}_{\text{int}} = \left[\mathcal{W}^{\text{MSSM}} + \text{h.c.} \right]_F \,, \tag{2.44}$$

which for the MSSM is defined by

$$\mathcal{W}^{\text{MSSM}} = \mu H_u \cdot H_d - y^u_{ij} \bar{U}_i Q_j \cdot H_u - y^d_{ij} \bar{D}_i Q_j \cdot H_d - y^e_{ij} \bar{E}_i L_j \cdot H_d \,. \tag{2.45}$$

Until now, excluding $\mathcal{L}^{\text{MSSM}}_{\text{soft}}$, the parameter μ of the bilinear $H_u \cdot H_d$ coupling remains the only newly introduced free parameter besides the ratio of the two Higgs vevs, denoted by $\tan\beta$ – defined and motivated below.

The superpotential of the MSSM $\mathcal{W}^{\text{MSSM}}$ does not include all terms allowed by SUSY and gauge invariance. The included terms have been constrained by requiring an additional symmetry called R-parity. Without R-parity conservation, terms violating baryon number B and lepton number L would be allowed. Amongst others, this would lead to unwanted rapid proton decay. R-parity for the component fields of a supermultiplet can be defined as

$$R = (-1)^{3(B-L)+2s} \,, \tag{2.46}$$

where s is the spin of a particle. In this way all SM particles are even, and all SUSY partners are odd under this parity. R-parity could emerge naturally in SUSY GUT theories including a spontaneously broken continuous $U(1)_{B-L}$ symmetry. In the MSSM, R-parity is an exact symmetry which has two phenomenologically important consequences: first, the *lightest supersymmetric particle* is rendered stable and thus serves as viable Dark Matter candidate if it is only weakly interacting. If it is charged, strong cosmological bounds on its relic density exist. These issues will be discussed in more detail in section 3.7. Second, at colliders SUSY particles are always produced in pairs and then subsequently decay into the LSP emitting SM particles. In many scenarios this leads to high-multiplicity signatures.

Many extensions of the MSSM allow for some amount of R-parity violation [69–73]. For completeness we list therefore in the following the corresponding R-parity violating terms of the superpotential allowed by gauge invariance and supersymmetry,

$$\mathcal{W}_{\not R}^{\text{MSSM}} = -\epsilon_i L_i \cdot H_u + \frac{1}{2}\lambda_{ijk} L_i \cdot L_j \bar{E}_k + \lambda'_{ijk} L_i \cdot Q_j \bar{D}_k + \frac{1}{2}\lambda''_{ijk} \bar{U}_i \bar{D}_j \bar{D}_k \,. \tag{2.47}$$

Soft SUSY breaking

As already discussed, SUSY cannot be an exact symmetry of nature but has to be broken at some scale. The dynamics of this breaking are far from clear and various models are under consideration. We will highlight some of the most important aspects and phenomenological implications in section 2.4. In the MSSM consequences of this breaking are parametrized introducing explicit SUSY breaking terms. However, the solution to the hierarchy problem should not be spoiled by these terms. Hence, only terms that do not introduce additional quadratic divergences are allowed. Such terms have mass dimension less than four and are called *soft breaking terms*. The most general ansatz for soft breaking terms involving chiral and vector superfields is given by

$$\mathcal{L}_{\text{soft}} = -\frac{1}{2}(M\lambda^a\lambda^a + \text{h.c.}) - \phi_i^*(m^2)_{ij}\phi_j + \left(\frac{1}{3!}A_{ijk}\phi_i\phi_j\phi_k - \frac{1}{2}B_{ij}\phi_i\phi_j + C_i\phi_i + \text{h.c.}\right). \tag{2.48}$$

Here, ϕ_i is the scalar part of a chiral superfield and λ a gaugino. The trilinear, bilinear, and linear couplings A_{ijk}, B_{ij}, and C_i and the mass terms m^2 and M are additional parameters of the theory. The corresponding gauge invariant Lagrangian for the MSSM is given by [74, 75]

$$\begin{aligned}
\mathcal{L}_{\text{soft}}^{\text{MSSM}} = &-\frac{1}{2}\left(M_1\ \tilde{B}\tilde{B} + M_2\ \tilde{W}^i\tilde{W}^i + M_3\ \tilde{g}^a\tilde{g}^a + \text{h.c.}\right) \\
&- \tilde{q}_{iL}^\dagger (m_{\tilde{Q}}^2)_{ij}\tilde{q}_{jL} - \tilde{u}_{iR}^*(m_{\tilde{U}}^2)_{ij}\tilde{u}_{jR} - \tilde{d}_{iR}^*(m_{\tilde{D}}^2)_{ij}\tilde{d}_{jR} \\
&- \tilde{l}_{iL}^\dagger (m_{\tilde{L}}^2)_{ij}\tilde{l}_{jL} - \tilde{e}_{iR}^*(m_{\tilde{E}}^2)_{ij}\tilde{e}_{jR} \\
&- m_{h_u}^2 h_u^\dagger h_u - m_{h_d}^2 h_d^\dagger h_d - (b\ h_u \cdot h_d + \text{h.c.}) \\
&- \left[(a^u)_{ij}\tilde{u}_{iR}\,\tilde{q}_{jL}\cdot h_u + (a^d)_{ij}\tilde{d}_{iR}\,\tilde{q}_{jL}\cdot h_d + (a^e)_{ij}\tilde{e}_{iR}\,\tilde{l}_{jL}\cdot h_d + \text{h.c.}\right].
\end{aligned} \tag{2.49}$$

Here, soft-masses for the gauginos M_1, M_2, M_3 are introduced in the first line, soft-masses for the squarks and sleptons in the second and third line respectively, soft Higgs-mass terms

and bilinear couplings in the fourth line and sfermion-sfermion-Higgs trilinear couplings in the fifth line. The trilinear couplings with indices i, j in family space are usually expressed in terms of Yukawa couplings $y_{ij}^{u,d,e}$,

$$a_{ij}^{f} = \left(y^{f} A_{f}\right)_{ij} . \tag{2.50}$$

A linear term ($\sim C_i$ in eq. (2.48)) is not included in eq. (2.49) due to gauge invariance.

Counting the number of free parameters introduced in in the MSSM, allowing in general for complex phases, we end up with 105 new parameters (including μ and $\tan\beta$). However, one should keep in mind that this is a mere parametrization and any realistic SUSY breaking dynamics reduces this number drastically. In section 2.3.3 we introduce a phenomenologically motivated parametrization with 19 free parameters.

2.3.2 Particle spectrum of the MSSM

In this section we want to introduce the physical particle spectrum of the MSSM at tree-level. First we explain EWSB within the MSSM, focusing on the differences with respect to the SM. Afterwards, we discuss the fermion, sfermion and gaugino mass eigenstates including soft breaking contributions.

EWSB sector

The Higgs sector of the MSSM involves two complex Higgs doublets with hypercharge $Y = \pm 1$. This results in eight d.o.f. of which, after both doublets develop individual vevs, three would-be Goldstone bosons give mass to the W and Z bosons. The remaining five d.o.f. constitute the five physical Higgs bosons of the MSSM: two are neutral and CP-even, h^0 and H^0, one is neutral and CP-odd, A^0, and two are charged, $H^{\pm}$. Still, at tree-level two independent parameters are sufficient to describe the Higgs sector of the MSSM, as explained in the following.

The scalar Higgs potential of the MSSM is given by

$$\begin{aligned} V_h = {} & (m_{h_u}^2 + |\mu|^2) h_u^{\dagger} h_u + (m_{h_d}^2 + |\mu|^2) h_d^{\dagger} h_d + (b h_u \cdot h_d + \text{h.c.}) \\ & + \frac{g_1^2 + g_2^2}{8} (h_u^{\dagger} h_u - h_d^{\dagger} h_d)^2 + \frac{g_2^2}{2} |h_d^{\dagger} h_u|^2 . \end{aligned} \tag{2.51}$$

In contrast to the SM, here all Higgs self-interaction terms are determined by gauge-couplings. As in the SM, the Higgs fields of the MSSM develop non-vanishing vevs in their uncharged components,

$$\langle h_d \rangle = \frac{1}{\sqrt{2}} \begin{pmatrix} v_1 \\ 0 \end{pmatrix} , \qquad \langle h_u \rangle = \frac{1}{\sqrt{2}} \begin{pmatrix} 0 \\ v_2 \end{pmatrix} . \tag{2.52}$$

In principle, the scalar potential of the MSSM also includes the scalar sfermions. For large enough couplings these could also develop non-vanishing vevs resulting in dangerous *charge or color breaking* (CCB) minima. Hence, non-occurrence of such CCBs can be translated into theoretical upper bounds on couplings in the sfermion sector and thus on the viable

MSSM parameter space. This will be discussed in more detail and the special case of large stau-stau-Higgs couplings in section 7.1.4 and Appendix C respectively. When ignoring the sfermion contributions in the Higgs potential (2.51), the requirements for non-zero vevs and a bounded-from-below potential yields the conditions

$$m_{h_u}^2 + m_{h_d}^2 + 2|\mu|^2 > 2|b|\,, \tag{2.53}$$

$$(m_{h_u}^2 + |\mu|^2)(m_{h_d}^2 + |\mu|^2) < b^2\,. \tag{2.54}$$

Clearly, in unbroken SUSY ($m_{h_u}^2 = m_{h_d}^2 = b = 0$) EWSB would not be possible.

Now, in analogy to the SM, the MSSM Higgs fields are expanded around their ground states,

$$h_d = \begin{pmatrix} \frac{1}{\sqrt{2}}(v\cos\beta + \phi_1 + i\chi_1) \\ h_1^- \end{pmatrix}, \qquad h_u = \begin{pmatrix} h_2^+ \\ \frac{1}{\sqrt{2}}(v\sin\beta + \phi_2 + i\chi_1) \end{pmatrix}, \tag{2.55}$$

where we introduced the important parameter

$$\tan\beta = \frac{v_2}{v_1} \tag{2.56}$$

and relate the MSSM vevs v_1, v_2 via $v = \sqrt{v_1^2 + v_2^2} \approx 246$ GeV with the SM Higgs ground state. In this way the masses for the massive SM gauge bosons are determined in the very same way as in the SM (see section 2.1). This expansion (2.55) is plugged into the Higgs potential (2.51) and yields the Higgs mass eigenstates after diagonalization of the quadratic terms. The neutral CP-even Higgses h^0, H^0 are related to ϕ_1, ϕ_2; the neutral CP-odd A^0 and the neutral Goldstone boson G^0 are related to χ_1, χ_2; and the charged Higgses $H^\pm$ and Goldstone bosons $G^\pm$ are related to $h_1^\pm, h_2^\pm$ via unitary transformations

$$\frac{1}{\sqrt{2}}\begin{pmatrix} H^0 \\ h^0 \end{pmatrix} = U(\alpha)\begin{pmatrix} \phi_1 \\ \phi_2 \end{pmatrix}, \quad \frac{1}{\sqrt{2}}\begin{pmatrix} G^0 \\ A^0 \end{pmatrix} = U(\beta')\begin{pmatrix} \chi_1 \\ \chi_2 \end{pmatrix}, \quad \begin{pmatrix} G^\pm \\ H^\pm \end{pmatrix} = U(\beta'')\begin{pmatrix} h_1^\pm \\ h_2^\pm \end{pmatrix}, \tag{2.57}$$

with a unitary matrix $U(\gamma)$,

$$U(\gamma) = \begin{pmatrix} \cos\gamma & \sin\gamma \\ -\sin\gamma & \cos\gamma \end{pmatrix}. \tag{2.58}$$

At tree-level $\beta' = \beta'' = \beta$ and the mixing angles α and β are related by

$$\tan 2\alpha = \tan 2\beta\, \frac{m_{A^0}^2 + m_Z^2}{m_{A^0}^2 - m_Z^2}\,. \tag{2.59}$$

The tree-level masses of the Higgs bosons and would-be Goldstone bosons are given by

$$m_{h^0,H^0}^2 = \frac{1}{2}\left(m_{A^0}^2 + m_Z^2 \mp \sqrt{(m_{A^0}^2 + m_Z^2)^2 - 4m_Z^2 m_{A^0}^2 \cos^2 2\beta}\right), \tag{2.60}$$

$$m_{A^0}^2 = b(\tan\beta + \cot\beta) = m_{h_d}^2 + m_{h_u}^2 + 2|\mu|^2\,, \tag{2.61}$$

$$m_{H^\pm}^2 = m_{A^0}^2 + m_W^2\,. \tag{2.62}$$

For convenience, m_{A^0} and $\tan\beta$ are usually chosen as free parameters in the MSSM Higgs sector. In this way the masses of the CP-even and the charged Higgses are fixed and particularly for the mass of the lighter neutral CP-even Higgs m_{h^0} the following lower bound applies

$$m_{h^0} < \min(m_{A^0}, m_{\mathrm{Z}})\,. \tag{2.63}$$

Such a light Higgs boson would have already been excluded by Higgs searches at LEP and could not explain the observed state at the LHC at ≈ 125 GeV. However, higher-order corrections to these tree-level predictions are large [76], and the leading (top) one-loop contributions including squark mixing effects shift m_{h^0} upwards by (assuming $m_{A^0} \gg m_{\mathrm{Z}}$) [77]

$$(\Delta m_{h^0}^{(1)})^2 = \frac{3g_2^2}{8\pi^2 m_{\mathrm{W}}^2} m_t^4 \left[-\log\frac{m_t^2}{M_S^2} + \frac{X_t^2}{M_S^2}\left(1 - \frac{1}{12}\frac{X_t^2}{M_S^2}\right)\right], \tag{2.64}$$

where $M_S = m_{A^0} \gg m_t$ is the scale of SUSY breaking and particularly of the diagonal elements of the top squark mixing matrix, as defined below, where also X_t is introduced parameterizing the off-diagonal elements of this mixing matrix. Thus, sizable stop masses and/or large stop left-right mixing, i.e., large A_t are necessary to give $m_{h^0} \approx 125$ GeV. Further implications from the LHC on MSSM Higgs phenomenology are given in section 3.5.

Fermion sector

Standard model fermions get their masses in a very similar way as in the SM: via a Yukawa coupling with the Higgs sector. However, at tree-level up-type fermions only couple to h_u and down-type fermions to h_d. Thus, relations between Yukawa couplings and masses are altered in the following way

$$\frac{\lambda_u}{\sqrt{2}} = \frac{m_u}{v_2} = \frac{m_u}{v\sin\beta}\,, \quad \frac{\lambda_d}{\sqrt{2}} = \frac{m_d}{v_1} = \frac{m_d}{v\cos\beta}\,, \quad \frac{\lambda_e}{\sqrt{2}} = \frac{m_e}{v_1} = \frac{m_e}{v\cos\beta}\,. \tag{2.65}$$

Therefore, Yukawa couplings of down-type fermions (relevant particularly for the third generation bottom and tau) can be enhanced significantly for large $1/\cos\beta \sim \tan\beta$.

Sfermion sector

After electroweak symmetry breaking the soft-breaking terms in the MSSM Lagrangian induce mixing between the left- and right-handed gauge eigenstates in the sfermion sector. Under the assumption of minimal flavor violation, as defined below, the sfermion mass matrices and trilinear couplings are diagonal in family space and no mixing occurs amongst different flavors. Here we show results for one family – generalization is straightforward. Furthermore, we assume all parameters to be real. Including all F-term, D-term and soft-term contributions, the sfermion-mass-squared matrix then reads in the basis of gauge eigenstates $(\tilde{f}_L, \tilde{f}_R)$, $\tilde{f} = \{\tilde{u}, \tilde{d}, \tilde{e}\}$:

$$M_{\tilde{f}}^2 = \begin{pmatrix} m_f^2 + m_{\mathrm{LL}}^2 & m_f X_f \\ m_f X_f & m_f^2 + m_{\mathrm{RR}}^2 \end{pmatrix} = (U_{\tilde{f}})^\dagger \begin{pmatrix} m_{\tilde{f}_1}^2 & 0 \\ 0 & m_{\tilde{f}_2}^2 \end{pmatrix} U_{\tilde{f}}, \tag{2.66}$$

with

$$\begin{aligned} m^2_{\mathrm{LL}} &= m^2_{\tilde{f}_L} + \left(I^3_f - Q_f \sin^2\theta_W\right) m^2_{\mathrm{Z}} \cos 2\beta, \\ m^2_{\mathrm{RR}} &= m^2_{\tilde{f}_R} + Q_f \sin^2\theta_W \, m^2_{\mathrm{Z}} \cos 2\beta, \\ X_f &= A_f - \mu\kappa \ . \end{aligned} \tag{2.67}$$

Here, $m_{\tilde{f}_L}$ and $m_{\tilde{f}_R}$ are the left-handed and right-handed sfermion soft-breaking masses, A_f is the trilinear coupling and $\kappa = \cot\beta$ for up-type squarks and $\kappa = \tan\beta$ for down-type squarks and electron-type sleptons. The off-diagonal terms are proportional to the fermion mass and thus negligible for first- and second-generation sfermions. For third generation sfermions we have to diagonalize their mass matrix and as indicated in (2.66), the mixing matrix can be diagonalized by an orthogonal 2×2 matrix $U_{\tilde{f}}$, parametrized by the sfermion mixing angle θ_f,

$$U_{\tilde{f}} = \begin{pmatrix} \cos\theta_f & \sin\theta_f \\ -\sin\theta_f & \cos\theta_f \end{pmatrix} . \tag{2.68}$$

The quadrant of θ_f is fixed such that $\tilde{f}_1$ is the lighter of the two eigenstates. Now, the sfermion mass eigenvalues squared are given by

$$m^2_{\tilde{f}_1,\tilde{f}_2} = m^2_f + \frac{1}{2}\left[m^2_{\mathrm{RR}} + m^2_{\mathrm{LL}} \mp \sqrt{(m^2_{\mathrm{LL}} - m^2_{\mathrm{RR}})^2 + 4m^2_\tau |X_\tau|^2}\right] , \tag{2.69}$$

and the mixing angle is determined by

$$\tan 2\theta_f = \frac{2m_f X_f}{m^2_{\mathrm{LL}} - m^2_{\mathrm{RR}}} , \qquad \text{and} \qquad \sin 2\theta_f = \det(U_{\tilde{f}}) \frac{2m_f X_f}{m^2_{\tilde{f}_1} - m^2_{\tilde{f}_2}}. \tag{2.70}$$

Equation (2.70) gives a direct relation between the mixing angle, the off-diagonal parameter X_f and the gauge eigenstates $(\tilde{f}_L, \tilde{f}_R)$ or mass eigenstates $(\tilde{f}_1, \tilde{f}_2)$.

The MSSM does only include right-handed (s)neutrinos, thus sneutrinos do not mix and their mass is given by

$$m_{\tilde{\nu}} = m^2_{\tilde{L}} + \frac{1}{2} m^2_Z \cos 2\beta \, . \tag{2.71}$$

Stau-Higgs couplings

In chapter 7 we are in particular interested in the stau sector of the MSSM and in couplings of the lighter stau with the different Higgs eigenstates. Thus, we discuss these couplings in detail in the following.

In the MSSM, the sfermions couple directly to the Higgs fields via dimensionful parameters. The stau-Higgs couplings are given by

$$\mathcal{L}_{\tilde{\tau}\tilde{\tau}\mathcal{H}} = \frac{g}{m_{\mathrm{W}}} \sum_{I,J=\mathrm{L,R}} \tilde{\tau}^*_I \, \tilde{C}[\tilde{\tau}^*_I, \tilde{\tau}_J, \mathcal{H}] \, \tilde{\tau}_J \, \mathcal{H} \, , \tag{2.72}$$

where $\mathcal{H}$ stands for any of the neutral Higgs and Goldstone bosons, $\mathcal{H} = h^0, H^0, A^0, G^0$ [78]. In the basis of the gauge eigenstates $(\tilde{\tau}_L, \tilde{\tau}_R)$, the reduced coupling $\tilde{C}[\tilde{\tau}_I^*, \tilde{\tau}_J, h^0]$ reads

$$\tilde{C}[\tilde{\tau}_I^*, \tilde{\tau}_J, h^0] = \begin{pmatrix} -\frac{\cos 2\theta_W}{2} m_{\mathrm{Z}}^2 s_{\alpha+\beta} + m_\tau^2 \frac{s_\alpha}{c_\beta} & \frac{m_\tau}{2}\left(A_\tau \frac{s_\alpha}{c_\beta} + \mu \frac{c_\alpha}{c_\beta}\right) \\ \frac{m_\tau}{2}\left(A_\tau \frac{s_\alpha}{c_\beta} + \mu \frac{c_\alpha}{c_\beta}\right) & -\sin^2\theta_W m_{\mathrm{Z}}^2 s_{\alpha+\beta} + m_\tau^2 \frac{s_\alpha}{c_\beta} \end{pmatrix} , \tag{2.73}$$

and $\tilde{C}[\tilde{\tau}_I^*, \tilde{\tau}_J, H^0]$ can be obtained upon the replacement $\alpha \to \alpha - \pi/2$. Here and in the rest of this thesis, the shorthand notation $c_\gamma \equiv \cos\gamma$ and $s_\gamma \equiv \sin\gamma$ is used. The reduced coupling for the CP-odd Higgs boson A^0 reads

$$\tilde{C}[\tilde{\tau}_I^*, \tilde{\tau}_J, A^0] = \begin{pmatrix} 0 & +i\,\frac{m_\tau}{2}\left(A_\tau \tan\beta + \mu\right) \\ -i\,\frac{m_\tau}{2}\left(A_\tau \tan\beta + \mu\right) & 0 \end{pmatrix} , \tag{2.74}$$

and $\tilde{C}[\tilde{\tau}_I^*, \tilde{\tau}_J, G^0]$ can be obtained upon the replacement: $A_\tau \tan\beta + \mu \to \mu \tan\beta - A_\tau$.

We are particularly interested in the couplings between the lighter mass eigenstate $\tilde{\tau}_1$ and the CP-even Higgs bosons h^0 and H^0. These can be found by diagonalizing the coupling matrix in (2.73) with the orthogonal matrix $U_{\tilde{\tau}}$ defined in (2.68):

$$C[\tilde{\tau}_1^*, \tilde{\tau}_1, h^0] = \left(-\frac{1}{2}c_{\theta_\tau}^2 + \sin^2\theta_W c_{2\theta_\tau}\right) m_{\mathrm{Z}}^2 s_{\alpha+\beta} + m_\tau^2 \frac{s_\alpha}{c_\beta} + \frac{m_\tau}{2}\left(A_\tau \frac{s_\alpha}{c_\beta} + \mu \frac{c_\alpha}{c_\beta}\right) s_{2\theta_\tau} \ . \tag{2.75}$$

The coupling $C[\tilde{\tau}_1^*, \tilde{\tau}_1, H^0]$ can be read from (2.75) after the replacement $\alpha \to \alpha - \pi/2$, whereas the diagonal coupling to the CP-odd Higgs boson A^0 vanishes: $C[\tilde{\tau}_1^*, \tilde{\tau}_1, A^0] = 0$.
In the decoupling limit ($m_{A^0} \gg m_Z$) where $a \to \beta - \frac{\pi}{2}$ and for large $\tan\beta$ the couplings read

$$C[\tilde{\tau}_1^*, \tilde{\tau}_1, h^0] \overset{m_{A^0} \gg m_Z, \tan\beta \gg 1}{\simeq} m_{\mathrm{Z}}^2 \left(\frac{1}{2}c_{\theta_\tau}^2 - \sin^2\theta_W c_{2\theta_\tau}\right) c_{2\beta} + \frac{m_\tau}{2}\left(\mu \tan\beta - A_\tau\right) s_{2\theta_\tau} \ , \tag{2.76}$$

$$C[\tilde{\tau}_1^*, \tilde{\tau}_1, H^0] \overset{m_{A^0} \gg m_Z, \tan\beta \gg 1}{\simeq} -m_\tau^2 \tan\beta - \frac{m_\tau}{2}\left(A_\tau \tan\beta + \mu\right) s_{2\theta_\tau} \ . \tag{2.77}$$

Thus, the SUSY parameters μ and A_τ enter proportional to $\sin 2\theta_\tau$ and the couplings peak at $\theta_\tau = \pi/4$. In the coupling with the lighter (heavier) Higgs the term proportional to μ (A_τ) is enhanced by large $\tan\beta$.

Gaugino sector

The superpartners of the electroweak gauge bosons, the electroweak gauginos together with the superpartners of the Higgses, the Higgsinos, can be separated into two classes with identical quantum numbers and thus possible large mixing. On the one hand, there are the neutral *neutralinos* $\tilde{\chi}_i^0$. They are Majorana fermions and mixed states of $(\Psi^0)^T = (\tilde{B}^0, \tilde{W}^3, \tilde{h}_d^0, \tilde{h}_u^0)$. Their mass matrix is given by

$$M_{\tilde{N}^0} = \begin{pmatrix} M_1 & 0 & -c_\beta\, s_W\, m_Z & s_\beta\, s_W\, m_Z \\ 0 & M_2 & c_\beta\, c_W\, m_Z & -s_\beta\, c_W\, m_Z \\ -c_\beta\, s_W\, m_Z & c_\beta\, c_W\, m_Z & 0 & -\mu \\ s_\beta\, s_W\, m_Z & -s_\beta\, c_W\, m_Z & -\mu & 0 \end{pmatrix} , \tag{2.78}$$

with $s_W = \sin\theta_W$ and $c_W = \cos\theta_W$. This matrix can be diagonalized by a 4×4 unitary matrix N yielding the mass eigenstates

$$M_{\tilde{\chi}^0} = N^* M_{\tilde{N}^0} N^\dagger \,. \tag{2.79}$$

On the other hand, there are the positively and negatively charged *charginos*, mixtures of $(\Psi^\pm)^T = (\tilde{W}^\pm, \tilde{h}^\pm_{u,d})$. They are Dirac fermions with a mass matrix

$$M_{\tilde{C}^\pm} = \begin{pmatrix} M_2 & \sqrt{2}\sin\beta\, m_W \\ \sqrt{2}\cos\beta\, m_W & \mu \end{pmatrix} . \tag{2.80}$$

This matrix can be diagonalized by a bi-unitary transformation with V for the positive and U for the negative states, giving the chargino mass eigenstates

$$M_{\tilde{\chi}^\pm} = U^* M_{\tilde{C}^\pm} V^\dagger \,. \tag{2.81}$$

The *gluino* is the superpartner of the gluon. In the MSSM it is a Majorana fermion and does not mix with any other particle. Its tree-level mass arises purely from the soft-breaking $SU(3)_C$ mass term,

$$m_{\tilde{g}} = M_3 \,. \tag{2.82}$$

2.3.3 Parametrization of the MSSM

The kinetic and gauge-kinetic terms of the MSSM Lagrangian (eqs. (2.42) and (2.43)) are fully determined by parameters already present in the SM. The superpotential of the MSSM, eq. (2.45), only introduces the μ parameter and indirectly via EWSB the ratio of the Higgs vevs, $\tan\beta$. However, the parametrization of SUSY breaking via soft breaking terms in eq. (2.49) introduces a plethora of new parameters: the gaugino soft-mass terms $M_{1,2,3}$ and the Higgs bilinear coupling b are in general complex; the sfermion soft-mass matrices $m_{\tilde{f}}$ and the trilinear couplings a^f are hermitian 3×3 matrices in family space; the Higgs soft-masses $m_{h_{u,d}}$ are real. All together without additional assumptions, as already mentioned, 105 new parameters are introduced in terms of couplings, masses and complex phases. But many of these parameters are strongly constrained particularly by the non-observation of FCNC [79, 80] or extra CP violation [81]. This can be solved by the assumption of *minimal flavor violation* (MFV), i.e., assuming no new CP violation besides from the CKM matrix (all new parameters to be real) and assuming all mass matrices and trilinear couplings to be diagonal in family space. This leaves 33 new parameters in the general *MFV MSSM*.

This number can be further reduced to 19 new parameters assuming that soft masses of the first and second generation are equal and including only the most relevant (third generation) trilinear couplings A_t, A_b, A_τ. Thus, the free parameters of this *p19MSSM* are

$$\mu,\ m_A^0,\ \tan\beta,\ M_1,\ M_2,\ M_3,\ A_t,\ A_b,\ A_\tau, \tag{2.83}$$

$$\begin{aligned} &m_{\tilde{Q}} = m_{\tilde{u}_L} = m_{\tilde{d}_L} = m_{\tilde{c}_L} = m_{\tilde{s}_L},\ m_{\tilde{U}} = m_{\tilde{u}_R} = m_{\tilde{c}_R},\ m_{\tilde{D}} = m_{\tilde{d}_R} = m_{\tilde{s}_R}, \\ &m_{\tilde{L}} = m_{\tilde{e}_L} = m_{\tilde{\mu}_L},\ m_{\tilde{E}} = m_{\tilde{e}_R} = m_{\tilde{\mu}_R}, \\ &m_{\tilde{Q}_3} = m_{\tilde{t}_L} = m_{\tilde{b}_L},\ m_{\tilde{U}_3} = m_{\tilde{t}_R},\ m_{\tilde{D}_3} = m_{\tilde{b}_R},\ m_{\tilde{L}_3} = m_{\tilde{\tau}_L},\ m_{\tilde{E}_3} = m_{\tilde{\tau}_R} \,. \end{aligned} \tag{2.84}$$

We will make continuous use of this parametrization in this thesis.

The constrained MSSM

A further simplification can be achieved assuming additional constraints imposed by the details of the dynamics of SUSY breaking. In general, this results in different relations between soft breaking parameters at some higher scale. The weak scale parameters are then obtained by MSSM RGE running. Such running is efficiently implemented, e.g., in the computer programs `SPheno` [82], `SOFTSUSY` [83] and `SUSY-HIT` [84]. Aspects of SUSY breaking are discussed in the next section. Here, we merely want to introduce a benchmark framework inspired by minimal gravity mediation of SUSY breaking, as discussed below, called *Constrained MSSM* (CMSSM).

Within the CMSSM universal gaugino masses $m_{1/2}$, universal scalar soft masses m_0 and universal trilinear couplings A_0 are assumed at the GUT scale Λ_{GUT},

$$\begin{aligned} m_{1/2} &= M_1 = M_2 = M_3\,, \\ m_0 &= m_{\tilde{Q}_i} = m_{\tilde{U}_i} = m_{\tilde{D}_i} = m_{\tilde{L}_i} = m_{\tilde{E}_i} = m_{h_u} = m_{h_d}\,, \\ A_0 &= A_t = A_b = A_\tau\,. \end{aligned} \tag{2.85}$$

Additionally, $\tan\beta$ is defined at the scale of EWSB and the sign of the μ parameter has to be fixed. This leaves four parameters plus one sign to determine the full MSSM low-energy spectrum.

Such a gaugino mass unification at the GUT scale is present in many SUSY breaking scenarios. It is motivated by the unification of the gauge couplings, as the (squared) gauge couplings run in the very same way as the gaugino soft masses. Gaugino unification at the GUT scale results in an approximate relation of the gaugino mass parameters at the EW scale,

$$\begin{aligned} M_3(\Lambda_{\text{GUT}}) = M_2(\Lambda_{\text{GUT}}) &= M_1(\Lambda_{\text{GUT}}) \\ \Longrightarrow M_3(m_{\text{Z}}) &= \frac{\alpha_s}{\alpha}\sin^2\theta_W M_2(m_{\text{Z}}) = \frac{5}{3}\frac{\alpha_s}{\alpha}\cos^2\theta_W M_1(m_{\text{Z}}) && \text{(2.85a)} \\ \Longrightarrow M_1(m_{\text{Z}}) &: M_2(m_{\text{Z}}) : M_3(m_{\text{Z}}) \approx 1:2:7\,. && \text{(2.85b)} \end{aligned}$$

Therefore, in models with gaugino mass unification the lightest neutralino $\tilde{\chi}_1^0$ is often both, bino and rather light.

2.4 Aspects of SUSY breaking

As mentioned already several times, SUSY, if realized in nature, has to be a broken symmetry. In section 2.3.1 SUSY was explicitly broken by soft breaking terms. However, this can clearly only be a parametrization of the details of an unknown dynamical/spontaneous breaking. In the following, we first argue that SUSY breaking has to happen outside of the MSSM, i.e., in a hidden sector. Second, two well-studied models mediating the breaking of SUSY to the visible are shortly introduced. Namely we discuss (super)gravity mediation (SUGRA) [85, 86] and gauge mediation (GMSB) [87–90] of supersymmetry breaking. However, a detailed introduction and comparison of these mediation schemes is beyond the scope of this thesis.

2.4.1 Tree-level SUSY breaking

In order to spontaneously break SUSY, i.e., $Q_A |0\rangle \neq 0$ and $\bar{Q}^{\dot{A}} |0\rangle \neq 0$, the vacuum has to have positive energy: $\langle 0| H |0\rangle > 0$. Thus, one or more of the scalar d.o.f. in the spectrum must acquire a non-vanishing vev. This is actually only possible for the auxiliary F- and/or D-term fields of a chiral/vector supermultiplet. Thus, a SUSY theory gets spontaneously broken at tree-level if and only if the system of equations

$$F_i = 0, \qquad D^a = 0 \tag{2.86}$$

cannot be solved for any values of the fields. After spontaneous breaking of global symmetry, a massless Nambu-Goldstone mode appears in the spectrum with the same quantum numbers as the broken generator. Thus, in the case of global SUSY breaking, a massless Weyl fermion, the *goldstino* appears.

In the literature several models trying to achieve such breaking have been proposed. Here, we only want to mention the two most important ones and explain their flaws for phenomenological applications.

- Fayet-Iliopoulos or D-term breaking [91, 92]:

  Here, the D-term can acquire a vev due to a linear term in the Lagrangian,

  $$\mathcal{L}_{FI} = -\kappa^2 D\,, \tag{2.87}$$

  where κ is a constant of mass dimension 1. This term is gauge invariant only for an abelian gauge symmetry. Thus, in the MSSM the D-term of the $U(1)_Y$ vector superfield could have this form. However, such a term (2.87) would then also introduces dangerous CCB minima for the sleptons and squarks and is thus phenomenologically forbidden.

- O'Raifeartaigh or F-term breaking [93]:

  In F-term SUSY breaking a set of chiral superfields and a corresponding superpotential is chosen in such a way that

  $$F_i = -\frac{\delta W^*}{\delta \phi^{*i}} = 0 \tag{2.88}$$

  have no simultaneous solution. This can, for example, be achieved with three chiral superfields $\Phi_{1,2,3}$ and the following superpotential

  $$\mathcal{W} = -k^2 \Phi_1 + m \Phi_2 \Phi_3 + \frac{y}{2} \Phi_1 \Phi_3^2\,. \tag{2.89}$$

  Such a superpotential is allowed if particularly Φ_1 (the field with the linear term in the superpotential) is a gauge singlet. The resulting scalar potential is given by

  $$V = |F_1|^2 + |F_2|^2 + |F_3|^2\,, \tag{2.90}$$

  with

  $$F_1 = k^2 - \frac{y}{2}\phi_3^{*2}\,, \quad F_2 = -m\phi_3^*\,, \quad F_3 = -m\phi_2^* - y\phi_1^*\phi_3^*\,. \tag{2.91}$$

Clearly, F_1 and F_2 cannot simultaneously be zero, hence SUSY is broken. The scale of SUSY breaking is fixed by the parameter k^2. However, there is a priori no reason why $k^2 \ll \Lambda_{\text{Planck}}$, which is phenomenologically necessary. Many more sophisticated models try to explain this hierarchy dynamically. Furthermore, within the MSSM there is no gauge-singlet chiral superfield which could take the role of Φ_1.

Besides the problems mentioned individually for D- and F-term breaking, there are two general problems of tree-level SUSY breaking in the MSSM. First, there is no gaugino-gaugino-scalar coupling in the MSSM. Thus, in general it is difficult to give mass to the gauginos via spontaneous SUSY breaking. Second, various sum rules can be deduced for tree-level SUSY breaking, linking fermion masses with the the masses of the sfermion partners. Thus, at least some of the squarks and/or sleptons would have to be unacceptably light.

2.4.2 Hidden sector SUSY breaking

For the reasons mentioned in the previous section, SUSY, if realized in Nature, is most likely broken in a *hidden sector*, i.e., in a particle sector with no or only very small couplings to the superfields of the MSSM – the *visible sector*. The breaking of SUSY is transmitted from the hidden to the visible sector via a *messenger sector* with an associated mass scale Λ_M. In the following we briefly introduce two models where spontaneous SUSY breaking at a scale Λ_s is mediated via (i) gravitational interactions, i.e., $\Lambda_M = \Lambda_{\text{Planck}}$ or (ii) gauge interactions with $\Lambda_M < \Lambda_{\text{Planck}}$. However, many more viable models are studied in the literature.

Gravity mediation of SUSY breaking

The necessary ingredients for gravitational interactions mediating SUSY breaking are automatically introduced by promoting SUSY to a local symmetry, which is often denoted *supergravity* [94], due to the following reason: from eqs. (2.25) and (2.26) we see that requiring local SUSY invariance also requires local invariance under general coordinate transformations, which directly leads to General Relativity. Additionally, in the same way as for gauge invariance, promoting SUSY to be a local symmetry introduces a new spin-3/2 gauge fermion. Such a particle can be understood as the SUSY partner of the graviton, called *gravitino*, $\tilde{G}$. The gravitino is an unavoidable implication of SUSY theories including gravity [31, 95]. Similar to the Higgs mechanism of spontaneous breaking of a gauge symmetry, the gravitino acquires a mass $m_{\tilde{G}}$ in the course of SUSY breaking via the so-called super-Higgs mechanism [94]. This mass depends on the details of the model and can vary from the eV scale beyond the TeV scale. Thus, $m_{\widetilde{G}}$ can naturally be lighter than any MSSM particle.

Depending on its mass the gravitino can play an important role in early Universe cosmology, as discussed in section 3.7.2. In this thesis we cannot give a general introduction into supergravity and resulting interactions. For this we refer to the available literature [96].

If we assume SUSY to be broken in the hidden sector by a non-vanishing $\langle F \rangle \neq 0$, the soft parameters in the visible sector are expected to be of order

$$m_{\text{soft}} \approx \frac{\langle F \rangle}{\Lambda_{\text{Planck}}}\,, \tag{2.92}$$

where their precise value is model dependent. In the simplest ansatz, called *minimal supergravity* (mSUGRA), treating all chiral superfields symmetrically, they are determined by

$$m_{1/2} = f\frac{\langle F\rangle}{\Lambda_{\text{Planck}}}\,, \qquad m_0^2 = m_{\tilde{G}} = k\frac{|\langle F\rangle|^2}{\Lambda_{\text{Planck}}^2}\,, \qquad A_0 = \alpha\frac{\langle F\rangle}{\Lambda_{\text{Planck}}} \tag{2.93}$$

at some high scale (below the Planck scale). The parameters f, k, α depend on the details of the underlying model. Clearly, this motivates the relations in eq. (2.85). The framework of mSUGRA is the simplest ansatz for supergravity SUSY breaking. Indeed, beyond mSUGRA various non-universality assumptions, e.g., non-universal gaugino soft masses (NUGM) or non-universal Higgs soft masses (NUHM) might be motivated. Furthermore, the gravitino mass $m_{\tilde{G}}$ is a free parameter in general.

Gauge mediation of SUSY breaking

In gauge mediation scenarios the soft breaking terms are generated due to radiative corrections of messenger fields at the loop level. These messenger fields are chiral superfields of mass M_M, charged under the SM gauge groups. Thus, soft masses are identical for scalars with equal quantum numbers (avoiding possible problems with FCNCs) and are expected to be of the order

$$m_{\text{soft}} \approx \frac{g^2}{16\pi^2}\frac{\langle F\rangle}{M_M}\,, \tag{2.94}$$

where again their precise value is model dependent.

Within GMSB models gauginos acquire masses through one-loop diagrams, while scalar masses are generated at the two-loop level. Within the simplest GMSB model, mGMSB, the messenger fields form complete representations of $SU(5)$ and the gaugino and sfermion soft masses are given by

$$M_i \approx \frac{g_i}{4\pi}\frac{\langle F\rangle}{M_M}\,, \qquad m_{\tilde{f}_i}^2 \approx \sum_{j=1,2,3}\frac{g_j}{16\pi^2}\frac{|\langle F\rangle|^2}{M_M^2}\,, \tag{2.95}$$

Trilinear couplings A_{ijk} are also generated at the two loop level, however, as they have mass dimension one, they are suppressed compared to M_i and $m_{\tilde{f}_i}$, i.e.,

$$A_{ijk} \approx 0\,. \tag{2.96}$$

Therefore, within GMSB (at least in its minimal version) the lightest Higgs mass is typically too light to be in agreement with the observation of a Higgs at ≈ 125 GeV.

Within GMSB models the gravitino mass is given by

$$m_{\tilde{G}} = \frac{1}{\sqrt{3}}\frac{\langle F\rangle}{\Lambda_{\text{Planck}}}. \tag{2.97}$$

Thus, the gravitino is usually expected to be much lighter than in gravity mediated SUSY breaking scenarios.

Chapter 3

SUSY phenomenology at colliders and in the cosmos

In this chapter we want to give a short introduction into SUSY phenomenology at colliders and in the early Universe.

Concerning colliders we focus on the LHC and investigate different production mechanisms and resulting direct experimental signatures of SUSY particles. At the same time we highlight recent results from the experiments at the LHC and discuss their implications. First, in section 3.1 we quickly introduce the LHC. Second, in section 3.2 possible collider signatures of SUSY are mentioned. Third, the different sectors of the MSSM are investigated independently. The colored sector, i.e., squarks and gluinos, are discussed in section 3.3, the electroweak sector is discussed in section 3.4, and the Higgs sector in section 3.5. In section 3.6 possible indirect constraints from the flavor sector are mentioned.

Concerning early Universe phenomenology we investigate two scenarios in section 3.7. First, the lightest neutralino is assumed to be the LSP. Second, an *extremely weakly interacting particle* (EWIP) outside the MSSM is assumed to be the LSP.

3.1 The LHC and its experiments

The LHC is a proton–proton collider at CERN[1]. During the first phase in 2010 and 2011 it operated with a center of mass energy of $\sqrt{S} = 7$ TeV and delivered an integrated luminosity of $\mathcal{L} \approx 5\ \text{fb}^{-1}$. Afterwards the center of mass energy was increased to $\sqrt{S} = 8$ TeV and during the year 2012 an integrated luminosity of $\mathcal{L} \approx 23\ \text{fb}^{-1}$ was delivered to each of the two general purpose experiments operating at the LHC. Right now the LHC is being upgraded and will restart data taking presumably early 2015 with a center of mass energy of $\sqrt{S} = 13 - 14$ TeV. At such energies and with a design luminosity of $\mathcal{L}_{\text{inst}} = 10^{34}\ \text{cm}^{-2}\text{s}^{-1} = 100\ \text{pb}^{-1}s^{-1}$ more than $300\ \text{fb}^{-1}$ are planned to be accumulated eventually.

At the LHC two general-purpose detectors are operating: the *ATLAS* experiment and the *CMS* experiment. They are designed to search for a SM Higgs particle and for BSM physics.

[1]Besides with protons the LHC can also be operated with lead nuclei. However, physics of resulting heavy-ion collisions and the corresponding experiment ALICE will not be covered in this thesis.

Furthermore, *LHCb* investigates B-mesons, in particular their CP properties and rare decays.

3.2 Collider signatures for SUSY

Possible collider signatures of the MSSM or SUSY in general are manifold. Here we want to briefly discuss the ones relevant for this thesis. For a detailed introduction into SUSY phenomenology see for example ref. [62].

On the one hand, SUSY particles could be produced directly at collider experiments. Experimental signatures at such experiments very much depend on the lifetime and nature of the LSP. In R-parity conserving scenarios the LSP is stable. In such a scenario a neutralino LSP serves as a viable dark matter candidate and at colliders any produced SUSY particle eventually decays into the LSP, which in case of the neutralino LSP escapes the detectors unobserved. In these decays additional SM particles are emitted. Producing colored SUSY particles, always additional jets are emitted. Thus, the resulting experimental signatures for neutralino LSP scenarios is "multi-jets plus missing transverse energy ($\not{E}_T$)". Additionally, electroweakly charged SUSY particles can be produced directly in the hard process or indirectly in the decays of squarks and gluinos, emitting additional SM leptons or gauge bosons. These can also be searched for by the experiments. Moreover, in particular decays of stop quarks yield a large number of b-jets, which can be tagged in the experimental analyses.

However, the neutralino is not the only possible LSP and thus dark matter candidate within SUSY theories. For example, the gravitino can easily be the LSP. As couplings of all MSSM particles to the gravitino are Planck-scale suppressed, the *next to lightest supersymmetric particle* might become long-lived in terms of detector scales. This has important experimental consequences. For a neutralino NLSP again missing energy signatures are expected. More strikingly, for a charged NLSP (e.g. a stau or a stop) signatures of *charged massive particles* (CHAMP) should occur. The signature of a CHAMP traversing a detector is a slowly moving minimal ionizing particle with high transverse-momentum p^{T}. In the experiments, this results in a long time-of-flight (TOF) and an anomalously large ionization-energy loss rate (dE/dx). Since the CHAMP loses energy primarily through low-momentum-transfer interactions, it will be highly penetrating and will likely be reconstructed as a slow-moving muon [97–105]. Again, CHAMP signatures might be accompanied by additional jets and/or leptons from cascade decays.

On the other hand, indirect contributions of SUSY particles via quantum effects could alter sensitive observables. Amongst others, EWPOs like Z-pole observables or the mass of the W-boson m_{W}, the anomalous magnetic moment of the muon, rare decays in the SM, like $b \to s\gamma$ or $\mu \to e\gamma$, or effective Higgs couplings could all be affected by virtual SUSY contributions. Thus, such observables can be used to place stringent bounds on the relevant parameter space or even provide significant indications for physics beyond the SM in case of deviations.

3.3 Colored sector

For not too heavy squarks and gluinos, their production is expected to be the dominant source of SUSY particle production at a hadron collider like the LHC. In the following we discuss relevant production channels and decay modes at leading order. Afterwards, in section 3.3.1 corresponding higher-order corrections available in the literature are discussed. In section 3.3.2 the current experimental status is reviewed. Finally, in section 3.3.3 the relevance for future parameter determination is highlighted.

Production

First *leading order* (LO) cross section predictions for squark and gluino production processes at hadron colliders were already made many years ago [106–110] and are reviewed in [39]. These LO predictions yield cross sections at order $\mathcal{O}(\alpha_s^2)$, where the following parton processes contribute:

$$\begin{aligned}
\tilde{q}\tilde{q} \text{ production:} \quad & q_i + q_j \longrightarrow \tilde{q}_i + \tilde{q}_j \text{ and c.c.} \\
\tilde{q}\bar{\tilde{q}} \text{ production:} \quad & q_i + \bar{q}_j \longrightarrow \tilde{q}_k + \bar{\tilde{q}}_l \\
& g + g \longrightarrow \tilde{q}_i + \bar{\tilde{q}}_i \\
\tilde{q}\tilde{g} \text{ production:} \quad & q_i + g \longrightarrow \tilde{q}_i + \tilde{g} \text{ and c.c.} \\
\tilde{g}\tilde{g} \text{ production:} \quad & q_i + \bar{q}_i \longrightarrow \tilde{g} + \tilde{g} \\
& g + g \longrightarrow \tilde{g} + \tilde{g} \\
\tilde{t}\bar{\tilde{t}} \text{ production:} \quad & q_i + \bar{q}_i \longrightarrow \tilde{t} + \bar{\tilde{t}} \\
& g + g \longrightarrow \tilde{t} + \bar{\tilde{t}} \,.
\end{aligned} \tag{3.1}$$

Here, $i, j, k, l = \{u, d, c, s, b\}$ and all chirality combinations are summed over. Stops are treated independently. They are only produced diagonally (with equal chiralities) via quark–antiquark annihilation and gluon–gluon fusion, since the top contribution in the proton is negligible. Production of squark–squark pairs is possible via t-channel quark–quark annihilation. For first generation squarks, this proceeds via valence-quark contributions. For all other squarks and all further production channels, sea-quark contributions are necessary. In case of squark–antisquark production, gluon–gluon and quark–antiquark initial states contribute, where only from the quark–antiquark initial state via a t-channel diagram flavor and chirality non-diagonal squarks can be produced. Gluino–squark pairs are only produced from gluon-quark initial states. Finally, production of gluino pairs is again possible by gluon–gluon fusion and by quark–antiquark annihilation.

The given classification in different squark and gluino channels is purely organizational. At higher orders of perturbation theory and/or including the corresponding decays such a classification is not strictly possible and has to be altered. This will be discussed in detail in sections 4.2.1 and 4.3.2.

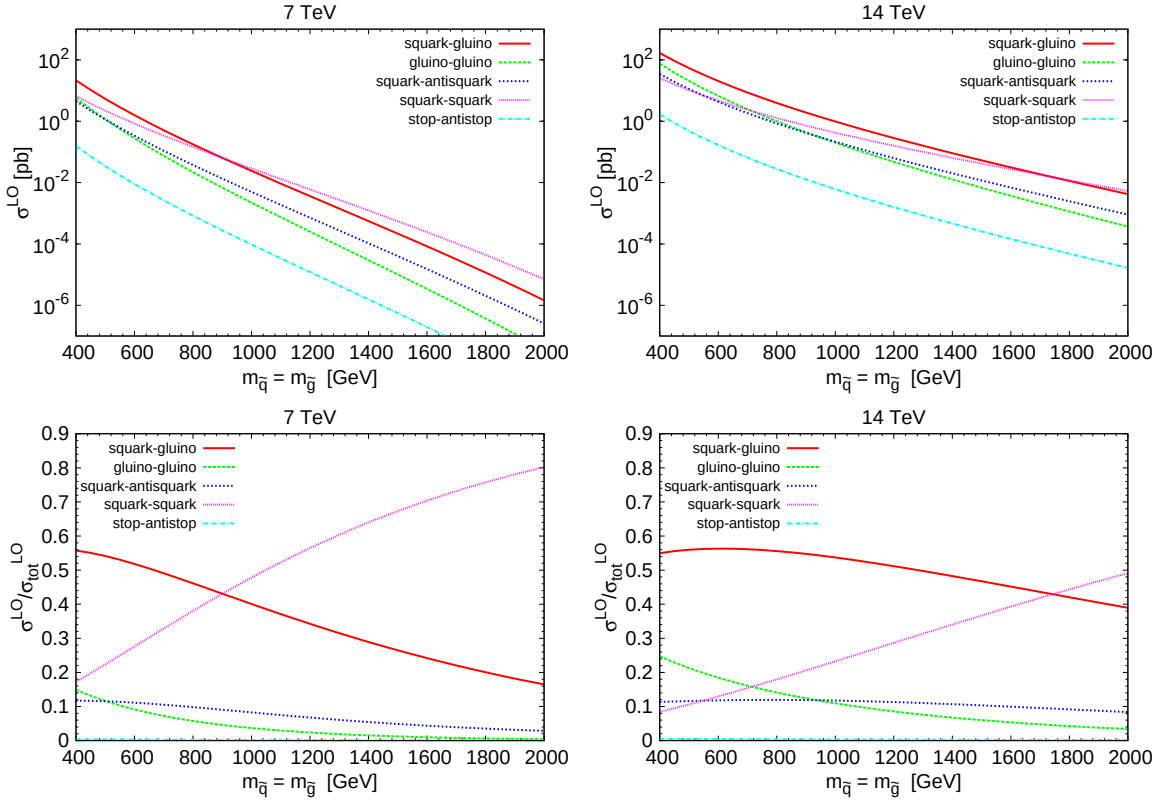

Figure 3.1: Top: LO cross sections σ^{LO} in pb (top) for $\tilde{q}\tilde{g}, \tilde{g}\tilde{g}, \tilde{q}\bar{\tilde{q}}, \tilde{q}\tilde{q}$ and $\tilde{t}\bar{\tilde{t}}$ production; bottom: ratios between individual channels and the sum of all the considered channels $\sigma^{\mathrm{LO}}/\sigma^{\mathrm{LO}}_{\mathrm{tot}}$. Both shown at the LHC with $\sqrt{S} = 7$ TeV (left) and $\sqrt{S} = 14$ TeV (right). Cross sections and ratios are shown as function of a common mass for the gluino and all squarks $m_{\tilde{q}} = m_{\tilde{g}}$.

The LO hadronic production cross sections for the different channels, $\sigma^{(0)}_{pp\to\tilde{s}\tilde{s}'}$, with $\tilde{s} = \{\tilde{g}, \tilde{q}, \bar{\tilde{q}}, \tilde{t}, \bar{\tilde{t}}\}$, can be obtained convoluting the partonic ones

$$\sigma^{(0)}_{pp\to\tilde{s}\tilde{s}'} = \int_{\tau_0}^{1} d\tau\, \mathcal{L}_{ab}(\tau)\, \hat{\sigma}^{(0)}_{ab\to\tilde{s}\tilde{s}'}(\tau)\,, \tag{3.2}$$

where the parton luminosity $\mathcal{L}_{ab}(\tau)$ is defined by

$$\mathcal{L}_{ab}(\tau) = \frac{1}{1+\delta_{ab}} \int_{\tau}^{1} \frac{dx}{x} \left[f_a(x,\mu_F)\, f_b\Big(\frac{\tau}{x},\mu_F\Big) + (a \leftrightarrow b)\right], \tag{3.3}$$

with $f_{a/b}(x,\mu_F)$ being the *parton distribution function* (PDF) of the quark/gluon a/b at the factorization scale μ_F with momentum fraction x inside the proton. τ denotes the ratio between the squared center-of-mass energies of the partonic and hadronic processes, $\tau = s/S$, and the kinematic production threshold corresponds to $\tau_0 = (m_{\tilde{s}} + m_{\tilde{s}'})^2/S$.

In the upper part of figure 3.1 we plot the LO hadronic production cross sections for all channels listed in (3.1) as a function of a common squark and gluino mass $m_{\tilde{q}} = m_{\tilde{g}} (= m_{\tilde{t}})$.

We use the MSTW08 PDF set [111] at LO consistently with the strong coupling constant $\alpha_s(\mu_R)$ they provide. Factorization scale μ_F and renormalization scale μ_R are set to the common mass $\mu = \mu_R = \mu_F = m_{\tilde{q}} = m_{\tilde{g}}$. In the left/right plot we show in pb cross sections for the LHC with 7 TeV and 14 TeV respectively. For the considered mass range cross sections vary by up to seven orders of magnitude and increase between one and four orders when going from 7 TeV to 14 TeV.

In the lower part of figure 3.1 we plot the ratio between the individual cross sections and the sum of all considered channels. We see that for large masses, due to the valence quark initial state, the squark–squark channel increases compared to all other channels. Stop–anti-stop production is suppressed compared to all other channels and thus hardly visible in these ratio-plots.

Additionally, at order $\mathcal{O}(\alpha_s\alpha)$ squarks can be produced in combination with neutralinos and charginos:

$$\begin{aligned} \tilde{q}\tilde{\chi}^0 \text{ production:} \quad & q_i + g \longrightarrow \tilde{q}_i + \tilde{\chi}^0_k\,, \qquad k = 1,\ldots,4\,, \\ \tilde{q}\tilde{\chi}^\pm \text{ production:} \quad & q_i + g \longrightarrow \tilde{q}_j + \tilde{\chi}^\pm_l\,, \qquad l = 1,2, \quad i \neq j\,, \end{aligned} \tag{3.4}$$

where the charge conjugated processes are also possible.

Decays

The dominant decay modes for squarks and gluinos depend on the mass hierarchy between them. For $m_{\tilde{g}} > m_{\tilde{q}_{ia}}$, with $a = \{L, R\}$, the dominant leading order decays considering light-flavor squarks ($i, j = u, d, c, s$) are

$$\tilde{g} \to q\ \tilde{q}_{iL/R}\,, \tag{3.5}$$

$$\tilde{q}_{iL/R} \to q_i\ \tilde{\chi}^0_k\,, \qquad k = 1,\ldots,4\,, \tag{3.6}$$

$$\tilde{q}_{iL} \to q'_j\ \tilde{\chi}^\pm_l\,, \qquad l = 1,2, \quad i \neq j\,, \tag{3.7}$$

where the first decay is of order $\mathcal{O}(\alpha_s)$ and the other two of order $\mathcal{O}(\alpha)$. For $m_{\tilde{q}_{ia}} > m_{\tilde{g}}$, the dominant decays are

$$\tilde{q}_{iL/R} \to q_i\ \tilde{g}\,, \tag{3.8}$$

$$\tilde{g} \to q_i\ q_i\ \tilde{\chi}^0_k\,, \quad k = 1,\ldots,4\,, \tag{3.9}$$

$$\tilde{g} \to q_i\ q'_j\ \tilde{\chi}^\pm_l\,, \quad l = 1,2, \quad i \neq j\,, \tag{3.10}$$

where the gluino decays in a three-body decay via an off-shell squark. If kinematically accessible a strong decay always dominates any available weak decays. The ratio of the branching ratios (BR) between the different decay modes into neutralinos and charginos depends on their mixing – left-handed squarks dominantly decay into wino-like neutralinos and charginos; right-handed squarks dominantly into bino-like ones. Decays into Higgsino-like neutralinos and charginos are suppressed due to the small Yukawa coupling of the light-flavor squarks. Further decays of the neutralinos and charginos are discussed in section 3.4.

For stops and sbottoms left–right mixing due to large off-diagonal elements in the squark mixing matrix, eq. (2.66), can lead to large mass splittings between the different mass eigenstates. Furthermore couplings to Higgses and Higgsinos cannot be neglected anymore. Therefore, decay patterns in particular of the heavier mass eigenstates $\tilde{t}_2, \tilde{b}_2$ can become much more complex and are highly parameter dependent.

3.3.1 Precision calculations

Calculation of squark and gluino production including NLO corrections in perturbation QCD has been performed quite some time ago [38, 112–114]. These corrections can be large ($10\% - 70\%$, depending on the process and the parameters) and have to be included in any viable phenomenological study due to the otherwise enormous scale uncertainties (including NLO corrections, the scale uncertainty on inclusive cross sections is typically reduced to around $20\% - 30\%$). Besides the scale uncertainty, PDF uncertainties dominate the error of theoretical predictions of sparticle production processes.

Already in [38], differential distributions at NLO are presented for the produced squarks and gluinos. Here, NLO correction factors (K-factors) look rather flat in phase space. Therefore, in the experimental analyses, they are used as a global multiplicative factor to the LO cross section. However, a systematic study of the differential behavior of these K-factors has never been performed. Furthermore, in [38] and in the corresponding public computer code `Prospino 2` [115], which can calculate LO cross sections and NLO K-factors efficiently, NLO corrections for squark–squark production are always summed over the various flavor and chirality combinations of the produced (light-flavor) squarks. Realistic physical observables do depend on the chiralities through the decay modes which are in general quite different. In a recent publication, NLO QCD corrections to squark and gluino production were reevaluated treating all flavors and chiralities independently [116]. In a very recent calculation, squark-pair production was investigated at NLO matched to a parton shower and including LO decays [117]. Again, all flavors and chiralities were treated independently and results were explicitly found to be in agreement with the ones presented here.

In figure 3.2 we illustrate the importance of NLO QCD corrections to squark and gluino production processes. We show NLO QCD K-factors

$$K^{\mathrm{NLO}} = \frac{\sigma^{\mathrm{NLO}}}{\sigma^{\mathrm{LO}}}\,, \tag{3.11}$$

obtained with `Prospino 2` for all relevant channels defined in (3.1) as a function of a common mass for all squarks and gluinos $m_{\tilde{q}} = m_{\tilde{g}}$. In the left plot we show K-factors for the LHC with $\sqrt{S} = 7$ TeV and in the right plot for $\sqrt{S} = 14$ TeV. As in figure 3.1 we use MSTW08 PDF sets. LO and NLO PDF sets and the associated α_s are chosen for the corresponding predictions respectively. In figure 3.2 we observe in general large K-factors up to 1.8 for $\tilde{g}\tilde{g}$ production at $m_{\tilde{q}} = m_{\tilde{g}} = 2$ TeV and $\sqrt{S} = 7$ TeV. In the considered mass range all K-factors yield large positive corrections apart from $\tilde{q}\bar{\tilde{q}}$ production at $\sqrt{S} = 7$ TeV where corrections turn negative for $m_{\tilde{q}} = m_{\tilde{g}} \gtrsim 1.4$ TeV. In general K-factors decrease going from $\sqrt{S} = 7$ TeV to $\sqrt{S} = 14$ TeV.

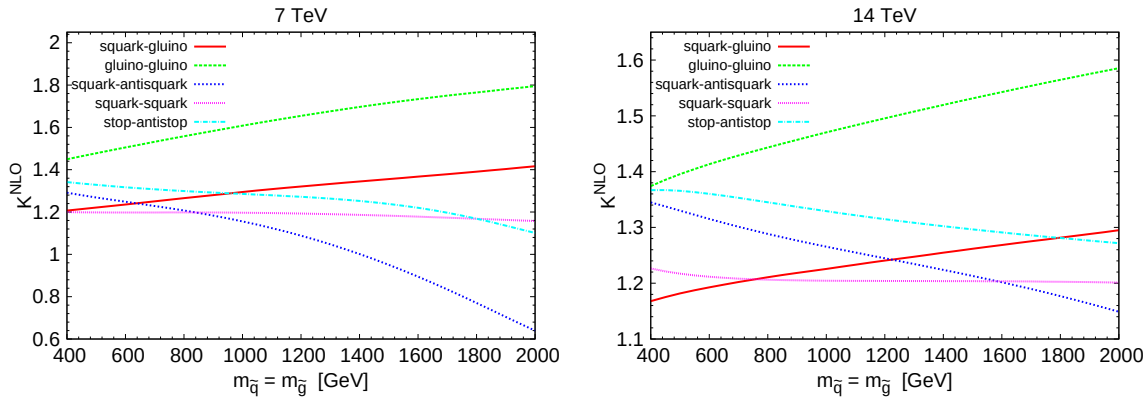

Figure 3.2: NLO QCD K-factors for $\tilde{q}\tilde{g}, \tilde{g}\tilde{g}, \tilde{q}\bar{\tilde{q}}, \tilde{q}\tilde{q}$ and $\tilde{t}\bar{\tilde{t}}$ production at the LHC with $\sqrt{S} =$ 7 TeV (left) and $\sqrt{S} = 14$ TeV (right) obtained with `Prospino 2`, shown as function of a common mass for the gluinos and all squarks $m_{\tilde{q}} = m_{\tilde{g}}$.

Also results beyond NLO in QCD were calculated, based on resummation techniques [118–126]. These corrections increase the inclusive cross sections by typically about $2\% - 30\%$ and further reduce the scale uncertainty. Predictions for squark and gluino production including resummation of soft gluon emission at next-to-leading-logarithmic (NLL) accruacy are available via grids in the `NLL-fast` [127] software package. Moreover, electroweak contributions can also give sizeable corrections. At leading order they were first calculated in [128, 129] and at NLO in [130–136]. In detail, those corrections depend strongly on the model parameters and on the flavor/chiralities of the squarks.

A similar amount of work has been put into the calculation of higher order corrections to decays of (colored) sparticles, with focus mainly on integrated decay widths and branching ratios. NLO QCD corrections to the decay of light squarks into neutralinos and charginos were first calculated in refs. [137, 138] and to heavy squarks also in ref. [138] and in [139]. Corrections to the total decay width of light squarks are in general moderate (below 10%) and can change sign, depending on the involved mass ratios. However, for very small mass splittings between the decaying squark and the neutralinos/charginos, these corrections increase significantly. Higher-order corrections to the decay of top-squarks are in general sizeable, but they depend strongly on the mixing in the heavy squark sector. Related to this mixing also decays into weak gauge bosons or Higgs bosons can become relevant [140, 141], receiving large higher order corrections [142–144]. Decays of a gluino into a light squark and a quark at NLO QCD together with the decay of a light squark into a gluino and a quark have been calculated in [145]. Corresponding decays involving stops were presented in [146]. All these decays including their NLO QCD corrections have been implemented in the public computer programs `SDECAY` [147] and `SUSY-HIT` [84]. Besides NLO QCD, also NLO electroweak corrections to squark decays into neutralinos and charginos have been investigated in the literature [148, 149] and can give sizeable contributions. These corrections often compensate those from QCD on the level of integrated decay widths, however, they depend strongly on the model parameters. Corresponding NLO electroweak corrections for third generation squark decays

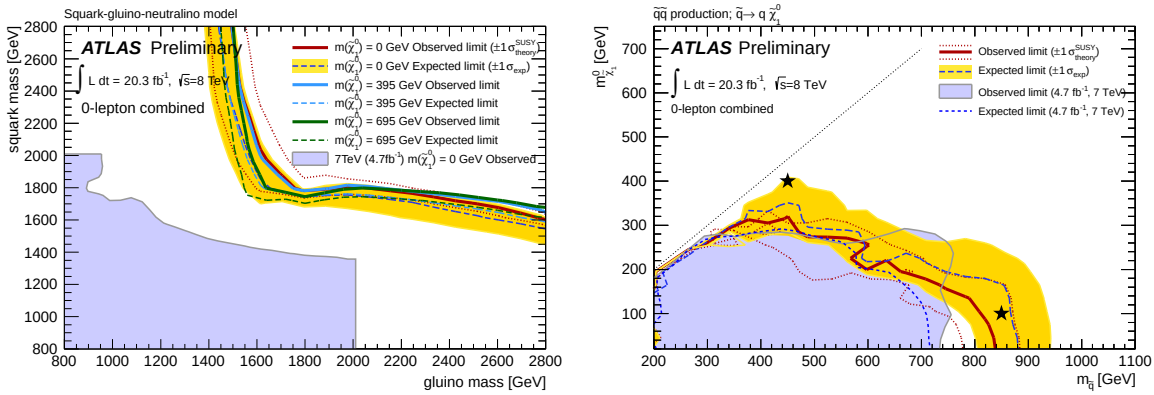

Figure 3.3: Exclusion limits obtained by the ATLAS collaboration in their all-hadronic analyses with "0 leptons, 2-6 jets and $\not{E}_T$" using the full currently available dataset at 8 TeV [158]. Left: interpretation in a squark–gluino simplified model with $m_{\tilde{\chi}_1^0} = 0$. Right: interpretation assuming only squark–squark production and a decoupled gluino. Both plots are taken from ref. [158].

have been studied in [150–153].

As already mentioned before, most of the discussed studies of higher-order corrections focused on inclusive observables or considered differential distributions in unphysical final states, like SUSY particles. Few studies were performed investigating invariant mass distributions of SM particles emitted from cascade chains including various higher-order corrections [154, 155]. Finally, in refs. [156, 157] the production of sparticles was studied at tree level matched to a parton shower including additional hard jets. In these works large deviations from the LO prediction with or without showering were found particularly in the high-p^{T} tail for scenarios with compressed spectra. In this thesis we go beyond these estimates and in chapter 4 (and following) we provide a fully differential description of production and decay of squark–squark pairs at NLO.

3.3.2 Experimental status

A stunning amount of analyses searching for SUSY in various experimental final states have been presented already during the first phase of the LHC. Unfortunately, no deviation from SM background predictions has been found so far – as it has been the case for previous searches at the Large Electron Positron (LEP) collider at CERN and the Tevatron at Fermilab. In this work we can not give a comprehensive overview on all relevant search-analyses. Instead we want to highlight the all-hadronic searches most relevant for squark and gluino production assuming a $\tilde{\chi}_1^0$ LSP [158–163], as already motivated in section 3.2. Here, a significant branching ratio of squarks and gluinos decaying directly into the $\tilde{\chi}_1^0$ is assumed, resulting in an all-hadronic "multi-jets plus missing energy" signature. Differences in the analyses performed by the ATLAS and CMS collaborations occur due to alternative strategies for background rejection, however, the resulting reach in parameter space is comparable. In section 5.2.2 we explore one of such analyses for each of the experiments in detail.

As an example, in figure 3.3 we show simplified model interpretations of the latest ATLAS search in the all-hadronic channel [158]. In the left plot of figure 3.3 all squark and gluino production channels are included. All other SUSY particles but the $\tilde{\chi}_1^0$ are decoupled. The $\tilde{\chi}_1^0$ is assumed to be massless and all branching ratios into the $\tilde{\chi}_1^0$ to be 100%. In this simplified model, squark and gluino masses are excluded up to about 1600 GeV. In the right plot also the gluino is decoupled and only squark-pair productionis considered. Resulting limits are weaker and for a massless neutralino, squarks up to about 850 GeV are excluded. For heavier neutralinos these limits become much weaker or non-existing at some point, as jets from the squark decays become soft and do not pass the cuts applied in the experimental search.

3.3.3 Parameter determination

Once a clear signal for physics beyond the Standard Model is established, the character and parameters of the underlying model have to be determined. Only a precise and non-ambiguous determination of TeV-scale parameters allows reconstruction of the underlying theory [164, 165] and, e.g., in case of SUSY, investigation of different breaking scenarios. Moreover, different BSM models result in similar signatures at the LHC, so even the determination of the general model would be a major challenge [166]. In recent years various techniques tackling these challenges have been developed. Many of those rely on the occurrence of cascade decay chains of colored particles. For a review of mass determination techniques see for example ref. [167].

However many of these techniques require a rather large sample of signal events. But, as bounds on SUSY particles (especially light squarks and gluinos) are pushed to higher values by the experimental searches, many of the proposed sophisticated kinematic methods for parameter determination might not be feasible with low signal statistics due to a rather heavy spectrum. Therefore, inclusive quantities like event rates become more interesting [168]. Thus, precision studies for cross sections including realistic experimental cuts are desirable.

3.4 Electroweak sector

Production

For not too heavy squarks and gluinos production of neutralinos, charginos and sleptons from cascade decays of colored particles is assumed to be dominant. However, they can also be hadroproduced directly at order $\mathcal{O}(\alpha^2)$.

Neutralinos and charginos can be produced diagonally $\tilde{\chi}_i^0\tilde{\chi}_i^0$, $\tilde{\chi}_i^\pm\tilde{\chi}_i^\pm$ or off-diagonally $\tilde{\chi}_i^0\tilde{\chi}_j^0$, $\tilde{\chi}_i^\pm\tilde{\chi}_j^\pm$, $\tilde{\chi}_i^0\tilde{\chi}_j^\pm$. For both processes, two types of diagrams contribute at leading order. On the one hand, they can be produced in Drell-Yan type processes. On the other hand, t-channel squark diagrams contribute. NLO QCD corrections have been calculated in [169] and are included in `Prospino 2`.

At leading order sleptons are only produced via Drell–Yan-type processes [170] and will be discussed in detail in chapter 7. Corresponding higher-order corrections include NLO

corrections [169, 171], resummation improved results at NLL accuracy [172–174] and, since recently, NLO results matched to a parton shower [175, 176]. The NLO QCD results are available via `Prospino 2` and the NLL results via the program `Resummino` [177]. These predictions are in principle valid for sleptons of all generations.

Contributions from $b\bar{b}$ annihilation and from gluon fusion were studied in refs. [178–180], which assumed no left-right mixing. While this limit is usually a good approximation for first and second generation sleptons, the mixing between the (third generation) stau gauge eigenstates can be substantial. Moreover, the $b\bar{b}$ and gg channels are not included in the stau-pair production cross section predictions provided by the general purpose Monte Carlo simulation codes such as `Pythia` [181] or `Herwig` [182]. In chapter 7 we present a study which considers all three of the mentioned direct stau production mechanisms with particular emphasis on potentially sizeable left-right mixing.

Decays

In $\tilde{\chi}_1^0$ LSP scenarios sleptons always decay into a kinematically available lighter neutralino or chargino state, emitting a lepton

$$\tilde{l}/\tilde{\nu} \to l/\nu \; \tilde{\chi}_k^0 \,, \qquad k = 1, \ldots, 4 \,, \tag{3.12}$$

$$\tilde{l}/\tilde{\nu} \to \nu/l \; \tilde{\chi}_l^\pm \,, \qquad l = 1, 2 \,, \tag{3.13}$$

where $m_{\tilde{l}/\tilde{\nu}} > m_{\tilde{\chi}_i^0/\tilde{\chi}_i^\pm}(+m_l)$. In other scenarios, e.g. where the $\tilde{\tau}_1$ is the lightest MSSM particle or where a small mass splitting does not allow for an on-shell decay, also three-body decays of heavier sleptons might become relevant.

Decay patterns of neutralinos and charginos are more complex. If kinematically available they decay into lighter sleptons (or even squarks), otherwise again into neutralinos and charginos via three-body decays. For large enough mass splittings they can also decay into lighter neutralino/chargino states emitting SM gauge bosons or Higgs bosons.

3.4.1 Experimental status

As in the case of strong production, experimental analyses searching for electroweak production of SUSY particles at the LHC are manifold. Despite much smaller cross sections they are very successful in constraining large regions of the parameter space, where before the LHC, best limits were mostly set by LEP. However, these limits usually depend on various assumptions, e.g., on-shell decays via sleptons or SM gauge bosons are often assumed, see for example ref. [183, 184]. Here we only want to discuss current limits on direct production of staus, as this will be the main subject of chapters 7 and 8.

Constraints on direct stau production

For decaying staus, i.e., in $\tilde{\chi}_1^0$ LSP scenarios, best model-independent limits are still set by LEP [39] and for $m_{\tilde{\tau}_1} - m_{\tilde{\chi}_1^0} > 10$ GeV they are given by

$$m_{\tilde{\tau}_1} \gtrsim 82 \text{ GeV} \,. \tag{3.14}$$

On the other hand, long-lived staus occur naturally in SUSY extensions of the SM in which the LSP is an EWIP. In such settings, a directly produced stau will usually appear as a CHAMP. Searches for such long-lived staus at LEP set the following model-independent limit [39, 185]:

$$m_{\tilde{\tau}_1} \gtrsim 87.5 \text{ GeV} . \tag{3.15}$$

Moreover, searches for long-lived staus in proton-antiproton collisions with $\sqrt{S} = 1.96$ TeV at the Tevatron [104, 186] have led to the following upper limit on the stau production cross section [104]:

$$\sigma(\sqrt{S} = 1.96 \text{ TeV}) \lesssim 10 \text{ fb} . \tag{3.16}$$

This was the experimental status when the study presented in chapter 7 and 8 was published in [1]. In a recent analysis [187] using an integrated luminosity of $\mathcal{L} = 4.7\,\text{fb}^{-1}$, the CMS experiment sets the limit

$$m_{\tilde{\tau}_1} \gtrsim 223 \text{ GeV} \tag{3.17}$$

for directly produced long-lived staus. Furthermore, preliminary results including data from the 8 TeV run have been presented in [188] and the following limit is given

$$m_{\tilde{\tau}_1} \gtrsim 339 \text{ GeV} , \tag{3.18}$$

again for direct production of staus only. These limits exclude parts of the parameter region and benchmarks presented here. However, general results are unaffected and in section 8.5 we elaborate on the current status and future prospects.

3.5 Higgs sector

Production channels and decay modes of MSSM Higgs particles, corresponding collider signatures and higher-order corrections are manifold and cannot be discussed here. For a review within the MSSM and the SM see refs. [189] and [190]. Instead, here we quickly want to emphasize important implications of the recent Higgs searches at the LHC.

As mentioned in chapter 1 both the ATLAS collaboration and the CMS collaboration recently discovered a Higgs particle h with a mass ≈ 125 GeV. Including all currently available data of various sensitive channels the two collaborations state (preliminary) masses m_h and signal strengths μ (in terms of the SM rate for a given mass) for the new Higgs boson [191, 192]:

$$\text{ATLAS}: \quad m_h = 125.5 \pm 0.2^{+0.5}_{-0.6} \text{ GeV} , \qquad \mu = 1.43 \pm 0.16 \pm 0.14 , \tag{3.19}$$

$$\text{CMS}: \quad m_h = 125.7 \pm 0.3 \pm 0.3 \text{ GeV} , \qquad \mu = 0.80 \pm 0.14 , \tag{3.20}$$

where if explicitly stated the first and second errors are statistical and systematical respectively. The combined and individual signal strengths for all channels are in good agreement

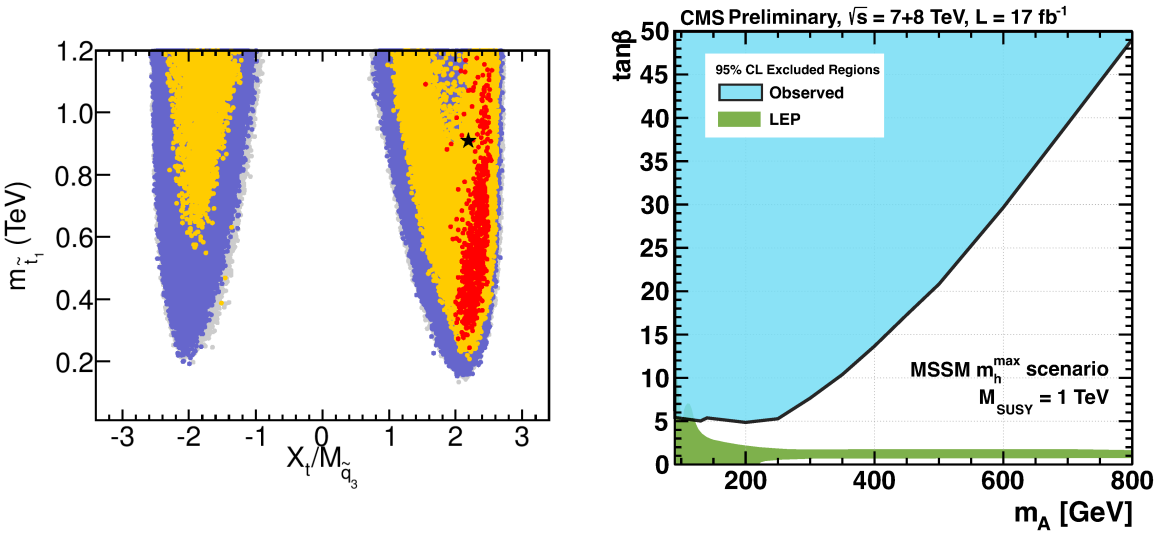

Figure 3.4: Left: best fit region in the $X_t/m_{\tilde{Q}_3} - m_{\tilde{t}_1}$ plane of the MSSM including various Higgs, EWPO and flavor observables as inputs. Taken from: [193]. Right: 95% C.L. exclusion limits obtained by the CMS collaboration in the $m_{A^0} - \tan\beta$ plane of the $m_h^{\max}$ benchmark scenario. Taken from: [194].

with SM predictions. A slight enhancement in the branching ratio BR($h \to \gamma\gamma$) is observed by ATLAS and was observed by CMS in earlier analyses. A possible explanation within the MSSM is discussed in section 7.1.3. In general, the agreement with SM predictions in all Higgs observables points towards the MSSM decoupling limit $m_{A^0} \gg m_Z$, where the lightest MSSM Higgs particle h^0 is SM-like and can be identified with h. On the other hand, the observed Higgs could in principle also be identified with the heavier neutral CP-even H^0 [193]. Now, $m_{A^0} \sim Z^0$ and the lighter h^0 could have been missed by Higgs searches at LEP due to reduced couplings to SM gauge bosons.

As already discussed in section 2.3.2 the observed mass m_h requires that the mass m_h^0 receives sizeable quantum corrections in order to identify the lightest MSSM Higgs h^0 with the observed one. As shown in eq. (2.64) such large corrections in turn require large stop masses and/or mixing and hence large X_t. In ref. [193] a global fit in the MSSM (with 7 parameters) was performed including the Higgs mass measurements and available signal strengths together with EWPOs and flavor observables as inputs. In that scan the MSSM Higgs masses where evaluated at the two-loop level with the computer program `FeynHiggs` [195]. The resulting best-fit region in the $X_t/m_{\tilde{Q}_3} - m_{\tilde{t}_1}$ plane is shown in figure 3.4(left). From this plot we see that for light stop masses, i.e., $m_{\tilde{t}_1} \gtrsim 200$ GeV, the off-diagonal element in the stop mixing matrix has indeed to be large, $|X_t/m_{\tilde{Q}_3}| \approx 2$. Furthermore, even lighter stop masses and in particular $m_{\tilde{t}_1} < m_t$, are excluded as a result of this fit. For heavier stop masses, $m_{\tilde{t}_1} \gtrsim 1$ TeV, stop-mixing has still to be considerable $|X_t/m_{\tilde{Q}_3}| > 1$.

Additionally, there are important constraints on the Higgs sector of the MSSM in scenarios

with large $\tan\beta$ and small m_{A^0} from Higgs searches in the $\tau\bar{\tau}$ and $b\bar{b}$ channels. As shown in section 2.3.2, Yukawa-couplings of down-type fermions are enhanced for large $\tan\beta$. Currently most stringent (preliminary) exclusions from the LHC experiments are given in [194] and [160]. As an example, in figure 3.4(right) the 95% C.L. exclusions from searches in the $\tau\bar{\tau}$ channel presented in [194] are shown in the $m_{A^0} - \tan\beta$ plane of the m_h^{max} benchmark scenario (defined in [196, 197]). Here, e.g., $m_{A^0} \lesssim 800$ GeV is excluded for $\tan\beta \gtrsim 50$ and $m_{A^0} \lesssim 500$ GeV for $\tan\beta \gtrsim 20$.

3.6 Flavor sector

There are important constraints from the flavor sector, and in particular from observables in the B-sector, on the relevant SUSY parameter space. For example the recent observation of the decay $B_s \to \mu^+\mu^-$ at LHCb points towards a branching ratio [198]

$$\text{BR}(B_s \to \mu^+\mu^-) = 3.2^{+1.5}_{-1.2} \times 10^{-9} \text{ @ 95\% CL} , \tag{3.21}$$

which is in good agreement with the SM prediction $\text{BR}(B_s \to \mu^+\mu^-)_{\text{SM}} = 3.23 \pm 0.27 \times 10^{-9}$ from [199] and thus sets stringent limits on the relevant SUSY parameter space. Particularly parameter regions with large $\tan\beta$ and small m_{A^0}, where additional SUSY penguin-diagrams could contribute strongly to $\text{BR}(B_s \to \mu^+\mu^-)$, are disfavored. When the results of chapters 7 and 8 were first published, the most stringent bound on this decay was considerably weaker [200],

$$\text{BR}(B_s \to \mu^+\mu^-) < 4.3 \times 10^{-8} \text{ @ 95\% CL} . \tag{3.22}$$

Furthermore, also the measurement [200] of

$$\text{BR}(b \to s\gamma) = (3.55 \pm 0.33) \times 10^{-4} \tag{3.23}$$

gives relevant constraints, as again additional SUSY contributions, in particular from chargino and charged-Higgs loops, can be large. Many more rare B-meson and in general flavor changing decays constrain the SUSY parameter space. See for example ref. [201] for an overview.

3.7 SUSY in the cosmos

Possible implications of SUSY for cosmological processes are diverse. Here we want to focus on the role of the LSP as a viable dark matter candidate. This possibility is connected with cosmological bounds obtained from observations of the CMB, implications of the BBN and structure formation or direct and indirect dark matter searches. Additionally, SUSY particles might play an important role during inflation (see for example ref. [202] or ref. [203]) and/or leptogenesis (see ref. [204] and references therein).

Here we want to discuss three viable dark matter candidates provided by supersymmetry: the lightest neutralino, the gravitino and the axino. The neutralino is a formidable WIMP, while the gravitino and the axino fall in the class of EWIPs, as discussed below. In the following, we briefly explain for these three models how the correct relic dark matter density can be

achieved and highlight important cosmological constraints. In most of this thesis we assume a neutralino LSP, however, in chapter 8 possible consequences of an EWIP LSP scenario are scrutinized.

Other SUSY particles could also be considered as dark matter candidates. Particularly a sneutrino LSP is weakly charged and could in principle provide the correct relic density. However, all sneutrinos of the MSSM have already been excluded as dark matter candidates from direct detection experiments [205]. But a sterile or right-handed sneutrino in extensions of the MSSM could indeed be a viable candidate [206]. Many other alternative extensions of the MSSM, not even speaking about non-SUSY models, include interesting dark matter candidates, see ref. [207] and references therein.

3.7.1 Neutralino dark matter

The prime dark matter candidate within R-parity conserving SUSY theories is the lightest neutralino. It is only weakly interacting, in many GUT-constrained models its mass is $\mathcal{O}(100\text{ GeV})$ and due to eq. (2.85a) it is naturally the LSP. Despite these compelling features there is one major obstacle: the thermal relic abundance of neutralinos typically exceeds the observed value, given in eq. (2.22). Thus, efficient annihilation mechanisms had to take place in the early Universe in order to save the neutralino as dark matter candidate. Such efficient mechanisms can for example be found in the

- bulk region, where sleptons are relatively light and two neutralinos can efficiently annihilate via a t-channel slepton exchange into a pair of leptons,
- coannihilation region, where the neutralino is very close in mass with, e.g., a light stop, stau, or chargino, and the neutralino and the particle close in mass can efficiently coannihilate into SM particles,
- heavy Higgsino / focus point region, where the neutralino is relatively heavy and due to large higgsino components it can efficiently annihilate into massive SM gauge bosons,
- Higgs or Z resonance region: for $2\,m_{\tilde{\chi}_1^0} \approx m_{A^0}, m_{\mathrm{Z}}$ efficient annihilation is possible via a pseudoscalar Higgs boson A^0 or Z boson resonance,
- light Higgsino region, which is the only viable annihilation mechanism for very light neutralinos ($m_{\tilde{\chi}_1^0} \lesssim 30\text{GeV}$). Here, the neutralino annihilates efficiently due to non-vanishing Higgsino components via a t-channel stau exchange into a pair of taus.

All these annihilation mechanisms select different MSSM parameter regions and result in distinct collider signatures.

Furthermore, direct dark matter detection experiments set limits on spin-independent and spin-dependent elastic neutralino-nucleon scattering cross sections, see for example ref. [208] and ref. [209]. Current neutralino annihilation in our galaxy (and its satellites) can be searched for in gamma-ray or neutrino experiments, see for example ref. [210–212] and ref. [213, 214] respectively. Also, post-freeze–out annihilation in the early Universe could have left observable imprints in the CMB [215] or could have altered the predictions of BBN [216].

3.7.2 Gravitino and axino dark matter

The gravitino falls into the class of extremely weakly interacting particles as its couplings to MSSM particles are suppressed by the Planck scale Λ_{Planck}; it is (almost) always the LSP in GMSB models and easily the LSP in SUGRA models. Another EWIP, the fermionic axino, is introduced in Peccei-Quinn extensions of the MSSM. Its mass $m_{\widetilde{a}}$ is a model dependent parameter and can be smaller than all MSSM particles; couplings to MSSM patricles are suppressed by the Peccei-Quinn (PQ) scale $f_{\text{PQ}} \gtrsim 6 \times 10^8$ GeV [39, 217], i.e., the scale where the Peccei-Quinn symmetry is broken.

Both EWIPs are viable DM candidates. There is even the possibility that the gravitino and axino are both simultaneously lighter than the lightest MSSM particle. We refer to refs. [218–222] for studies of resulting cosmological and phenomenological implications.

The correct relic density of gravitino dark matter can be achieved from thermal production in the hot SUSY-QCD plasma right after inflation or non-thermally from NLSP decays [223–227]. The thermal relic gravitino density for a standard cosmological history, i.e., without additional release of entropy, is given by

$$\Omega_{\widetilde{G}}^{TP} = \sum_{i=1}^{3} \omega_i g_i^2(T_R) \left[1 + \frac{M_i^2(T_R)}{3m_{\widetilde{G}}^2}\right] \ln\left(\frac{k_i}{g_i(T_R)}\right)\left(\frac{m_{\widetilde{G}}}{100\ \text{GeV}}\right)\left(\frac{T_R}{10^{10}\ \text{GeV}}\right) \tag{3.24}$$

with $\omega_{1,2,3} = (0.018, 0.044, 0.117)$ and $k_{1,2,3} = (1.266, 1.312, 1.271)$ for $U(1)_Y$, $SU(2)_L$, and $SU(3)_C$ respectively [225]. Thus, it scales essentially linearly with the reheating temperature T_R and depends quadratically on the ratio between the gaugino mass parameters M_i at the scale of reheating and the gravitino mass $m_{\widetilde{G}}$.

For the axino, viable parameter regions with the correct relic density from thermal and/or non-thermal axino production are model dependent and investigated in refs. [221, 228–231].

In both EWIP dark matter scenarios the NLSP might become long-lived due to suppressed couplings. Thus, the NLSP can then decay during or after BBN and the emitted SM particles can reprocess the primordial abundances of deuterium, helium, and lithium [232–235], spoiling the agreement between predictions of BBN and observations of light element abundances. Resulting constraints in the $\tilde{\tau}_1$ NLSP case are discussed in detail in section 7.1.

Part II

Combining production and decay of squarks at NLO QCD

Chapter 4

Combining production and decay

In this and the following chapters we want to present a calculation of combined squark–squark production and decay at NLO in SUSY-QCD. In this chapter, we first motivate such a calculation in section 4.1. Second, in section 4.2 the theoretical approach of the combined calculation is presented. Third, in sections 4.3 and 4.4 we explain the calculation at NLO of, respectively, separate squark–squark production and decay, both being part of the factorizable NLO corrections to the combined process. In the following chapters, two phenomenological applications are presented. On the one hand, in chapter 5 squark–squark production is combined with direct decays into two lightest neutralinos. On the other hand, in chapter 6 for the same production process one squark decays directly into the lightest neutralino and the other one into the second-lightest neutralino, which subsequently decays into two leptons and the lightest neutralino via an on-shell intermediate slepton.

4.1 Motivation

In section 3.3.1 an overview of the current status of theoretical predictions for squark and gluino processes including higher orders was given. Such precise and reliable theoretical predictions are necessary for several reasons:

- corrections (particularly NLO QCD to the production) are large, so inclusion of higher-order corrections is necessary for a reliable phenomenological prediction,
- similarly, inclusion of higher-order corrections drastically reduces theoretical uncertainties,
- thus, such corrections are needed to set accurate exclusion limits,
- to possibly refine experimental search strategies in problematic parameter regions, and
- in case of discovery, to precisely determine the parameters of the underlying model, as explained in section 3.3.3.

Until now precision studies of sparticle production at the LHC, as discussed in section 3.3.1, have focused on inclusive cross sections, without taking into account phase-space cuts that have to be applied in any experimental analysis. Although these inclusive quantities are of

fundamental interest, both for exclusion limits and for parameter determination, they are not directly observable in high-energy collider experiments. Thus, a fully differential prediction including higher-orders in all relevant stages of the process (eventually matched to an NLO parton shower) is desirable. This requires the calculation of NLO effects for processes with intermediate massive unstable particles. Thus, off-shell effects of order $\mathcal{O}(\Gamma_X/m_X)$, where Γ_X is the width of the intermediate particle X and m_X its mass, might become important and should be investigated.

In this work, we systematically study squark–squark production and subsequent electroweak decays at NLO in QCD. This calculation is performed within the *narrow-width approximation* (NWA), thus treating intermediate squarks on-shell. In this approximation, at NLO, virtual and real corrections factorize into corrections to on-shell production and decay subprocesses. However, the NWA neither includes off-shell effects of the intermediate unstable squarks nor the full NLO corrections: besides factorizable corrections also non-factorizable contributions have to be considered where a separation into production and decay is not possible. Furthermore, single-resonant or non-resonant contributions, which correspond to diagrams with a sub-dominant pole structure but an identical final state, are also not included in the NWA. Still, in the narrow-width approximation a fully differential description of final states (jets, leptons, LSPs) including well-defined (factorizable) NLO QCD corrections is possible and realistic kinematic cuts on the momenta of the final state particles can be applied. These corrections are expected to yield the dominant part of the NLO contributions.

In the following section we discuss several approximations at LO and NLO for calculating processes involving unstable particles. There, we introduce a gauge-invariant splitting into factorizable and non-factorizable NLO corrections, where we also explain the general procedure, applied in the following chapters, for calculating factorizable corrections in the NWA as a formal expansion in the strong coupling. Besides the discussed approximations, many more can be found in the literature, particularly in the context of 4-fermion predictions for LEP2 [236].

4.2 Methods

In this section we want to introduce the methods applied in our calculation of squark–squark production and decay at NLO. Although we consider this particular process in the following chapters, the methods explained in this section are general and can in principle be applied to any process with intermediate massive unstable colored particles and in particular to other squark/gluino production channels and decay modes.

Since unstable particles cannot be described as asymptotic states, also no S-matrix elements exist for them. Therefore, from a theoretical point of view such particles should only be interpreted as intermediate states, appearing as poles in the S-matrix with finite imaginary part. Technically, in any calculation of massive unstable particles on-shell singularities have to be regularized by a finite width. Such a width is automatically introduced in the propagator

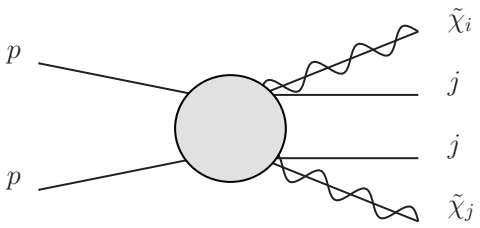

Figure 4.1: Illustration of the process under consideration. The circle illustrates all lowest order hadronic contributions to the given final state.

of an unstable particle via Dyson summation of self-energy contributions

$$\frac{1}{k^2 - M_0^2} \sum_{n=0}^{\infty} \left(\frac{-\Sigma(k^2)}{k^2 - M_0^2} \right)^n = \frac{1}{k^2 - M_0^2 + \Sigma(k^2)}\,, \tag{4.1}$$

where M_0 is the bare mass of the intermediate particle and Σ its self-energy contribution, which is related to its width Γ via the optical theorem: $\Gamma \sim \frac{1}{M} \operatorname{Im} \Sigma(M^2)$. However, via a simple replacement of propagators with their regularized version, only parts of higher-order contributions are included, and results might become gauge dependent. I.e. , Ward identities can be violated. A consistent calculation, e.g., within the *complex mass scheme*, manifestly preserves gauge invariance at any order of perturbation theory (see for example ref. [237] for a definition of the complex mass scheme at leading order), however such a calculation is technically involved, often computationally prohibitive and will not be pursued here. Approximations used in this work at LO and NLO are discussed in the following.

4.2.1 Born approximations

To be specific, we want to consider the process illustrated in figure 4.1, i.e. the hadroproduction of two jets $j = \{q, \bar{q}, g\}$ and two electroweak gauginos $\tilde{\chi}_l = \{\tilde{\chi}_l^0, \tilde{\chi}_l^\pm\}$ at LO,

$$pp \to jj\tilde{\chi}_i\tilde{\chi}_j(+X)\,. \tag{4.2}$$

The two gauginos are assumed to be stable for the moment. If unstable they decay via an electroweak decay chain which is unaffected by NLO QCD corrections[1]. For $\chi_{i,j} = \tilde{\chi}_1^0$ this processes directly contributes to the experimental signature $pp \to 2j + \not{E}_T(+X)$, which chapter 5 is dedicated to.

Within the MSSM the dominant contribution to process (4.2) comes from on-shell or nearly on-shell intermediate squarks, if kinematically available. Thus, the complete leading-order matrix element for the corresponding partonic process can be expanded in poles of different orders and is given by

$$\mathcal{M} = \frac{R_{12}(k_1^2, k_2^2, \{\theta_i\})}{(k_1^2 - M_{\tilde{q}_1}^2)(k_2^2 - M_{\tilde{q}_2}^2)} + \frac{R_1(k_1^2, k_2^2, \{\theta_i\})}{k_1^2 - M_{\tilde{q}_1}^2} + \frac{R_2(k_1^2, k_2^2, \{\theta_i\})}{k_2^2 - M_{\tilde{q}_2}^2} + N(k_1^2, k_2^2, \{\theta_i\})\,, \tag{4.3}$$

[1] From three-body decays or from the decay of SM gauge bosons or Higgs bosons in the electroweak decay chain, colored objects can still be emitted. However, corresponding QCD corrections are sub-leading.

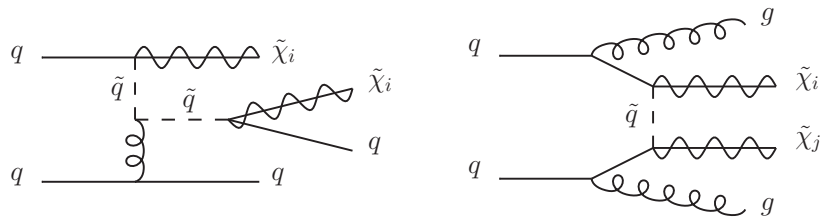

Figure 4.2: Illustrative single-pole (left) and non-resonant (right) diagrams not contributing in DPA.

where k_1, k_2 are the momenta and masses of the intermediate squarks $\tilde{q}_1, \tilde{q}_2$. Here, for simplicity we do not specify flavor, chirality or charge of these squarks. $\{\theta_i\}$ denotes all other kinematic variables and R_{12}, R_1 and R_2 denote the corresponding residues; N is a regular non-resonant contribution. The residues and the position of the poles (cf. Appendix A.1)

$$M^2_{\tilde{q}_i} = (M^0_{\tilde{q}_i})^2 - \Sigma_{\tilde{q}_i}(M^2_{\tilde{q}_i}) = m^2_{\tilde{q}_i} - i m_{\tilde{q}_i}\Gamma_{\tilde{q}_i}\,, \tag{4.4}$$

are gauge invariant quantities, where $m_{\tilde{q}_i}$ are the physical (real) masses of the unstable squarks and $\Gamma_{\tilde{q}_i}$ their finite width.

In the *double-pole approximation* (DPA) only the first term in the pole expansion of eq. (4.3) is kept:

$$\mathcal{M}^{\mathrm{DPA}} = \frac{R_{12}(k_1^2, k_2^2, \{\theta_i\})}{(k_1^2 - m^2_{\tilde{q}_1} + i m_{\tilde{q}_1}\Gamma_{\tilde{q}_1})(k_2^2 - m^2_{\tilde{q}_i} + i m_{\tilde{q}_2}\Gamma_{\tilde{q}_2})}\,. \tag{4.5}$$

Diagrams that contain only one pole ($\sim R_{1,2}$) of $\tilde{q}_i$ are suppressed by $\mathcal{O}(\Gamma_{\tilde{q}_j}/m_{\tilde{q}_j})$ and diagrams without a squark pole ($\sim N$) by $\mathcal{O}(\Gamma_{\tilde{q}_i}\Gamma_{\tilde{q}_j}/m_{\tilde{q}_j} m_{\tilde{q}_j})$. On the one hand, this can be seen as an approximation for the calculation of process (4.2). On the other hand, taking into account the organizational classes of hadroproduction of SUSY particles, as explained in section 3.3, the terms proportional to the single poles ($\sim R_{1,2}$) can be considered as NLO contributions to squark–gaugino production including the squark decay (a corresponding example diagram is shown in figure 4.2 on the left); and the non-resonant term ($\sim N$) as NNLO contributions to gaugino–gaugino production (a corresponding example diagram is shown in figure 4.2 on the right). Still, in a general off-shell calculation, only including all these contributions ensures a gauge invariant result.

In the *resonant scheme* the residue in eq. (4.5) is put on-shell via a mapping of the full four particle space $d\Pi_{4f}$. In this scheme the LO partonic cross section of (4.2) is given by

$$\sigma^{(0)}_{\mathrm{res}} = \frac{1}{2s}\int d\Pi_{4f}\frac{|R_{12}(m^2_{\tilde{q}_1}, m^2_{\tilde{q}_1}, \{\theta_i\})|^2}{((k_1^2 - m^2_{\tilde{q}_1})^2 + m^2_{\tilde{q}_1}\Gamma^2_{\tilde{q}_1})\,((k_2^2 - m^2_{\tilde{q}_2})^2 + m^2_{\tilde{q}_2}\Gamma^2_{\tilde{q}_2})}\,, \tag{4.6}$$

where s is the squared total energy of the process in the center of mass system. The resonant scheme defined in this way always gives a gauge invariant result, however, such a procedure is not valid below threshold, i.e., we require $\sqrt{s} > m_{\tilde{q}_1} + m_{\tilde{q}_2}$. Furthermore, the applied mapping

is not uniquely defined and resulting predictions depend on its details.

In the limit $\Gamma_{\tilde{q}_i}/m_{\tilde{q}_i} \to 0$, the *narrow-width approximation*, the resonating contributions in eq. (4.6) can be approximated for each squark by

$$\int_{-\infty}^{+\infty} \frac{dk_i^2}{(k_i^2 - m_{\tilde{q}_i}^2)^2 + m_{\tilde{q}_i}^2 \Gamma_{\tilde{q}_i}^2} = \frac{\pi}{m_{\tilde{q}_i} \Gamma_{\tilde{q}_i}} \delta(k_i^2 - m_{\tilde{q}_i}^2)\,, \tag{4.7}$$

neglecting terms of order $\mathcal{O}(\Gamma_{\tilde{q}_i}/m_{\tilde{q}_i})$. For intermediate squarks (i.e. scalar particles), in NWA the phase-space integration of the squared amplitude for the total cross section of the $2 \to 4$ processes trivially factorizes into production and decay parts, unambiguously defined. At the hadronic level (convoluted with PDFs as in eq. (3.2)), the LO cross section for process (4.2) gets the form

$$\sigma^{(0)}_{\text{NWA}}(pp \to \tilde{q}_1\tilde{q}_2 \to q\tilde{\chi}_i q'\tilde{\chi}_j) = \sigma^{(0)}_{pp\to\tilde{q}_1\tilde{q}_2} \cdot \text{BR}^{(0)}_{\tilde{q}_1\to q\tilde{\chi}_i} \cdot \text{BR}^{(0)}_{\tilde{q}_2\to q'\tilde{\chi}_j}\,, \tag{4.8}$$

with the LO hadronic production cross section $\hat{\sigma}^{(0)}_{pp\to\tilde{q}_1\tilde{q}_2}$ and the LO branching ratios $\text{BR}^{(0)}$ for the squark decays into gauginos. For a decay into a neutralino the flavor of the emitted quark matches the flavor of the decaying squark; for a decay into a chargino the emitted quark is of the flavor of the corresponding $SU(2)$ partner.

A direct generalization of eq. (4.8) yields the cross section in a completely differential form, which can be written as

$$d\sigma^{(0)}_{\text{NWA}}(pp \to \tilde{q}_1\tilde{q}_2 \to q\tilde{\chi}_i q'\tilde{\chi}_j) = d\sigma^{(0)}_{pp\to\tilde{q}_1\tilde{q}_2} \frac{1}{\Gamma^{(0)}_{\tilde{q}_1}} d\Gamma^{(0)}_{\tilde{q}_1\to q\tilde{\chi}_i} \frac{1}{\Gamma^{(0)}_{\tilde{q}_2}} d\Gamma^{(0)}_{\tilde{q}_2\to q'\tilde{\chi}_j}\,. \tag{4.9}$$

Therein, $\Gamma^{(0)}_{\tilde{q}_1}$ and $\Gamma^{(0)}_{\tilde{q}_2}$ denote the LO total widths of the two squarks; $d\Gamma^{(0)}_{\tilde{q}_1\to q\tilde{\chi}_i}$ and $d\Gamma^{(0)}_{\tilde{q}_2\to q'\tilde{\chi}_j}$ are the respective differential decay distributions boosted to the moving frames of $\tilde{q}_1$ and $\tilde{q}_2$.

4.2.2 NLO approximations

The narrow-width approximation can directly be extended to NLO performing a formal expansion in the strong coupling α_s of all terms in eq. (4.9),

$$d\sigma_{pp\to\tilde{q}_1\tilde{q}_2} = d\sigma^{(0)}_{pp\to\tilde{q}_1\tilde{q}_2}(\alpha_s^2) + d\sigma^{(1)}_{pp\to\tilde{q}_1\tilde{q}_2}(\alpha_s^3) + \dots\,, \tag{4.10}$$

$$d\Gamma_{\tilde{q}_k\to q\tilde{\chi}_l} = d\Gamma^{(0)}_{\tilde{q}_k\to q\tilde{\chi}_l}(\alpha_s^0) + d\Gamma^{(1)}_{\tilde{q}_k\to q\tilde{\chi}_l}(\alpha_s) + \dots\,, \tag{4.11}$$

$$\Gamma_{\tilde{q}_k} = \Gamma^{(0)}_{\tilde{q}_k}(\alpha_s^0) + \Gamma^{(1)}_{\tilde{q}_k}(\alpha_s) + \dots\,. \tag{4.12}$$

Thus, the NLO prediction of the process (4.2) via resonant squark–squark production, i.e.,

$$pp \to \tilde{q}_1\tilde{q}_2 \to qq'\tilde{\chi}_i\tilde{\chi}_j(+X)\,, \tag{4.13}$$

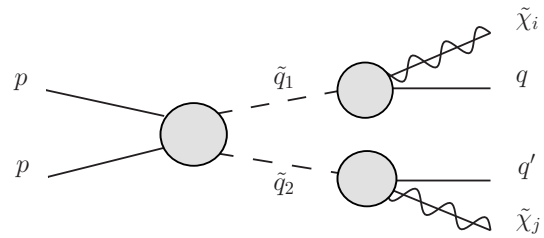

Figure 4.3: Illustration of the factorizable NLO corrections to (4.13). The circles indicate all contributions to the production up to $\mathcal{O}(\alpha_s^3)$ and the decays up to $\mathcal{O}(\alpha_s)$.

can in NWA at the hadronic level be written as

$$
\begin{aligned}
d\sigma^{(0+1)}_{\text{NWA}}(pp \to \tilde{q}_1\tilde{q}_2 \to q\tilde{\chi}_i^0 q'\tilde{\chi}_j^0(+X)) \;=\; & \\
& \frac{1}{\Gamma^{(0)}_{\tilde{q}_1}\,\Gamma^{(0)}_{\tilde{q}_2}} \Big[d\sigma^{(0)}_{pp\to\tilde{q}_1\tilde{q}_2}\, d\Gamma^{(0)}_{\tilde{q}_1\to q\tilde{\chi}_i^0}\, d\Gamma^{(0)}_{\tilde{q}_2\to q'\tilde{\chi}_j^0} \left(1 - \frac{\Gamma^{(1)}_{\tilde{q}_1}}{\Gamma^{(0)}_{\tilde{q}_1}} - \frac{\Gamma^{(1)}_{\tilde{q}_2}}{\Gamma^{(0)}_{\tilde{q}_2}}\right) \\
& + d\sigma^{(0)}_{pp\to\tilde{q}_1\tilde{q}_2}\, d\Gamma^{(1)}_{\tilde{q}_1\to q\tilde{\chi}_i^0}\, d\Gamma^{(0)}_{\tilde{q}_2\to q'\tilde{\chi}_j^0} \;+\; d\sigma^{(0)}_{pp\to\tilde{q}_1\tilde{q}_2}\, d\Gamma^{(0)}_{\tilde{q}_1\to q\tilde{\chi}_i^0}\, d\Gamma^{(1)}_{\tilde{q}_2\to q'\tilde{\chi}_j^0} \\
& + d\sigma^{(1)}_{pp\to\tilde{q}_1\tilde{q}_2(X)}\, d\Gamma^{(0)}_{\tilde{q}_1\to q\tilde{\chi}_i^0}\, d\Gamma^{(0)}_{\tilde{q}_2\to q'\tilde{\chi}_j^0} \Big], \qquad (4.14)
\end{aligned}
$$

which is again manifestly gauge invariant. The LO term in the first line of eq. (4.14) gets a global correction factor from the NLO contribution to the total widths; the second and third line involve the NLO virtual and real radiation corrections to the decay distributions and the production cross section, respectively. In this way corrections to the production and to the decays factorize and can be calculated independently, as illustrated in figure 4.3. In NWA the intermediate squarks in figure 4.3 are on-shell and the blobs indicate higher order corrections including real gluon radiation. The factorized calculations are presented in section 4.3 for the production and section 4.4 for the decay. An analogous treatment has been used, e.g., for the calculation of NLO corrections to top pair production and decay in the SM [238, 239] and recently for scalar top production and decay in extensions of the SM, including the MSSM [240].

The NWA, however, can only account for a subset of the complete NLO QCD corrections of the given process. For example, interactions between initial and final state quarks, interactions between final state quarks of the two decays and (clearly) general off-shell effects are not included. Still, corrections of the former type can both give large double resonant contributions in the soft gluon limit and could thus be numerically important compared to general off-shell corrections, which are suppressed at NLO by at least $\mathcal{O}(\alpha_s\Gamma_{\tilde{q}}/m_{\tilde{q}})$. In the following we sketch how such *non-factorizable corrections* can be calculated as an independent gauge-invariant subset.

Non-factorizable corrections

Starting from the double-pole approximation, two classes of diagrams contributing at NLO can be identified. First, contributions already illustrated in figure 4.3 belong to the class of

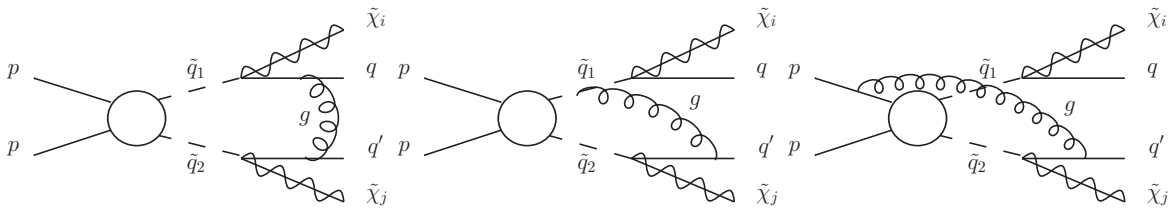

Figure 4.4: Illustration of manifestly non-factorizable NLO corrections to (4.13). The circle indicates the lowest order contribution to the hadronic production of a squark-pair.

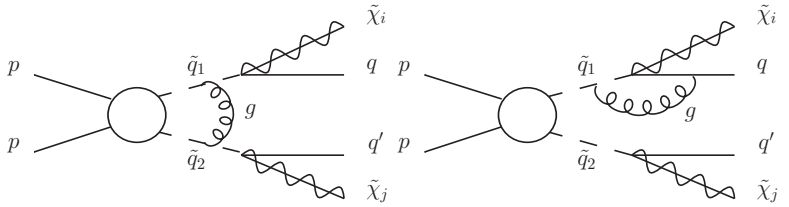

Figure 4.5: Illustration of non-manifestly non-factorizable NLO corrections to (4.13). The circle indicates the lowest order contribution to the hadronic production of a squark-pair.

factorizable corrections. These corrections can be attributed either to production or to one of the decays. In the on-shell limit of the intermediate squarks the resulting cross section is given by eq. (4.14). For the second class of diagrams, the *non-factorizable corrections*, such a separation is not possible; a set of (virtual) example diagrams for this class is shown in figure 4.4. Superficially, such diagrams do not yield an overall double-pole. Indeed, corresponding real radiation diagrams (obtained by cutting a gluon line) are clearly not double-resonant for hard gluons. However, this is very well the case in the soft-limit of the exchanged/radiated gluon. From a physical point of view such soft gluons induce relatively long range forces and thus allow for interactions between different stages of the process. In this soft-limit the non-factorizable corrections can be written as

$$d\sigma^{\mathrm{NF}} = d\sigma^{(0)}_{\mathrm{res}}\,\delta^{\mathrm{NF}}\,, \tag{4.15}$$

i.e., by multiplying the resonant differential cross section, defined in eq. (4.6), with a scalar factor δ^{NF}. As already mentioned NWA cannot be applied here. The complete NLO correction to (4.13) in DPA then reads

$$d\sigma^{(0+1)} = d\sigma^{(0+1)}_{\mathrm{NWA}} + d\sigma^{\mathrm{NF}}\,. \tag{4.16}$$

The just given classification into factorizable and non-factorizable contributions can only be illustrative. The summed matrix elements at NLO in DPA themselves are not gauge-invariant. Thus, also a general gauge-invariant splitting between factorizable and non-factorizable contributions has to be performed carefully. This is not possible on a purely diagrammatic basis. Diagrams interconnecting different stages of the process, as already illustrated in figure 4.4, always yield non-factorizable corrections – called *manifestly non-factorizable*. Ad-

ditionally, further diagrams, illustrated in figure 4.5, contribute to factorizable and to non-factorizable corrections – called *non-manifestly non-factorizable*. For example the left diagram in figure 4.5 can be understood as part of the factorizable corrections in the production stage if the two propagators attached to the decays are resonant, otherwise it gives a non-factorizable correction. On the other hand, the diagram on the right of figure 4.5 can be understood as a factorizable correction in the decay stage if the propagator close to the production is resonant and otherwise as a non-manifestly non-factorizable contribution. Again, similar arguments hold for the corresponding real radiation contributions, obtained cutting a gluon line. A gauge invariant splitting between factorizable and non-manifestly non-factorizable contributions is explicitly illustrated in the following.

Gauge invariant splitting

The key point in the splitting between factorizable and non-factorizable corrections is that in the soft limit contributions from non-manifestly non-factorizable diagrams can be split into different currents which contribute either to the production, to one of the decays, or yield non-factorizable contributions [241, 242].

Considering for example the emission of a virtual gluon from a squark-line in diagrams like the ones shown in figure 4.5, the two adjacent squark propagators can be written in a partial fraction decomposition

$$\frac{1}{[k^2 - M_{\tilde{q}}^2][(k+q)^2 - M_{\tilde{q}}^2 + i\epsilon]} = \frac{1}{2kq + i\epsilon}\left(\frac{1}{(k+q)^2 - M_{\tilde{q}}^2} - \frac{1}{k^2 - M_{\tilde{q}}^2 + i\epsilon}\right). \tag{4.17}$$

Here $M_{\tilde{q}}^2$ includes the width of the squark, as defined in eq. (4.4). The momentum of the radiated gluon is given by q, such that $k+q$ is the momentum of the squark inside the loop and k the one outside of the loop. The ϵ prescription is needed to ensure causality in any step of the calculation.

Applying such a decomposition, the right diagram in figure 4.5 can for example be manipulated in the following way

$$\mathcal{M} = i16\pi\alpha_s C\ \mathcal{M}^{\mathrm{DPA}} \int \frac{d^4q}{(2\pi)^4} \frac{k_1 p_1}{(q^2 + i\epsilon)(2p_1 q + i\epsilon)(k_1^2 - M_{\tilde{q}_1}^2 + 2k_1 p_1 + i\epsilon)} \tag{4.18}$$

$$= i16\pi\alpha_s C\ \mathcal{M}^{\mathrm{DPA}} \int \frac{d^4q}{(2\pi)^4} \frac{1}{(q^2 + i\epsilon)} \frac{k_1 p_1}{(2k_1 q + i\epsilon)(2p_1 q + i\epsilon)} \left(1 - \frac{k_1^2 - M_{\tilde{q}_1}^2}{k_1^2 - M_{\tilde{q}_1}^2 + 2k_1 q + i\epsilon}\right), \tag{4.19}$$

where C is a color factor, irrelevant for our discussion, that depends on the color structure of $\mathcal{M}^{\mathrm{DPA}}$. The momentum of the external quark the gluon is attached to, is denoted by p_1. The non-factorizable corrections are only relevant in the soft limit. Therefore any q dependance was dropped in the numerator of eq. (4.18). Now, the first term in eq. (4.19) can directly be identified with a factorizable correction to the corresponding squark decay. The second term remains as non-factorizable correction, which is enhanced in the soft limit $q \to 0$. The singularity in this limit is partly regulated by the squark width.

A similar procedure including a partial fraction decomposition is possible for corresponding real radiation diagrams. Summing virtual and real contributions of all non-factorizable

contributions (manifestly and non-manifestly), only a small number of diagrams yield non-vanishing contributions. Actually, only non-factorizable contributions from the left diagram in figure 4.5, the left diagram in figure 4.4 and the diagram in the center of figure 4.4 (plus the one where the gluon is attached to the other squark/final state quark) together with their real radiation interferences yield a non-zero contribution to the correction factor δ^{NF}.

The gauge independence of this procedure can be checked projecting the gluons in the corresponding real contributions onto their longitudinal component and verifying that their contribution vanishes when the factorizable and non-factorizable corrections are combined separately (in fact also when separating factorizable corrections into production and decay).

Alternatively, the non-factorizable corrections can be defined simply subtracting the on-shell factorizable corrections from the full $\mathcal{O}(\alpha_s)$ corrections in DPA [243]. Both procedures are equivalent in DPA.

In this thesis we do not present results for non-factorizable corrections to (4.13). However, numerical effects seem to be small (below 1 %), both on the level of distributions and integrated cross sections. A detailed study is under way and will be presented elsewhere.

4.3 Squark–squark production

In this section we calculate on-shell squark–squark production at LO and NLO, which is an essential prerequisite for combining production and decay in the calculation of factorizable NLO contributions to squark–squark production processes. In the following we present analytical LO differential partonic cross sections and explain details of the NLO calculation. Here, special care is given to the treatment of soft and collinear singularities and to additional quark radiation, including the discussion of different schemes for avoiding an important double counting problem.

4.3.1 LO squark–squark production

Amplitudes and cross sections for squark production depend on the flavors (indices i, j) and on the chiralities (indices a, b) of the squarks. Here, we only consider light-flavor squarks. Thus, corresponding quarks can be treated massless.

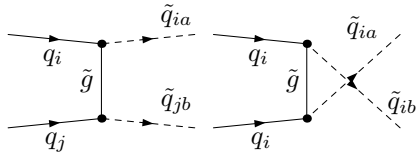

Figure 4.6: Tree-level Feynman diagrams for squark-squark production.

If the two produced squarks are of the same flavor, t- and u-channel gluino exchange diagrams, shown in figure 4.6, contribute. For squarks of the same chirality, the partonic cross section reads

$$\frac{d\hat{\sigma}^{(0)}_{q_i q_i \to \tilde{q}_{ia}\tilde{q}_{ia}}}{dt} = \frac{\pi\alpha_s^2}{9s^2}\, m_{\tilde{g}}^2 s \left(\frac{1}{(t-m_{\tilde{g}}^2)^2} + \frac{1}{(u-m_{\tilde{g}}^2)^2} + \frac{2/3}{(u-m_{\tilde{g}}^2)(t-m_{\tilde{g}}^2)} \right), \tag{4.20}$$

where s, t and u are the usual Mandelstam variables for a $2 \to 2$ process. For different chiralities and $m_q = 0$, the interference between the t- and u-channel diagrams is absent, yielding

$$\frac{d\hat{\sigma}^{(0)}_{q_i q_i \to \tilde{q}_{ia}\tilde{q}_{ib}}}{dt} = \frac{2\pi\alpha_s^2}{9s^2} \left(\frac{-st - (t-m_{\tilde{q}_{ia}}^2)(t-m_{\tilde{q}_{ib}}^2)}{(t-m_{\tilde{g}}^2)^2} + \frac{-su - (u-m_{\tilde{q}_{ia}}^2)(u-m_{\tilde{q}_{ib}}^2)}{(u-m_{\tilde{g}}^2)^2} \right). \tag{4.21}$$

On the other hand, if the two squarks are of different flavors, there is no u-channel exchange diagram; hence, the partonic cross section for equal chiralities is given by

$$\frac{d\hat{\sigma}^{(0)}_{q_i q_j \to \tilde{q}_{ia}\tilde{q}_{ja}}}{dt} = \frac{2\pi\alpha_s^2}{9s^2} \frac{m_{\tilde{g}}^2 s}{(t-m_{\tilde{g}}^2)^2}, \tag{4.22}$$

and for different chiralities by

$$\frac{d\hat{\sigma}^{(0)}_{q_i q_j \to \tilde{q}_{ia}\tilde{q}_{jb}}}{dt} = \frac{2\pi\alpha_s^2}{9s^2} \frac{-(t-m_{\tilde{q}_{ia}}^2)(t-m_{\tilde{q}_{ib}}^2) - st}{(t-m_{\tilde{g}}^2)^2}. \tag{4.23}$$

Besides the dominating QCD contributions, there are also tree-level electroweak production channels [128, 135] with chargino and neutralino exchange, which can interfere with the QCD amplitude providing a contribution to the cross-section of $\mathcal{O}(\alpha\alpha_s)$. In principle these terms can be numerically of similar importance as the NLO QCD $\mathcal{O}(\alpha_s^3)$ corrections we are investigating here. However, those contributions are neglected for the presented study.

Now, the LO hadronic differential production cross section, $d\sigma^{(0)}_{pp\to\tilde{q}\tilde{q}'}$, can be obtained as in eq. (3.2),

$$d\sigma^{(0)}_{pp\to\tilde{q}\tilde{q}'} = \int_{\tau_0}^{1} d\tau\, \mathcal{L}_{qq'}(\tau)\, d\hat{\sigma}^{(0)}_{qq'\to\tilde{q}\tilde{q}'}(\tau)\,, \tag{4.24}$$

where the parton luminosity $\mathcal{L}_{qq'}(\tau)$ is defined in eq. (3.3).

4.3.2 NLO squark–squark production

The NLO QCD corrections to squark–squark production have been known for many years [38] and an efficient public code (`Prospino 2`) is available for the calculation of inclusive cross sections at NLO. However, for a systematic study including the decay of the squarks, also the complete differential cross section is necessary. To this purpose, we perform an independent (re)calculation of the NLO QCD corrections, where we treat the masses for $\tilde{q}_L$, $\tilde{q}_R$ and all chirality and flavor configurations independently. In the previous calculation [38] different squark chiralities are treated as mass degenerate and NLO contributions are always summed over all chirality and flavor combinations.

NLO calculations, in general, involve treatment of infrared and collinear divergences in intermediate steps. Since our calculation does not involve any diagrams with non-Abelian vertices, infrared singularities can be regularized by a gluon mass (λ). Collinear singularities, in analogy, can be regularized by a quark mass (m_q), that is kept at zero everywhere else in the calculation. The cancellation of these two kinds of singularities is obtained by summing the virtual loop contributions and the real gluon bremsstrahlung part, with subsequent mass factorization in combination with the choice of the parton densities.

The complete NLO corrections to the differential cross section can be written symbolically in the following way:

$$d\sigma^{(1)}_{pp\to\tilde{q}\tilde{q}'(X)} = d\sigma^{\text{virtual+soft}}_{pp\to\tilde{q}\tilde{q}'(g)} + d\sigma^{\text{coll}}_{pp\to\tilde{q}\tilde{q}'(g)} + d\sigma^{\text{hard}}_{pp\to\tilde{q}\tilde{q}'g} + d\sigma^{\text{real-quark}}_{pp\to\tilde{q}\tilde{q}'\bar{q}^{(\prime)}}\,. \tag{4.25}$$

With $d\sigma^{\text{virtual+soft}}_{pp\to\tilde{q}\tilde{q}'(g)}$ we denote the summed contributions from the renormalized virtual corrections and soft gluon emission; $d\sigma^{\text{coll}}_{pp\to\tilde{q}\tilde{q}'(g)}$ corresponds to initial state collinear gluon radiation including the proper subtraction term for the collinear divergences; $d\sigma^{\text{hard}}_{pp\to\tilde{q}\tilde{q}'g}$ denotes the remaining hard gluon emission outside the soft and collinear phase space regions. $d\sigma^{\text{real-quark}}_{pp\to\tilde{q}\tilde{q}'\bar{q}^{(\prime)}}$ is the contribution from real quark emission from additional quark–gluon initial states contributing at NLO. All these terms are discussed in the following paragraphs.

Technically, the calculation of the loop corrections and real radiation contributions is performed separately for every flavor and chirality combination, $q_i q_j \to \tilde{q}_{ia}\tilde{q}_{jb}$, where we

employ the computer codes `FeynArts` [244] and `FormCalc` [245, 246]. Appendix A.3 shows a collection of the contributing Feynman diagrams. In the numerical analysis presented in the following chapters loop integrals are numerically evaluated with `LoopTools` [245].

Renormalization of the virtual contributions

For a UV finite result, the virtual contributions have to be calculated including appropriate NLO counterterms. They can explicitly be found in Appendix A.1. The necessary mass and field renormalization constants are determined according to the on-shell scheme, as also shown in Appendix A.1.

The renormalization of the QCD coupling constant ($\delta g_s = g_s\,\delta Z_{g_s}$) has to be done in accordance with the scheme for α_s in the PDFs, the $\overline{\text{MS}}$ scheme with five flavors. Thus, contributions from the top-quark, the squarks and the gluino have to be excluded from the running of α_s, i.e. eq. (2.21) with β_0 evaluated with the MSSM field content. This corresponds to the renormalization constant [38]

$$\delta Z_{g_s} = -\frac{\alpha_s}{4\pi}\Big[\Delta\frac{\beta_0^{\text{MSSM}}}{2} + \frac{1}{3}\log\frac{m_t^2}{\mu_R^2} + \log\frac{m_{\tilde{g}}^2}{\mu_R^2} + \frac{1}{12}\sum_{\tilde{q}}\log\frac{m_{\tilde{q}}^2}{\mu_R^2}\Big]\,, \tag{4.26}$$

with the UV divergence $\Delta = 2/\epsilon - \gamma_E + \log(4\pi)$ and the renormalization scale μ_R. β_0^{MSSM} is the leading term of the β-function of the QCD coupling in the MSSM,

$$\beta_0^{\text{MSSM}} = \left(\frac{11}{3}N_C - \frac{2}{3}n_f\right) + \left(-\frac{2}{3} - \frac{2}{3}N_C - \frac{n_f+1}{3}\right) = 3\,. \tag{4.27}$$

Here, $n_f = 5$ is the number of active flavors and $N_C = 3$. The first term corresponds to contributions from light degrees of freedom, the gluon and the light quarks; the second term to heavy particle contributions from the top quark, the gluino and the squarks.

In our calculation we choose to use dimensional regularization for the calculation, in accordance with the $\overline{\text{MS}}$ scheme employed for the PDFs we use. This breaks the supersymmetric Slavnov-Taylor identity that relates the qqg vertex function and the $q\tilde{q}\tilde{g}$ vertex function at one-loop order. However, this identity can be restored (see ref. [38, 247]) by an extra finite shift of the $\hat{g}_s$ coupling in the $q\tilde{q}\tilde{g}$ vertex with respect to g_s in the qqg vertex,

$$\hat{g}_s = g_s(1 + \delta Z_{\hat{g}_s})\,, \qquad \delta Z_{\hat{g}_s} = \delta Z_{g_s} + \frac{\alpha_s}{3\pi}\,. \tag{4.28}$$

Virtual corrections and real gluon radiation

In the term $d\sigma^{\text{virtual+soft}}_{pp\to\tilde{q}\tilde{q}'(g)}$ virtual and soft contributions are added at the parton level, i.e.,

$$d\hat{\sigma}^{\text{virtual+soft}}_{qq'\to\tilde{q}\tilde{q}'(g)}(\tau) \;=\; d\hat{\sigma}^{\text{virtual}}_{qq'\to\tilde{q}\tilde{q}'}(m_q,\lambda) + d\hat{\sigma}^{\text{soft}}_{qq'\to\tilde{q}\tilde{q}'(g)}(m_q,\lambda,\Delta E)\,, \tag{4.29}$$

which yields after convolution with PDFs

$$d\sigma^{\text{virtual+soft}}_{pp\to\tilde{q}\tilde{q}'(g)} \;=\; \int_{\tau_0}^{1} d\tau\;\mathcal{L}_{qq'}(\tau)\,d\hat{\sigma}^{\text{virtual+soft}}_{qq'\to\tilde{q}\tilde{q}'(g)}(\tau)\,. \tag{4.30}$$

The second term $d\hat{\sigma}^{\text{soft}}_{qq'\to\tilde{q}\tilde{q}'(g)}$ in eq. (4.29) contains the contributions from real gluon emission integrated over the soft-gluon phase space with $E_g < \Delta E$. In this regime the eikonal approximation [248, 249] can be applied, i.e., a generic real emission matrix element, where a gluon is attached to an external particle with momentum p_i can be written as

$$\mathcal{M}^{i}_{qq'\to\tilde{q}\tilde{q}'g} = g_s \frac{\epsilon p_i}{\pm p\cdot k}\mathcal{M}^{c_i}_{qq'\to\tilde{q}\tilde{q}'}\,, \tag{4.31}$$

where ϵ denotes the polarization and k the momentum of the gluon; $\mathcal{M}^{c_i}_{qq'\to\tilde{q}\tilde{q}'}$ is the born matrix element including the color structure of the gluon radiation, which depends on the particle emitting the gluon; as does the sign in the denominator: a plus sign refers to initial state radiation, a minus sign to final state radiation. In this way, the soft gluon contribution factorizes and can be written as a multiplicative "eikonal" correction factor to the LO cross section. The denominator of this eikonal factor can be written as

$$\frac{1}{p\cdot k} = \frac{1}{p^0 k^0(1-|\vec{p}|/p^0\cos\theta_{ig})}\,, \tag{4.32}$$

where θ_{ig} is the angle between the emitter and the gluon. Integrating over the gluon phase-space, this term diverges in the soft limit, $k^0 \to 0$ and for a massless emitter, i.e., $|\vec{p}| = p^0$ also in the collinear limit $\cos\theta_{ig} \to 1$. Both singularities cancel against similar divergences in the virtual contributions and/or appropriate mass factorization. However, in the course of the calculation these divergences have to be regularized. Here, both singularities are regularized via a mass parameter; soft ones via a fictitious gluon mass λ and collinear ones via a finite quark mass m_q. Alternatively, e.g., the dipole subtraction method can be used [250].

The differential cross-section in the soft limit is obtained by summing all soft gluon matrix elements, squaring them, summing over gluon polarizations and integrating over the soft gluon phase space ($E_g < \Delta E$). This can be done analytically [251, 252]. Defining $\epsilon_i = 1$ for incoming and $\epsilon_i = -1$ for outgoing particles, the soft gluon contribution at partonic level can be written as follows, using the label assignment $\{q, q', \tilde{q}, \tilde{q}'\} \leftrightarrow \{1, 2, 3, 4\}$:

$$d\hat{\sigma}^{\text{soft}}_{qq'\to\tilde{q}\tilde{q}'(g)}(m_q, \lambda, \Delta E) = -\frac{\alpha_s}{2\pi}\Big\{\sum_{i,j=1;i\le j}^{4}\epsilon_i\epsilon_j\, I_{ij}\Big\}\, d\hat{\sigma}^{(0)}_{qq'\to\tilde{q}\tilde{q}'}\,. \tag{4.33}$$

The I_{ij} involve the bremsstrahlung integrals $\mathcal{I}_{ij}$ of [252] and weight factors $C^{(tt,ut,uu)}_{\tilde{q}\tilde{q}'}$ due to the color structure. In our calculation the color structures are different for emission from t and u channel diagrams. Hence, the various appearing bremsstrahlung integrals enter the cross section with different weights. Accordingly, we decompose the partonic LO cross section for $qq' \to \tilde{q}\tilde{q}'$ in the following way in obvious notation,

$$d\hat{\sigma}^{(0)}_{qq'\to\tilde{q}\tilde{q}'} = d\hat{\sigma}^{(tt)}_{\tilde{q}\tilde{q}'} + d\hat{\sigma}^{(ut)}_{\tilde{q}\tilde{q}'} + d\hat{\sigma}^{(uu)}_{\tilde{q}\tilde{q}'} = \Big[C^{(tt)}_{\tilde{q}\tilde{q}'} + C^{(ut)}_{\tilde{q}\tilde{q}'} + C^{(uu)}_{\tilde{q}\tilde{q}'}\Big]\, d\hat{\sigma}^{(0)}_{qq'\to\tilde{q}\tilde{q}'}\,, \tag{4.34}$$

where the coefficients $C^{(tt,ut,uu)}_{\tilde{q}\tilde{q}'}$ for the individual channels can be easily read off from the LO cross sections in eqs. (4.20)–(4.23). Explicit expressions for I_{ij} including the color factors are listed in eq. (A.9) of Appendix A.2. Summing $d\hat{\sigma}^{(0)}_{qq'\to\tilde{q}\tilde{q}'}(m_q, \lambda, \Delta E)$ and $d\hat{\sigma}^{\text{virtual}}_{qq'\to\tilde{q}\tilde{q}'}(m_q, \lambda)$

the dependence on λ cancels analytically, leaving a residual logarithmic dependence on the cut-off parameter $\delta_s = 2\Delta E/\sqrt{s}$.

Additionally, the term $d\sigma^{\text{virtual+soft}}_{pp\to\tilde{q}\tilde{q}'(g)}$ still depends on the quark mass m_q owing to the initial-state collinear singularities. This dependence cancels by adding the real collinear radiation term $d\sigma^{\text{coll}}_{pp\to\tilde{q}\tilde{q}'(g)}$ resulting from hard gluon emission into a cone with opening angle $\Delta\theta$ around the two quarks in the initial state and mass factorization for the PDFs via addition of a proper subtraction term,

$$d\sigma^{\text{coll}}_{pp\to\tilde{q}\tilde{q}'(g)} = d\sigma^{\text{coll-cone}}_{pp\to\tilde{q}\tilde{q}'(g)}(m_q, \Delta\theta) + d\sigma^{\text{sub-pdf}}_{pp\to\tilde{q}\tilde{q}'}(m_q, \Delta E)\,. \tag{4.35}$$

Here the color factor is trivial, $(T^c)^2 = C_F = \frac{4}{3}$, as only squared matrix elements produce collinear divergences. The collinear gluon emission into a narrow cone around the emitting particle yields the following contribution that corresponds to the results of [253] with the replacement $\alpha Q_q^2 \to C_F\alpha_s$,

$$d\sigma^{\text{coll-cone}}_{pp\to\tilde{q}\tilde{q}'(g)}(m_q, \Delta\theta) = \int_{\tau_0}^1 d\tau \int_\tau^1 \frac{dx}{x} \int_x^{1-\delta_s} \frac{dz}{z}\, \mathcal{L}^{\text{coll}}_{qq'}(\tau, x, z)\; d\hat{\sigma}^{\text{coll-cone}}_{qq'\to\tilde{q}\tilde{q}'(g)}(\tau, z)\,. \tag{4.36}$$

The partonic collinear cross section can be written as

$$d\hat{\sigma}^{\text{coll-cone}}_{qq'\to\tilde{q}\tilde{q}'}(\tau, z) = d\hat{\sigma}^{(0)}_{qq'\to\tilde{q}\tilde{q}'}(\tau)\; \frac{4}{3\pi}\alpha_s \left[\frac{1+z^2}{1-z}\log\left(\frac{s\,\delta_\theta}{2m_q^2 z}\right) - \frac{2z}{1-z}\right], \tag{4.37}$$

with $\delta_\theta = 1-\cos\Delta\theta \simeq \Delta\theta^2/2$. The variable z is the ratio between the momenta of the emitter parton after and before the emission. The z-dependent luminosity is given by

$$\mathcal{L}^{\text{coll}}_{qq'}(\tau, x, z) = \frac{1}{1+\delta_{qq'}}\left[f_q\Big(\frac{x}{z}, \mu_F\Big)\; f_{q'}\Big(\frac{\tau}{x}, \mu_F\Big) + f_q(\frac{\tau}{x}, \mu_F)\, f_{q'}\Big(\frac{x}{z}, \mu_F\Big)\right]. \tag{4.38}$$

The collinear PDF subtraction term for phase-space slicing in accordance with the $\overline{\text{MS}}$ scheme, can be written as

$$\begin{aligned} d\sigma^{\text{sub-pdf}}_{pp\to\tilde{q}\tilde{q}'} = &-2\int_{\tau_0}^1 d\tau \int_\tau^1 \frac{dx}{x}\int_x^{1-\delta_s}\frac{dz}{z}\,\mathcal{L}^{\text{coll}}_{qq'}(\tau, x, z)\; d\hat{\sigma}^{\text{sub1}}_{qq'\to\tilde{q}\tilde{q}'}(\tau, z) \\ &-2\int_{\tau_0}^1 d\tau\; \mathcal{L}_{qq'}(\tau)\; d\hat{\sigma}^{\text{sub2}}_{qq'\to\tilde{q}\tilde{q}'}(\tau)\,, \end{aligned} \tag{4.39}$$

where at parton level, the z-dependent part of the subtraction term for one quark is given by

$$d\hat{\sigma}^{\text{sub1}}_{qq'\to\tilde{q}\tilde{q}'}(\tau, z) = d\hat{\sigma}^{(0)}_{qq'\to\tilde{q}\tilde{q}'}(\tau)\; \frac{2}{3\pi}\alpha_s \left[\frac{1+z^2}{1-z}\log\left(\frac{\mu_F^2}{(1-z)^2 m_q^2}\right) - \frac{1+z^2}{1-z}\right], \tag{4.40}$$

involving the factorization scale μ_F, whereas the z-independent part

$$d\hat{\sigma}^{\text{sub2}}_{qq'\to\tilde{q}\tilde{q}'}(\tau) = d\hat{\sigma}^{(0)}_{qq'\to\tilde{q}\tilde{q}'}(\tau)\; \frac{4}{3\pi}\alpha_s \left[1 - \log(\delta_s) - \log^2(\delta_s) + \left(\log(\delta_s) + \frac{3}{4}\right)\log\left(\frac{\mu_F^2}{m_q^2}\right)\right] \tag{4.41}$$

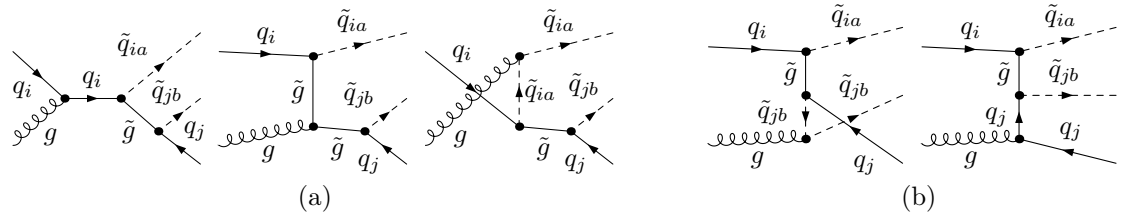

Figure 4.7: Resonant (a) and non-resonant (b) diagrams contributing to $q_i g \to \tilde{q}_{ia}\tilde{q}_{jb}\bar{q}_j$.

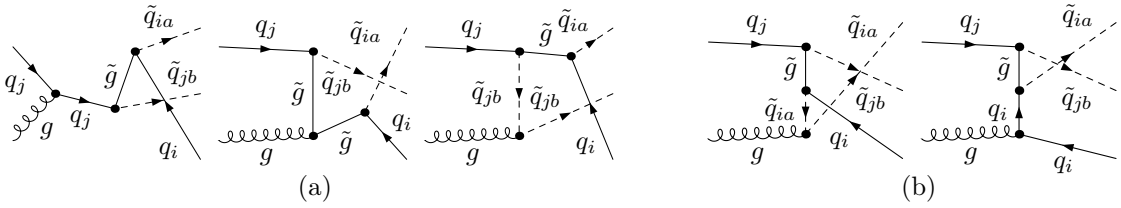

Figure 4.8: Resonant (a) and non-resonant (b) diagrams contributing to $q_j g \to \tilde{q}_{ia}\tilde{q}_{jb}\bar{q}_i$.

contains also the soft-gluon phase space cut δ_s. In the sum $d\sigma^{\text{virtual+soft}}_{pp\to\tilde{q}\tilde{q}'(g)} + d\sigma^{\text{coll}}_{pp\to\tilde{q}\tilde{q}'(g)}$ any dependence on m_q is canceled.

Finally, we have to add $d\sigma^{\text{hard}}_{pp\to\tilde{q}\tilde{q}'(g)}$ from the residual hard gluon emission outside the collinear region, which cancels the dependence on the slicing parameters δ_s for the soft and δ_θ for the collinear region. The used $2 \to 3$ phase-space for the real radiation is adapted to efficiently map around the singular regions.

Real quark radiation

At NLO also contributions from gluon-initiated subprocesses $q_i g \to \tilde{q}_{ia}\tilde{q}_{jb}\bar{q}_j$ and $q_j g \to \tilde{q}_{ia}\tilde{q}_{jb}\bar{q}_i$ open up and have to be included for a consistent treatment of NLO PDFs. Diagrams for these two subprocesses can be divided into resonant (figure 4.7(a) and 4.8(a)) and non-resonant (figure 4.7(b) and 4.8(b)) diagrams, where in the resonant diagrams the intermediate gluino can be on-shell. The appearing on-shell singularity is regularized including a decay width for the gluino in its propagator:

$$\frac{1}{p^2_{\tilde{g}} - m^2_{\tilde{g}}} \longrightarrow \frac{1}{p^2_{\tilde{g}} - m^2_{\tilde{g}} + i m_{\tilde{g}}\Gamma_{\tilde{g}}}\,. \tag{4.42}$$

As discussed below this width is a pure regulator and not the physical gluino width. This resonant production channel via on-shell gluinos corresponds basically to LO production of a squark–gluino pair with subsequent gluino decay. Such contributions are generally classified as squark–gluino production (see section 3.3) and have to be removed here to not double-count their contributions in the complete calculation including all channels. The same type of problem is discussed, e.g., in [254] in the context of NLO corrections to single top quark production, where quark radiation creates configurations corresponding to top quark pair production.

In a general context, combining production and decay for all colored SUSY particles ($\tilde{q}, \tilde{q}^*$ and $\tilde{g}$), also off-shell configurations from resonant diagrams appear. In this context, the off-

shell contributions from resonant diagrams in figure 4.7(a) and 4.8(a) can in the same way be classified as production and decay of squark–gluino pairs.

The most important difference in calculations with and without including decays is the role of the colored supersymmetric particles. In one case they belong to the final state, in the other one they are intermediate states. Thus, due to the quark radiation at NLO, a separation of squark–gluino and squark–squark channel contributions to a particular final state is only an intermediate organizational instrument. It is important to remember that our NLO calculation of the production of squark–squark pairs is meant as a necessary ingredient of eq. (4.14). Our primary goal is the consistency of the calculation at NLO of the full process with decays included and not only of the production of squarks.

In the following, we address the structure of the various terms contributing to the real quark radiation and explain the subtraction of arising collinear divergences. Afterwards, we introduce different approaches to perform the subtraction of the resonant contributions corresponding to squark–gluino production (with a subsequent gluino decay).

In the case of different flavors $i \neq j$, there are two parton processes which provide NLO differential cross sections for real quark emission, given by

$$d\hat{\sigma}_{q_i g \to \tilde{q}_{ia} \tilde{q}_{jb} \bar{q}_j} \sim d\Pi_{(2\to3)} \left[\overline{\left| \mathcal{M}_{\text{nonres},i} \right|^2} + 2\text{Re}\overline{\left(\mathcal{M}_{\text{nonres},i} \mathcal{M}^*_{\text{res},i} \right)} + \overline{\left| \mathcal{M}_{\text{res},i} \right|^2} \right] , \tag{4.43}$$

$$d\hat{\sigma}_{q_j g \to \tilde{q}_{ia} \tilde{q}_{jb} \bar{q}_i} \sim d\Pi_{(2\to3)} \left[\overline{\left| \mathcal{M}_{\text{nonres},j} \right|^2} + 2\text{Re}\overline{\left(\mathcal{M}_{\text{nonres},j} \mathcal{M}^*_{\text{res},j} \right)} + \overline{\left| \mathcal{M}_{\text{res},j} \right|^2} \right] ,$$

where *overline* represents the usual summing and averaging of external helicities and colors and $d\Pi_{(2\to3)}$ is the usual phase-space element for three particles in the final state. $\mathcal{M}_{\text{res},i}$ and $\mathcal{M}_{\text{nonres},i}$ correspond to the diagrams of figure 4.7(a) and figure 4.7(b), respectively, and $\mathcal{M}_{\text{res},j}$ and $\mathcal{M}_{\text{nonres},j}$ to those of figure 4.8(a) and figure 4.8(b).

For the case of equal flavors $i = j$ the partonic contribution is

$$d\hat{\sigma}_{q_i g \to \tilde{q}_{ia} \tilde{q}_{ib} \bar{q}_i} \sim d\Pi_{(2\to3)} \left[\overline{|\mathcal{M}_{\text{nonres}}|^2} + 2\text{Re}\overline{(\mathcal{M}_{\text{nonres}} \mathcal{M}^*_{\text{res}})} + \overline{|\mathcal{M}_{\text{res}}|^2} \right] , \tag{4.44}$$

with $\mathcal{M}_{\text{res}}$ from the diagrams of figure 4.7(a) and figure 4.8(a), which we will call $\mathcal{M}_{\text{res},1}$ and $\mathcal{M}_{\text{res},2}$ in this case; $\mathcal{M}_{\text{nonres}}$ is the part from the diagrams of figure 4.7(b) and figure 4.8(b). The term $2\text{Re}\overline{\left(\mathcal{M}_{\text{res},1} \mathcal{M}^*_{\text{res},2} \right)}$ appears only for equal chiralities ($a = b$) and flavors of the squarks. We describe the subtractions for the case with equal flavor; analogous arguments apply to the different-flavor case.

In the practical calculation of the real quark radiation contributions, one has to integrate over the phase space of the final state quark. The squared non-resonant terms lead to initial state collinear singularities. As in the gluonic case, these singular terms have to be subtracted since they are factorized and absorbed into the PDFs. Like in the case of gluon radiation, we divide the emission of a quark into a collinear and a non-collinear region. Since no IR singularities occur a separation into soft and hard quark emission is not required. The corresponding

hadronic cross section reads

$$d\sigma^{\text{real-quark}}_{pp\to\tilde{q}_{ia}\tilde{q}_{jb}\bar{q}^{(\prime)}} = \sum_{k=i,j}\frac{1}{1+\delta_{ij}}\left[d\sigma^{\text{coll-quark}}_{pp\to\tilde{q}_{ia}\tilde{q}_{jb}\bar{q}_k}(\Delta\theta) + d\sigma^{\text{noncoll-quark}}_{pp\to\tilde{q}_{ia}\tilde{q}_{jb}\bar{q}_k}(\Delta\theta)\right] . \tag{4.45}$$

Here, the non-collinear contribution, i.e. $\theta > \Delta\theta$, given by

$$d\sigma^{\text{noncoll-quark}}_{pp\to\tilde{q}_{ia}\tilde{q}_{jb}\bar{q}_{j/i}}(\Delta\theta) = \int_{\tau_0}^1 d\tau\, \mathcal{L}^{\text{noncoll-quark}}_{i/j}(\tau)\; d\hat{\sigma}_{q_{i/j}g\to\tilde{q}_{ia}\tilde{q}_{jb}\bar{q}_{j/i}}(\tau)\,, \tag{4.46}$$

is obtained convoluting the partonic cross section $d\hat{\sigma}_{q_{i/j}g\to\tilde{q}_{ia}\tilde{q}_{jb}\bar{q}_{j/i}}$ with the parton luminosity for non-collinear quark radiation

$$\mathcal{L}_i(\tau)^{\text{noncoll-quark}} = 2\int_\tau^1 \frac{dx}{x}\, g(x,\mu_F) f_i\Big(\frac{\tau}{x},\mu_F\Big) . \tag{4.47}$$

Resonant contributions in $d\hat{\sigma}_{q_{i/j}g\to\tilde{q}_{ia}\tilde{q}_{jb}\bar{q}_{j/i}}(\tau)$ have to be subtracted as explained below.

On the other hand, collecting in one formula the collinear cone emission of a quark and the subtraction term for the PDFs one finds

$$d\sigma^{\text{coll-quark}}_{pp\to\tilde{q}_{ia}\tilde{q}_{jb}\bar{q}_{j/i}}(\Delta\theta) = \int_{\tau_0}^1 d\tau \int_\tau^1 \frac{dx}{x}\int_x^1 \frac{dz}{z}\, \mathcal{L}^{\text{coll-quark}}_{i/j}(\tau,x,z)\; d\hat{\sigma}^{\text{coll-quark}}_{q_{i/j}g\to\tilde{q}_{ia}\tilde{q}_{jb}\bar{q}_{j/i}}(\tau,z)\,,$$

with

$$\begin{aligned} d\hat{\sigma}^{\text{coll-quark}}_{q_{i/j}g\to\tilde{q}_{ia}\tilde{q}_{jb}\bar{q}_{j/i}}(\tau,z) = {}& d\hat{\sigma}^{(0)}_{q_iq_j\to\tilde{q}_{ia}\tilde{q}_{jb}}\cdot \\ & \cdot\frac{\alpha_s}{2\pi}P_{qg}(z)\left[\log\Big(\frac{s(1-z)^2\,\delta_\theta}{2m_q^2 z}\Big) + 2z(1-z) - \log\Big(\frac{\mu_F^2}{m_q^2}\Big)\right], \end{aligned} \tag{4.48}$$

where $P_{qg}(z)$ is the gluon–quark splitting function

$$P_{qg}(z) = \frac{1}{2}[z^2 + (1-z)^2] \tag{4.49}$$

and the parton luminosity for collinear quark radiation is given by

$$\mathcal{L}_i(\tau,x,z)^{\text{coll-quark}} = \; 2\; g\left(\frac{x}{z},\mu_F\right) f_i\Big(\frac{\tau}{x},\mu_F\Big)\;, \tag{4.50}$$

involving the gluon distribution function $g(x,\mu_F)$.

Individually the collinear and non-collinear contributions depend on the residual slicing parameter $\delta_\theta = 1-\cos\Delta\theta$. In the sum any dependence cancels.

Subtraction schemes

Here we want to introduce two strategies to avoid the double-counting of terms in $d\sigma^{\text{real-quark}}_{pp\to\tilde{q}_{ia}\tilde{q}_{jb}\bar{q}^{(\prime)}}$ already contained in the LO contribution from the squark–gluino channel to the same final state:

- DS: Diagram Subtraction,
- DR: Diagram Removal.

The DR and DS schemes defined in the following are almost equal to the approaches extensively studied in [254].

In the DS scheme the contribution from the LO on-shell production of a squark–gluino pair with the gluino decaying into a squark is subtracted:

$$\begin{aligned} d\hat{\sigma}^{DS}_{q_i g\to\tilde{q}_{ia}\tilde{q}_{ib}\bar{q}_i} \;\sim\; & \left[\overline{\left|\mathcal{M}_{\text{nonres}}\right|^2} + 2\text{Re}\overline{(\mathcal{M}_{\text{nonres}}\mathcal{M}^*_{\text{res}})} + \overline{\left|\mathcal{M}_{\text{res}}\right|^2}\right] d\Pi_{(2\to3)} \\ & - \left[\overline{\left|\mathcal{M}_{\text{res},1}\right|^2} + \overline{\left|\mathcal{M}_{\text{res},2}\right|^2}\right] d\Pi_{(2\to2)\times(1\to2)} \;. \end{aligned} \tag{4.51}$$

In eq. (4.51), $d\Pi_{(2\to2)\times(1\to2)}$ is the phase-space with three particles in the final state applying consistently the on-shell condition $(p_{\tilde{q}} + p_q)^2 = m^2_{\tilde{g}}$ for the two different resonant cases. Eq. (4.51) is conceptually equal to the DS scheme explained in [254] and the "Prospino scheme" in [38, 255]; in practice our approach is slightly different. This is explained in more detail in Appendix A.4. We subtract at global level exactly what we would obtain from LO on-shell production of a squark–gluino pairs with the gluino decaying into a squark. This is done by producing two different sets of events corresponding to the two lines of eq. (4.51), respectively. In [38, 254, 255] a local subtraction of the on-shell contribution involving a mapping or reshuffling of momenta from the general $d\Pi_{2\to3}$ phase-space into an equivalent on-shell configuration is performed. These two implementations of the DS scheme give slightly different results even in the limit $\Gamma_{\tilde{g}} \to 0$. The DS scheme, both in the local approach and in the global approach, defined in eq. (4.51), is gauge invariant in the limit $\Gamma_{\tilde{g}} \to 0$. Therefore, the decay width of the gluino is used as a numerical regulator and not as a physical parameter.

In an extreme approach, the quark radiation contribution could even be completely excluded from the NLO corrections in the squark–squark channel. Then, all diagrams, resonant and non-resonant, constituting a gauge-invariant subset, have to be included in the squark–gluino production and decay channel (in this way, we would alter the organizational separation of squark/gluino channels). Since the term $\overline{|\mathcal{M}_{\text{nonres}}|^2}$ contains initial state collinear singularities, also the subtraction term of the PDFs has then to be excluded and computed within the squark–gluino channel. It is worth mentioning, that even if we want to include only on-shell configurations in all production and decay channels for the resonant intermediate supersymmetric particles (as intensively discussed in section 4.2), quark radiation in the NLO corrections unavoidably introduces off-shell contributions.

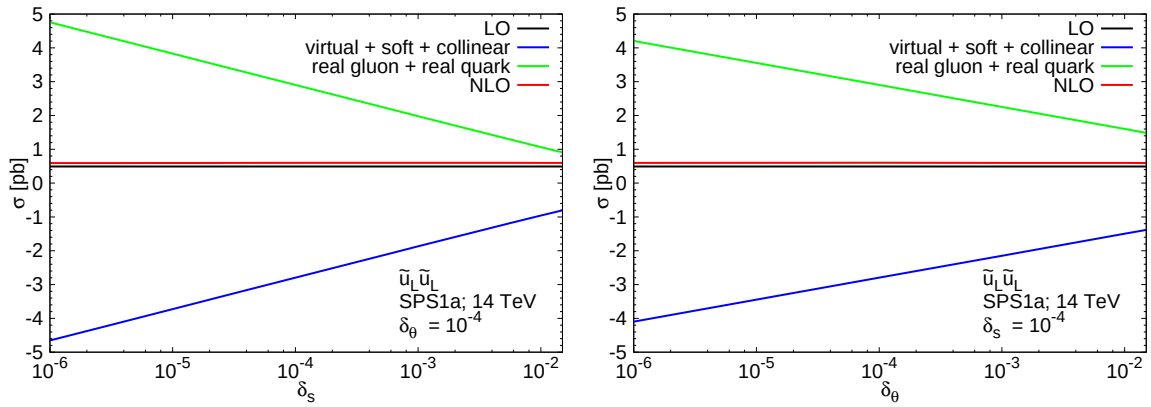

Figure 4.9: Dependence on the residual slicing parameters δ_s and δ_θ of the virtual+soft+collinear (blue) and hard gluon and quark radiation (green) contributions of the NLO corrections ΔNLO to the partial decay width $\Gamma_{\tilde{u}_2\to u\tilde{\chi}_1^0}$ for the parameter point SPS1a as introduced in section 5.2.1. Also shown is the sum of these contributions (red) and the LO contribution (black).

The DR scheme represents, in a certain sense, an intermediate step between the DS scheme and a complete removal as explained above. Here, one removes, from a diagrammatic perspective, the minimal set of contributions in the squared amplitude that contain a resonant gluino. In our calculation this results in

$$d\hat{\sigma}^{DR}_{q_i g\to\tilde{q}_{ia}\tilde{q}_{ib}\bar{q}_i} \sim \quad d\Pi_{(2\to3)}\left[\overline{|\mathcal{M}_{\text{nonres}}|^2} + 2\text{Re}\overline{(\mathcal{M}_{\text{nonres}}\mathcal{M}^*_{\text{res}})} + \delta_{ab}\ 2\text{Re}\overline{\left(\mathcal{M}_{\text{res},1}\mathcal{M}^*_{\text{res},2}\right)}\right]. \tag{4.52}$$

In the different flavor cases the third term in eq. (4.52) does not appear. Comparing eq. (4.52) with eq. (4.44), it is clear that the resonant terms $\overline{|\mathcal{M}_{\text{res},1}|^2}$ and $\overline{|\mathcal{M}_{\text{res},2}|^2}$ are removed. In the definition of DR given in [254] also the interference term $2\text{Re}\overline{(\mathcal{M}_{\text{nonres}}\mathcal{M}^*_{\text{res}})}$ is removed (with a study of the impact of this contribution), whereas in our definition of the DR scheme, we keep this interference term. Although the DR scheme formally violates gauge invariance, a consistent description is achieved when the procedure presented here is combined with off-shell contributions of all channels. In any case, the narrow-width approximation, both in the DR and the DS scheme is not an exact description; as an approximation it has a natural uncertainty arising from missing off-shell contributions and non-factorizable NLO corrections.

In our numerical results we basically employ the DR scheme, however, we compare it with results in the DS scheme, both for inclusive K-factors and for differential distributions.

Independence of unphysical regulators

Here we want to demonstrate that our final results for $d\sigma^{(1)}_{pp\to\tilde{q}\tilde{q}'(X)}$ do not dependent on any unphysical regulators. As an example, in figure 4.9 we plot the dependance on the slicing parameters δ_s (left) and δ_θ (right) for $\tilde{u}_L\tilde{u}_L$ production at the LHC with $\sqrt{S} = 14$ TeV for the

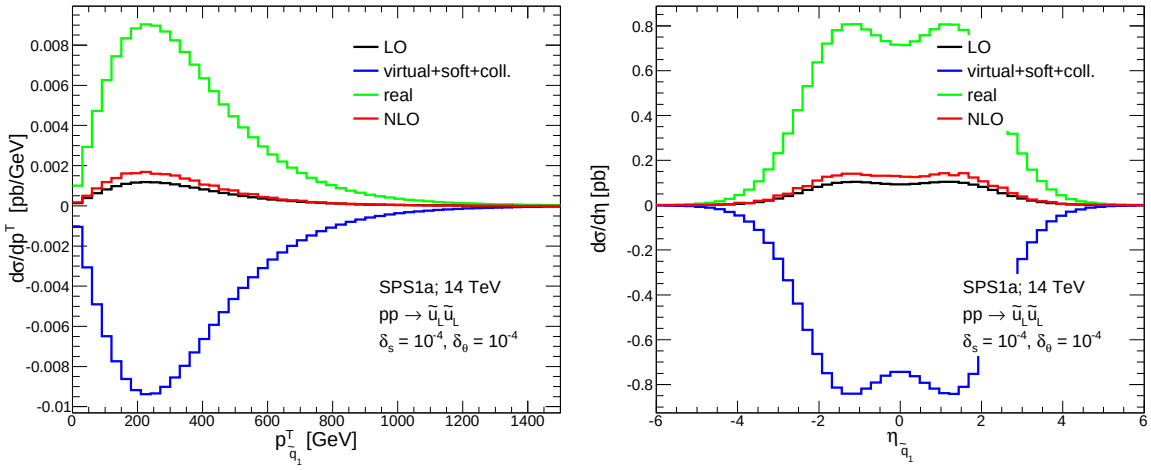

Figure 4.10: Differential distributions in $p_{\tilde{q}_1}^{\mathrm{T}}$ and $\eta_{\tilde{q}_1}$ for $\tilde{u}_L\tilde{u}_L$-production and benchmark point SPS1a at the LHC with $\sqrt{S} = 14$ TeV. Shown are the LO (black), virtual+soft+collinear (blue), real gluon and quark radiation (green) and summed NLO (red) contributions. Here, slicing parameters are chosen to $\delta_s = \delta_\theta = 10^{-4}$.

benchmark scenario SPS1a. This parameter point and all other input parameters are defined below in section 5.2.1. In figure 4.9 virtual, soft and collinear contributions for gluon radiation and collinear contributions for quark radiation are shown together in blue; real gluon and quark radiation contributions are shown together in green; the LO cross section is shown in black and the sum of all contributions, i.e., the NLO result is shown in red. For the calculation of the real quark radiation the DR scheme is used. Despite large cancellations between the different contributions, the NLO result is independent of the slicing parameters. We explicitly checked that this also holds at the differential level, where a similar amount of cancellations takes place. In figure 4.10 we show the different contributions to the full NLO predictions on the differential distributions in the transverse momentum $p_{\tilde{q}_1}^{\mathrm{T}}$ and pseudorapidity $\eta_{\tilde{q}_1}$ (defined in eq. (5.6)) of the first squark in $\tilde{u}_L\tilde{u}_L$ production. As before the parameter point SPS1a and $\sqrt{S} = 14$ TeV is chosen. The used regulators are chosen to $\delta_s = \delta_\theta = 10^{-4}$.

Again for the benchmark scenario SPS1a, in figure 4.11 we investigate the dependence on the total decay width of the gluino $\Gamma_{\tilde{g}}$ for $\tilde{u}_R\tilde{u}_R$ production. We show the LO prediction in black, the NLO prediction in the DR scheme with a straight red line and in the DS scheme with a dashed red line, where the left scale is used. As can be seen, the different contributions are independent of the gluino decay width used as a regulator. The difference between the DR and the DS scheme predictions is given by the squared resonant diagrams calculated with an off-shell phase-space subtracted by the same on-shell diagrams, cf., eqs. (4.51) and (4.52). In figure 4.11 these contributions are shown individually: the resonant off-shell contribution is shown in blue and the resonant on-shell contribution in green. For these, the right scale is used.

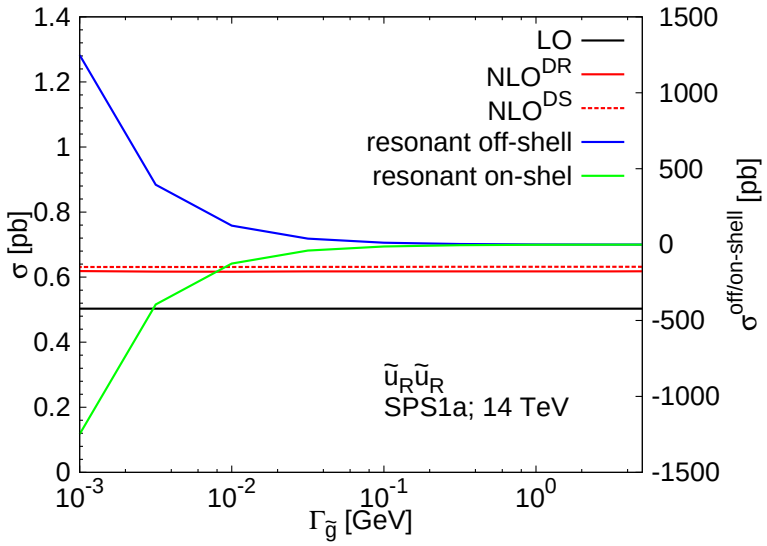

Figure 4.11: Dependence on the decay width of the gluino $\Gamma_{\tilde{g}}$ used as a regulator for the on-shell gluino contributions. Shown are the LO prediction in black, the NLO prediction in the DR scheme with a red straight line and the NLO prediction in the DS scheme with a red dashed line, where for these three predictions the left scale is used. The difference between the resonant off-shell (blue) and resonant on-shell gluino production (green) yields the difference between the DR and DS NLO predictions. For these resonant contributions the right scale is used.

4.4 Squark decay

4.4.1 Squark decay at LO

The LO partial decay width for a squark decaying into a neutralino and a quark, $\tilde{q}_{ia} \to q_i \tilde{\chi}_j^0$, depends on the flavor and chirality of the squark. For light-flavor squarks and thus $m_q = 0$, the width can be written as

$$\Gamma^{(0)}_{\tilde{q}_{ia} \to q_i \tilde{\chi}_j^0} = \frac{\alpha}{4} m_{\tilde{q}_{ia}} \Big(1 - \frac{m^2_{\tilde{\chi}_j^0}}{m^2_{\tilde{q}_{ia}}}\Big) f_a^2 \,. \tag{4.53}$$

The coupling constants f_a can be expressed in terms of the isospin I^q_{3L} and the charge e_q of the quark, together with the neutralino mixing matrix (N_{jk}) defined in eq. (2.79),

$$f_L = \sqrt{2}\Big[e_q N'_{j1} + (I^q_{3L} - e_q s^2_W) \frac{1}{c_W s_W} N'_{j2}\Big] \,, \tag{4.54}$$

$$f_R = -\sqrt{2}\Big[e_q N'_{j1} - e_q \frac{s_W}{c_W} N'_{j2}\Big] \,, \tag{4.55}$$

$$N'_{j1} = c_W N_{j1} + s_W N_{j2}, \qquad N'_{j2} = -s_W N_{j1} + c_W N_{j2} \,. \tag{4.56}$$

For a scalar particle decaying in its rest frame there is no preferred direction, and hence the differential decay distribution is isotropic. For squark decays into a neutralino and a quark, the decay distribution is thus simply given by

$$d\Gamma^{(0)}_{\tilde{q} \to q \tilde{\chi}_j^0} = \frac{1}{4\pi} \Gamma^{(0)}_{\tilde{q} \to q \tilde{\chi}_j^0} \, d\cos\theta \, d\phi \tag{4.57}$$

with polar angle θ and azimuth ϕ referring to the quark momentum.

4.4.2 NLO squark decay distribution

The differential decay width for $\tilde{q} \to q \tilde{\chi}_j^0$ at NLO is obtained in analogy to the steps in section 4.3.2 by adding the virtual loop corrections and the real gluon bremsstrahlung contribution from the soft, collinear, and hard non-collinear phase space regions, yielding the full NLO contribution in the form

$$d\Gamma^{(1)}_{\tilde{q} \to q \tilde{\chi}_j^0} = d\Gamma^{\text{virtual}}_{\tilde{q} \to q \tilde{\chi}_j^0} + d\Gamma^{\text{soft}}_{\tilde{q} \to q \tilde{\chi}_j^0 (g)} + d\Gamma^{\text{coll}}_{\tilde{q} \to q \tilde{\chi}_j^0 (g)} + d\Gamma^{\text{hard}}_{\tilde{q} \to q \tilde{\chi}_j^0 g} \,. \tag{4.58}$$

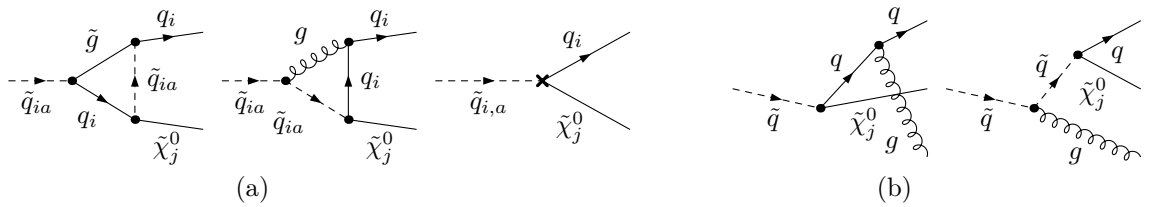

Figure 4.12: Loop and counterterm diagrams (a) and gluon radiation diagrams (b) for squark decays.

The virtual corrections $d\Gamma^{\text{virtual}}_{\tilde{q}\to q\tilde{\chi}^0_j}$ for $m_q = 0$ correspond to the two vertex loop diagrams in figure 4.12(a) and the vertex counterterm (indicated by the cross in figure 4.12(a)), which consists of the wave-function renormalization constants of the external quark and squark lines. As for the production amplitudes, the renormalization constants are determined in the on-shell renormalization scheme. Details on the vertex counter term can be found in Appendix A.1 and the explicit analytical expression is given in eq. (A.19) of Appendix A.5.

The term $d\Gamma^{\text{soft}}_{\tilde{q}\to q\tilde{\chi}^0_j(g)}$ can be calculated by an analogue strategy as for squark–squark production, yielding

$$d\Gamma^{\text{soft}}_{\tilde{q}\to q\tilde{\chi}^0_j(g)} \;=\; -\frac{2\alpha_s}{3\pi}\left\{\sum_{i,l=1;i<l}^{2}\epsilon_i\epsilon_l\,\mathcal{I}_{il}\right\} d\Gamma^{(0)}_{\tilde{q}\to q\tilde{\chi}^0_j}\,, \tag{4.59}$$

where the $\mathcal{I}_{ij}$ are explicitly given in eq. (A.10) of Appendix A.2.

In the decay collinear divergences emerge from gluon emission off the massless final state quarks.

Making again use of the results of [253], the collinear emission of gluons with energy larger than ΔE into a cone with opening angle $\Delta\theta$ yields the contribution

$$\begin{aligned} d\Gamma^{\text{coll}}_{\tilde{q}\to q\tilde{\chi}^0_j(g)} \;&= d\Gamma^{(0)}_{\tilde{q}\to q\tilde{\chi}^0_j} \\ &\cdot\frac{2\alpha_s}{3\pi}\left\{\frac{9}{2}-\frac{2}{3}\pi^2-\frac{3}{2}\log\left(\frac{2E^2_{q,\max}\,\delta_\theta}{m_q^2}\right)+2\log\left(\delta_s\right)\left[1-\log\left(\frac{2E^2_{q,\max}\,\delta_\theta}{m_q^2}\right)\right]\right\}, \end{aligned} \tag{4.60}$$

where $\delta_s = 2\Delta E/m_{\tilde{q}}$, $\delta_\theta = 1-\cos\left(\Delta\theta\right) \simeq \Delta\theta^2/2$, and

$$E_{q,\max} = \frac{m^2_{\tilde{q}} - m^2_{\tilde{\chi}^0_j}}{2m_{\tilde{\chi}^0_j}}\,, \tag{4.61}$$

the maximum energy available for the quark in the squark rest frame. Gluons with $\theta < \Delta\theta$ are recombined with the emitter quark into a quark with momentum $p_{\text{recomb}} = p_q + p_g$. In general, differential distributions in the quark momenta are dependent on the slicing parameter $\Delta\theta$. However, this dependence will disappear once a jet algorithm that is much more inclusive in the recombination of quarks and gluons, is applied (see descriptions in section 5.2).

The contribution $d\Gamma^{\text{hard}}_{\tilde{q}\to q\tilde{\chi}^0_j}$ from real emission of hard gluons ($E_g > \Delta E$) at large angles ($\theta > \Delta\theta$) is evaluated by numerical integration of the squared matrix elements obtained from the diagrams in figure 4.12(b).

Independence of unphysical regulators

Again, we want to demonstrate that our final results for $d\Gamma^{(1)}_{\tilde{q}\to q\tilde{\chi}^0_j}$ do not depend on any unphysical parameters. Here, as an example, in figure 4.13 we show the dependence on the slicing parameters δ_s (left) and δ_θ (right) of the partial decay width $\Gamma_{\tilde{u}_R\to u\tilde{\chi}^0_1}$ for the benchmark

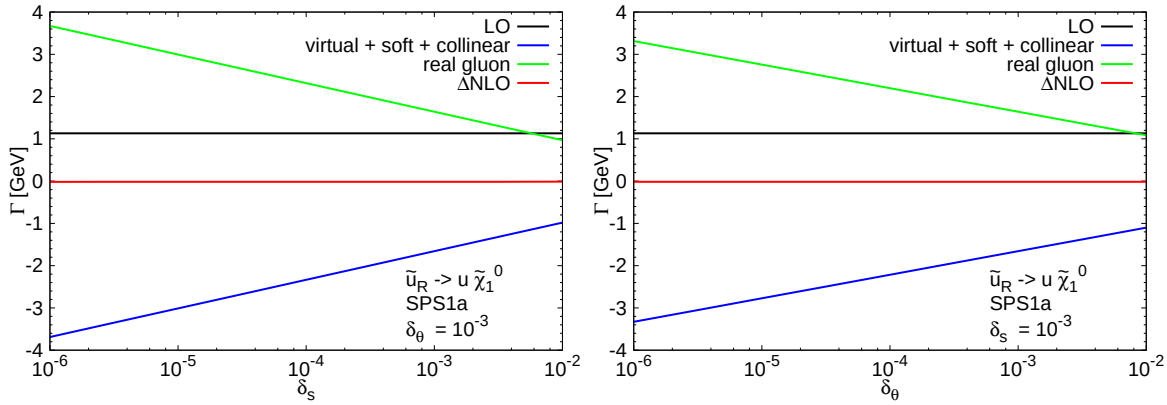

Figure 4.13: Dependence on the residual slicing parameters δ_s and δ_θ of the virtual+soft+collinear (blue) and hard radiation (green) contributions of the NLO corrections ΔNLO to the partial decay width $\Gamma_{\tilde{u}_2 \to u\tilde{\chi}_1^0}$ for the parameter point SPS1a as introduced in section 5.2.1. Also shown is the sum of these contributions (red) and the LO contribution (black).

scenario SPS1a. In figure 4.13 the sum of virtual, soft and collinear gluon contributions is shown in blue; real hard gluon contribution is shown in green; the LO partial decay width is shown in black and the sum of the NLO contributions, i.e., the NLO correction to the partial decay width, is shown in red. Despite large cancellations between the different contributions, the NLO result is independent of the slicing parameters. Again, we explicitly checked that this also holds at the differential level – once jets are defined in an infrared-safe way, i.e., using a well defined jet clustering algorithm.

4.4.3 Total decay width

The total squark decay width $\Gamma_{\tilde{q}}^{(0)}$ at LO is obtained by summing the partial decay widths of the 6 different possible decay channels into neutralinos and charginos (assuming always $m_{\tilde{g}} > m_{\tilde{q}}$):

$$\Gamma_{\tilde{q}}^{(0)} = \sum_{j=1}^{4} \Gamma_{\tilde{q}\to q\tilde{\chi}_j^0}^{(0)} + \sum_{j=1}^{2} \Gamma_{\tilde{q}\to q'\tilde{\chi}_j^\pm}^{(0)} \,. \tag{4.62}$$

The partial decay widths into neutralinos $\Gamma_{\tilde{q}\to q\tilde{\chi}_j^0}^{(0)}$ are given directly by eq. (4.53). For charginos, the partial decay widths $\Gamma_{\tilde{q}\to q'\tilde{\chi}_j^\pm}^{(0)}$ are also described by formula (4.53), with the specification $f_R = 0$ and

$$f_L = \frac{V_{j1}}{s_W} \quad \text{for} \quad \tilde{q} = \tilde{u}, \tilde{c}, \qquad f_L = \frac{U_{j1}}{s_W} \quad \text{for} \quad \tilde{q} = \tilde{d}, \tilde{s}, \tag{4.63}$$

for the coupling constants. Here, U, V are the mixing matrices in the chargino sector, defined in eq. (2.81).

For the total decay width at NLO, one has to calculate the NLO QCD corrections for each decay channel. This can be done analytically performing the full phase space integration over the three-particle final state with the radiated gluon and adding the corresponding loop contributions. The six partial decay widths contributing to $\Gamma_{\tilde{q}}^{(0+1)}$ at NLO can be expressed in terms of their respective LO result and an NLO form factor F^{QCD} which depends only on the mass ratios of the involved massive particles:

$$\Gamma^{(0+1)}_{\tilde{q}\to q\tilde{\chi}_j^0/q'\tilde{\chi}_j^\pm} = \Gamma^{(0)}_{\tilde{q}\to q\tilde{\chi}_j^0/q'\tilde{\chi}_j^\pm}\left[1+\frac{4}{3}\frac{\alpha_s}{\pi}F^{QCD}\left(\frac{m_{\tilde{\chi}_j^0/\tilde{\chi}_j^\pm}}{m_{\tilde{q}}},\frac{m_{\tilde{q}}}{m_{\tilde{g}}}\right)\right]. \tag{4.64}$$

The result for F^{QCD}, explicitly given in eq. (A.23), first calculated in [138] is confirmed by our independent calculation, which can be found in Appendix A.5.

In the threshold limit $\kappa = \frac{m_{\tilde{\chi}_j^0/\tilde{\chi}_j^\pm}}{m_{\tilde{q}}} \to 1$ the corrections from eq. (A.23) become very large and the given fixed-order calculation is not reliable. Relative corrections remain finite only after proper resummation, see for example ref. [155]. However, for all parameter points considered in the numerical evaluation in sections 5.2 and 6.4, NLO corrections are still sufficiently small and threshold problems are negligible.

Chapter 5

The simplest decay chain: direct decay

In this chapter we present an analysis of the signature of 2 jets + missing transverse energy, $2j + \not{E}_T(+X)$, from squark–squark production combined with the direct decay into lightest neutralinos, $pp \to \tilde{q}\tilde{q} \to jj\tilde{\chi}_1^0\tilde{\chi}_1^0(+X)$, at NLO QCD. As explained in chapter 4, in this way, we provide a consistent, fully differential calculation of the NLO QCD factorizable corrections to the given processes. In our calculation final state partons are clustered into jets and thus, we provide, a fully differential description of the physical signature $2j + \not{E}_T(+X)$ via on-shell squark–squark production and decay. In principle, our calculation does not depend on the hierarchy between the squarks and the gluino. However, in our numerical evaluation we only consider benchmark points where the mass $m_{\tilde{q}}$ of all light flavor squarks is smaller than the gluino mass ($m_{\tilde{g}} > m_{\tilde{q}}$); otherwise the decay of a squark into a gluino and a quark would be dominant.

Investigating here the squark–squark channel should be understood as a first step towards a fully differential prediction for all sparticle production channels at NLO. It is, however, also of practical importance, since from recent searches at the LHC mass bounds for squarks and gluinos are generically pushed to higher values and, as discussed in section 3.3, here squark–squark production (initiated from valence-quarks) yields the dominant channel.

In the following, in section 5.1, we first explicitly apply the considerations of the last chapter to the given process. Afterwards we present corresponding numerical results in section 5.2. There, we compare resulting differential distributions and inclusive rates with leading-order approximations rescaled by a flat K-factor. We also examine a possible impact for cut-and-count searches for supersymmetry at the LHC. Results and discussion of this chapter are largely based on ref. [3].

5.1 Method

We investigate the production of squark–squark pairs induced by proton-proton collisions, with subsequent decays of the squarks into the lightest neutralinos. Since we are interested in the experimental signature $2j + \not{E}_T(+X)$, all contributions from light-flavor squarks have to be included. Hence, the cross section is given by the sum over all independent flavor and

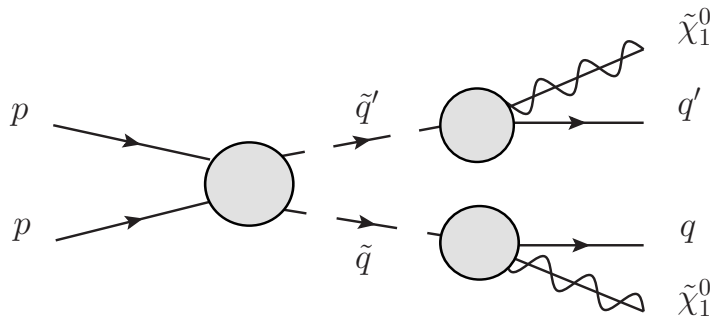

Figure 5.1: General structure of the factorizable NLO QCD corrections to the signature $2j + \not{E}_T(+X)$ via squark–squark production and direct decay into the lightest neutralino. The circles indicate all contributions to the production up to $\mathcal{O}(\alpha_s^3)$ and the decays up to $\mathcal{O}(\alpha_s)$.

chirality configurations,

$$d\sigma = \sum_{\tilde{q}_{ia}\tilde{q}_{jb}} \left[d\sigma(pp \to \tilde{q}_{ia}\tilde{q}_{jb} \to q_i\tilde{\chi}_1^0 q_j\tilde{\chi}_1^0(+X)) + d\sigma(pp \to \tilde{q}_{ia}^*\tilde{q}_{jb}^* \to \bar{q}_i\tilde{\chi}_1^0\bar{q}_j\tilde{\chi}_1^0(+X)) \right] . \quad (5.1)$$

Indices i, j denote the flavors of the (s)quarks and a, b their chiralities. At LO, the only partonic subprocesses that contribute to a given intermediate configuration $\tilde{q}_{ia}\tilde{q}_{jb}$ or $\tilde{q}_{ia}^*\tilde{q}_{jb}^*$ arise from quark and anti-quark pairs, respectively, $q_iq_j \to \tilde{q}_{ia}\tilde{q}_{jb} \to q_i\tilde{\chi}_1^0 q_j\tilde{\chi}_1^0$ and $\bar{q}_i\bar{q}_j \to \tilde{q}_{ia}^*\tilde{q}_{jb}^* \to \bar{q}_i\tilde{\chi}_1^0\bar{q}_j\tilde{\chi}_1^0$.

For simplifying the notation, we will write $qq' \to \tilde{q}\tilde{q}' \to q\tilde{\chi}_1^0 q'\tilde{\chi}_1^0$ whenever the specification of flavor and chiralities is not required [1]. Moreover, we will perform the discussion without the charge-conjugate subprocesses; they are, however, included in the final results.

The differential cross section for on-shell production of squark–squark pairs and subsequent decays at leading order is directly given by eq. (4.9). Following eq. (4.14), at NLO the factorizable corrections, illustrate in figure 5.1, can be written as

$$\begin{aligned} d\sigma^{(0+1)}_{\text{NWA}}(pp \to \tilde{q}\tilde{q}' \to q\tilde{\chi}_1^0 q'\tilde{\chi}_1^0(+X)) \;=\; & \\ & \frac{1}{\Gamma^{(0)}_{\tilde{q}}\,\Gamma^{(0)}_{\tilde{q}'}} \Big[d\sigma^{(0)}_{pp\to\tilde{q}\tilde{q}'}\, d\Gamma^{(0)}_{\tilde{q}\to q\tilde{\chi}_1^0}\, d\Gamma^{(0)}_{\tilde{q}'\to q'\tilde{\chi}_1^0} \Big(1 - \frac{\Gamma^{(1)}_{\tilde{q}}}{\Gamma^{(0)}_{\tilde{q}}} - \frac{\Gamma^{(1)}_{\tilde{q}'}}{\Gamma^{(0)}_{\tilde{q}'}}\Big) \\ & + d\sigma^{(0)}_{pp\to\tilde{q}\tilde{q}'}\, d\Gamma^{(1)}_{\tilde{q}\to q\tilde{\chi}_1^0}\, d\Gamma^{(0)}_{\tilde{q}'\to q'\tilde{\chi}_1^0} \;+\; d\sigma^{(0)}_{pp\to\tilde{q}\tilde{q}'}\, d\Gamma^{(0)}_{\tilde{q}\to q\tilde{\chi}_1^0}\, d\Gamma^{(1)}_{\tilde{q}'\to q'\tilde{\chi}_1^0} \\ & + d\sigma^{(1)}_{pp\to\tilde{q}\tilde{q}'(X)}\, d\Gamma^{(0)}_{\tilde{q}\to q\tilde{\chi}_1^0}\, d\Gamma^{(0)}_{\tilde{q}'\to q'\tilde{\chi}_1^0} \Big] , \end{aligned} \quad (5.2)$$

with the NLO contributions to cross section and widths $d\sigma^{(1)}, \Gamma^{(1)}, \ldots$ in obvious notation. All terms in eq. (5.2) were calculated in sections 4.3 and 4.4.

[1] In this notation $\tilde{q} = \tilde{q}'$ implies $q = q'$, but not vice versa.

5.1.1 Combining production and decay

In order to evaluate the terms contained in eq. (5.2), we produce, for all different combinations of light flavors and chiralities, weighted events for squark–squark production and squark decays. Production events for $pp \to \tilde{q}\tilde{q}'(X)$ are generated in the laboratory frame. Decay events for $\tilde{q} \to q\tilde{\chi}_1^0(g)$ and $\tilde{q}' \to q'\tilde{\chi}_1^0(g)$ are generated in the respective squark rest frame. Finally, $pp \to qq'\tilde{\chi}_1^0\tilde{\chi}_1^0(+X)$ events are obtained by boosting the decay events from the squark rest frames, defined by the production events, into the laboratory frame. The weights of the $pp \to qq'\tilde{\chi}_1^0\tilde{\chi}_1^0(+X)$ events are obtained combining the different LO and NLO weights of production and decay according to eq. (5.2). Phenomenological results derived by these combinations are presented in the following section.

5.2 Numerical results

Let us now turn to the numerical evaluation. In the following, we first specify the input parameters and benchmark scenarios we consider in 5.2.1. Then, in 5.2.2 a brief introduction to all considered distributions and observables is given. Finally, we present our numerical results in three different ways. Firstly, in section 5.2.3 we compare our results for inclusive production of squark–squark pairs with `Prospino 2` and investigate inclusive K-factors for different chirality and flavor combinations. Secondly, in section 5.2.4 we present several differential distributions for various benchmark scenarios and center-of-mass energies. Thirdly, in section 5.2.5 we investigate the impact of the considered higher-order corrections on total event rates and thus on cut-and-count searches for supersymmetry at the LHC.

5.2.1 Input parameters

Standard Model input parameters are chosen according to [256],

$$\begin{aligned} M_Z &= 91.1876 \text{ GeV}\,, & M_W &= 80.399 \text{ GeV}\,, & G_F &= 1.16637 \cdot 10^{-5} \text{ GeV}\,, \\ m_b^{\overline{\text{MS}}}(m_b) &= 4.2 \text{ GeV}\,, & m_t &= 173.3 \text{ GeV}\,, & m_\tau &= 1.777 \text{ GeV}\,. \end{aligned} \tag{5.3}$$

We use the PDF sets CTEQ6.6 [257] interfaced via the Les Houches Accord PDF (LHAPDF) interface [258] both for LO and NLO contributions. The strong coupling constant $\alpha_s^{\overline{\text{MS}}}(\mu_R)$ is also taken from this set of PDFs. Factorization scale μ_F and renormalization scale μ_R are, if not stated otherwise, set to a common value, $\mu = \mu_F = \mu_R = \overline{m_{\tilde{q}}}$, with $\overline{m_{\tilde{q}}}$ being the average mass of all light-flavor squarks of a given benchmark point.

For SUSY parameters, we refer to three different benchmark scenarios. First, we investigate the well studied CMSSM parameter point SPS1a [259]. Although being practically excluded by recent searches at the LHC [159, 161, 260], this point still serves as a valuable benchmark to compare with numerous numerical results available in the literature. Second, we study the CMSSM benchmark point 10.1.5 introduced in [261]. Due to its larger $m_{1/2}$ parameter, compared to SPS1a, squark and gluino masses are considerably larger, resulting in a generally reduced production cross section at the LHC. It was not excluded when this study was first published in [3], however it got excluded by most recent searches, which are

	m_0 [GeV]	$m_{1/2}$ [GeV]	A_0 [GeV]	$\tan\beta$	sign(μ)
SPS1a	100	250	−100	10	+
10.1.5	175	700	0	10	+
10.1.6	187.5	750	0	10	+

Table 5.1: High energy input parameters for the two considered CMSSM scenarios.

	M_1 [GeV]	M_2 [GeV]	M_3 [GeV]	A_i [GeV]	$\tan\beta$	sign(μ)
p19MSSM1A	300	2500	360	0	10	+

Table 5.2: Low energy input parameters for the p19MSSM1A scenario. The first two generation sfermion soft-masses (apart from the right handed sleptons) equal the gluino mass $m_{\tilde{f}^{\text{1st/2nd gen}}_{L/R}} = M_3$. All other parameters are at a higher scale $m_{\tilde{f}^{\text{3rd gen}}_{L/R}} = m_{\tilde{e}_R,\tilde{\mu}_R} = \mu = M_A = M_2$.

mentioned in section 3.3.2. The overall spectrum of 10.1.5, though shifted to larger masses, is very similar to the one of SPS1a. Third, we consider a phenomenological benchmark point defined at the scale $Q = 1$ TeV. We follow the definitions of [261], where such a point sits on a line called p19MSSM1. It can be parametrized by essentially one parameter, the gaugino mass parameter M_1. A unified parameter for the gluino and the light-generations sfermion soft masses $M_3 = m_{\tilde{f}^{\text{1st/2nd gen}}_{L/R}}$ is fixed to $M_3 = m_{\tilde{f}^{\text{1st/2nd gen}}_{L/R}} = 1.2\ M_1$ on this line and we choose $M_1 = 300$ GeV for our benchmark scenario p19MSSM1A. All other masses and parameters as well as the soft masses for the first two generation right-handed sleptons are at a higher scale and irrelevant for our analysis. This benchmark point is chosen to study a particular parameter region with rather light squarks and gluinos, which is difficult to exclude experimentally. Due to a small mass splitting between the $\tilde{\chi}^0_1$ and the light squarks (and gluino), resulting jets tend to be very soft and thus escape the experimental analyses. Particularly in such parameter regions precise theoretical prediction of the resulting SUSY signal including higher orders on the level of distributions seems to be necessary for a conclusive study.

Parameters of the CMSSM benchmark scenarios are defined universally at the GUT scale and are shown in table 5.1. Also listed are parameters for the CMSSM point 10.1.6, which is used in chapter 6. These input parameters act as boundary conditions for the renormalization group running of the soft-breaking parameters down to the SUSY scale M_{SUSY}. This running is performed with the program `SOFTSUSY` [83] which also calculates physical on-shell parameters for all SUSY mass eigenstates. We use the resulting on-shell parameters directly as input for

	$\tilde{u}_L$	$\tilde{u}_R$	$\tilde{d}_L$	$\tilde{d}_R$	$\tilde{g}$	$\tilde{\chi}^0_1$
SPS1a	563.6	546.7	569.0	546.6	608.5	97.0
10.1.5	1437.7	1382.3	1439.7	1376.9	1568.6	291.3
p19MSSM1A	339.6	394.8	348.3	392.7	414.7	299.1

Table 5.3: On-shell masses of the squarks, the gluino, and the lightest neutralino within the different SUSY scenarios considered. All masses are given in GeV.

		$\tilde{u}_L$	$\tilde{u}_R$	$\tilde{d}_L$	$\tilde{d}_R$	$\tilde{g}$
SPS1a	$\Gamma^{(0)}$	5.361	1.148	5.253	0.287	6.849
	$\Gamma^{(0+1)}$	5.357	1.131	5.255	0.283	
10.1.5	$\Gamma^{(0)}$	12.47	2.854	12.46	0.710	10.04
	$\Gamma^{(0+1)}$	12.31	2.821	12.30	0.702	
p19MSSM1A	$\Gamma^{(0)}$	$2.414 \cdot 10^{-3}$	0.1625	$3.411 \cdot 10^{-3}$	$3.917 \cdot 10^{-2}$	3.441
	$\Gamma^{(0+1)}$	$2.497 \cdot 10^{-3}$	0.1621	$3.503 \cdot 10^{-3}$	$3.912 \cdot 10^{-2}$	

Table 5.4: Leading order $\Gamma^{(0)}$ and next-to-leading order $\Gamma^{(0+1)}$ total widths of light squarks and gluino for the considered SUSY scenarios. All widths are given in GeV.

our calculation. Low scale soft input parameters for the p19MSSM1A benchmark scenario are given in table 5.2. The physical spectrum is equivalently calculated with `SOFTSUSY`. For all considered benchmark scenarios we summarize relevant low energy physical masses in table 5.3. Due to non-vanishing Yukawa corrections implemented in `SOFTSUSY`, the physical on-shell masses for second-generation squarks are slightly different from their first-generation counterparts. To simplify our numerical evaluation we set all second-generation squark masses to their first-generation counterparts. We checked that in the results this adjustment is numerically negligible. However, the general setup of our calculation is independent of this choice. For all considered benchmark scenarios the gluino is heavier than all light flavor squarks $m_{\tilde{g}} > m_{\tilde{q}}$. Thus, these squarks decay only into electroweak gauginos and quarks. For SPS1a and 10.1.5, right-handed squarks dominantly decay directly into the lightest neutralino $\tilde{\chi}_1^0$ (due to its bino nature). In contrary, left-handed squarks decay dominantly into heavier (wino-like) neutralinos and charginos, which subsequently decay via cascades into a $\tilde{\chi}_1^0$, and only a small fraction decays directly into a $\tilde{\chi}_1^0$. In this chapter we only investigate the direct decay of any light flavor squark into the lightest neutralino. For point p19MSSM1A all neutralinos and charginos, but the lightest one, are heavier than any light-flavor squark. Thus, only the direct decay is allowed and all channels contribute equally to the signature under consideration.

In table 5.4 we list all needed total decay widths of the squarks at LO and NLO, calculated as explained in section 4.4. NLO corrections in the total decay widths are of the order of a few percent for all three benchmark scenarios. The total decay width of the gluino is calculated with `SDECAY` at LO and also listed in table 5.4. In the calculation presented here this width is not used explicitly. Instead, we numerically employ the limit $\Gamma_{\tilde{g}} \to 0$. However we checked that, using the physical widths, all the results showed in the following present negligible differences.

Besides physical quantities, in our calculation phase-space slicing and regulator parameters enter as inputs in the calculation of virtual and real NLO contributions, as explained in sections 4.3 and 4.4. In the results shown in this chapter we set $\delta_s = 2 \cdot 10^{-4}$, $\delta_\theta = 10^{-4}$ and $m_q = 10^{-1.5}$ GeV, both for production and decay. Numerically we checked carefully that varying their values our results remain unchanged on the level of individual distributions once jets are recombined using a clustering algorithm, as explained below. We made sure that this holds for all terms of eq. (5.2) individually.

5.2.2 Observables and kinematical cuts

The physical signature we have in mind when calculating on-shell squark production and decay into the lightest neutralino is $2j + \not{E}_T$. Numerical results of our calculation are presented in this spirit. In order to arrive at an experimentally well defined two-jet-signature we always employ the anti-k_T[262] jet-clustering algorithm implemented in `FastJet` [263]. Thus, we provide a realistic prediction on the level of partonic jets [2]. In general we use a jet radius of $R = 0.4$, as in the SUSY searches performed by the ATLAS collaboration [159]. CMS instead uses a radius of $R = 0.5$ [161]. We employ $R = 0.5$ in the distributions and signatures used by CMS (i.e. particularly the α_T distribution as described below). Although we did not perform a systematic study, our results seem to be independent of this choice. After performing the jet clustering we sort the partonic jets by their transverse momentum p^{T}, and in the following analysis we keep only jets with

$$p^{\mathrm{T}}_{j_{1/2}} > 20 \text{ GeV}, \quad |\eta_j| < 2.8, \tag{5.4}$$

$$p^{\mathrm{T}}_{j_i} > 50 \text{ GeV}, \quad |\eta_j| < 3.0 \text{ (for CMS observables)}. \tag{5.5}$$

Cuts of eq. (5.4) are used everywhere but in the observables used specifically by CMS (α_T, as defined below), where cuts of eq. (5.5) are applied.

Before showing results for the experimental signature $2j + \not{E}_T(+X)$, we compare in section 5.2.3 values for NLO total cross sections of squark–squark production, without decay included, with results obtained from `Prospino 2`. In section 5.2.4 we investigate the effect of NLO corrections, for different benchmark points, on the following differential distributions:

- the transverse momentum of the two hardest jets $p^{\mathrm{T}}_{1/2}$,
- the pseudorapidity of the two hardest jets $\eta_{1/2}$, which is defined by

$$\eta = -\ln\left[\tan\left(\frac{\theta}{2}\right)\right] = \frac{1}{2}\left(\frac{|\vec{p}| + p_z}{|\vec{p}| - p_z}\right), \tag{5.6}$$

  where θ is the angle between $\vec{p}$ and the z-axis,
- the missing transverse energy $\not{E}_T$,
- the effective mass $m_{\text{eff}} = \sum_{i=1,2} p^{\mathrm{T}}_i + \not{E}_T$,
- the scalar sum of the p^{T} of all jets (visible after cuts of eq. (5.5)), $H_T = \sum_{i=1,2(,3)} p^{\mathrm{T}}_i$,
- the invariant mass of the two hardest jets $m_{\text{inv}}(jj)$,
- the cosine of the angle between the two hardest jets $\cos\Theta_{jj}$, which depends on the spin of the produced particles and therefore might help to distinguish SUSY from other BSM models [264],

[2] With the term partonic jets we mean that the jet-clustering-algorithm has been applied to events as produced from our calculation. No QCD showering or hadronization is included in the simulation.

- $\cos\hat{\Theta} = \tanh\left(\frac{\Delta\eta_{jj}}{2}\right)$, $\Delta\eta_{jj} = \eta_1 - \eta_2$, introduced in [265] as a possible observable for early spin determination at the LHC,
- the α_T variable, first defined in [266] as

$$\alpha_T = \frac{p_2^{\mathrm{T}}}{m_{\mathrm{inv}}(jj)}\,. \tag{5.7}$$

  For events with more than two hard jets, i.e., for hard real radiation events with three jets and $p_3^{\mathrm{T}} > 50$ GeV, these jets are reclustered into two pseudojets by minimizing the difference of the respective H_T of the two pseudojets, as explained in [267, 268]. Furthermore, in all α_T distributions we require $H_T > 350$ GeV as in [267] and also use the definition of α_T given in [267]: $\alpha_T = \frac{p_2^{\mathrm{T}}}{m_T(jj)}$, where $m_T(jj)$ is the transverse mass of the two (pseudo) jets defined as

$$m_T(jj) = \sqrt{\left(\sum_{i=1}^{2} E_{j_i}\right)^2 - \left(\sum_{i=1}^{2} p_{j_i}^x\right)^2 - \left(\sum_{i=1}^{2} p_{j_i}^y\right)^2}\,. \tag{5.8}$$

Searches for sparticle production performed by ATLAS are based on p^{T}, $\not{E}_T$ and m_{eff} cuts; CMS instead uses α_T to reduce SM backgrounds. In section 5.2.5 we examine NLO corrections in the resulting event rates after cuts. Explicitly we employ the following cuts used by ATLAS,

$$\begin{gathered} p_{j_1}^{\mathrm{T}} > 130 \text{ GeV},\ p_{j_2}^{\mathrm{T}} > 40 \text{ GeV},\ |\eta_{j_{1/2}}| < 2.8,\ \Delta\phi(j_{1/2}, \vec{\not{E}}_T) > 0.4, \\ m_{\mathrm{eff}} > 1 \text{ TeV},\ \not{E}_T/m_{\mathrm{eff}} > 0.3, \end{gathered} \tag{5.9}$$

in their two-jet analysis [159]. Here, $\Delta\phi(j_{1/2}, \vec{\not{E}}_T)$ denotes the angular separation between the two hardest jets and the direction of missing energy $\vec{\not{E}}_T$. Instead the CMS signal region [267] is defined as

$$\begin{gathered} p_{j_{1/2}}^{\mathrm{T}} > 100 \text{ GeV},\ |\eta_{j_1}| < 2.5,\ |\eta_{j_2}| < 3.0, \\ H_T > 350 \text{ GeV},\ \not{H}_T/\not{E}_T < 1.25,\ \alpha_T > 0.55, \end{gathered} \tag{5.10}$$

where $\not{H}_T$ is calculated from $\vec{H}_T$, i.e., including any jet with $p_j^{\mathrm{T}} > 50$ GeV.

5.2.3 Inclusive cross sections

In table 5.5 we list inclusive LO cross sections and corresponding NLO K-factors for the three benchmark scenarios SPS1a, 10.1.5, p19MSSM1A, varying the LHC center of mass energy $\sqrt{S} = 7, 8, 14$ TeV. K-factors, here and in the following, are always defined as ratios between NLO and LO predictions, where both, as stated above, are calculated using the same NLO PDFs and associated α_s. On the one hand, we list inclusive cross sections, $\sigma^{(0)}_{pp\to\tilde{q}\tilde{q}'}$, and K-factors for just the production of squark–squark pairs summed over all flavor and chirality combinations. These K-factors are calculated in the DR scheme defined in section 4.3.2. If not stated otherwise this scheme is used in the following. On the other hand, we list cross

benchmark	$\sqrt{S}$ [TeV]	$\sigma^{(0)}_{pp\to\tilde{q}\tilde{q}'}$	$K^{DR}_{pp\to\tilde{q}\tilde{q}'}$	$\sigma^{(0)}_{2j+\not{E}_T}$	$K_{2j+\not{E}_T}$
SPS1a	7	1.02 pb	1.37	0.37 pb	1.41
	8	1.49 pb	1.35	0.53 pb	1.40
	14	5.31 pb	1.28	1.74 pb	1.36
10.1.5	7	0.90 fb	1.57	0.45 fb	1.61
	8	2.62 fb	1.52	1.24 fb	1.56
	14	50.04 fb	1.40	20.41 fb	1.44
p19MSSM1A	7	7.90 pb	1.40	6.31 pb	1.50
	8	10.48 pb	1.39	8.35 pb	1.50
	14	29.01 pb	1.34	22.60 pb	1.47

Table 5.5: LO cross sections $\sigma^{(0)}_{pp\to\tilde{q}\tilde{q}'}$ and NLO K-factors for inclusive squark–squark production, $K^{DR}_{pp\to\tilde{q}\tilde{q}'}$, LO cross sections of inclusive combined squark–squark production and decay $\sigma^{(0)}_{2j+\not{E}_T}$ and corresponding K-factor $K_{2j+\not{E}_T}$, for the three benchmark scenarios SPS1a, 10.1.5, p19MSSM1A and center of mass energies $\sqrt{S} = 7, 8, 14$ TeV. In the combined predictions cuts of eq. (5.4) are applied.

section predictions for combined production and decay at LO $\sigma^{(0)}_{2j+\not{E}_T}$ and the corresponding NLO K-factors $K_{2j+\not{E}_T}$ calculated using eq. (5.2), again summed over all flavor and chirality combinations. Here, cuts defined in eq. (5.4) are applied and cross sections strongly decrease due to the branching into the lightest neutralino. All K-factors of the combined process are bigger than the corresponding K-factors of inclusive production. For point 10.1.5 (and thus rather heavy squarks) these increments are less than 5 %. For the other two benchmark points (and thus smaller squark masses) increments in the K-factors can be of the order of 10 % and increase with higher center of mass energies. In general, however, K-factors decrease with higher center of mass energies and increase with higher masses, both, for inclusive production and combined production and decay.

In table 5.6 we compare the inclusive production with combined production and decay for benchmark point 10.1.5 and $\sqrt{S} = 14$ TeV. Here, we list results for individual flavor and chirality combinations. In general, our calculation is set up to treat all $36 + c.c$ possible flavor and chirality combinations independently. However, for simplicity and to save computing time we always sum combinations with identical masses and matrix elements into 16 channels, both, for production and in the combination. This categorization follows the four possibilities discussed in section 4.3.1. For example, the channel $\tilde{u}_L\tilde{u}_L$ also includes $\tilde{c}_L\tilde{c}_L$ (and as everywhere else in this chapter, the charge conjugated processes). Similarly, the channel $\tilde{u}_L\tilde{d}_L$ also includes $\tilde{c}_L\tilde{s}_L$, $\tilde{u}_L\tilde{s}_L$ and $\tilde{c}_L\tilde{d}_L$; and the channel $\tilde{u}_L\tilde{c}_R$ also includes $\tilde{u}_R\tilde{c}_L$. K-factors, both, in just the production and in the combined result, vary by up to 15 % between different channels. Thus, an independent treatment seems adequate, as in general, squarks of different chiralities and thus different channels have very different decays and kinematic distributions. This can be seen from the order of magnitude differences of $\sigma^{(0)}_{2j+\not{E}_T}$ in table 5.6. As already seen in table 5.5, K-factors increase comparing inclusive production and the combined result (where the cuts given in eq. (5.4) are applied).

	$\sigma^{(0)}_{pp\to\tilde{q}\tilde{q}'}$ [fb]	$\sigma^{(0+1)}_{pp\to\tilde{q}\tilde{q}'}$ [fb]	$K^{DR}_{pp\to\tilde{q}\tilde{q}'}$	$\sigma^{(0)}_{2j+\not{E}_T}$ [fb]	$\sigma^{(0+1)}_{2j+\not{E}_T}$ [fb]	$K_{2j+\not{E}_T}$
$\tilde{u}_L\tilde{u}_L$	7.08	9.44	1.33	$1.22\cdot10^{-3}$	$1.68\cdot10^{-3}$	1.38
$\tilde{u}_R\tilde{u}_R$	8.64	11.5	1.33	8.25	11.36	1.38
$\tilde{d}_L\tilde{d}_L$	1.07	1.44	1.36	$2.82\cdot10^{-4}$	$3.96\cdot10^{-4}$	1.40
$\tilde{d}_R\tilde{d}_R$	1.39	1.88	1.35	1.33	1.84	1.39
$\tilde{u}_L\tilde{u}_R$	6.00	8.49	1.42	$7.78\cdot10^{-2}$	$11.33\cdot10^{-2}$	1.45
$\tilde{d}_L\tilde{d}_R$	$8.20\cdot10^{-1}$	1.19	1.45	$1.32\cdot10^{-2}$	$1.96\cdot10^{-5}$	1.49
$\tilde{u}_L\tilde{d}_L$	8.25	11.9	1.44	$1.76\cdot10^{-3}$	$2.62\cdot10^{-3}$	1.49
$\tilde{u}_R\tilde{d}_R$	10.5	15.1	1.44	10.00	14.92	1.49
$\tilde{u}_L\tilde{c}_L$	$3.28\cdot10^{-1}$	$4.33\cdot10^{-1}$	1.32	$5.65\cdot10^{-5}$	$7.73\cdot10^{-5}$	1.37
$\tilde{u}_R\tilde{c}_R$	$4.29\cdot10^{-1}$	$5.74\cdot10^{-1}$	1.34	$4.09\cdot10^{-1}$	$5.68\cdot10^{-1}$	1.39
$\tilde{d}_L\tilde{s}_L$	$1.95\cdot10^{-1}$	$2.75\cdot10^{-1}$	1.41	$5.16\cdot10^{-5}$	$7.5097\cdot10^{-5}$	1.46
$\tilde{d}_R\tilde{s}_R$	$2.71\cdot10^{-1}$	$3.87\cdot10^{-1}$	1.42	$2.59\cdot10^{-1}$	3.82	1.48
$\tilde{u}_L\tilde{d}_R$	2.44	3.50	1.44	$3.16\cdot10^{-2}$	$4.67\cdot10^{-2}$	1.48
$\tilde{u}_R\tilde{d}_L$	2.40	3.46	1.44	$3.87\cdot10^{-2}$	$5.70\cdot10^{-2}$	1.48
$\tilde{u}_L\tilde{c}_R$	$1.69\cdot10^{-1}$	$2.39\cdot10^{-1}$	1.41	$2.19\cdot10^{-3}$	$3.18\cdot10^{-3}$	1.46
$\tilde{d}_L\tilde{s}_R$	$9.51\cdot10^{-2}$	$1.39\cdot10^{-1}$	1.46	$1.52\cdot10^{-3}$	$2.29\cdot10^{-3}$	1.50
sum	50.04	69.86	1.40	20.41	29.32	1.44

Table 5.6: For the benchmark point 10.1.5 and a center of mass energy of $\sqrt{S} = 14$ TeV inclusive production cross sections at LO $\sigma^{(0)}_{pp\to\tilde{q}\tilde{q}'}$ and NLO $\sigma^{(0+1)}_{pp\to\tilde{q}\tilde{q}'}$ together with the corresponding K-factors $K_{pp\to\tilde{q}\tilde{q}'}$ are listed for all different flavor and chirality channels (as explained in the text). Also listed for all channels are LO $\sigma^{(0)}_{2j+\not{E}_T}$ and NLO $\sigma^{(0+1)}_{2j+\not{E}_T}$ predictions of combined production and decay and the corresponding K-factor $K_{2j+\not{E}_T}$, where the cuts of eq. (5.4) are applied. All cross sections are given in fb.

In table 5.7 we compare the different schemes defined in 4.3.2. In order to also consistently compare with `Prospino 2` results, we set, just here, the mass of all squarks to the average mass $\overline{m_{\tilde{q}}}$ for all benchmark points. In table 5.7 we show LO cross-sections and NLO K-factors from our calculation in the DR scheme, $K^{DR}_{pp\to\tilde{q}\tilde{q}'}$, and in the DS scheme, $K^{DS}_{pp\to\tilde{q}\tilde{q}'}$. We also list K-factors obtained from `Prospino 2`, $K^{\text{Prospino}}_{pp\to\tilde{q}\tilde{q}'}$, which we adjusted to use the same set of PDFs and definition of the strong coupling $\alpha_s(\mu_R)$ as in our calculation. The use of an average mass results in a small shift in the LO cross section and in the NLO K-factor $K^{DR}_{pp\to\tilde{q}\tilde{q}'}$ between table 5.5 and table 5.7. Numerical differences between K-factors in the DR scheme and the DS scheme are of the order of a few percent for SPS1a and p19MSSM1A and negligible for 10.1.5, as, for a heavier spectrum the gluon contribution in the PDFs is suppressed. Differences between $K^{DS}_{pp\to\tilde{q}\tilde{q}'}$ and $K^{\text{Prospino}}_{pp\to\tilde{q}\tilde{q}'}$ originate in the different on-shell subtraction approach. We checked numerically, excluding real quark radiation altogether, that inclusive NLO corrections from our calculation and results from `Prospino 2` are in perfect agreement.

benchmark	$\sqrt{S}$ [TeV]	$\sigma^{(0)}_{pp\to\tilde{q}\tilde{q}'}$	$K^{DR}_{pp\to\tilde{q}\tilde{q}'}$	$K^{DS}_{pp\to\tilde{q}\tilde{q}'}$	$K^{\text{Prospino}}_{pp\to\tilde{q}\tilde{q}'}$
SPS1a	7	1.01 pb	1.37	1.39	1.41
	8	1.48 pb	1.35	1.38	1.40
	14	5.31 pb	1.28	1.34	1.38
10.1.5	7	0.89 fb	1.58	1.58	1.59
	8	2.59 fb	1.53	1.53	1.54
	14	49.87 fb	1.39	1.40	1.41
p19MSSM1A	7	7.65 pb	1.39	1.41	1.37
	8	10.17 pb	1.37	1.41	1.37
	14	28.34 pb	1.31	1.39	1.38

Table 5.7: LO cross sections $\sigma^{(0)}_{pp\to\tilde{q}\tilde{q}'}$ and NLO K-factors for inclusive squark–squark production from our computation in the DR scheme, $K^{DR}_{pp\to\tilde{q}\tilde{q}'}$, in the DS scheme $K^{DS}_{pp\to\tilde{q}\tilde{q}'}$ and also from `Prospino 2`, $K^{\text{Prospino}}_{pp\to\tilde{q}\tilde{q}'}$. All squark masses taken to the average squark mass $\overline{m_{\tilde{q}}}$.

5.2.4 Differential distributions

Now we turn to the investigation of differential distributions.

First, we compare the differential scale dependence between our LO and NLO prediction. We do this by varying at the same time renormalization and factorization scale between $\mu/2 < \mu < 2\mu$, with $\mu = \overline{m_{\tilde{q}}}$. For SPS1a and an energy of $\sqrt{S} = 14$ TeV resulting LO and NLO bands are shown in blue and red in figure 5.2 for differential distributions in $p_1^{\text{T}}, p_2^{\text{T}}, \eta_1, \eta_2, \not{E}_T$ and H_T, and in figure 5.3 for $m_{\text{eff}}, m_{\text{inv}}(jj)$ and $\cos\Theta_{jj}$. In all considered distributions the scale dependence and thus the theoretical uncertainty is greatly reduced by our NLO calculation. At the same time, one should also note that large parts of the NLO bands are outside the LO bands. Still, for example in the p^{T} distributions, in the high-p^T tail the NLO bands move entirely inside the LO bands.

Second, in figure 5.4 we illustrate the difference between the schemes introduced in section 4.3.2 for the benchmark point SPS1a and a center of mass energy $\sqrt{S} = 14$ TeV. In figure 5.4 we show distributions in $\not{E}_T$ and H_T. These are the distributions where we observe the largest deviations between the DS and DR schemes. The upper part of these plots show the same band plots as already displayed at the bottom of 5.2, however in a log scale. In the lower part we show, for the DR scheme, the ratio of the NLO results at $\mu = 2\overline{m_{\tilde{q}}}$ and $\mu = \overline{m_{\tilde{q}}}/2$ over the LO results at $\mu = \overline{m_{\tilde{q}}}$. We also display the ratio between the NLO result in the DS scheme and the LO result, both at the central $\mu = \overline{m_{\tilde{q}}}$. In these two distributions the difference between the two schemes increases in the tail of the distributions. However the DS scheme remains within the theoretical uncertainty of the DR scheme. As explained the chosen distributions $\not{E}_T$ and H_T show the largest differences we observe for the benchmark points and energies considered.

Third, we investigate the change in the shape of distributions relevant for searches for supersymmetry at the LHC when going from LO to NLO. Here, we present distributions for

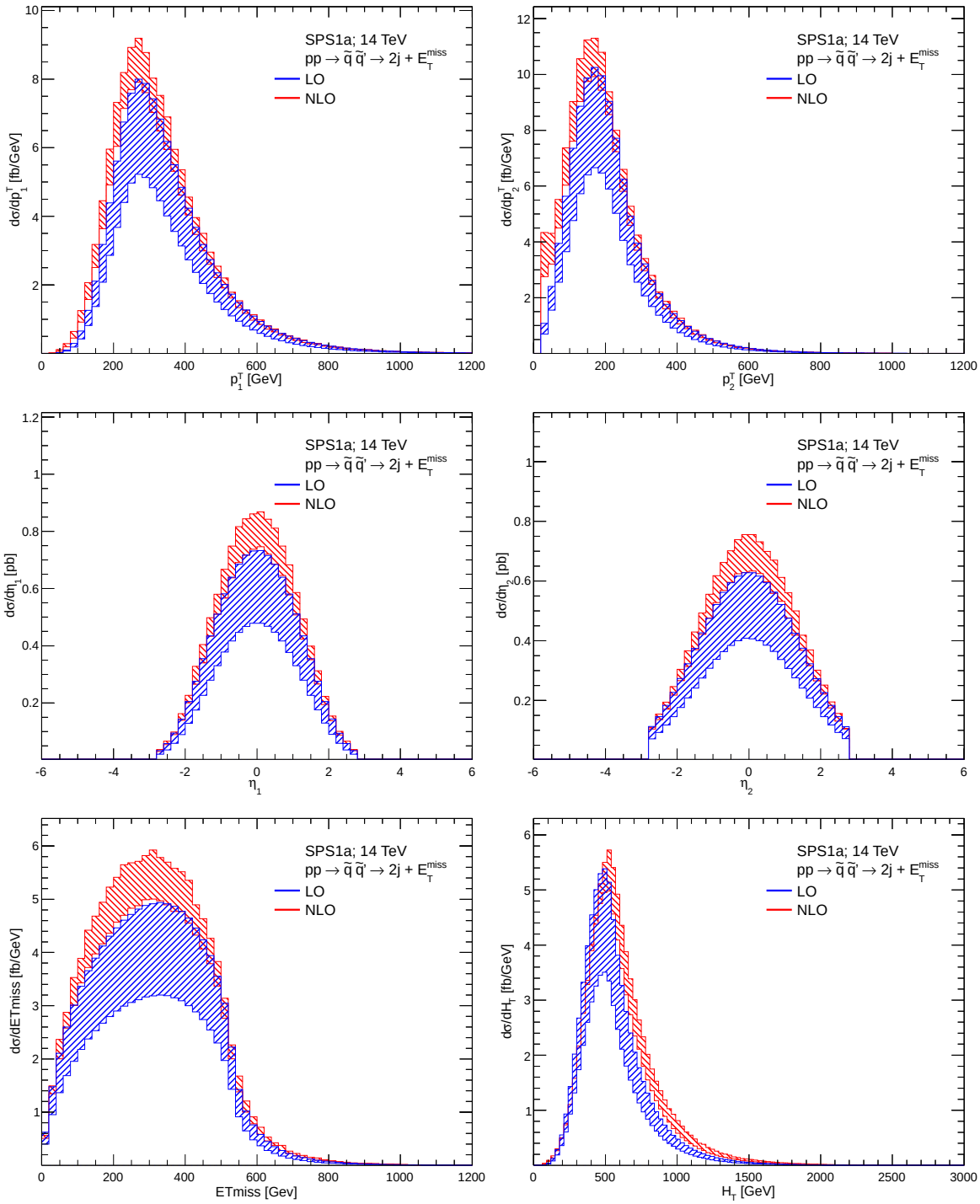

Figure 5.2: Differential distributions in $p_1^{\mathrm{T}}, p_2^{\mathrm{T}}$ (in fb/GeV), η_1, η_2 (in pb/GeV), $\not{E}_T$ and H_T (in fb/GeV) for SPS1a and $\sqrt{S} = 14$ TeV, where for, both, LO (blue) and NLO (red) the common renormalization and factorization scale is varied between $\mu/2$ and 2μ, with $\mu = \overline{m_{\tilde{q}}}$.

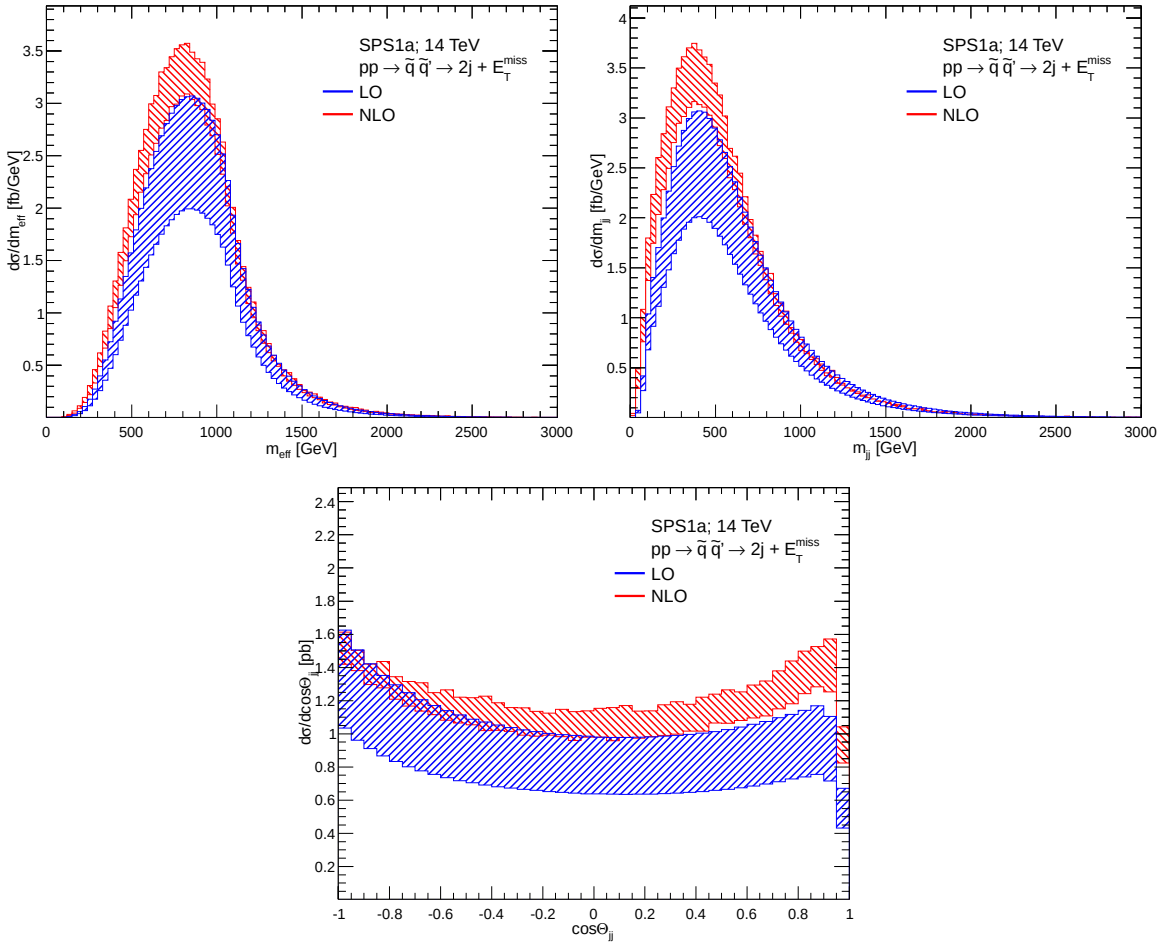

Figure 5.3: Differential distributions in $m_{\text{eff}}, m_{\text{inv}}(jj)$ (in fb/GeV) and $\cos\Theta_{jj}$ (in pb) for SPS1a and $\sqrt{S} = 14$ TeV, where for, both, LO (blue) and NLO (red) the common renormalization and factorization scale is varied between $\mu/2$ and 2μ, with $\mu = \overline{m_{\tilde{q}}}$.

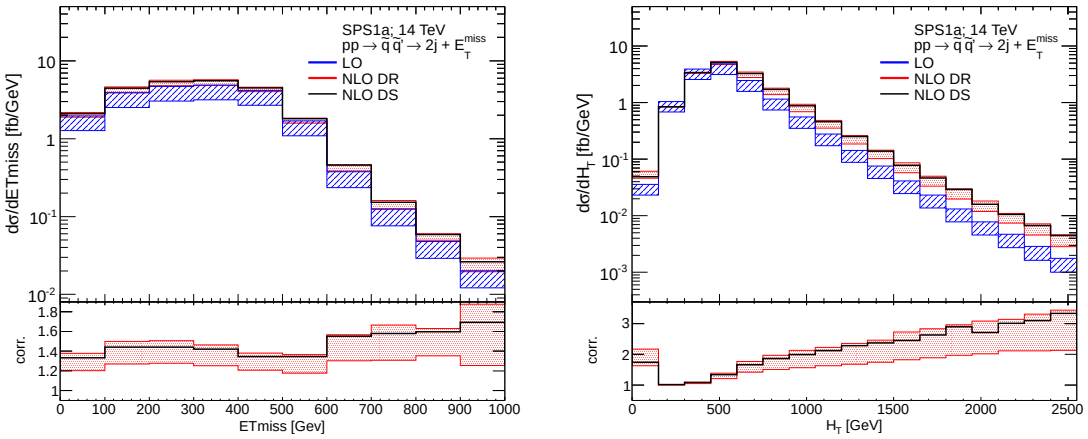

Figure 5.4: Differential distributions in $\not{E}_T$ and H_T (in fb/GeV) for SPS1a and $\sqrt{S} = 14$ TeV. In the upper part the common renormalization and factorization scale is varied between $\mu/2$ and 2μ, with $\mu = \overline{m_{\tilde{q}}}$ for LO (blue) and NLO^{DR} (red). In the lower part we show in red the ratio of the NLO^{DR} uncertainty band and the LO result (at scale $\mu = \overline{m_{\tilde{q}}}$). We also show in black the ratio of the NLO result in the DS scheme and the central LO result.

a center of mass energy $\sqrt{S} = 14$ TeV. Lower center of mass energies show qualitatively the same behavior. For benchmark point SPS1a plots are shown in figure 5.5, for 10.1.5 in figure 5.6 and for p19MSSM1A in figure 5.7. We present distributions in p_1^{T}, p_2^{T}, m_{eff}, $\not{E}_T$ (all in fb/GeV), where the ATLAS jet choice $R = 0.4$ and cuts of eq. (5.4) are applied. Also distributions in H_T (in fb/GeV) and in α_T (in pb) are displayed, where the CMS jet choice $R = 0.5$ and corresponding cuts of eq. (5.4) are applied. In the α_T distribution, events are reclustered into two pseudojets and a cut of $H_T > 350$ GeV is applied. In the upper part of any plot we show each distribution at LO in black, NLO in red and in blue the LO prediction rescaled by the ratio, K^{NLO}, between the integrated NLO and LO result. In the lower part of any plot we show the NLO divided by the rescaled LO $\cdot\, K^{\mathrm{NLO}}$ distribution. In this way we present corrections purely in the shape and not in the normalization of the distributions. For SPS1a and 10.1.5 corrections are qualitatively very similar and rather flat for p_1^{T}, p_2^{T} and $\not{E}_T$, as expected from [38]. Corrections in the (inclusive) H_T distribution grow for larger H_T and can be sizeable. This can be explained from the high-p^{T} behavior of the contribution from hard real gluon radiation to this observable. Corrections to the shape of the α_T observable change sign at the physical boundary [266] $\alpha_T = 0.5$ and fall off continuously in the signal region $\alpha_T > 0.55$.

Looking at the distributions of p19MSSM1A in figure 5.7 a completely different behavior of the NLO corrections cannot be missed. The tail of the p_1^{T}, p_2^{T}, m_{eff} and $\not{E}_T$ distributions completely departs from the LO predictions. This can be understood from the following considerations. Due to the small mass splitting between squarks and the $\tilde{\chi}_1^0$ for benchmark point p19MSSM1A, jets from squark decays tend to be soft. Now, the p^{T} of an additional jet (which can not be distinguished from the decay jets) from hard gluon radiation in the production can

easily be of the same order as the ones from squark decays and result in the given distortions. Such a behavior for compressed spectra was already partly discussed in [157], where sparticle production and decay including additional hard jets matched to a parton shower was investigated. We verified our findings by comparing LO predictions plus real hard gluon radiation in the production stage with a corresponding calculation performed with `MadGraph` [269]. The tail of the considered distributions can be described adequately only by inclusion of additional gluon radiation, which should thus be seen as the LO prediction for these phase-space regions. Still, only our full NLO calculation allows a consistent treatment of the entire distributions. Turning to the α_T distribution, shapes of the LO and NLO prediction are different and, here, we refrain from showing explicitly corrections in the shape or a rescaled LO prediction.

Next to the distributions shown in figures 5.5, 5.6 and 5.7, we also investigated pseudo-rapidity distributions of the two hardest jets $\eta_{1/2}$. Here, in the relevant region $|\eta_{1/2}| < 3.0$ corrections in the shapes are always smaller than about 5 % for all benchmark scenarios and energies.

In figure 5.8 we turn our attention towards angular distributions between the two hardest jets. On the left we show distributions in the invariant mass of the two hardest jets $m_{\text{inv}}(jj)$, on the right distributions in the cosine of the angle between the two hardest jets $\cos\Theta_{jj}$ are presented. Again results are shown for all three benchmark points and a center of mass energy $\sqrt{S} = 14$ TeV. Corrections in these distributions can be quite large. In general, in the full NLO results one observes an increase for small angles between the two hardest jets (up to 20 % in the $\cos\Theta_{jj}$ distributions). In the high-invariant-mass tail for SPS1a and 10.1.5 corrections are negative and grow to 40 % in the considered invariant mass range. Such corrections could potentially be absorbed into a dynamical renormalization/factorization scale definition, e.g., $\mu = H_T$; in-detail investigation is left to future work. In the invariant mass distribution of p19MSSM1A we observe the same deviation of the NLO result from the LO shape as already discussed above.

Finally, in figure 5.9 we investigate NLO corrections to the $\cos\hat{\Theta}$ distribution for the benchmark points SPS1a (top left), 10.1.5 (top right) and p19MSSM1A (bottom) at a center of mass energy of $\sqrt{S} = 14$ TeV. Corrections up to 15 % are observable. Still, the general shape and thus the potential for extraction of spin information about the intermediate squarks seems to be robust under higher order corrections.

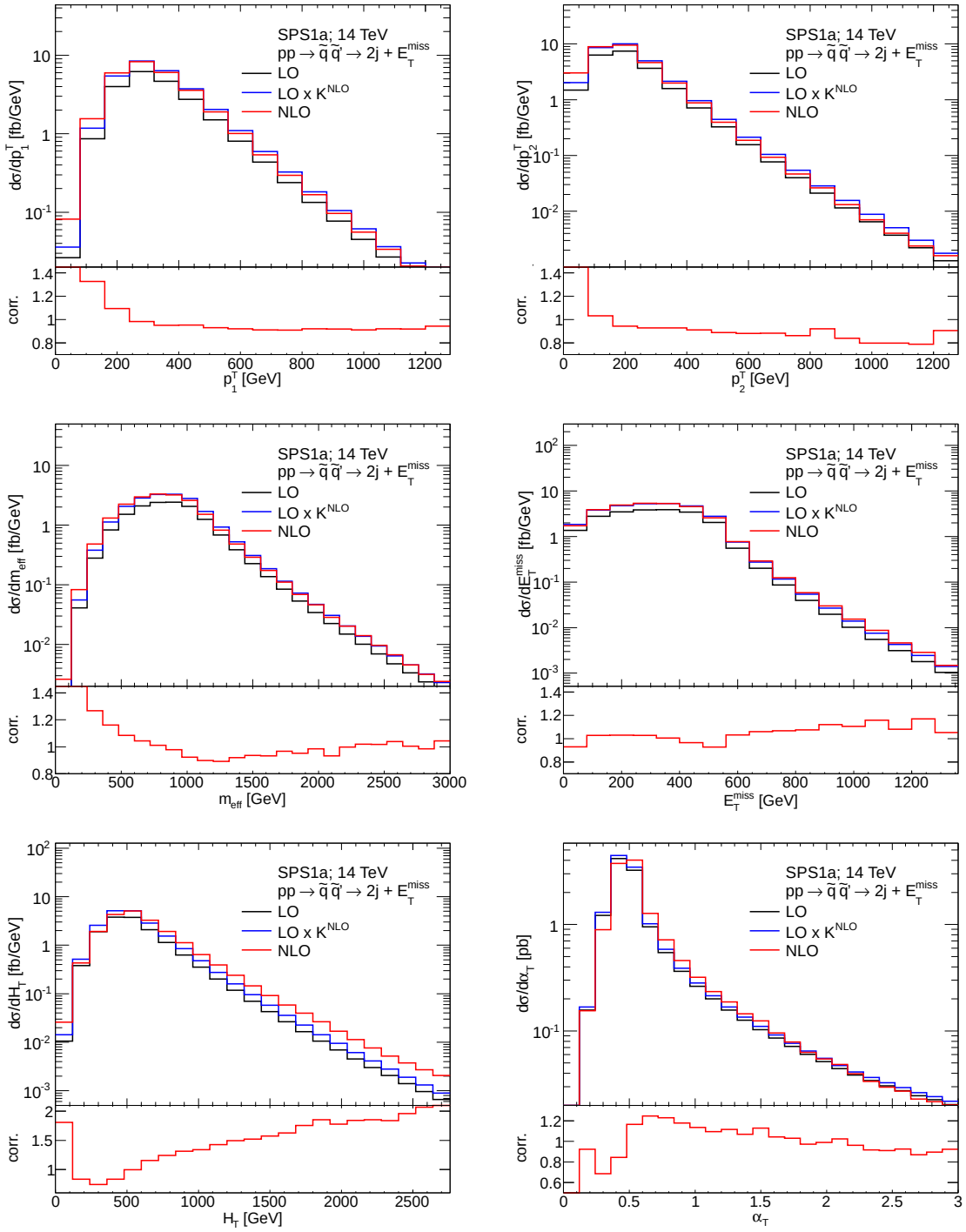

Figure 5.5: Differential distributions of benchmark point SPS1a at a center of mass energy $\sqrt{S} = 14$. In the upper part of the plots we show in black LO, in red NLO and in blue LO distributions rescaled by the ratio K^{NLO} between the integrated NLO and LO results. In the lower part of the plots NLO corrections in the shapes are shown, defined as the full NLO divided by the rescaled LO $\cdot\, K^{\mathrm{NLO}}$ distribution. From top left to bottom right we show differential distributions in p_1^{T}, p_2^{T}, m_{eff}, $\not{E}_T$, H_T (all in fb/GeV) and in α_T (in pb).

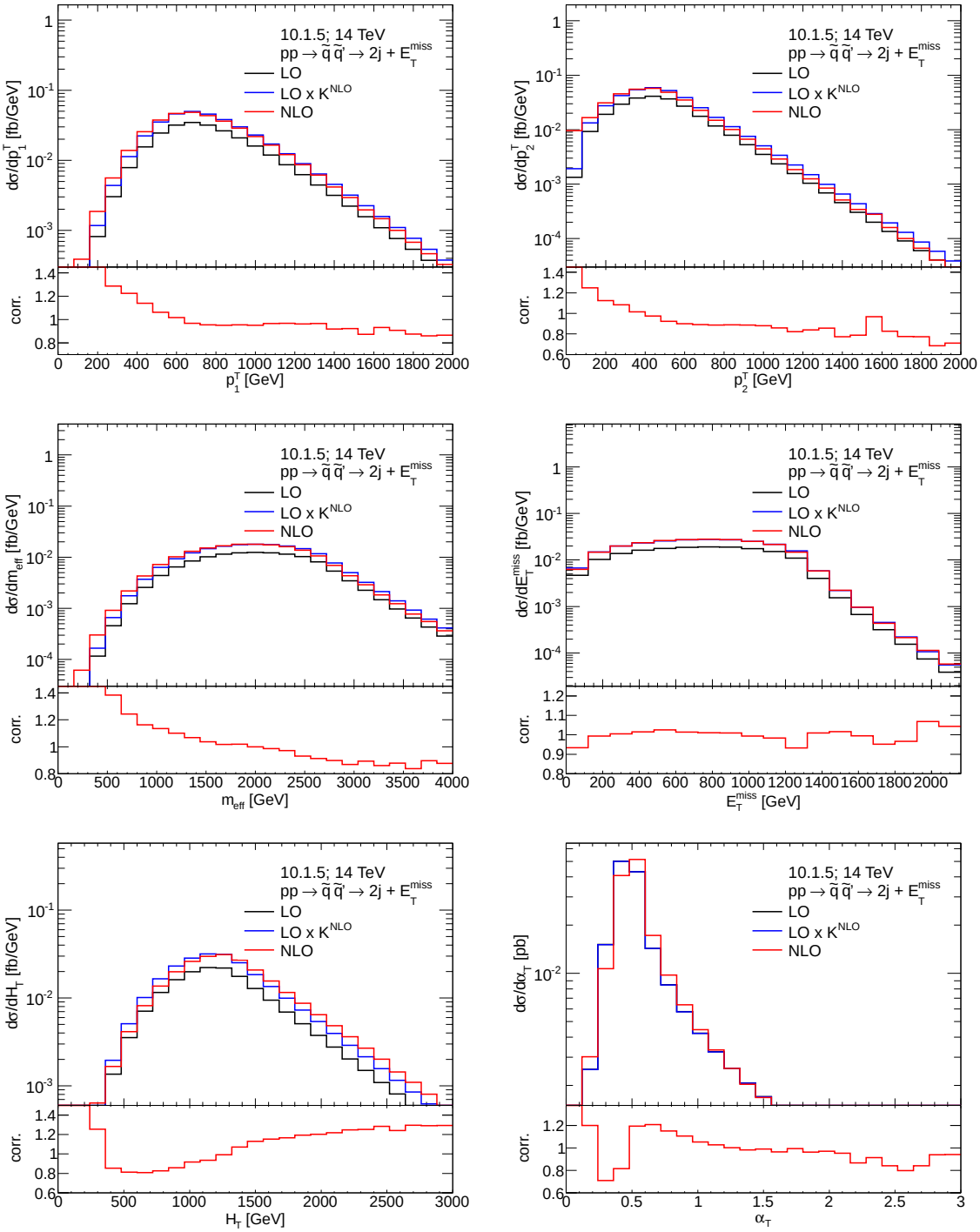

Figure 5.6: Differential distributions of benchmark point 10.1.5 at a center of mass energy $\sqrt{S} = 14$. In the upper part of the plots we show in black LO, in red NLO and in blue LO distributions rescaled by the ratio K^{NLO} between the integrated NLO and LO results. In the lower part of the plots NLO corrections in the shapes are shown, defined as the full NLO divided by the rescaled LO $\cdot\, K^{\mathrm{NLO}}$ distribution. From top left to bottom right we show differential distributions in p_1^{T}, p_2^{T}, m_{eff}, $\not{E}_T$, H_T (all in fb/GeV) and in α_T (in pb).

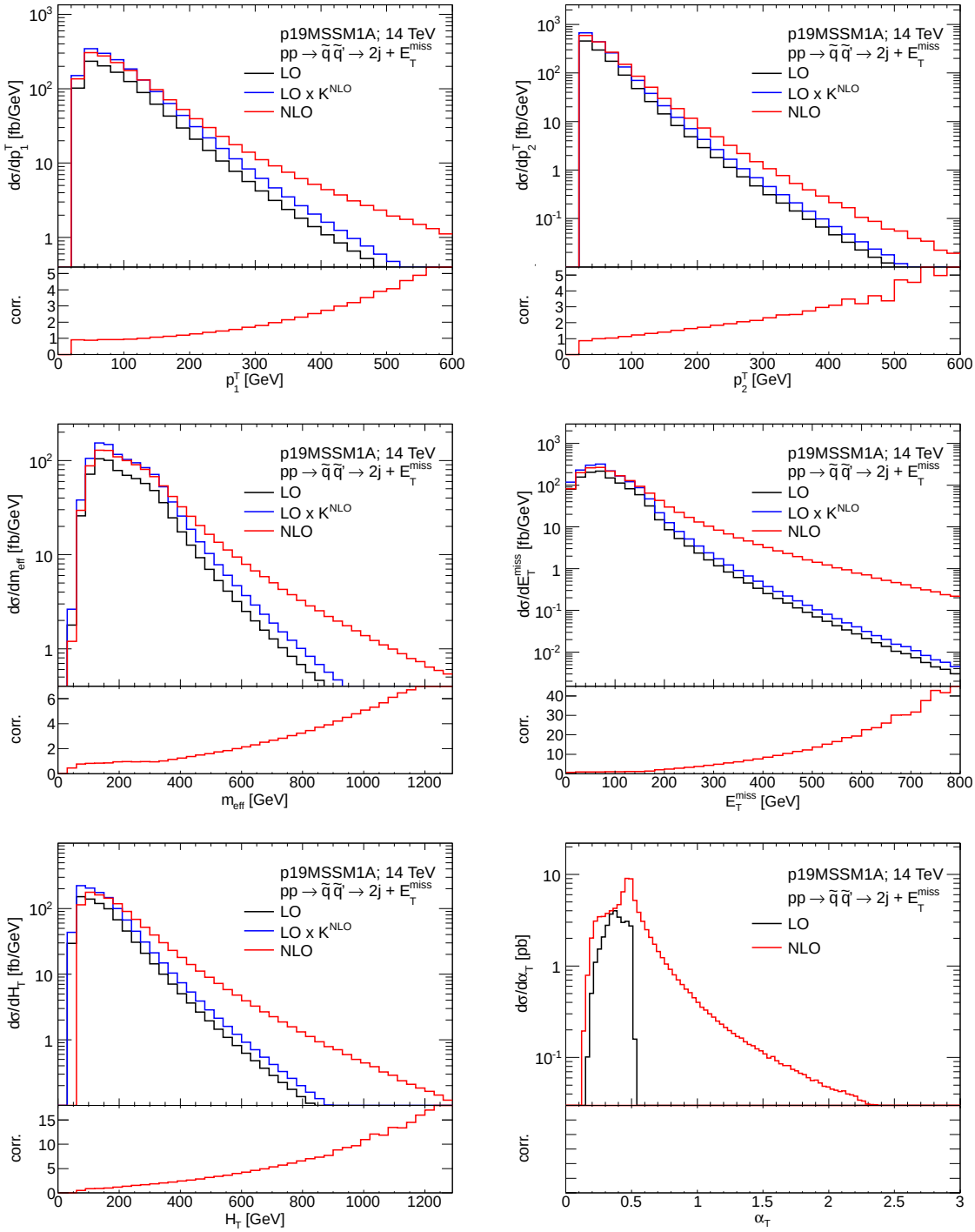

Figure 5.7: Differential distributions of benchmark point p19MSSM1A at a center of mass energy $\sqrt{S} = 14$. In the upper part of the plots we show in black LO, in red NLO and in blue LO distributions rescaled by the ratio K^{NLO} between the integrated NLO and LO results. In the lower part of the plots NLO corrections in the shapes are shown, defined as the full NLO divided by the rescaled LO $\cdot\, K^{\mathrm{NLO}}$ distribution. From top left to bottom right we show differential distributions in p_1^{T}, p_2^{T}, m_{eff}, $\not{E}_T$, H_T (all in fb/GeV) and in α_T (in pb).

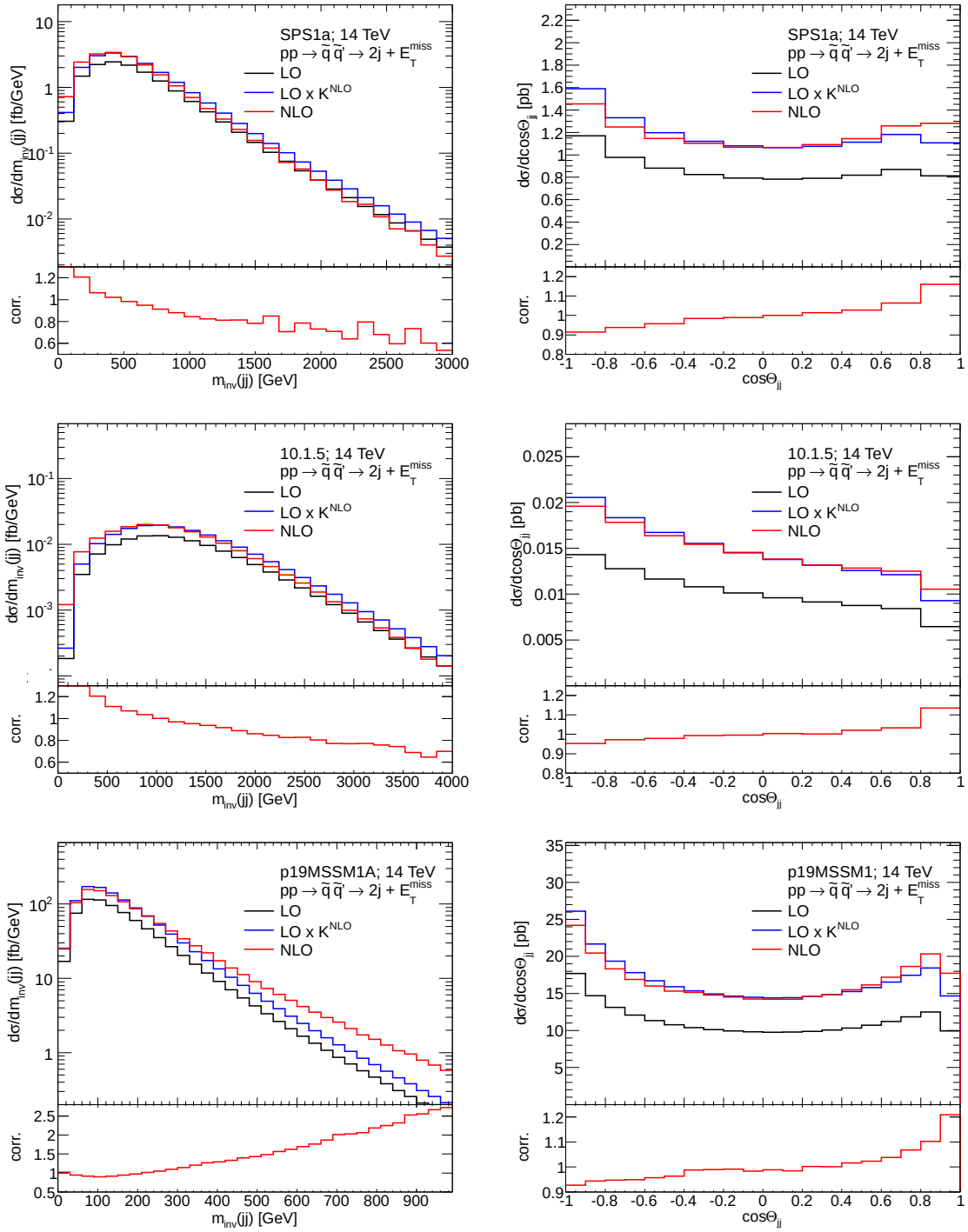

Figure 5.8: Distributions in the invariant mass $m_{\text{inv}}(jj)$ (in fb/GeV) and the cosine of the angle between the two hardest jets $\cos\Theta_{jj}$ (in pb) for the benchmark points SPS1a (top), 10.1.5 (middle), p19MSSM1A (bottom) and a center of mass energy $\sqrt{S} = 14$ TeV. In the upper part of the plots we show in black LO, in red NLO and in blue LO distributions rescaled by the ratio K^{NLO} between the integrated NLO and LO results. In the lower part of the plots NLO corrections in the shapes are shown, defined as the full NLO divided by the rescaled LO $\cdot\, K^{\text{NLO}}$ distribution.

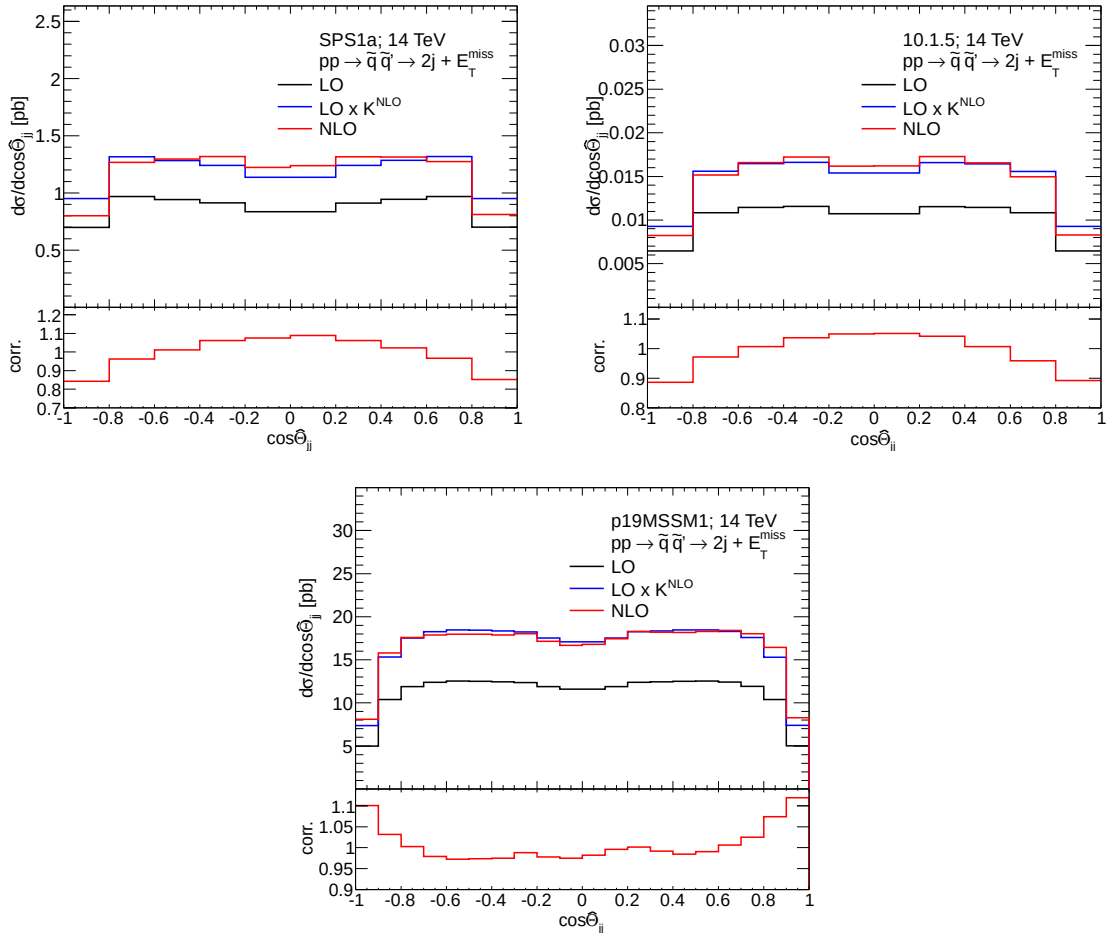

Figure 5.9: Distributions in $\cos\hat{\Theta}$ (in pb) for the benchmark points SPS1a (upper left), 10.1.5 (upper right) p19MSSM1A (bottom) at a center of mass energy of $\sqrt{S} = 14$ TeV. In the upper part of the plots we show in black LO, in red NLO and in blue LO distributions rescaled by the ratio K^{NLO} between the integrated NLO and LO results. In the lower part of the plots NLO corrections in the shapes are shown, defined as the full NLO divided by the rescaled $\mathrm{LO} \cdot K^{\mathrm{NLO}}$ distribution.

5.2.5 Event rates

After investigating inclusive cross sections and differential distributions, we now proceed to event rates, i.e., cross sections integrated on signal regions defined to reduce background contributions. By this study, we want to quantify a possible impact of our calculation on current searches for supersymmetry and future measurements of event rates at the LHC.

In table 5.8 we list cross sections after applying cuts of eq. (5.9) and in table 5.9 cross sections after applying cuts of eq. (5.10). We show LO and NLO cross sections for all three benchmark points and all three energies together with resulting K-factors. For comparison we again list inclusive K-factors of just production, already shown in table 5.5. From these results, a fully differential description of all squark and gluino channels including NLO effects in production and decay seems inevitable for a conclusive interpretation of SUSY searches (or signals) at the LHC. Numbers in table 5.8 and table 5.9 again show that, for compressed spectra like p19MSSM1A, a pure LO approximation is unreliable for a realistic phenomenological description of the experimental signatures considered here. Furthermore, as already suggested in [270] and expected from the differential distributions shown in section 5.2.4, in particular interpretations based on α_T seem to be highly affected by higher order corrections.

benchmarkpoint	**Energy [TeV]**	$\boldsymbol{N^{(0)}_{\mathrm{ATLAS}}}$	$\boldsymbol{N^{(0+1)}_{\mathrm{ATLAS}}}$	$\boldsymbol{K_{N_{\mathrm{ATLAS}}}}$	$\boldsymbol{K_{pp\to\tilde{q}\tilde{q}'}}$
SPS1a	7	0.066 pb	0.083 pb	1.26	1.37
	8	0.097 pb	0.121 pb	1.25	1.35
	14	0.347 pb	0.424 pb	1.22	1.28
10.1.5	7	0.313 fb	0.503 fb	1.61	1.57
	8	0.861 fb	1.344 fb	1.56	1.52
	14	13.82 fb	19.77 fb	1.43	1.40
p19MSSM1A	7	0.140 fb	20.76 fb	~ 150	1.40
	8	0.339 fb	37.96 fb	~ 110	1.39
	14	0.0044 pb	0.264 pb	~ 60	1.34

Table 5.8: LO $N^{(0)}_{\mathrm{ATLAS}}$ and NLO $N^{(0+1)}_{\mathrm{ATLAS}}$ cross section predictions and K-factors $K_{N_{\mathrm{ATLAS}}}$ for the three benchmark scenarios SPS1a, 10.1.5, p19MSSM1A and center of mass energies $\sqrt{S} = 7, 8, 14$ TeV where the cuts of eq. (5.9) are applied. For comparison we also list is the inclusive NLO production K-factor $K_{pp\to\tilde{q}\tilde{q}'}$ already shown in table 5.5.

benchmarkpoint	**Energy [TeV]**	$\boldsymbol{N^{(0)}_{\mathrm{CMS}}}$	$\boldsymbol{N^{(0+1)}_{\mathrm{CMS}}}$	$\boldsymbol{K_{N_{\mathrm{CMS}}}}$	$\boldsymbol{K_{pp\to\tilde{q}\tilde{q}'}}$
SPS1a	7	0.112 pb	0.141 pb	1.26	1.37
	8	0.157 pb	0.197 pb	1.25	1.35
	14	0.488 pb	0.614 pb	1.26	1.28
10.1.5	7	0.201 pb	0.261 pb	1.30	1.57
	8	0.542 fb	0.674 fb	1.24	1.52
	14	8.129 fb	8.884 fb	1.09	1.40
p19MSSM1A	7	10^{-6} pb	0.095 pb	$\mathcal{O}(10^4)$	1.40
	8	10^{-6} pb	0.151 pb	$\mathcal{O}(10^4)$	1.39
	14	$2 \cdot 10^{-5}$ pb	0.687 pb	$\mathcal{O}(10^4)$	1.34

Table 5.9: LO $N^{(0)}_{\mathrm{CMS}}$ and NLO $N^{(0+1)}_{\mathrm{CMS}}$ cross section predictions and K-factors $K_{N_{\mathrm{CMS}}}$ for the three benchmark scenarios SPS1a, 10.1.5, p19MSSM1A and center of mass energies $\sqrt{S} = 7, 8, 14$ TeV where the cuts of eq. (5.10) are applied. For comparison we also list is the inclusive NLO production K-factor $K_{pp\to\tilde{q}\tilde{q}'}$ already shown in table 5.5.

Chapter 6

The "golden" decay chain

In this chapter we present an analysis at NLO QCD of the contribution from squark-squark production to the experimental signature of 2 jets + 2 leptons + missing transverse energy, $2j + l^+l^- + \not{E}_T(+X)$, with opposite-sign same flavor leptons, taking into account decays and experimental cuts. We consider the case in which one squark is left-handed and decays via the "qll-chain", also known as "golden" decay chain,

$$\tilde{q}_L \to \quad q\ \tilde{\chi}_2^0 \quad \to q\ l^\pm\ \tilde{l}_{L/R}^\mp \to q\ l^\pm\ l^\mp\ \tilde{\chi}_1^0\,, \tag{6.1}$$

i.e., the squark decays into a quark and a second lightest neutralino $\tilde{\chi}_2^0$, which subsequently decays via an intermediate slepton into a pair of opposite-sign same-flavor (OS-SF) leptons and a lightest neutralino $\tilde{\chi}_1^0$; the other squark decays directly into the lightest neutralino

$$\tilde{q}_R \to \quad q\ \tilde{\chi}_1^0 \quad . \tag{6.2}$$

Thus we provide, for the first time, a fully differential description at NLO QCD of the contribution to the signature $2j + l^+l^-(\text{OS-SF}) + \not{E}_T(+X)$ from the process

$$pp \to \tilde{q}_L\tilde{q}'_R \to q\tilde{\chi}_1^0 q' l^\pm l^\mp \tilde{\chi}_1^0\,. \tag{6.3}$$

On the one hand we study the effects of the NLO corrections on invariant mass distributions which can be used for future parameter determination. On the other hand we analyze the impact on predictions for cut-and-count searches using the given experimental signature.

The outline of this chapter is the following. In section 6.1 we first give an overview on the relevance and phenomenology of the considered decay chain. Afterwards, in section 6.2 we explicitly apply the considerations of chapter 4 to the given process and explain details of the calculation of the considered decay chain at NLO in section 6.3. Finally, in section 6.4 we present the numerical results. Section 6.4 is divided in three subsections: the discussion of the considered benchmark scenarios, the analysis of NLO corrections to the isolated decay chain, and finally the discussion, for combined production and decay, of NLO effects on invariant mass distributions and also on event rates after kinematical cuts. Results and discussion of this chapter are largely based on ref. [4].

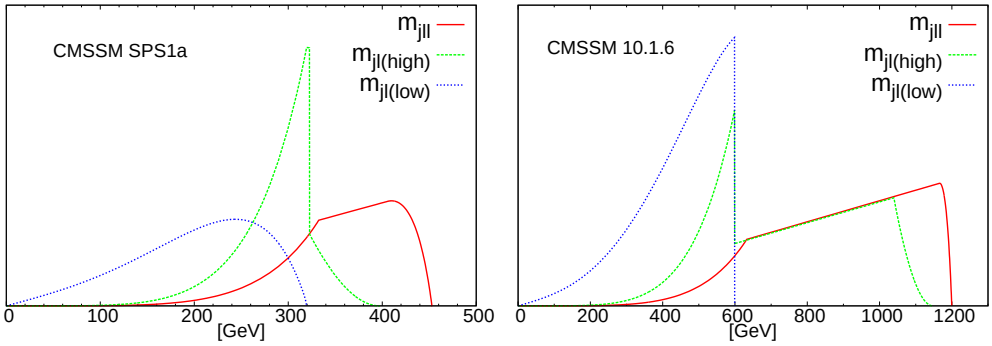

Figure 6.1: Shapes of the m_{jll}, $m_{jl(\text{high})}$ and $m_{jl(\text{low})}$ distributions for SPS1a and 10.1.6 at LO.

6.1 Overview

The decay chain (6.1) was introduced in [271, 272] and studied in many subsequent works [155, 273–289]. These analyses showed that measurements of resulting invariant mass distribution endpoints and shapes can be exploited to determine the masses of the intermediate SUSY particles. Relations between the most important endpoints and the intermediate masses are given in Appendix B. Shapes of various relevant invariant mass distributions have first been calculated analytically at LO in [276] and they might be important to resolve ambiguities in mass measurements from kinematic endpoints [290]. In figure 6.1, for illustrative purposes, normalized invariant mass distributions in m_{jll}, $m_{jl(\text{high})}$ and $m_{jl(\text{low})}$ are displayed for two benchmark points (with details given in the corresponding sections of this chapter). At this point we only want to emphasize that such shapes are very sensitive to the model parameters. For a precise analysis higher-order corrections have to be investigated, as they can distort shapes and affect the accuracy of endpoint determination techniques.

Such invariant mass distributions, due to correlations between particles in the decay chain, can also be used for spin measurements of the intermediate sparticles [291]. In this way, e.g., a SUSY model can be discriminated from an Universal Extra Dimension (UED) model, see e.g., [292, 293] and [294–304]. Additionally, besides observables based on invariant mass distributions, the signature $2j + l^+l^-(\text{OS-SF}) + \not{E}_T(+X)$ can be used for SUSY searches at the LHC. Basic kinematical cuts can reduce SM backgrounds significantly and already now stringent bounds on relevant parameter regions have been obtained [305, 306]. Furthermore, resulting rates can also be used for parameter determination within a global fit [168].

In all these analyses a detailed understanding of theoretical uncertainties and effects from higher-order contributions is necessary, requiring precise predictions at a fully differential level including NLO corrections in production and decay. In [155] the "qll-chain" was investigated at NLO QCD in the squark rest frame. There, real gluon radiation contributions are given in a fully analytical form and leading soft and collinear gluon contributions are resummed. Furthermore, for the LHC a combined analysis using LO production matrix elements is presented. In their numerical analysis the authors of [155] concentrate on the effect on distributions sensitive to spin correlations. In the present chapter we continue the analysis

of higher-order corrections of the "qll-chain" by combining the production of squark pairs and their subsequent decays at the NLO level in a consistent way. This allows for a systematic study of the important jet combinatorial issues in the presence of more than one final-state jet, emerging from both real radiation at NLO and the combination of decay and production [286].

The study of the signature $2j+l^+l^-(\text{OS-SF})+\not{E}_T(+X)$ presented here includes the contribution from squark–squark production, which constitutes the dominant production channel in the case of heavy squarks and gluinos, as already pointed out in the previous chapters. Thus, this work should be understood as a first step towards a calculation including all channels and also off-shell and non-factorizable corrections.

In our analysis we assume $\tilde{\chi}_1^0$ and $\tilde{\chi}_2^0$ to be mainly bino- and wino-like respectively, as they appear in large parameter regions of models with unified gaugino masses at the GUT scale (see eq. (2.85a)). In such scenarios the other decays, e.g., $\tilde{q}_L \to \tilde{\chi}_1^0 q$ and $\tilde{q}_R \to \tilde{\chi}_2^0 q$, are highly suppressed for squarks of the first and second generation. Furthermore, in the benchmark scenarios we consider, all relevant squarks are lighter than the gluino $\tilde{g}$, so squarks can exclusively decay into neutralinos and charginos.

6.2 Method

The combined process we investigate here is illustrated in figure 6.2. The considered factorizable NLO QCD corrections only affect the production stage and the QCD part of the two squark decays. The electroweak decay chain is unaffected.

At LO the only partonic subprocess that contributes to a given intermediate $\tilde{q}_L\tilde{q}'_R$ ($\tilde{q}_L^*\tilde{q}_R'^*$) configuration arises from a quark (anti-quark) pair qq' ($\bar{q}\bar{q}'$) in the initial state. We will perform the following discussion without referring to the charge-conjugate subprocesses; in the final results, however, we include the charge-conjugate processes explicitly. Indeed, due to chirality-dependent interactions, the decay of an anti-squark has to be treated independently from the corresponding squark decay.

Using the theoretical framework explained in chapter 4 and applied for two direct de-

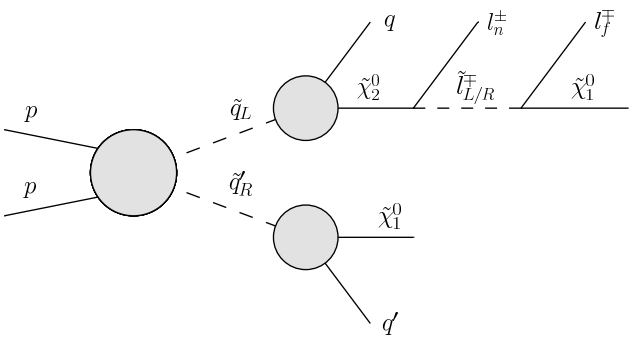

Figure 6.2: General structure of factorizable NLO QCD corrections to the given process.

cays in chapter 5, we include here the NLO factorizable corrections in the narrow-width-approximation to the process defined in eq. (6.3). Reproducing again 4.14, for any flavor configuration, a systematic expansion of the differential cross section in the strong coupling α_s yields

$$
\begin{aligned}
d\sigma^{(0+1)}_{\mathrm{NWA}}(pp \to \tilde{q}_L \tilde{q}'_R \to q\tilde{\chi}^0_1 q' l^+ l^- \tilde{\chi}^0_1 (+X)) \;=\; & \qquad (6.4)\\
& \frac{1}{\Gamma^{(0)}_{\tilde{q}_L}\,\Gamma^{(0)}_{\tilde{q}'_R}} \Big[d\sigma^{(0)}_{pp\to\tilde{q}_L\tilde{q}'_R}\, d\Gamma^{(0)}_{\tilde{q}_L\to q\tilde{\chi}^0_1 l^+l^-}\, d\Gamma^{(0)}_{\tilde{q}'_R\to q'\tilde{\chi}^0_1} \left(1 - \frac{\Gamma^{(1)}_{\tilde{q}_L}}{\Gamma^{(0)}_{\tilde{q}_L}} - \frac{\Gamma^{(1)}_{\tilde{q}'_R}}{\Gamma^{(0)}_{\tilde{q}'_R}}\right) \\
& + d\sigma^{(0)}_{pp\to\tilde{q}_L\tilde{q}'_R}\, d\Gamma^{(1)}_{\tilde{q}_L\to q\tilde{\chi}^0_1 l^+l^-}\, d\Gamma^{(0)}_{\tilde{q}'_R\to q'\tilde{\chi}^0_1} \;+\; d\sigma^{(0)}_{pp\to\tilde{q}_L\tilde{q}'_R}\, d\Gamma^{(0)}_{\tilde{q}_L\to q\tilde{\chi}^0_1 l^+l^-}\, d\Gamma^{(1)}_{\tilde{q}'_R\to q'\tilde{\chi}^0_1} \\
& + d\sigma^{(1)}_{pp\to\tilde{q}_L\tilde{q}'_R}\, d\Gamma^{(0)}_{\tilde{q}_L\to q\tilde{\chi}^0_1 l^+l^-}\, d\Gamma^{(0)}_{\tilde{q}'_R\to q'\tilde{\chi}^0_1} \Big] .
\end{aligned}
$$

The calculation of the ingredients of eq. (6.4) is presented in sections 4.3 and 4.4. However, details of the treatment of the decay chain, i.e., terms $d\Gamma^{(0,1)}_{\tilde{q}_L\to q\tilde{\chi}^0_1 l^+l^-}$ are addressed in section 6.3. On the basis of eq. (6.4) intermediate events for production and decay are combined in analogy to the strategy explained in section 5.1.1.

6.3 Calculation of the squark decay chain

The structure of the decay chain is illustrated in figure 6.3. With $l^\pm_n$ and $l^\mp_f$ we indicate, respectively, the lepton emerging from the $\tilde{\chi}^0_2$ decay, the *near lepton*, and the lepton emerging from the slepton decay, the *far lepton*. Experimentally these leptons are indistinguishable. Figure 6.3 represents, in a compact notation, the four Feynman diagrams contributing to the tree level amplitude for the decay $\tilde{q}_L \to q l^+ l^- \tilde{\chi}^0_1$. They correspond to the two cases $\tilde{q}_L \to q l^+_n l^-_f \tilde{\chi}^0_1$ and $\tilde{q}_L \to q l^-_n l^+_f \tilde{\chi}^0_1$ with a left- or right-handed intermediate (anti)slepton.

For non-degenerate left- and right-handed sleptons, as in the scenarios investigated in this chapter, in NWA the structure of the squared amplitude of this decay chain becomes much simpler. In the limit $\frac{\Gamma}{m} \to 0$ for the sleptons and for $\tilde{\chi}^0_2$, the interferences between different diagrams vanish and the phase-space of the intermediate particles can be treated on-shell. In this way LO and NLO contributions to the differential distribution for the decay chain in

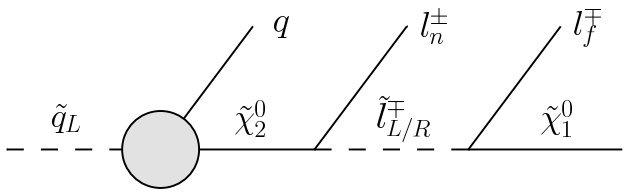

Figure 6.3: Structure of the decay chain. NLO QCD corrections involve only the first step $\tilde{q}_L \to q\tilde{\chi}^0_2$.

m [GeV]	$\tilde{u}_L$	$\tilde{u}_R$	$\tilde{d}_L$	$\tilde{d}_R$	$\tilde{g}$	$\tilde{l}_L$	$\tilde{l}_R$	$\tilde{\chi}_2^0$	$\tilde{\chi}_1^0$
SPS1a	563.6	546.7	569.0	546.6	608.5	202.4	144.1	180.2	97.0
10.1.6	1531.7	1472.2	1533.6	1466.1	1672.1	536.6	340.6	592.4	313.3

Table 6.1: On-shell masses of the first generation squarks and sleptons, the gluino and the lightest and second lightest neutralino within the different SUSY scenarios considered. All masses are given in GeV.

Figure 6.3 can be written as follows,

$$d\Gamma^{(0,1)}_{\tilde{q}_L \to q l^+ l^- \tilde{\chi}_1^0} = \sum_{\sigma=\pm 1/2} \frac{d\Gamma^{(0,1)}_{\tilde{q}_L \to q \tilde{\chi}^0_{2,\sigma}}}{\Gamma_{\tilde{\chi}_2^0}} \left[d\Gamma_{\tilde{\chi}^0_{2,\sigma} \to l_n^+ l_f^- \tilde{\chi}_1^0} + d\Gamma_{\tilde{\chi}^0_{2,\sigma} \to l_n^- l_f^+ \tilde{\chi}_1^0} \right] . \tag{6.5}$$

The index σ represents the helicity of $\tilde{\chi}_2^0$. In our calculation we keep, at LO and NLO, the full helicity dependence. Technically this is achieved using, both at LO and at NLO, matrix elements for the entire chain and setting consistently the different on-shell conditions according to the intermediate states for the various contributions. In this way, the sum over the helicity states is automatically performed and off-shell effects can be switched on easily in a further study. The two terms contained in the square brackets of eq. (6.5) correspond to the two different charge configurations for near and far leptons in the decay of $\tilde{\chi}_2^0$. Both configurations, in general, get contributions from left- and the right-handed sleptons.

As mentioned above, we concentrate on scenarios where the $\tilde{\chi}_2^0$ is dominantly wino-like. Thus, in the considered decay chain the coupling to a right-handed slepton, $\tilde{l}_R$, is heavily suppressed compared to the corresponding decay chain via a left-handed $\tilde{l}_L$. Only if the decay into a left-handed slepton is kinematically forbidden, $m_{\tilde{l}_L} > m_{\tilde{\chi}_2^0} > m_{\tilde{l}_R}$, the decay via a $\tilde{l}_R$ can contribute substantially. Basically also the decay of the $\tilde{\chi}_2^0$ into a OS-SF lepton pair via a Z boson contributes when kinematically allowed; these effects are, however, numerically not significant for the benchmark points considered here.

The calculation of $d\Gamma^{(1)}_{\tilde{q}_L \to q \tilde{\chi}^0_{2,\sigma}}$ is performed following the procedure explained in section 4.4.2. The rest of the electroweak decay chain is not affected by NLO QCD corrections.

6.4 Numerical results

In this section we present the numerical results of our calculation. First, we specify input parameters and relevant observables. Second, NLO corrections to the decay chain, eq. (6.1), not combined with the production, are investigated in the squark rest frame. Third, we present the combined results.

6.4.1 Parameters and observables

Standard Model input parameters are again as listed in (5.3). As PDF set we also again use CTEQ6.6 [257] with the associated $\alpha_s^{\overline{\rm MS}}(\mu_R)$ at NLO; and as before, renormalization scale

BR [%]	$\tilde{q}_R \to \tilde{\chi}_1^0$	$\tilde{q}_R \to \tilde{\chi}_2^0$	$\tilde{q}_L \to \tilde{\chi}_1^0$	$\tilde{q}_L \to \tilde{\chi}_2^0$	$\tilde{\chi}_2^0 \to \tilde{l}_L^\pm$	$\tilde{\chi}_2^0 \to \tilde{l}_R^\pm$	$\tilde{\chi}_2^0 \to Z$
SPS1a	98.5	1.0	1.5	31.2	–	13.1	–
10.1.6	99.8	0.03	1.5	32.1	28.4	0.2	0.2

Table 6.2: Branching ratios for the decay of squarks into $\tilde{\chi}_1^0$ and $\tilde{\chi}_2^0$ and for the decay of a $\tilde{\chi}_2^0$ into right- and left-handed sleptons. Squarks and leptons of the first two families are considered, where branchings into second and first generation sleptons and their charge-conjugate contributions are summed.

μ_R and factorization scale μ_F are both set to the average mass of all light-flavor squarks, $\mu = \mu_F = \mu_R = \overline{m_{\tilde{q}}}$.

Numerical results in this chapter are presented for two representative benchmark scenarios and the LHC with a center of mass energy of $\sqrt{S} = 14$ TeV. We choose the two CMSSM scenarios SPS1a and 10.1.6 defined in table 5.1. The scenario SPS1a was already used in the numerical evaluation of chapter 5. Both scenarios, SPS1a and 10.1.6 are experimentally excluded by now. However, 10.1.6 only by the latest searches performed by the experimental collaborations at the LHC. Very similar parameter points with slightly heavier squark masses will be tested in the near future. Sparticle on-shell masses, as obtained with `SOFTSUSY`, relevant for our analysis are listed in table 6.1. As in chapter 5, we set all second-generation masses equal to their first-generation counterparts, ignoring finite shifts due to different Yukawa interactions.

In both benchmark scenarios the gluino is heavier then all light flavor squarks. Thus, all these squarks decay exclusively into charginos and neutralinos. In table 6.2 corresponding branching ratios, calculated with `SDECAY`, are listed, where we average the value of the branching ratios for up and down type squarks, which, however, differ at most by $\sim 1\%$. Differences between branching ratios at LO and NLO for squark decays are negligible (less than per mill) for the considered scenarios and so not shown. The right-handed squarks decay dominantly directly into the bino-like $\tilde{\chi}_1^0$, the left-handed squarks into the $\tilde{\chi}_2^0$ and the lighter chargino, $\tilde{\chi}_1^\pm$.

In table 6.2 we also list branching ratios for the second lightest neutralino into light flavor sleptons. Branching ratios into first and second-generation sleptons are identical, and in table 6.2 we sum those contributions. For benchmark point SPS1a only the right-handed $\tilde{l}_R$ is lighter then the $\tilde{\chi}_2^0$. Thus, next to the decay into a τ-slepton, this is the only available two-body decay. In our numerical analysis of SPS1a, both for the decay chain alone and combined with the production, only the decay via a right-handed slepton is considered. In contrast, for 10.1.6 both sleptons are lighter than the $\tilde{\chi}_2^0$. Due to its wino-like nature the $\tilde{\chi}_2^0$ here decays dominantly into the left-handed $\tilde{l}_L$ despite the smaller mass of the $\tilde{l}_R$. For simplification in our numerical analysis of 10.1.6 only the decay via a left-handed slepton is considered. As can be seen from table 6.2, the contribution from the decay into a $\tilde{l}_R$ (and also into $\tilde{\chi}_1^0 Z$) can be safely neglected.

In all numerical results presented in the following we employ the anti-k_T jet clustering algorithm with a jet radius of $R = 0.4$ implemented in `FastJet`. Furthermore we define a jet

to fulfill the cut conditions

$$p_{j_i}^T \geq 20 \text{ GeV}\,, \qquad |\eta_{j_i}| \leq 2.8\,. \tag{6.6}$$

When analyzing combined production and decay in section 6.4.3, the following realistic experimental cuts are applied:

$$\begin{aligned} p_{j_1}^T &\geq 150 \text{ GeV}\,, & p_{j_2}^T &\geq 100 \text{ GeV}\,, \\ |\eta_{j,l}| &\leq 2.5\,, & p_{l_{1,2}}^T &\geq 20 \text{ GeV (OS-SF)}\,, \\ \not{E}_T &\geq 100 \text{ GeV}\,, \end{aligned} \tag{6.7}$$

where we implicitly require the two leptons to have opposite charge and same flavor (OS-SF). Such cuts efficiently reduce SM backgrounds [274, 305, 306]. Furthermore, we assume that contributions from leptonic decays of τ-leptons (from remaining SM processes or from the signal decay chain with an intermediate tau sleptons), and from SUSY decay chains involving charginos or $W^\pm$ bosons, are removed in the standard way by subtracting events with opposite-sign different-flavor (OS-DF) lepton pairs, see e.g. [167, 271, 273–275].

6.4.2 Squark decay chain

Here we want to investigate NLO corrections to the isolated decay chain eq. (6.1) evaluated in the squark rest frame. In figure 6.4 we show various invariant mass distributions at LO and NLO in the final state leptons and jet(s) for the benchmark scenario SPS1a. As explained in section 6.1, shapes of such distributions are very important for the determination of masses and spins of sparticles. In order to highlight NLO corrections purely in the shapes, here and in section 6.4.3 we show all distributions, both at LO and at NLO, normalized to unity.

Two kinds of combinatorial problems arise in studying invariant mass distributions involving the final state leptons and jet(s). First, from an experimental point of view we cannot distinguish between the near and the far lepton on an event-by-event basis. This is a well known problem and many solutions have been suggested in the literature, see e.g. [167]. Second, it is not obvious which jet to choose to build the desired invariant mass distributions. Considering only the isolated decay chain starting with $\tilde{q}_L$, at LO only the jet from the squark decay is present in the final state. But at higher orders, due to real gluon radiation, further jets can be present. Here we always choose the hardest available jet to build the invariant mass distributions, as done in [155].

In the upper left/right part of figure 6.4 we show (unobservable) distributions in the invariant mass of the hardest jet and the negatively/positively charged near/far lepton from the decay chain $\tilde{u}_L \to j l_n^- l_f^+ \tilde{\chi}_1^0$. Here and in the remainder of this section we do not apply any cuts, but the jet definition cuts in eq. (6.6). In the center left/right part, on the other hand, we show (again unobservable) distributions in the invariant mass of the hardest jet and the negatively/positively charged far/near lepton from the decay chain with the opposite charges for far and near leptons, $\tilde{u}_L \to j l_n^+ l_f^- \tilde{\chi}_1^0$. Finally, in the lower part of figure 6.4 we show, in some sense, the sums of the two previous contributions. These distributions are in principle experimentally observable (after combination with the corresponding production process). The lower left/right panel shows the invariant mass of the hardest jet and the negatively/positively charged lepton summed over near and far contributions (m_{jl^-} and m_{jl^+}).

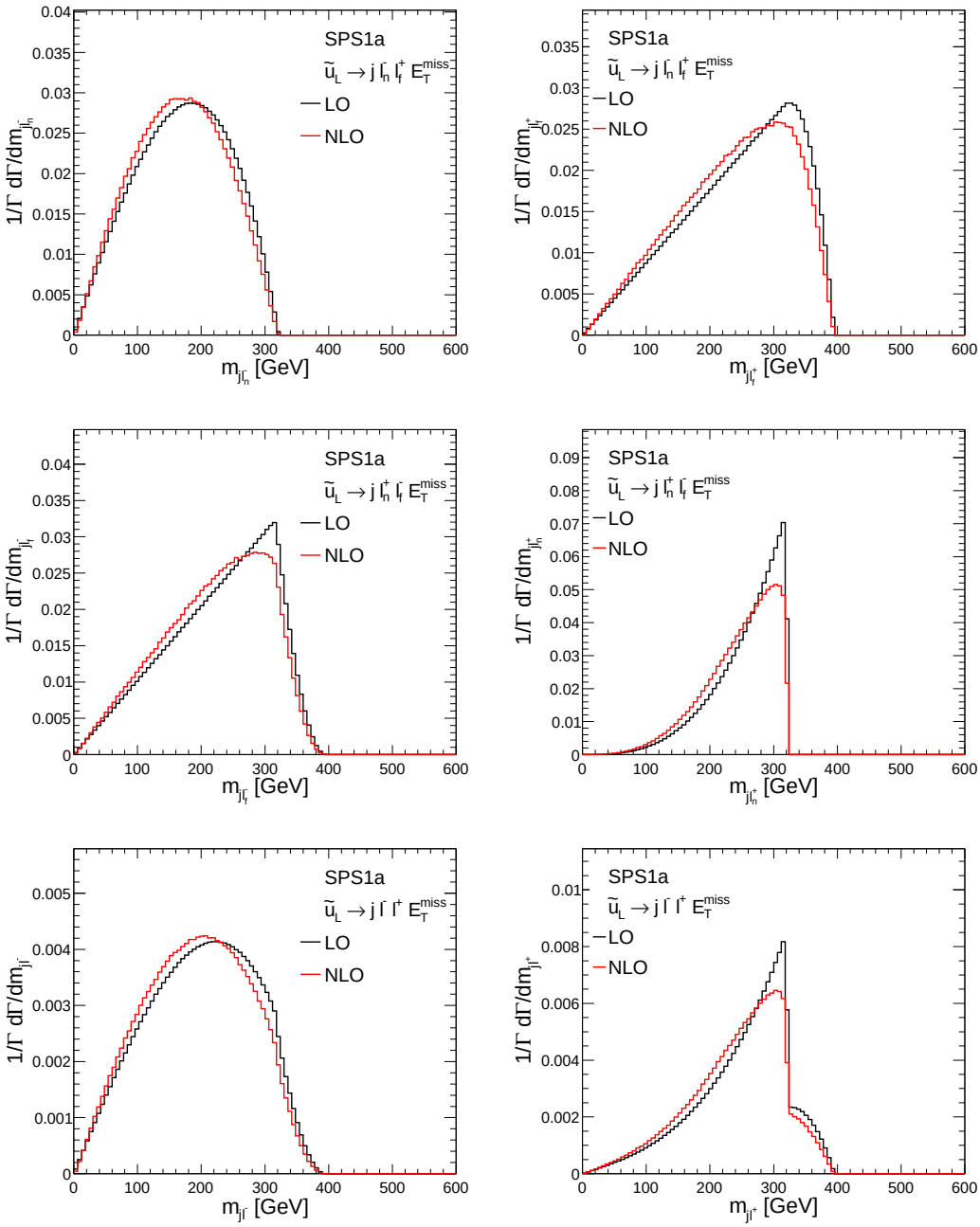

Figure 6.4: Normalized differential distributions for SPS1a in m_{jl_f}, m_{jl_n} for the two unobservable decays $\tilde{u}_L \to j l_n^- l_f^+ \tilde{\chi}_1^0$ (upper two) and $\tilde{u}_L \to j l_n^+ l_f^- \tilde{\chi}_1^0$ (central two) and in m_{jl^+} and m_{jl^-} (lower two) where contributions from the two decays are summed.

In the case of the decay of a left-handed anti-squark, all the distributions introduced so far are equal to the charge-conjugate ones of the corresponding squark, e.g., the $m_{jl_n^+}$ distribution from an $\tilde{u}_L^*$ decay chain is equal to the $m_{jl_n^-}$ distribution from an $\tilde{u}_L$ decay chain. Hence, the analogue of figure 6.4 for $\tilde{q}_L^*$ would present the shapes of the distributions of the left column exchanged with the ones of the right column. These differences between squarks and anti-squarks do not appear for quantities that are inclusive in the different charges of the leptons.

In all of the plots in figure 6.4 NLO corrections tend to shift the distributions to smaller invariant masses, however, locations of endpoints are unaffected. Kinematical edges in the NLO predictions are rounded off compared to LO, still, overall shapes of the considered contributions seem to be unaltered. Results and distributions of the same type, as already stated, have been calculated in [155]. In their numerical evaluation the slightly different parameter point SPS1a' was investigated resulting in LO shapes somewhat different from those presented here. Qualitatively the NLO corrections shown in [155] for SPS1a' and ours for SPS1a agree. Moreover, we also investigated distributions and corrections for SPS1a' and found agreement with [155], though, in reference [155] a different jet algorithm is used. Still, results for SPS1a' presented there for $y_c = 0.002$ agree nicely with our results obtained using the anti-k_T jet clustering algorithm.

In figure 6.5 we look at a different set of invariant mass distributions again for SPS1a: $m_{jl(\text{low})}$, $m_{jl(\text{high})}$, m_{jll} and $m_{jll(\text{thresh})}$. For $m_{jl(\text{low})}$ and $m_{jl(\text{high})}$ we select on an event-by-event basis the smaller and higher invariant mass between one of the leptons and the hardest jet. m_{jll} is the invariant mass between the hardest jet and the two leptons and $m_{jll(\text{thresh})}$ is the same distribution where the additional constraint on the invariant mass of the two leptons $\frac{m_{ll}^{\max}}{\sqrt{2}} < m_{ll}$ is applied. Here, $m_{ll}^{\max}$ is the well measurable endpoint of the dilepton invariant mass distribution, for which in our numerical analysis we use the theoretical endpoints, $m_{ll}^{\max} = 80.0, 203.8$ GeV for SPS1a and 10.1.6 respectively, cf. eq. (B.2) in Appendix B. All these invariant mass distributions are in principle experimentally measurable and have been discussed extensively in the literature [167, 271, 274, 275] (and references therein). From a measurement of their upper (and in case of $m_{jll(\text{thresh})}$ the lower) endpoints one can extract relations for the masses of the intermediate sparticles. These relations often show ambiguities and particularly measurements like the threshold of $m_{jll(\text{thresh})}$ might help to resolve these. Alternatively, shapes of the presented invariant mass distributions might help to overcome these difficulties. Let us now look at the NLO corrections to these invariant mass distributions. Overall, again, distributions are shifted to smaller invariant masses. Also, upper kinks of m_{jll} and $m_{jll(\text{thresh})}$ are rounded off. These shifts might result in a slightly lowered accuracy in the measurement of the upper endpoints. Furthermore, the threshold of the $m_{jll(\text{thresh})}$ is diluted due to NLO corrections, as the theoretical lower endpoint of the $m_{jll(\text{thresh})}$ distribution is given by $m_{jll(\text{thresh})}^{\min} = 215.4$ GeV for SPS1a and $m_{jll(\text{thresh})}^{\min} = 437.1$ GeV for 10.1.6, cf. eq. (B.9) in Appendix B. Thus, a precise measurement of this observable seems to be questionable.

The same set of invariant mass distributions, $m_{jl(\text{low})}$, $m_{jl(\text{high})}$, m_{jll} and $m_{jll(\text{thresh})}$, is shown in figure 6.6 for the parameter point 10.1.6 and the corresponding decay chain involving

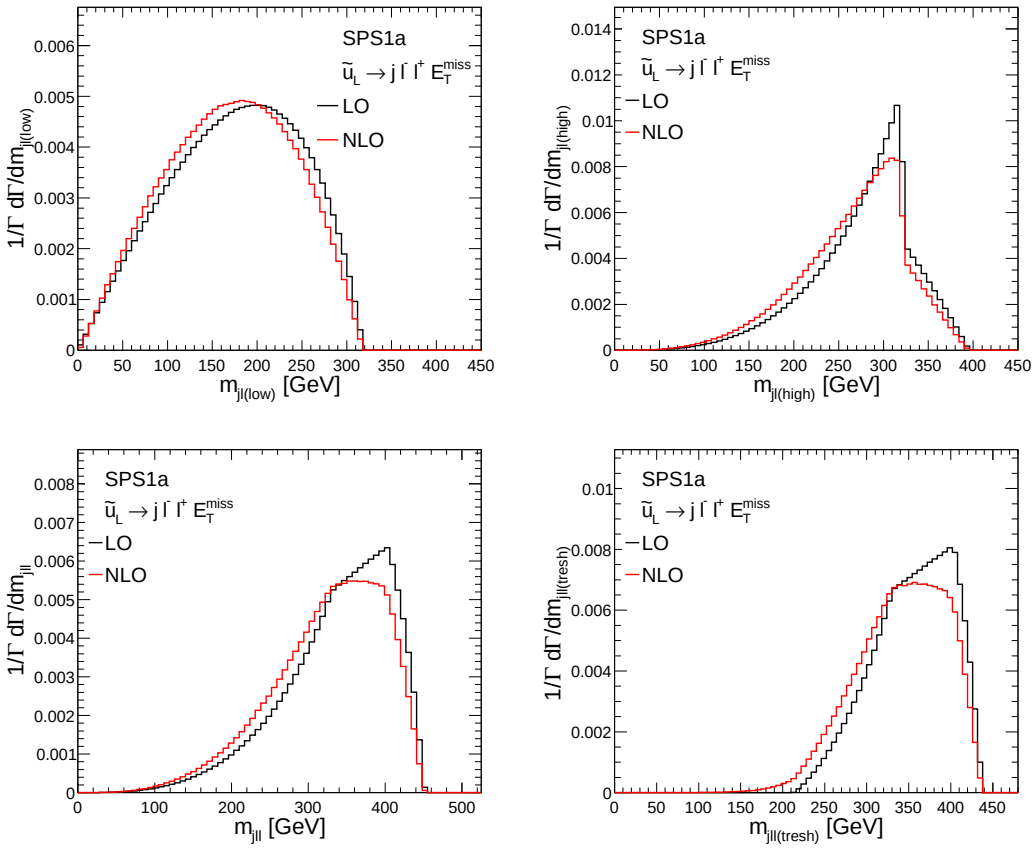

Figure 6.5: LO and NLO normalized differential distributions for SPS1a in $m_{jl(\mathrm{low})}$, $m_{jl(\mathrm{high})}$, m_{jll} and $m_{jll(\mathrm{thresh})}$ (from top left to bottom right) for the decay chain $\tilde{q}_L \to q\ \tilde{\chi}_2^0 \to q\ l^{\pm}\ \tilde{l}_R^{\mp} \to q\ l^{\pm}\ l^{\mp}\ \tilde{\chi}_1^0$.

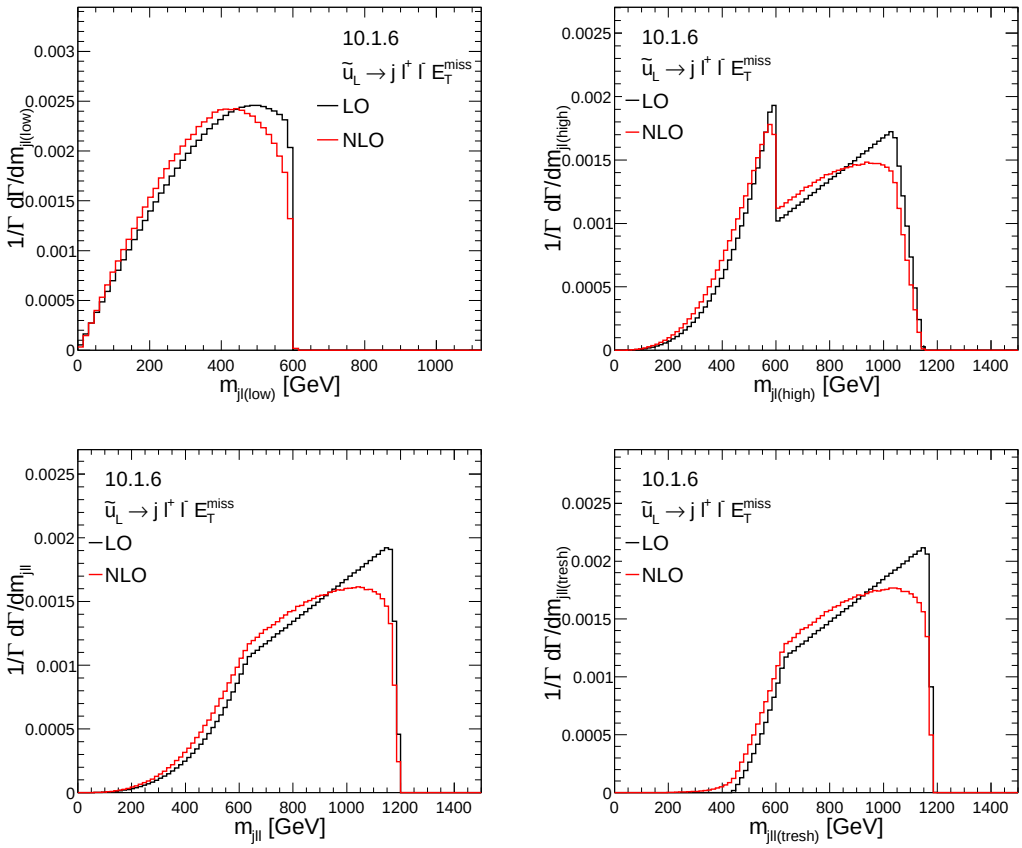

Figure 6.6: LO and NLO normalized differential distributions for 10.1.6 in $m_{jl(\text{low})}$, $m_{jl(\text{high})}$, m_{jll} and $m_{jll(\text{thresh})}$ (from top left to bottom right) for the decay chain $\tilde{q}_L \to q\ \tilde{\chi}_2^0 \to q\ l^{\pm}\ \tilde{l}_L^{\mp} \to q\ l^{\pm}\ l^{\mp}\ \tilde{\chi}_1^0$.

a $\tilde{l}_L$. For the main part, again, NLO corrections shift the differential distributions to smaller invariant masses and round off the upper kinks. Particularly for $m_{jl(\text{low})}$ this might result in a smaller possible experimental accuracy for determining the upper endpoint. Apart from the rounding off of the kinks, general shapes of the distributions are mostly unaltered by NLO corrections. Also, a possible dilution of the lower endpoint of $m_{jll(\text{thresh})}$ due to NLO corrections seems to be less severe for 10.1.6 compared to SPS1a.

6.4.3 Combination of production and decay

Now the combined process, eq. (6.3), should be investigated, where cuts defined in eq. (6.7) have been applied.

As already pointed out, the considered NLO QCD corrections only affect the first step of the decay chain directly. Nevertheless, indirectly these corrections can indeed change the boost of the intermediate $\tilde{\chi}_2^0$ and thus also affect, e.g., the kinematics of the final state leptons. In figure 6.7 we show the p^{T} distribution of the hardest lepton for 10.1.6 at 14 TeV as an example. As before, in the upper panel LO is shown in black, NLO in red and LO rescaled with a flat K-factor in blue; corrections of the NLO compared to the LO rescaled by a flat K-factor are shown in the lower panel. Corrections in the shape of $p_{l_1}^{\text{T}}$ are rather mild – about 5% in the tail of the shown range. Consequently, in the following we want to investigate if this also holds for more complex observables. First, we analyze various differential distributions important for parameter determination. Afterwards, we examine the impact of the corrections on inclusive OS-SF dilepton observables and thus on searches currently performed at the LHC.

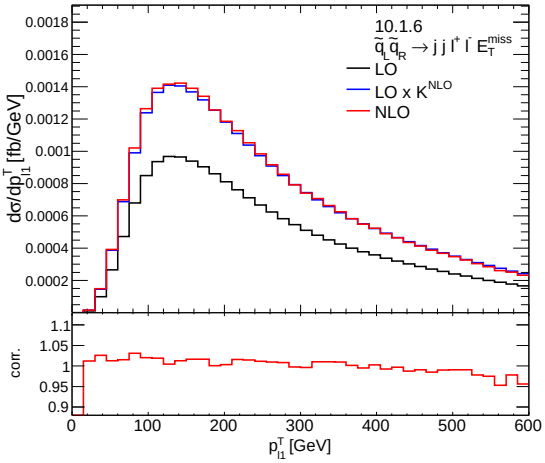

Figure 6.7: Differential distribution in $p_{l_1}^{\text{T}}$ of benchmark point 10.1.6 at a center of mass energy $\sqrt{S} = 14$. In the upper part of the plots we show in black LO, in red NLO and in blue LO distributions rescaled by the ratio K^{NLO} between the integrated NLO and LO results. In the lower part of the plots NLO corrections in the shapes are shown, defined as the full NLO divided by the rescaled LO $\cdot\, K^{\text{NLO}}$ distribution.

Invariant mass distributions

When combining production and decay, already at LO a combinatorial problem arises when looking at invariant mass distributions. As already mentioned in section 6.4.2 it is not clear which jet to choose for building the different invariant masses. Just choosing the hardest jet as was done in section 6.4.2 does not seem to be sensible, since the jet from the second decay, present already at LO, is often the hardest one. This is a well known problem in the application of the endpoint methods for mass determination and various methods have been developed to reduce this ambiguity. The easiest method is to always use the jet which gives, e.g., the smaller m_{jll} value. In this way one improves the measurements of the upper endpoints without losing statistics. However, shapes are heavily distorted already at LO. In principle there are advanced techniques to solve this problem, amongst others, full kinematic event reconstruction [307] or hemisphere techniques [308–310]. However, these techniques are quite involved, parameter point dependent and not generically applicable. Here, we apply consistency cuts, also discussed in [275] to reduce the impact of the jet combinatorics ambiguity. Applying such consistency cuts means that we accept only events where one jet j_i out of the two hardest jets j_i, j_k gives an invariant mass smaller than $m_{jll}^{\max}$ and the other jet j_k an invariant mass larger than $m_{jll}^{\max}$,

$$m_{j_i ll} < m_{jll}^{\max} < m_{j_k ll} \ . \tag{6.8}$$

Now j_i will be used in the following to build the invariant mass distributions. This technique[1] is very efficient in reducing the jet combinatorics ambiguity, however, event rates are also reduced (see section 6.4.3 and particularly table 6.3).

In figure 6.8 we show for SPS1a the same invariant mass distributions as already shown in figure 6.5. Here, production and decays are combined at NLO and cuts of eq. (6.7) and further consistency cuts are applied. Due to the NLO corrections, distributions are in general shifted to smaller invariant masses. Comparing just LO predictions in figure 6.8 and figure 6.5, particularly m_{jll} and $m_{jll(\text{thresh})}$ show a slightly different behavior introduced by the consistency cuts: the plateau is less prominent in figure 6.8. Here, again we observe a dilution of the threshold in the $m_{jll(\text{thresh})}$ distribution at NLO. Similar observations can be made looking at figure 6.9 (and comparing with figure 6.6) for the combined results of parameter point 10.1.6. Overall, changes to the shapes are moderate and, concerning the measurements of the upper endpoints only for $m_{jl(\text{low})}$ an experimentally detectable effect is expected. Here we want to note one thing: the consistency cuts, eq. (6.8), are based only on m_{jll} and this is why, already at LO, we observe contributions also beyond the theoretical upper endpoint. This effect is enhanced at NLO.

From the discussion above, usefulness of the threshold of $m_{jll(\text{thresh})}$ seems questionable. Additionally, a measurement of a lower endpoint is always subject to large experimental backgrounds [277, 282]. As this threshold was introduced to solve ambiguities in the mass determination due to the near-far indistinguishability, new techniques for this purpose have

[1] From an experimental point of view the endpoint $m_{jll}^{\max}$ is assumed to be measured in a first step where for example always the jet yielding the smaller $m_{jll}$is chosen. Here, we use the theoretical endpoints, eq. (B.5), $m_{jll}^{\max} = 450.6, 1147.7$ GeV for SPS1a and 10.1.6 respectively.

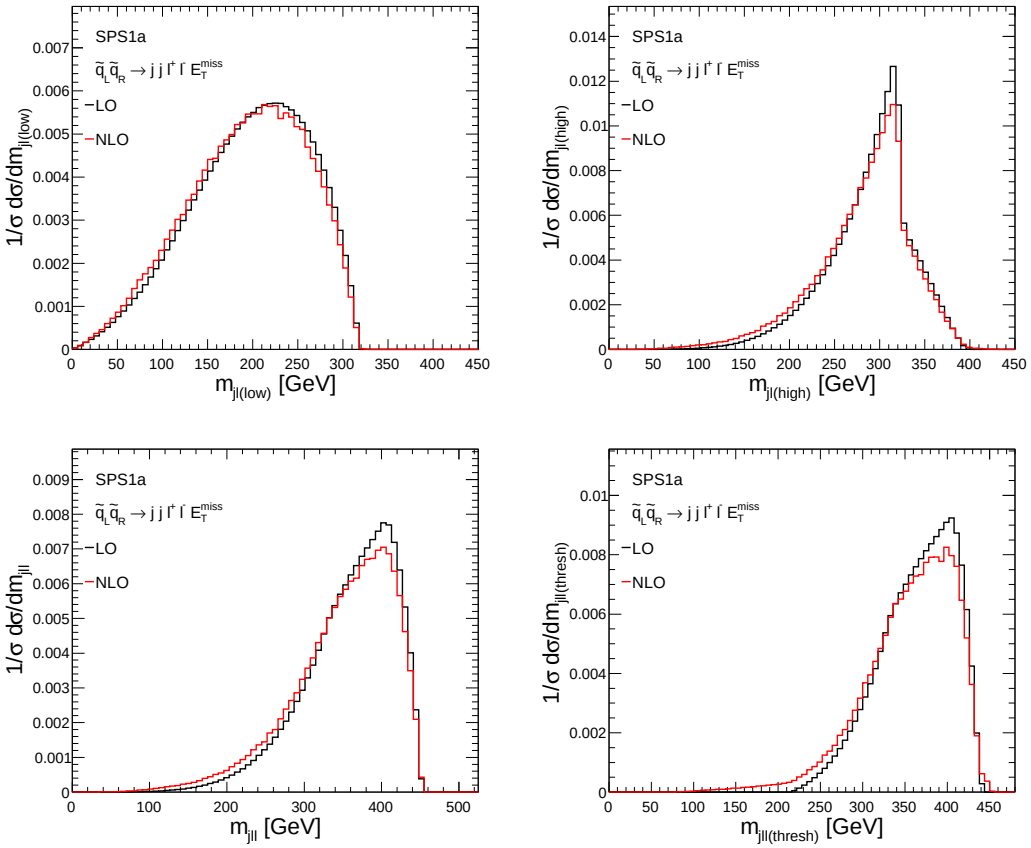

Figure 6.8: LO and NLO normalized differential distributions for SPS1a in $m_{jl(\mathrm{low})}$, $m_{jl(\mathrm{high})}$, m_{jll} and $m_{jll(\mathrm{thresh})}$ (from top left to bottom right) for combined production and decay.

been invented. In [282] the authors argue that all invariant mass distributions used for mass determination from the given decay chain should be build symmetrically under the interchange $l^{\mathrm{near}} \leftrightarrow l^{\mathrm{far}}$. In this spirit they introduce a new set of invariant mass distributions,

$$m^2_{jl(u)} \equiv m^2_{jl_n} \cup m^2_{jl_f}\,, \tag{6.9}$$

$$m^2_{jl(d)} \equiv |m^2_{jl_n} - m^2_{jl_f}|\,, \tag{6.10}$$

$$m^2_{jl(s)} \equiv m^2_{jl_n} + m^2_{jl_f} \text{ and} \tag{6.11}$$

$$m^2_{jl(p)} \equiv m_{jl_n} \cdot m_{jl_f}\,, \tag{6.12}$$

where the distribution $m^2_{jl(u)}$ is build simply adding the distributions in $m^2_{jl_n}$ and $m^2_{jl_n}$. In figure 6.10 we show the normalized LO and NLO distributions in $m^2_{jl(u)}, m^2_{jl(d)}, m^2_{jl(s)}$ and $m^2_{jl(p)}$ against a quadratic scale. Shapes of these distributions are slightly changed due to NLO corrections, however, the possibility of measuring their upper endpoints (both endpoints in the case of $m_{jl(\mathrm{u})}$) seems to be unaffected.

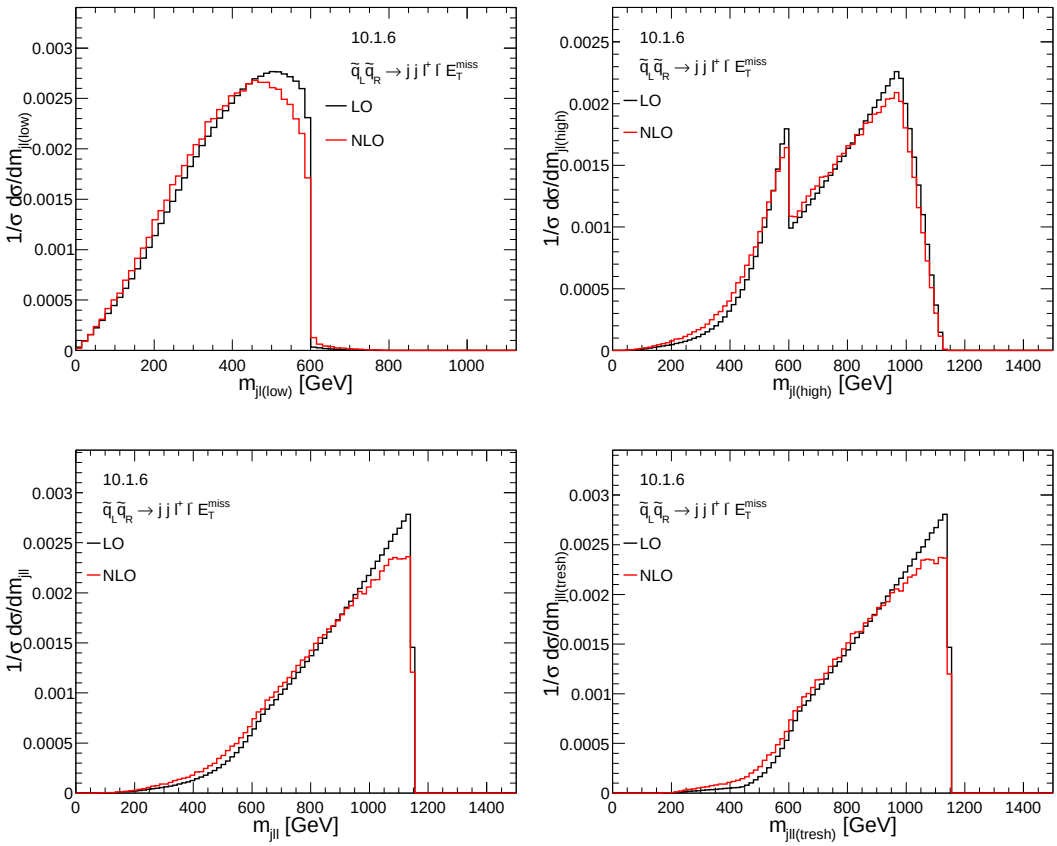

Figure 6.9: LO and NLO normalized differential distributions for 10.1.6 in $m_{jl(\text{low})}$, $m_{jl(\text{high})}$, m_{jll} and $m_{jll(\text{thresh})}$ (from top left to bottom right) for combined production and decay.

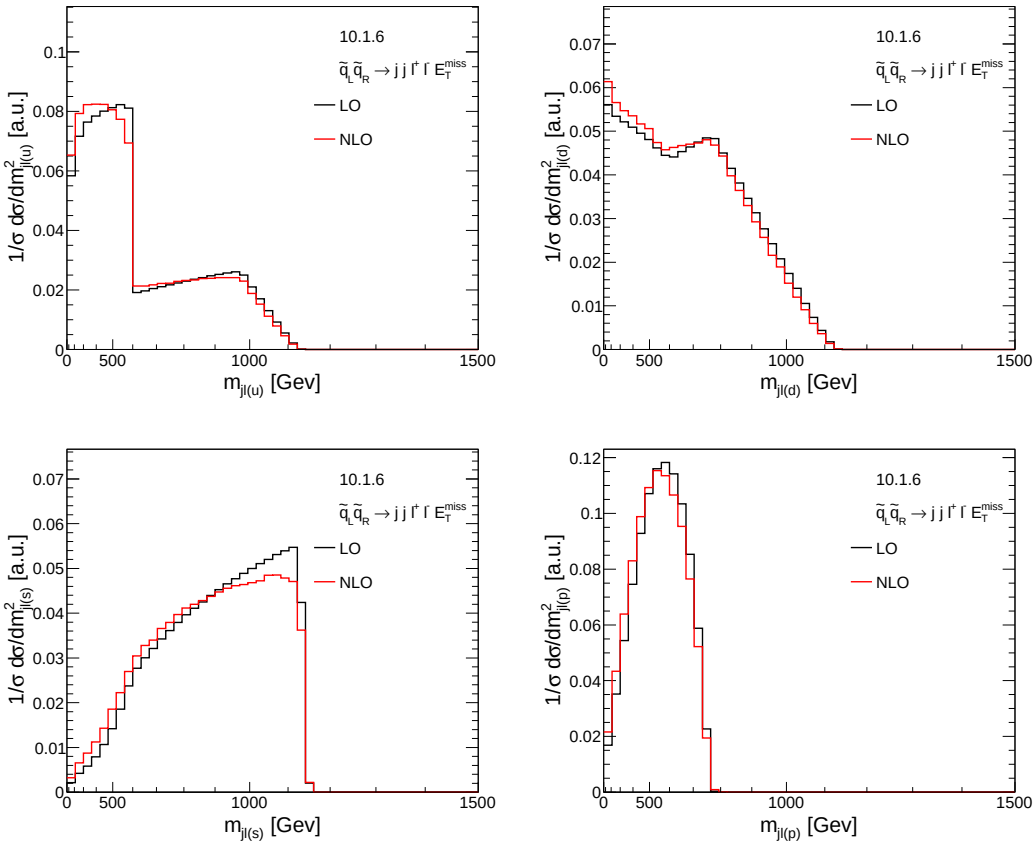

Figure 6.10: LO and NLO normalized differential distributions for 10.1.6 in $m_{jl(\mathrm{u})}$, $m_{jl(\mathrm{d})}$, $m_{jl(\mathrm{s})}$ and $m_{jl(\mathrm{p})}$ (from top left to bottom right) for combined production and decay shown with a quadratic scale.

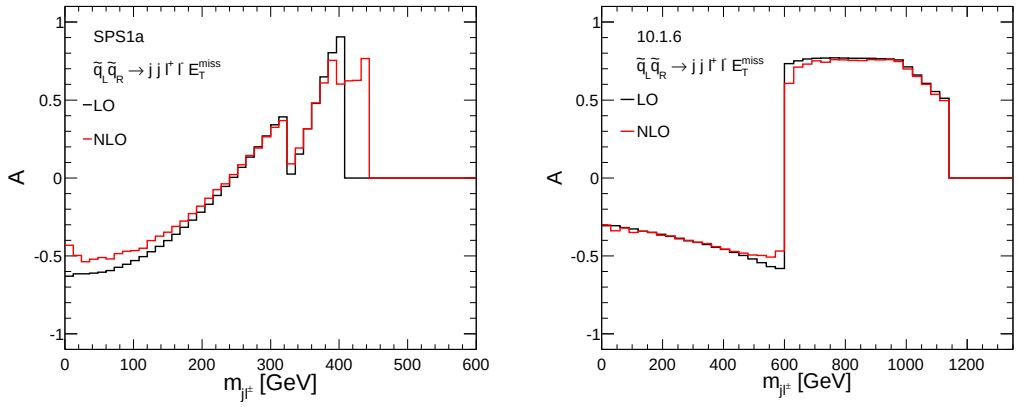

Figure 6.11: LO and NLO normalized differential distributions for SPS1a (top) and 10.1.6 (bottom) in the asymmetry A for combined production and decay.

Besides for mass determination, the given decay chain can also be used for spin determination or, more precisely, for spin distinction. As pointed out in [291] and many subsequent works, the asymmetry between the m_{jl^+} and m_{jl^-} distributions defined as

$$A = \frac{d\sigma/dm_{jl^+} - d\sigma/dm_{jl^-}}{d\sigma/dm_{jl^+} + d\sigma/dm_{jl^-}} \tag{6.13}$$

can help to discriminate between a SUSY model and other models like Universal Extra Dimensions (UED) with a similar decay chain where the intermediate particles have different spins [292]. In figure 6.11 we show LO and NLO predictions for this asymmetry for SPS1a (left) and 10.1.6. Again, cuts of eq. (6.7) and consistency cuts have been applied. The potential for spin determination and/or model discrimination seems to be unaltered by NLO QCD corrections. For SPS1a at NLO there is a contribution beyond the upper endpoint not present for this observable at LO. This NLO contribution passes the consistency cuts which are based on the endpoint of the m_{jll} distribution. However, expected event rates in this region of the asymmetry distribution are experimentally negligible.

Inclusive observables

The experimental signature of two jets, two OS-SF leptons and missing energy can, besides for parameter determination, also be used for searches for supersymmetry. At the LHC, using this signature, cut-and-count searches have been performed in the analyses of the 7 and 8 TeVruns [305, 306] and will be performed also at 14 TeV. Consequently, precise calculations of inclusive cross sections for the specific signal region used in the cut-and-count searches are necessary for reliable interpretations and derived limits.

First, we discuss the differences between predictions in our approximation and rescaling LO with a flat K-factor from NLO corrections to squark-squark production without including decays and cuts. Second, we look at the impact of the additional consistency cuts defined in eq. (6.8).

	$N^{(0)}_{2j+2l+\not{E}_T}$	$N^{(0),\text{cons. cuts}}_{2j+2l+\not{E}_T}$	$K_{N_{2j+2l+\not{E}_T}}$	$K^{\text{cons. cuts}}_{N_{2j+2l+\not{E}_T}}$	$K_{pp\to\tilde{q}_L\tilde{q}'_R}$	$K_{pp\to\tilde{q}\tilde{q}'}$
SPS1a	38.2 fb	23.0 fb	1.36	1.23	1.34	1.28
10.1.6	0.628 fb	0.243 fb	1.46	1.39	1.44	1.41

Table 6.3: LO $N^{(0)}$ and NLO $N^{(0+1)}$ cross section predictions and K-factors K_N for the two benchmark scenarios SPS1a, 10.1.6 at a center of mass energy $\sqrt{S} = 14$ TeV where the cuts of eq. (6.7) are applied. For comparison we also list the inclusive NLO production K-factor $K_{pp\to\tilde{q}\tilde{q}'}$ and $K_{pp\to\tilde{q}_L\tilde{q}'_R}$.

In table 6.3 various integrated quantities at 14 TeV for the parameter points SPS1a and 10.1.6 are listed. Starting from the first column on the left we display: the total cross section at LO $N^{(0)}_{2j+2l+\not{E}_T}$ in the signal region defined by the cuts of eq. (6.7), the total cross section at LO after consistency cuts $N^{(0),\text{cons. cuts}}_{2j+2l+\not{E}_T}$, together with the corresponding K-factors $K_{N_{2j+2l+\not{E}_T}}$ and $K^{\text{cons. cuts}}_{N_{2j+2l+\not{E}_T}}$. Furthermore, we list the K-factors for the production only including all $\tilde{q}_L\tilde{q}'_R$ channels $K_{pp\to\tilde{q}_L\tilde{q}'_R}$ and including also all other chirality configurations $K_{pp\to\tilde{q}\tilde{q}'}$.

The difference between the K-factors including the cuts defining the signal region, $K_{N_{2j+2l+\not{E}_T}}$, and the K-factors for production of $\tilde{q}_L\tilde{q}_R$ pairs, $K_{pp\to\tilde{q}_L\tilde{q}_R}$, is small, namely 2%. This difference increases to 8% for SPS1a and 5% for 10.1.6 if the K-factor for just the production includes also the other chirality configurations, $K_{pp\to\tilde{q}\tilde{q}'}$. Thus, for the scenarios analyzed here, NLO corrections can be safely approximated rescaling LO predictions with the K-factor obtained for the production part, provided that only the contributing chirality configurations are included in the calculation of the K-factor. This feature, however, cannot easily be generalized; for example, as can be seen from table 6.3, applying consistency cuts increases the differences between these two approximations.

Consistency cuts are designed for the study of distributions relevant for parameter determination, as the ones discussed in the previous section. However, they decrease the cross sections, as can be seen comparing $N^{(0)}_{2j+2l+\not{E}_T}$ and $N^{(0),\text{cons. cuts}}_{2j+2l+\not{E}_T}$, without adding any obvious benefit in the context of searches. On the other hand, so far, we did not discuss the different normalization of the LO and NLO distributions shown in the previous sections. The values of $K^{\text{cons. cuts}}_{N_{2j+2l+\not{E}_T}}$ are exactly the ratios between the normalization of the LO and NLO results. These values are smaller than the K-factors obtained without consistency cuts. As discussed, such cuts are introduced to solve the jet combinatorial problem. Doing so, they also reduce (positive) contributions from real radiation of a gluon or a quark at NLO and consequently reduce the resulting K-factors. Thus, in contrast to the case without consistency cuts applied, fully differential factorizable corrections have to be taken into account for a precise estimation of NLO effects.

Part III

Direct stau production

Chapter 7

Direct production of staus

In this chapter we present a calculation for direct $\tilde{\tau}_1$-pair production cross sections and kinematical distributions at hadron colliders. Our calculations include Drell–Yan (DY) processes, b-quark annihilation, and gluon fusion, with all third generation mixing effects taken into account. The obtained cross sections are independent of the lifetime of the produced stau. Still, in chapter 8 we interpret our findings with a special focus on scenarios with long-lived staus.

First, in section 7.1 we want to review the motivation for studying direct stau production. Interesting parameter regions are highlighted and relevant constraints are discussed. Collider limits for direct stau production were already discussed in section 3.4.1. Second, section 7.2 presents our calculation of direct stau production at hadron colliders. Here we show our cross section results for the Tevatron and the LHC and compare the Drell–Yan contributions to those from $b\bar{b}$-annihilation and gluon fusion. Results and the discussion of direct stau production presented here and in the following chapter are largely based on refs. [1] and [2].

7.1 Motivation

There are well-motivated scenarios in which the lighter stau $\tilde{\tau}_1$ is central, both, for cosmology and collider phenomenology. In fact, in large regions of the parameter space of many SUSY breaking models, the lighter stau $\tilde{\tau}_1$ is very light due to large Yukawa contributions in its RGE running from the GUT scale down to the EW scale. It is even often the lightest SUSY particle in the MSSM spectrum, to which we refer as the *lightest ordinary SUSY particle* (LOSP). The phenomenology, both, for colliders and for cosmology depends crucially on the nature of the LSP and the resulting lifetime of the stau. In the following we first elaborate on the case of a $\tilde{\tau}_1$-LOSP and EWIP LSP. Second, the $\tilde{\chi}_1^0$ LSP and $\tilde{\tau}_1$ NLSP case is considered.

While restrictive upper limits exist on the abundance of a stable charged massive particle (CHAMP) [39], the $\tilde{\tau}_1$ LOSP becomes a viable possibility in scenarios in which the LSP is an EWIP, such as the gravitino or the axino, see section 3.7.2 (or in scenarios with broken

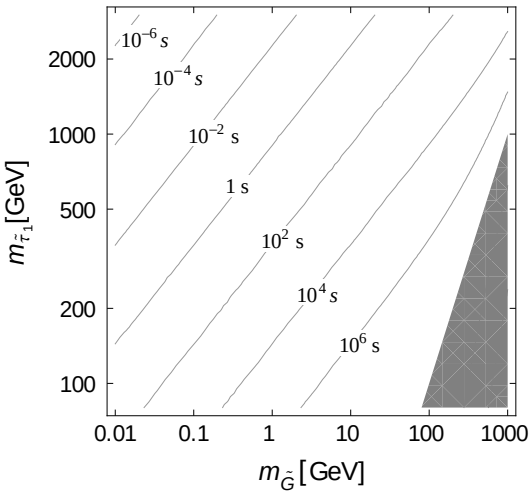

Figure 7.1: Iso-lifetime contours of a $\tilde{\tau}_1$ from the decay $\tilde{\tau}_1 \to \widetilde{G}\tau$ as a function of the stau mass $m_{\tilde{\tau}_1}$ and the gravitino mass $m_{\widetilde{G}}$. In the gray area in the bottom right the $\tilde{\tau}_1$ is the LSP.

R-parity). For example in the gravitino LSP case, the lifetime of the stau is given by [311]

$$\tau_{\tilde{\tau}_1} = \Gamma^{-1}(\tilde{\tau}_1 \to \widetilde{G}\tau) = \frac{48\pi m_{\widetilde{G}}^2 M_{\text{Planck}}^2}{m_{\tilde{\tau}_1}^5} \left(1 - \frac{m_{\widetilde{G}}^2}{m_{\tilde{\tau}_1}^2}\right)^{-4} , \tag{7.1}$$

and shown in figure 7.1 as a function of the stau mass $m_{\tilde{\tau}_1}$ and the gravitino mass $m_{\widetilde{G}}$. Due to a suppression by the reduced Planck mass $M_{\text{Planck}} = 2.4\ 10^{181}$ this lifetime is generally large on the scale of detector experiments and can even easily exceed $\tau_{\tilde{\tau}_1} > 10^4\ s$ relevant for BBN constraints as discussed below. Consequently, the $\tilde{\tau}_1$ LOSP appears long-lived in the collider detectors as a quasi-stable muon-like particle. Such scenarios will come with distinctive signatures that are very different from those in the $\tilde{\chi}_1^0$ LSP case [312–322]. In fact, direct $\tilde{\tau}_1$-pair production events will be easier to identify experimentally if the $\tilde{\tau}_1$ is quasi-stable. It may even be possible to stop initially slow staus within the main detectors [221, 323–325] or in some additional dedicated stopping detectors [312, 326–328] for analyses of their late decays.

The cosmological implications of a long-lived $\tilde{\tau}_1$ depend on its lifetime $\tau_{\tilde{\tau}_1}$, its mass $m_{\tilde{\tau}_1}$, and its primordial relic abundance prior to decay

$$Y_{\tilde{\tau}_1} \equiv n_{\tilde{\tau}_1}/s\,, \tag{7.2}$$

where $n_{\tilde{\tau}_1}$ is its comoving number density prior to decay and s the entropy density. For example, in the R-parity conserving case with an EWIP LSP, each $\tilde{\tau}_1$ NLSP decays into one LSP which contributes to the DM density Ω_{DM}. Moreover, $\tau_{\tilde{\tau}_1}$ can exceed 1–100 s in scenarios with a gravitino or axino LSP, as discussed above. Hence, as explained in section 3.7.2, the stau might decay during or after BBN, releasing dangerous amounts of electromagnetic or colored

[1] In case of an axino LSP the decay of a stau is similarly suppressed by the PQ breaking scale f_a [221, 228, 229].

energy. Negatively charged $\tilde{\tau}_1$'s may even form bound states with the primordial nuclei leading to catalyzed BBN (CBBN) of lithium-6 and beryllium-9 [329–334]. The DM abundance and the observationally inferred primordial abundances of the light elements thereby impose $\tau_{\tilde{\tau}_1}$-dependent upper limits on the yield $Y_{\tilde{\tau}_1}$ which translate into cosmological constraints on the parameter space of the respective SUSY models; cf. [221, 226, 235, 330, 332, 334–339] and references therein.

The cosmological constraints on scenarios with long-loved staus $\tilde{\tau}_{\heartsuit}$ are often quite restrictive with potentially severe implications for collider phenomenology and cosmology. For example, the CBBN constraints on gravitino LSP scenarios can point to heavy colored sparticles, such as a gluino with mass $m_{\tilde{g}} \gtrsim 2.5$ TeV [226, 330, 332, 337], so that direct stau production would be particularly important for SUSY discoveries at the LHC. Moreover, together with $\Omega_{\rm DM}$ limiting the thermally produced EWIP density [223–227, 230, 231] from above, the CBBN constraints can restrict the post-inflationary reheating temperature to $T_{\rm R} \ll 10^9$ GeV [226, 339], which disfavors the viability of thermal leptogenesis with hierarchical heavy Majorana neutrino masses [340–344]. In light of those findings, it is remarkable that parameter regions exist in which one finds an exceptionally small relic $\tilde{\tau}_1$ abundance [345, 346] which may respect the (C)BBN limits on $Y_{\tilde{\tau}_1}$ so that the above restrictions do no longer apply. Details of such exceptional yields and resulting favored parameter regions are discussed in section 7.1.2. In this work we address the question whether such a scenario with efficient primordial stau annihilation can be identified by considering direct $\tilde{\tau}_1$-pair production at hadron colliders.

Before proceeding, let us comment briefly on direct stau production events in the neutralino dark matter case. While the $\tilde{\tau}_1$ with its electric charge cannot be DM, it can be the next-to-lightest SUSY particle (NLSP) in an R-parity conserving realization of SUSY. If the lightest neutralino $\tilde{\chi}_1^0$ is the LSP, a stau NLSP, that is almost as light as the $\tilde{\chi}_1^0$, can participate via coannihilation in the primordial freeze-out of the $\tilde{\chi}_1^0$. In fact, such a coannihilation scenario might be the key for an agreement of the relic $\tilde{\chi}_1^0$ density $\Omega_{\tilde{\chi}_1^0}$ with the DM density $\Omega_{\rm DM}$; cf. [63, 64, 347–350] and references therein. The direct pair production of such light $\tilde{\tau}_1$'s can then have a sizeable cross section at hadron colliders even if the colored sparticles are substantially more massive, as indicated by recent searches at the LHC.

In an R-parity conserving realization of SUSY, each of those produced $\tilde{\tau}_1$'s will decay rapidly into a $\tilde{\chi}_1^0$ and a tau. Thus, an excess in missing transverse energy together with leptons and/or reconstructed tau jets is the expected signature of such a scenario. However, for small mass splittings between $\tilde{\tau}_1$ and $\tilde{\chi}_1^0$, as required in coannihilation scenarios, the decay products might be soft and thus experimentally challenging to detect. Leaving such studies for further work, we focus in the following more on scenarios with a long-lived $\tilde{\tau}_1$ LOSP. Nevertheless, our calculations of direct stau production cross sections apply also to $\tilde{\chi}_1^0$ dark matter scenarios.

In the following we explain the possibility of particularly efficient primordial stau annihilation processes leading to an exceptionally small thermal relic stau abundance such that restrictive cosmological constraints can be evaded. Subsequently, a second motivation is given: a light stau with large $\tilde{\tau}_1 \tilde{\tau}_1^* h^0$ couplings can lead to an enhancement in the branching ratio $BR(h^0 \to \gamma\gamma)$ [351, 352] together with enhanced direct stau production cross sections. We

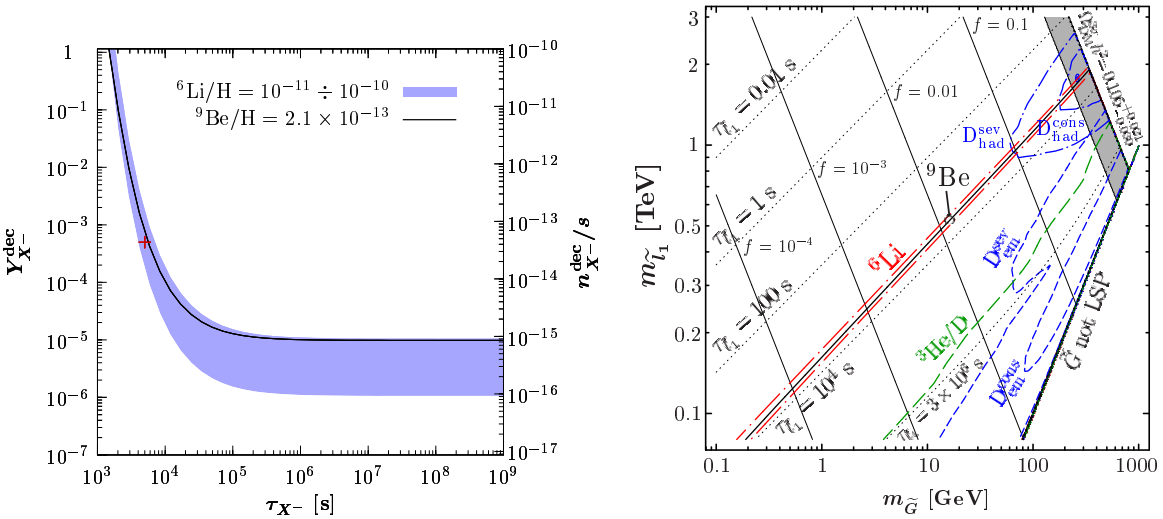

Figure 7.2: Left: contour plot of CBBN abundance yields of ^{6}Li and ^{9}Be as a function of $\tau_{X^-} = \tau_{\tilde{\tau}_1}$. The y-axis on the right-hand side indicates the yield $Y_{\tilde{\tau}_1}$. Right: cosmological constraints on $m_{\widetilde{G}}$ and $m_{\tilde{l}_1} = m_{\tilde{\tau}_1}$ for a yield $Y_{\tilde{\tau}_1}$ given by eq. (7.3). Due to CBBN, the region below the (red) solid and the long-dash-dotted lines is disfavored by observationally inferred abundances of ^{9}Be and ^{6}Li, respectively. Both plots taken from: [334].

summarize the conditions required for such behaviors and emphasize that the potential occurrence of a (color and) charge breaking (CCB) vacuum, besides general limits from flavor observables, as discussed in 3.6, can give restrictions in the relevant parameter regions.

7.1.1 Cosmological constraints

Let us now turn to long-lived staus in the early Universe, the potential cosmological implications and associated constraints. The relic stau abundance $Y_{\tilde{\tau}_1}$ prior to decay depends on $m_{\tilde{\tau}_1}$, the left-right mixing of the $\tilde{\tau}_1$ and other details of the SUSY model, and on the early thermal history of the Universe. For a standard thermal history with a reheating temperature $T_{\rm R}$ that exceeds $m_{\tilde{\tau}_1}/20$, there was a period in which the $\tilde{\tau}_1$ LOSP was in thermal equilibrium with the primordial plasma. At the freeze-out temperature $T_{\rm f} \lesssim m_{\tilde{\tau}_1}/20$, at which the $\tilde{\tau}_1$ annihilation rate equals the Hubble rate, the by then non-relativistic staus $\tilde{\tau}_1$'s decouple from the thermal plasma. Taking into account all possible (co-)annihilation channels, the associated Boltzmann equation can be solved numerically [353, 354]. For a dominantly right-handed stau, $\tilde{\tau}_1 \simeq \tilde{\tau}_{\rm R}$, the annihilation is dominated by the electroweak processes illustrated in figure 7.3(a). The resulting yield is found to be governed mainly by $m_{\tilde{\tau}_1}$,

$$Y_{\tilde{\tau}_1} \simeq (0.4 - 2.0) \times 10^{-13} \left(\frac{m_{\tilde{\tau}_1}}{100 \text{ GeV}} \right), \tag{7.3}$$

where larger values of the prefactor account for possible mass degeneracies and associated effects such as stau-slepton and/or stau-neutralino coannihilation [226, 355–357].

Confronting the yield (7.3) with the CBBN constraints, shown in figure 7.2(left), the

following upper limit on the stau lifetime emerges [329, 334]

$$\tau_{\tilde{\tau}_1} \lesssim 5 \times 10^3 \text{ s} . \tag{7.4}$$

For the cases with the gravitino LSP and the axino LSP, this implies $m_{\tilde{\tau}_1}$-dependent upper limits on the gravitino mass $m_{\widetilde{G}}$ [334] , as shown in figure 7.2(right), and the PQ scale f_a (cf. figure 5 in ref. [358]), respectively. In particular, a Peccei–Quinn scale $f_{\rm PQ}$ around the scale of grand unification $\Lambda_{\rm GUT}$ is in conflict with the CBBN constraint for the $m_{\tilde{\tau}_1}$ range accessible at the LHC [358]. Moreover, these CBBN limits on $m_{\widetilde{G}}$ and $f_{\rm PQ}$ tighten also the upper limits on the reheating temperature $T_{\rm R}$ imposed by $\Omega_{\rm EWIP} \leq \Omega_{\rm DM}$, as discussed in section 3.7.2. Furthermore, they disfavor the kinematical $m_{\widetilde{G}}$ determination [335] and thereby both the mentioned $\Lambda_{\rm Planck}$ determination [311] and the probing of $T_{\rm R}$ at colliders [225]. The resulting $T_{\rm R}$ limits can then be in considerable tension with $T_{\rm R} \gtrsim 10^9$ GeV required for viable thermal leptogenesis with hierarchical heavy Majorana neutrino masses [340–344].

For CMSSM scenarios with a gravitino LSP, as introduced in section 3.7.2, the CBBN constraints have been found to be particularly restrictive [226, 330, 332, 336, 337]. Here, the $\tilde{\tau}_1$ LOSP case occurs in a large region of the parameter space and in particular for $m_0^2 \ll m_{1/2}^2$. The CBBN constraint (7.4) – which emerges for $Y_{\tilde{\tau}_1}$ given by (7.3) – can then be translated into the following $m_{\widetilde{G}}$-dependent limits [332, 337]:

$$m_{1/2} \;\geq\; 0.9 \text{ TeV} \left(\frac{m_{\widetilde{G}}}{10 \text{ GeV}}\right)^{2/5} , \tag{7.5}$$

$$T_{\rm R} \;\leq\; 4.9 \times 10^7 \text{ GeV} \left(\frac{m_{\widetilde{G}}}{10 \text{ GeV}}\right)^{1/5} , \tag{7.6}$$

where the latter accounts also for $\Omega_{\widetilde{G}} \leq \Omega_{\rm DM}$. For $m_{\widetilde{G}}$ at the GeV scale, the lower limit (7.5) then implies heavy colored sparticles that will be difficult to probe at the LHC. As already mentioned above, this provides additional motivation for this work since a SUSY discovery could still be possible via direct stau pair production.

7.1.2 Exceptionally small thermal relic stau abundances

The $T_{\rm R}$ limit (7.6) illustrates the mentioned tension with thermal leptogenesis being a viable explanation of the baryon asymmetry in the Universe.[2] In fact, this tension has motivated studies of scenarios with non-standard thermal history in which $Y_{\tilde{\tau}_1}$ is diluted by significant entropy production after decoupling and before BBN [226, 331, 359] and scenarios with R-parity violation [71] such that (7.4) is respected. Nevertheless, even with a standard thermal history and R-parity conservation, there is a way to evade the CBBN constraints[3]: efficient stau annihilation mechanisms which allow exceptionally small yields

$$Y_{\tilde{\tau}_1} \lesssim 2 \times 10^{-15} . \tag{7.7}$$

[2] In scenarios that are less constrained than the CMSSM, the $T_{\rm R}$ limit will be more relaxed if the ratio of the masses $m_{\tilde{g}}$ and $m_{\tilde{\tau}_1}$ is smaller than $m_{\tilde{g}}/m_{\tilde{\tau}_1} > 6$ encountered in the $\tilde{\tau}_1$ LOSP region of the CMSSM [335].

[3] There are other cosmological constraints on $Y_{\tilde{\tau}_1}$ in addition to the considered CBBN constraints. The $Y_{\tilde{\tau}_1}$ limits imposed by these other constraints are typically at most equally restrictive and are usually evaded also for $Y_{\tilde{\tau}_1}$ satisfying (7.7); cf. section 1 in ref. [346].

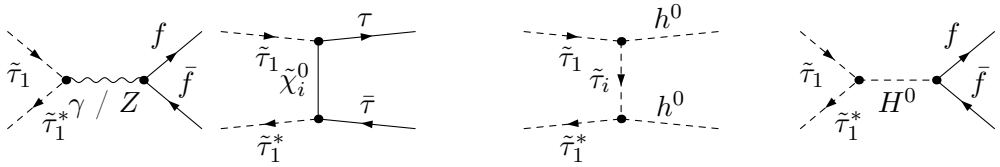

(a) (b) (c)

Figure 7.3: Illustrative Feynman diagrams for stau annihilation dominated by (a) EW processes, (b) large $\tilde{\tau}_1\tilde{\tau}_1^* h^0$ couplings and (c) a H^0 resonance.

For such a yield, the $\tau_{\tilde{\tau}_1}$ limit (7.4) is no longer applicable and the larger values of $m_{\widetilde{G}}$ or $f_{\rm PQ}$ are not disfavored. In this way $T_{\rm R} \gtrsim 10^9$ GeV and standard thermal leptogenesis may be viable. For the $\widetilde{G}$ LSP case, also the region $0.1 m_{\tilde{\tau}_1} \lesssim m_{\widetilde{G}} < m_{\tilde{\tau}_1}$, in which the kinematical $m_{\widetilde{G}}$ determination [311] is expected to be viable, is no longer disfavored.

Such efficient stau annihilation mechanisms require

- enhanced $\tilde{\tau}_1\tilde{\tau}_1^* h^0$ couplings [345, 346], where diagrams like the one shown in figure 7.3(b) contribute dominantly,
- and/or the pattern $2m_{\tilde{\tau}_1} \simeq m_{H^0}$ [346], where the staus annihilate via a heavy Higgs resonance, as illustrated in figure 7.3(c).

In light of these appealing features, let us discuss the conditions that lead to enhanced stau-Higgs couplings. As shown in detail in section 2.3.2, the stau-stau-Higgs couplings are governed by $\tan\beta$, μ, and the trilinear coupling A_τ. These parameters determine also the admixture of the left-handed and right-handed gauge eigenstates, $\tilde{\tau}_{\rm L}$ and $\tilde{\tau}_{\rm R}$, in the lighter stau mass eigenstate

$$\tilde{\tau}_1 = \cos\theta_\tau \tilde{\tau}_{\rm L} + \sin\theta_\tau \tilde{\tau}_{\rm R} \ . \tag{7.8}$$

Thereby, there is a relation between the size of the stau-Higgs couplings and the stau mixing angle θ_τ. This becomes more explicit in the decoupling limit [360] in which the light CP-even Higgs boson h^0 is much lighter than H^0 and the CP-odd Higgs boson A^0. As given in eq. (2.76), the $\tilde{\tau}_1\tilde{\tau}_1 h^0$ coupling is proportional to $\sin 2\theta_\tau$ and the off-diagonal term in the stau-mass squared matrix, $X_\tau = A_\tau - \mu\tan\beta$, while, as given in eq. (2.77) the $\tilde{\tau}_1\tilde{\tau}_1 H^0$ coupling is proportional to $(A_\tau \tan\beta + \mu)\sin 2\theta_\tau$. Thus, the absolute value of these couplings becomes maximal for $\theta_\tau \to \pi/4$, which corresponds to maximal left-right mixing in (7.8), and sizeable for large $\tan\beta$ and large absolute values of μ and/or A_τ. In the corresponding parameter regions, on which we focus in this work, one then finds enhanced stau-Higgs couplings and the mentioned efficient stau annihilation that can lead to (7.7).

Here, we investigate whether it can be possible to find manifestations of an exceptionally small yield (7.7) when studying the direct production of quasi-stable staus in current collider experiments. As we will see in the next sections, for this purpose it is crucial to consider not only the Drell–Yan process but to also include the additional channels from $b\bar{b}$ annihilation and gg fusion in the cross section calculation.

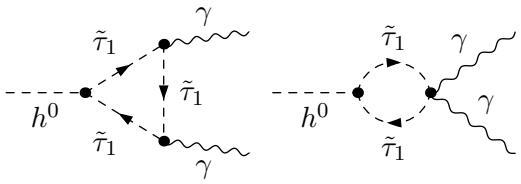

Figure 7.4: Illustrative Feynman diagrams for the decay $h^0 \to \gamma\gamma$ mediated by a stau loop.

7.1.3 Possible enhancement in BR(h $\to \gamma\gamma$)

Without direct hints for new particles, deviations from SM predictions in sensitive observables could be an indirect hint for new physics at the TeV scale. A prime example is the possibility to measure and test the Higgs boson rates in the different production and decay channels at the LHC. Given enough data, in such a way the Higgs boson couplings can eventually be measured [361]. Already the dominant SM Higgs production channel at the LHC, gluon-fusion, is loop induced and thus in principle sensitive to new physics. Instead, here we want to highlight the possibility for an enhancement of the branching ratio $\mathrm{BR}(h^0 \to \gamma\gamma)$ due to a strongly mixed light stau. Within the SM, the decay $h^0 \to \gamma\gamma$ is dominated by top-quark and W boson loops, both contributing with different signs, and is of the order $\mathrm{BR}(h^0 \to \gamma\gamma)_{\mathrm{SM}} \approx 10^{-3}$. In [351, 352] it was shown that a light stau 90 GeV $\lesssim m_{\tilde{\tau}_1} \lesssim$ 150 GeV with large stau-stau-Higgs couplings, as discussed above, can lead to an enhancement of the Higgs branching ratio,

$$R_{\gamma\gamma} = \mathrm{BR}(h^0 \to \gamma\gamma)_{\mathrm{MSSM}} \;/\; \mathrm{BR}(h^0 \to \gamma\gamma)_{\mathrm{SM}} \tag{7.9}$$

of up to $R_{\gamma\gamma} \approx 2$, via diagrams like the ones shown in figure 7.4. The relevant parameter region is very similar to the one discussed above with a large stau mixing due to large $X_\tau \sim \mu \tan\beta$.

First measurements from both experiments, ATLAS and CMS, indicated such an excess compared to the SM prediction, $R_{\gamma\gamma} > 1.5$ @ 95% C.L. [27, 28, 362]. A stau as light as required for such an excess, 90 GeV $\lesssim m_{\tilde{\tau}_1} \lesssim$ 150 GeV, is excluded in scenarios where the stau is long-lived, however viable in scenarios with a $\tilde{\chi}_1^0$ LSP.

In a very recent study using a larger data set and a refined analysis, CMS did not find any excess [363]. At the moment the experimental situation is not clear and more data and new analyses are needed to settle the issue, however, after the latest results by CMS it seems unlikely that new physics is hiding in the $h \to \gamma\gamma$ channel.

7.1.4 Constraints from CCBs

In the considered parameter region, theoretical constraints might become important for large stau-Higgs couplings. These regions can be associated with unwanted deep charge breaking minima in the scalar MSSM potential [345, 346, 364–367]. Still, this will be a viable scenario if the quantum transition rate to the CCB minimum is so small that the lifetime of our electroweak vacuum exceeds the age of the Universe. By studying the decay of the electroweak vacuum with the 'bounce method' [368] in an effective potential approach [369], as explained

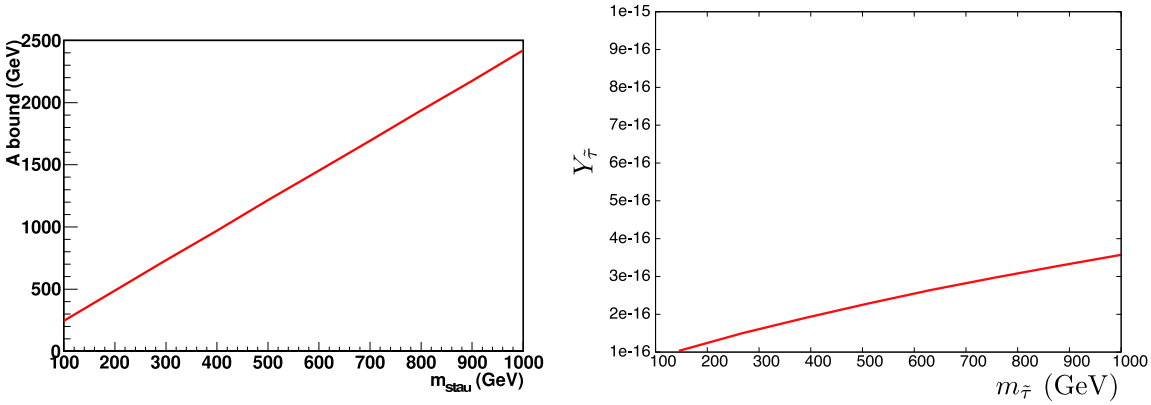

Figure 7.5: Left: CCB bound on the stau–stau–heavy-Higgs coupling $\mathcal{A}_{H^0\tilde{\tau}_1\tilde{\tau}_1}$ as a function of the stau mass for $2m_{\tilde{\tau}_1} = m_{H^0}$. Right: stau yield $Y_{\tilde{\tau}_1}$ as a function of $m_{\tilde{\tau}_1}$ for $\mathcal{A}_{H^0\tilde{\tau}_1\tilde{\tau}_1} = 1.3 \times m_{\tilde{\tau}_1}$ and $m_{H^0} = 2m_{\tilde{\tau}_1}$. Both plots taken from [370].

in Appendix C, it has been found from a fit in the relevant parameter space that a viable scenario with large $\tilde{\tau}_1\,\tilde{\tau}_1^* h^0$ coupling has to respect the following[4] metastability condition [365]:

$$\begin{aligned}\mu \tan\beta \;<\; & 213.5\,\sqrt{m_{\tilde{L}_3} m_{\tilde{E}_3}} - 17.0\,(m_{\tilde{L}_3} + m_{\tilde{E}_3}) \\ & + 4.52 \times 10^{-2}\ \text{GeV}^{-1} (m_{\tilde{L}_3} + m_{\tilde{E}_3})^2 - 1.30 \times 10^4\ \text{GeV}\,,\end{aligned} \tag{7.10}$$

where $m_{\tilde{L}_3}$ and $m_{\tilde{E}_3}$ are respectively the left-handed and right-handed stau soft breaking masses. However, this condition is not as rigid as, for example, bounds from direct SUSY particle searches or flavor changing decays, since only the exponential contribution to the decay of the electroweak vacuum can be evaluated easily, while a calculation of the full width of the decay into the CCB minimum is highly non-trivial. Nevertheless, scenarios in which an exceptional yield (7.7) results only from enhanced stau-Higgs couplings [345, 346] can be disfavored by the CCB constraint (7.11), if taken at face value (cf. sections 8.2 and 8.3 and ref. [364]).

In scenarios with $2m_{\tilde{\tau}_1} \simeq m_{H^0}$, primordial stau annihilation can proceed efficiently via the H^0 resonance and thereby lead to an exceptionally small $Y_{\tilde{\tau}_1}$. Here, the annihilation channel $\tilde{\tau}_1\tilde{\tau}_1^* \to b\bar{b}$ turned out to be the most relevant one, which also benefits from enhanced stau-Higgs couplings. However, because of the H^0 resonance, an exceptional yield (7.7) is already possible with more moderate values of $\tan\beta$, μ, and A_τ [346]. Thereby, such scenarios can lead to (7.7) and still respect the discussed CCB constraints – even for rather large $m_{\tilde{\tau}_1}$ as shown in [370]. In [370] the maximal $\tilde{\tau}_1\tilde{\tau}_1 H^0$ coupling, $\mathcal{A}_{H^0\tilde{\tau}_1\tilde{\tau}_1} = \frac{g}{m_W} C[\tilde{\tau}_1^*, \tilde{\tau}_1, H^0]$ is determined as a function of $m_{\tilde{\tau}_1}$ for $2m_{\tilde{\tau}_1} = m_{H^0}$. We show this result in figure 7.5(left). For example, a coupling $\mathcal{A}_{H^0\tilde{\tau}_1\tilde{\tau}_1} = 1.3 \times m_{\tilde{\tau}_1}$ is safe from potential CCBs and the resulting stau yield $Y_{\tilde{\tau}_1}$ as a function of $m_{\tilde{\tau}_1}$, again for $m_{H^0} = 2m_{\tilde{\tau}_1}$, is shown in figure 7.5(right). Clearly, yields

[4] In an earlier version of [365] the authors stated the result $\mu \tan\beta < 76.9\,\sqrt{m_{\tilde{L}_3} m_{\tilde{E}_3}} + 38.7\,(m_{\tilde{L}_3} + m_{\tilde{E}_3}) - 1.04 \times 10^{-4}$ GeV , which was used in [1]. Numerical differences between the two results are at most 15%. The updated result, in general, relaxes CCB constraints.

respecting (7.7) can in principle always be achieved, given $m_{H^0} \approx 2m_{\tilde{\tau}_1}$, $\theta_\tau \approx \pi/4$ and large enough A_τ (cf. eq. (2.77)).

7.2 Direct production of staus at hadron colliders

In this section we calculate the cross section for direct stau pair production at hadron colliders. We describe the relevant production channels and the methods used in our calculations. In the numerical results we show the dependence on the relevant SUSY parameters and provide predictions for the Tevatron and the LHC. The obtained cross sections are independent of the stau lifetime and thus also applicable for scenarios where the stau is unstable.

Within the MSSM, stau pairs can be produced directly at hadron colliders,

$$pp(p\bar{p}) \to \tilde{\tau}_i \tilde{\tau}_j^*, \tag{7.11}$$

where $\tilde{\tau}_i$ denotes any of the two stau mass eigenstates. After electroweak symmetry breaking the soft-breaking terms in the MSSM Lagrangian induce a mixing among the particles of identical color and electric charge. In the sfermion sector, left-handed and right-handed gauge eigenstates mix to form mass eigenstates, as explained in section 2.3.2. The mixing is proportional to the mass of the SM partner fermion and can thus be sizeable for sleptons of the third generation. In the following, we concentrate on the production of the lighter $\tilde{\tau}_1 \tilde{\tau}_1^*$ pairs. Results for $\tilde{\tau}_2 \tilde{\tau}_2^*$ and $\tilde{\tau}_1 \tilde{\tau}_2^*$ production can be obtained in close analogy. Their production cross sections, however, are suppressed by the heavier $\tilde{\tau}_2$ mass. Additionally, non-diagonal $\tilde{\tau}_1 \tilde{\tau}_2^*$ production requires a chiral coupling and thus, e.g., photon-mediated channels are absent.

7.2.1 Direct $\tilde{\tau}_1 \tilde{\tau}_1^*$ production channels

At hadron colliders the leading contribution to direct $\tilde{\tau}_1 \tilde{\tau}_1^*$ production arises at $\mathcal{O}(\alpha^2)$ from the $q\bar{q}$ induced Drell–Yan type process, see figure 7.6 (a).

On the partonic level the differential cross section is given by

$$\frac{d\hat{\sigma}^{\mathrm{DY}}_{q\bar{q}\to\tilde{\tau}_1\tilde{\tau}_1}}{dt} = 2\pi\alpha^2 \, \frac{ut - m^4_{\tilde{\tau}_1}}{s^4} \left[e_q^2 + \frac{g^2_{\tilde{\tau}_1\tilde{\tau}_1} (g_{\mathrm{V}}^{q\,2} + g_{\mathrm{A}}^{q\,2})}{(1 - M_Z^2/s)^2} - \frac{2 e_q \, g_{\mathrm{V}}^q \; g_{\tilde{\tau}_1\tilde{\tau}_1}}{1 - M_Z^2/s} \right], \tag{7.12}$$

where

$$g_{\tilde{\tau}_1\tilde{\tau}_1} = \frac{(4 s_W^2 - 1) - \cos 2\theta_\tau}{4 c_{\mathrm{W}} s_{\mathrm{W}}}, \quad g_{\mathrm{V}}^q = \frac{I_{3L}^q - 2 e_q s_{\mathrm{W}}^2}{2 c_{\mathrm{W}} s_{\mathrm{W}}}, \quad g_{\mathrm{A}}^q = \frac{I_{3L}^q}{2 c_{\mathrm{W}} s_{\mathrm{W}}}, \tag{7.13}$$

with $s_W = \sin\theta_W$, $c_W = \cos\theta_W$ and u, t, s being the usual Mandelstam variables for a $2 \to 2$ process. q denotes the annihilating quark flavor, I_{3L}^q its isospin and e_q its charge. Clearly, the Drell–Yan production cross section only depends on the stau mass $m_{\tilde{\tau}_1}$ and the stau mixing angle θ_τ.

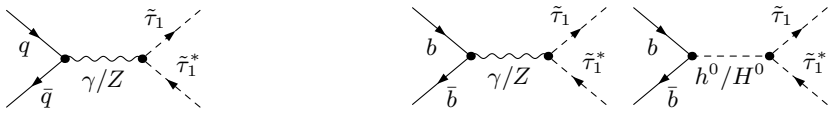

(a) (b)

Figure 7.6: Feynman diagrams for stau pair production (a) via the Drell–Yan process and (b) via $b\bar{b}$ annihilation. Here, $q = \{u, d, c, s\}$.

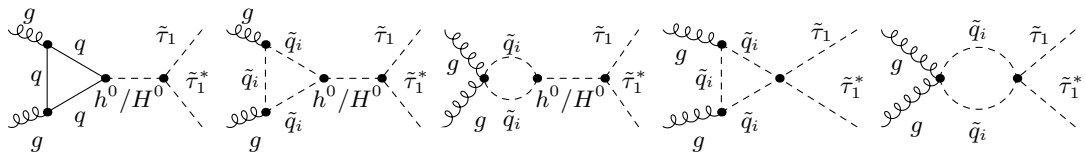

Figure 7.7: Feynman diagrams for the gluon fusion contribution to stau pair production. The quarks q and squarks $\tilde{q}_i$, $i = 1, 2$, running in the loops can be of any flavor.

At the same order of perturbation theory, stau pairs can also be produced from $b\bar{b}$ annihilation, mediated by the neutral gauge bosons (γ, Z) and by the neutral CP-even Higgs bosons (h^0, H^0). Corresponding Feynman diagrams are displayed in figure 7.6 (b). This channel is suppressed by the low bottom-quark density inside protons, but can be enhanced by on-shell Higgs propagators and by large bottom-Higgs and stau-Higgs couplings in certain regions of the SUSY parameter space. Note that the CP-odd Higgs and Goldstone bosons, A^0 and G^0, do not couple to a diagonal $\tilde{\tau}_i\tilde{\tau}_i^*$ pair at tree-level and, in absence of CP violating effects in the MSSM, there is also no induced mixing between the CP-even and the CP-odd Higgs boson states at higher orders of perturbation theory. The A^0 and G^0 bosons thus do not enter our calculation.

Gluon-induced $\tilde{\tau}_1\tilde{\tau}_1^*$ production is only possible at the one-loop level, mediated by a quark or squark loop, as shown in figure 7.7. Even though these contributions are formally of higher orders, $\mathcal{O}(\alpha_s^2\alpha^2)$, they can give sizeable contributions at the proton-proton machine LHC at high center-of-mass energies, where the gg luminosity is significantly higher than the $q\bar{q}$ luminosity.

Let us note again that the additional $b\bar{b}$ and gg channels are not included in the general purpose Monte Carlo event generators like `Pythia` [181] or `Herwig` [182]. We use the programs `FeynArts` [244] and `FormCalc` with `LoopTools` [245] to generate and calculate the amplitudes corresponding to the Feynman diagrams of figures 7.6 and 7.7. The Higgs boson masses and the H^0 width are computed with `FeynHiggs`. We include $\mathcal{O}(\alpha_s^2\alpha^2)$ QCD and SUSY-QCD corrections at NLO for the Drell–Yan channel predictions calculated with `Prospino 2`, by scaling our cross sections with the respective K-factors, $K \equiv \sigma_{\mathrm{NLO}}/\sigma_{\mathrm{LO}}$. Furthermore, we use resummed effective $b\bar{b}h^0$ and $b\bar{b}H^0$ vertices for the gluon fusion and $b\bar{b}$ contributions, as explained below in section 7.2.2. We do not include higher-order QCD and SUSY-QCD corrections to the Higgs-mediated channels. These are expected to be positive and similar to the results for on-shell Higgs production, see ref. [189] and references therein. In this way our

analysis gives a conservative estimate of the enhancement effects from the $b\bar{b}$ and gluon fusion production channels. Note also that additional contributions to the direct $\tilde{\tau}_1\tilde{\tau}_1^*$ production can arise from W^+W^- fusion. Those however would be smaller by at least one order of magnitude compared to the discussed channels [178] and are not included in our analysis.

At hadron colliders, the gluon-fusion and $b\bar{b}$-annihilation processes with an s-channel Higgs boson can become resonant in regions of the SUSY parameter space in which the Higgs boson is heavier than the two produced staus. For intermediate $\tilde{\tau}_1$ masses respecting the robust LEP limit $m_{\tilde{\tau}_1} \geq 82$ GeV [39], the lighter CP-even Higgs boson, h^0, is expected to be too light to go on-shell (particularly identifying it with the recently observed state at $\approx 125\,\text{GeV}$). This is different for the heavier H^0 boson. In parameter regions with $m_{H^0} \geq 2m_{\tilde{\tau}_1}$ we regularize the on-shell singularity including the total decay width of the H^0 boson, Γ^0_H, in its propagator,

$$\frac{1}{p^2 - m^2_{H^0}} \longrightarrow \frac{1}{p^2 - m^2_{H^0} + im_{H^0}\Gamma_{H^0}}\,.$$

From the partonic production cross sections, hadronic results are obtained convoluting with PDFs, as shown in eq. (3.2).

7.2.2 Resummation in the sbottom sector

As motivated in section 7.1, we are particularly interested in parameter regions with enhanced stau–Higgs couplings and thus typically in scenarios with large $\tan\beta$. It has been known for a long time [371–375] that radiative corrections to the $b\bar{b}h^0/b\bar{b}H^0$ vertex can be important especially for large $\tan\beta$ and drive down related cross sections compared to the tree-level results. As shown in [375, 376] the leading $\tan\beta$-enhanced corrections can be resummed to all orders in perturbation theory by using an appropriate effective bottom-quark mass, m_b^{eff}, and effective $b\bar{b}h^0/b\bar{b}H^0$ couplings. We adopt this approach, as explained in detail in the following.

The Higgs sector in the MSSM corresponds to a two-Higgs doublet model, where the down-type quarks couple to h_d and the up-type quarks to h_u. After spontaneous symmetry breaking, the up- (down-)type quarks gain masses by coupling to the non-zero h_u (h_d) vacuum expectation values v_2 (v_1). At tree-level, the bottom-quark mass m_b is given by

$$m_b = \lambda_b v_1, \tag{7.14}$$

where λ_b is the $b\bar{b}h_d$ Yukawa coupling. However, radiative corrections induce an effective $b\bar{b}h_u$ coupling $\Delta\lambda_b$ that can significantly alter the tree-level relation [371–375]. These higher-order contributions do not decouple at low energies and are enhanced by $\tan\beta$,

$$\begin{aligned} m_b &= \lambda_b v_1 + \Delta\lambda_b v_2 = \lambda_b v_1 \left(1 + \frac{\Delta\lambda_b}{\lambda_b}\tan\beta\right) \\ &\equiv \lambda_b v_1 \left(1 + \Delta m_b\right). \end{aligned} \tag{7.15}$$

As shown in ref. [375], the leading $\tan\beta$ enhanced terms can be resummed to all orders via an effective bottom-quark Yukawa coupling $\lambda_b^{\text{eff}} \equiv m_b^{\text{eff}}/v_1$. The dominant contributions to Δm_b

arise from gluino-sbottom and chargino-stop loops,

$$\Delta m_b = \frac{2\alpha_s}{3\pi} M_3 \mu \tan\beta \; I(m_{\tilde{b}_1}, m_{\tilde{b}_2}, m_{\tilde{g}}) + \frac{\lambda_t^2}{16\pi^2} \mu A_t \tan\beta \; I(m_{\tilde{t}_1}, m_{\tilde{t}_2}, \mu), \tag{7.16}$$

with the gluino mass M_3, the lighter (heavier) sbottom mass $m_{\tilde{b}_1}$ ($m_{\tilde{b}_2}$) the trilinear coupling A_t in the stop sector, the lighter (heavier) stop mass $m_{\tilde{t}_1}$ ($m_{\tilde{t}_2}$), and the loop function

$$I(a,b,c) = \frac{1}{(a^2-b^2)(b^2-c^2)(a^2-c^2)} \left[a^2 b^2 \log\frac{a^2}{b^2} + b^2 c^2 \log\frac{b^2}{c^2} + c^2 a^2 \log\frac{c^2}{a^2} \right]. \tag{7.17}$$

Further neutralino-sbottom contributions are proportional to the weak coupling g^2 and thus subleading. Here we follow refs. [136, 376] and use a $\overline{\text{DR}}$ definition of the effective mass to take large logarithms from the running Yukawa coupling into account. The effective Yukawa coupling λ_b^{eff} is then defined as follows,

$$\lambda_b^{\text{eff}} = \frac{1}{v_1} \frac{m_b^{\overline{\text{DR}}}(\mu_R) + m_b \, \Delta m_b}{1 + \Delta m_b} \equiv \frac{m_b^{\overline{\text{DR}},\text{eff}}}{v_1}, \tag{7.18}$$

where the second term in the numerator is necessary to avoid double counting of the resummed terms. The $\overline{\text{DR}}$ bottom mass at the renormalization scale μ_R can be obtained from the on-shell bottom-quark mass, m_b^{OS}, and the UV-finite parts of the bottom-quark self-energy (here in Lorentz decomposition),

$$m_b^{\overline{\text{DR}}}(\mu_R) = m_b^{\text{OS}} + \frac{m_b}{2} \left(\Sigma_L^{\text{fin.}}(m_b) + \Sigma_R^{\text{fin.}}(m_b) + 2\,\Sigma_S^{\text{fin.}}(m_b) \right), \tag{7.19}$$

with

$$m_b^{\text{OS}} = m_b^{\overline{\text{MS}}}(M_Z)\, b^{\text{shift}}, \qquad b^{\text{shift}} = 1 + \frac{\alpha_s}{\pi} \left(\frac{4}{3} - \log\frac{[m_b^{\overline{\text{MS}}}(M_Z)]^2}{M_Z^2} \right). \tag{7.20}$$

Further $\tan\beta$ enhancement effects arise in the trilinear couplings involving Higgs–bottom interactions. They can be resummed and taken into account by modifying the $b\bar{b}\mathcal{H}$ couplings $g_{b\bar{b}\mathcal{H}}$, with $\mathcal{H} = \{h^0, H^0, A^0\}$. The combined effect of the resummation in the relation between λ_b and m_b and of the resummation in the Higgs–bottom vertices is accounted for by performing the following substitutions in the couplings,

$$\begin{aligned}
&g_{bbh^0} \to g_{bbh^0}\big|_{\lambda_b \to \lambda_b^{\text{eff}}} \left(1 - \frac{\Delta m_b}{\tan\beta \tan\alpha} \right), \qquad && g_{bbA^0} \to g_{bbA^0}\big|_{\lambda_b \to \lambda_b^{\text{eff}}} \left(1 - \frac{\Delta m_b}{\tan^2\beta} \right), \\
&g_{bbH^0} \to g_{bbH^0}\big|_{\lambda_b \to \lambda_b^{\text{eff}}} \left(1 + \Delta m_b \frac{\tan\alpha}{\tan\beta} \right), \qquad && g_{bbG^0} \to g_{bbG^0}\,.
\end{aligned} \tag{7.21}$$

The coupling involving the Goldstone boson G^0 is not modified since the contribution from the vertex corrections exactly compensates the contribution of the bottom-Yukawa coupling resummation.

7.2.3 Numerical results

Let us now investigate numerical results for direct $\tilde{\tau}_1 \tilde{\tau}_1^*$ production at hadron colliders. Here, our focus is on the impact of the $b\bar{b}$-annihilation and the gluon-fusion channels, in comparison to the contribution from the Drell–Yan process.

The cross section for direct stau production depends mainly on $m_{\tilde{\tau}_1}$, m_{H^0}, $\tan\beta$, and on θ_τ (or equivalently on μ and A_τ). It also depends on the H^0 boson width, Γ_{H^0}, and thus indirectly on the entire SUSY mass spectrum. In addition, squark masses enter indirectly via the loops in the gluon-fusion channel and, as e.g. the trilinear coupling A_t in the stop sector, via the effective bottom couplings.

We use the following input parameters in our numerical study. As a starting point, we choose a $\tilde{\tau}_1$-LOSP scenario with moderate squark masses and a large stau–Higgs coupling, fixed by the following soft-breaking parameters at the low scale:

$$\begin{aligned} M_1 = M_2 = M_3 = 1.2 \text{ TeV}, \qquad & A_t = A_b = A_\tau = 600 \text{ GeV}, \\ m_{\tilde{Q}_i} = m_{\tilde{U}_i} = m_{\tilde{D}_i} = 1 \text{ TeV}, \qquad & m_{\tilde{L}_{1/2}} = m_{\tilde{E}_{1/2}} = 500 \text{ GeV}. \end{aligned} \tag{7.22}$$

If not stated otherwise, we choose

$$\begin{aligned} \theta_\tau = 45^\circ, \qquad & m_{\tilde{\tau}_1} = 200 \text{ GeV}, \\ \tan\beta = 30, \qquad & \mu = 500 \text{ GeV}, \qquad m_A = 400 \text{ GeV}, \end{aligned} \tag{7.23}$$

as inputs for the third-generation sleptons and for the Higgs-sector. With these parameters, the considered scenario falls into the decoupling limit of the MSSM [360] where $m_{H^0} \approx m_A$. Note that the chosen value of $\tan\beta$ (and also of μ) is rather moderate compared to the cosmologically motivated scenarios considered in ref. [346] and discussed in section 7.1.2.

From the input parameters (7.22) and (7.23), we calculate the physical MSSM parameters using tree-level relations for sfermions, neutralinos, and charginos. Physical masses are then passed to `Prospino 2` to calculate the Drell–Yan K-factors at NLO in QCD and SUSY-QCD. The NLO corrections to the Drell–Yan channel typically amount to 20–40% in the considered parameter space. SM input parameters are chosen according to [256],

$$\begin{aligned} M_Z = 91.1876 \text{ GeV}, \qquad & M_W = 80.4248 \text{ GeV}, \qquad G_F = 1.16637 \times 10^{-5} \text{ GeV}, \\ m_b^{\overline{\text{MS}}}(M_Z) = 2.936 \text{ GeV}, \qquad & m_t = 173.1 \text{ GeV}, \qquad m_\tau = 1.776 \text{ GeV}. \end{aligned} \tag{7.24}$$

We use the MSTW08LO set of PDFs consistently with the strong coupling constant $\alpha_s(\mu_R)$ they provide. Factorization and renormalization scales are set to the mass of the produced stau $\mu = \mu_R = \mu_F = m_{\tilde{\tau}_1}$.

At this point we want to mention again that our calculation of the $b\bar{b}$ and gg channels is formally at LO. By using an effective bottom-quark mass, m_b^{eff}, and effective $b\bar{b}h^0/b\bar{b}H^0$ couplings, however, the dominant $\tan\beta$ enhanced corrections are included in our results. Nevertheless, we do not consider non-$\tan\beta$ enhanced higher-order corrections, and the remaining renormalization and factorization scale dependence yields a large theoretical uncertainty to

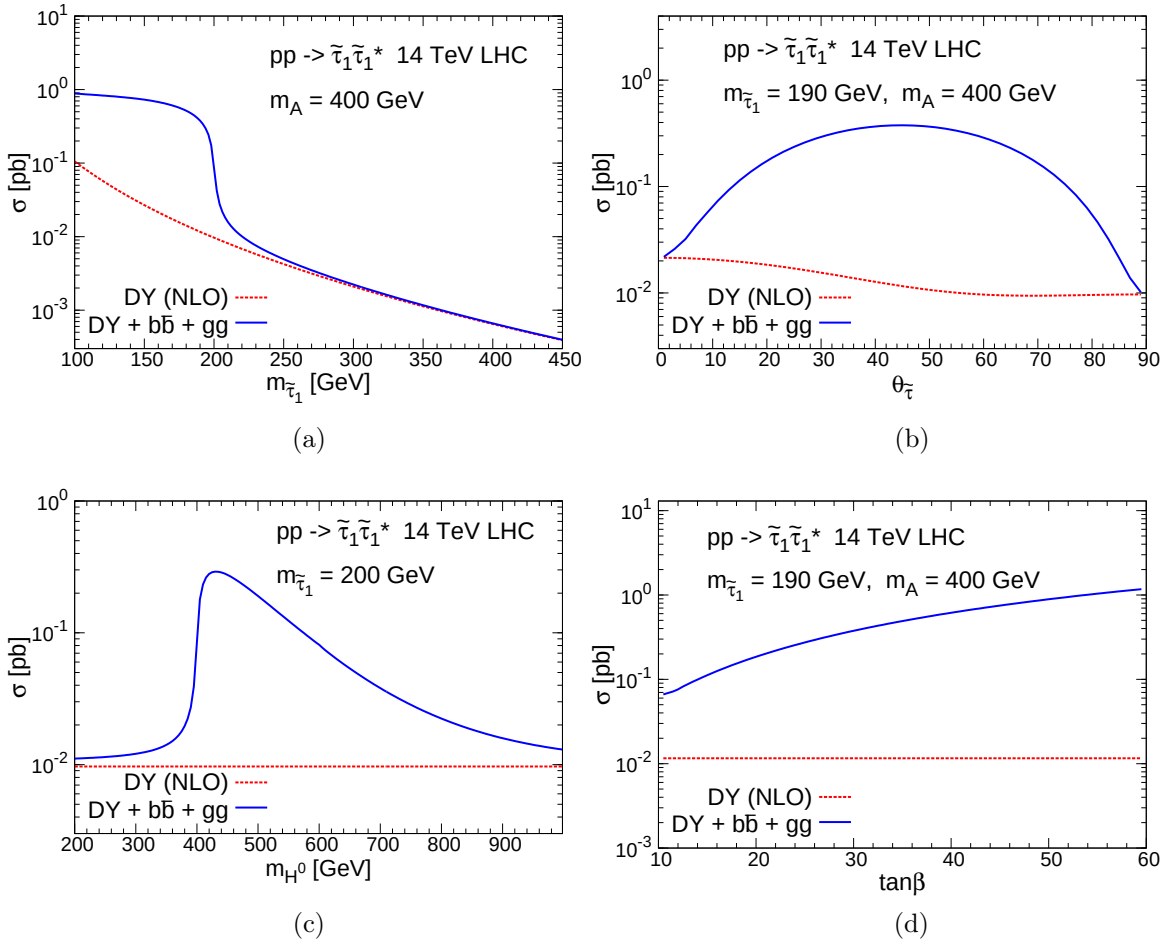

Figure 7.8: Cross section of direct $\tilde{\tau}_1\tilde{\tau}_1^*$-pair production (solid lines, blue) and the Drell–Yan prediction (dashed lines, red) at the LHC with $\sqrt{S} = 14$ TeV as a function of (a) $m_{\tilde{\tau}_1}$, (b) θ_τ, (c) m_{H^0}, and (d) $\tan\beta$. No kinematical cuts are applied. SUSY input parameters are as given in (7.22) and (7.23) if not varied or unless stated otherwise in the legend of the respective panel. Note that $m_{H^0} \approx m_A$ (decoupling limit) holds in most of the shown regions.

our cross section predictions. A more detailed study at NLO would be desirable, taking also uncertainties due to the dependence on the PDF set, and the bottom-quark PDF in particular, into account.

In figure 7.8 we show the direct production cross section for $\tilde{\tau}_1\tilde{\tau}_1^*$ pairs at the LHC with $\sqrt{S} = 14$ TeV as a function of (a) $m_{\tilde{\tau}_1}$, (b) θ_τ, (c) m_{H^0}, and (d) $\tan\beta$. The remaining SUSY parameters are basically fixed according to (7.22) and (7.23). In figures 7.8 (b) and 7.8 (d), we move to $m_{\tilde{\tau}_1} = 190$ GeV, where stau production is possible via on-shell H^0 exchange. The dashed (red) lines show the Drell–Yan (DY) cross section at NLO, whereas the solid (blue) lines include the additional $b\bar{b}$ and gg contributions. The Drell–Yan cross section depends only on $m_{\tilde{\tau}_1}$ and θ_τ, as already mentioned above. It decreases strongly for increasing $\tilde{\tau}_1$ masses and varies with θ_τ by a factor that can be at most slightly larger than 2. As shown in

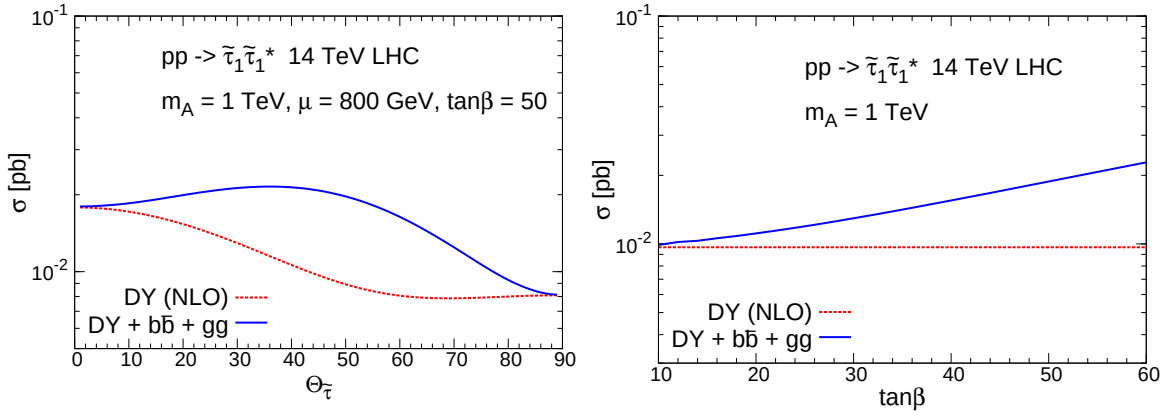

(a) (b)

Figure 7.9: Cross section of direct $\tilde{\tau}_1\tilde{\tau}_1^*$-pair production (solid lines, blue) and the Drell–Yan prediction (dashed lines, red) at the LHC with $\sqrt{S} = 14$ TeV as a function of (a) θ_τ and (b) $\tan\beta$. No kinematical cuts are applied. SUSY input parameters as given in (7.22) and (7.23) if not varied or stated otherwise. Note that here $m_{H^0} \approx m_A = 1$ TeV (decoupling limit).

figure 7.8 (b), this factor takes on its largest value for $\theta_\tau \approx 0$, i.e., for an almost left-handed $\tilde{\tau}_1$. The factor of ≈ 2 difference between the Drell–Yan cross sections at $\theta_\tau \approx 0$ and $\theta_\tau \approx \pi/2$ can be deduced from eq. (7.12) and is determined mainly by different gauge couplings of the left-handed and right-handed states. It is independent of $m_{\tilde{\tau}_1}$ and hardly affected when going from $\sqrt{S} = 14$ TeV to 7 TeV.

The impact of the $b\bar{b}$ and gg channels depends strongly on the mass hierarchy between $\tilde{\tau}_1$ and H^0, as can clearly be seen in figures 7.8 (a) and 7.8 (c). If $m_{H^0} > 2m_{\tilde{\tau}_1}$, these additional channels can change the direct production cross section by more than one order of magnitude with respect to the Drell–Yan result. At the threshold $m_{H^0} = 2m_{\tilde{\tau}_1}$, the $b\bar{b}$ and gg contributions drop steeply and are less important for $m_{H^0} \ll 2m_{\tilde{\tau}_1}$.

Figures 7.8 (b) and 7.8 (d) illustrate the dependence of the total direct production cross section on the parameters θ_τ and $\tan\beta$ that govern the stau-Higgs-coupling strength. Here, the total direct production cross section is dominated by on-shell Higgs production. Thus, the dependence on θ_τ and $\tan\beta$ reflects the $\tilde{\tau}_1\tilde{\tau}_1^* H^0$ coupling, discussed in section 7.1.2 and given in section 2.3.2. As shown there and illustrated here, this coupling is basically proportional to $\sin 2\theta_\tau$ and also to $\tan\beta$ (or more precisely to $A_\tau \tan\beta$). The additional contributions from the $b\bar{b}$ and gg channels are tiny in cases of very small mixing, $\theta_\tau \to 0, \pi$, whereas this minimum is not exactly at $\theta_\tau = 0, \pi$ but slightly above/below, as can be seen from eq. (2.75). In turn, they become most important for maximal mixing, i.e., at $\theta_\tau \approx \pi/4$. There, the additional contributions push up the total direct production cross section by up to two orders of magnitude for very large $\tan\beta$ and are already sizeable for small $\tan\beta$.

Let us now turn to a scenario where the H^0 is very heavy and thus almost decoupled, $m_{H^0} = 1$ TeV. We again investigate the dependence of the total cross section on θ_τ and $\tan\beta$,

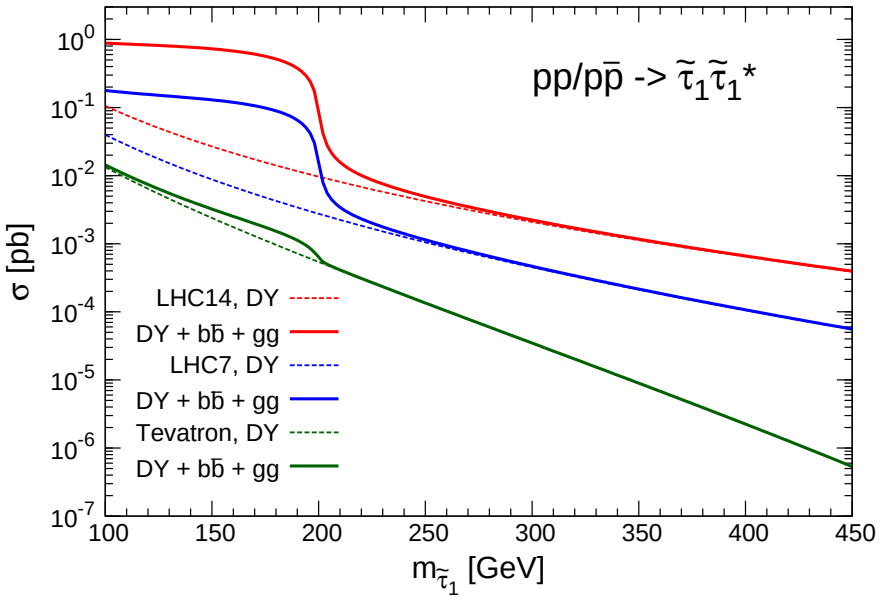

Figure 7.10: Direct $\tilde{\tau}_1\tilde{\tau}_1^*$-pair production cross sections as a function of $m_{\tilde{\tau}_1}$ for the SUSY scenario with (7.22) and (7.23) at the LHC with $\sqrt{S} = 14$ TeV (top, red) and 7 TeV (middle, blue) and the Tevatron with $\sqrt{S} = 1.96$ TeV (bottom, green). The Drell–Yan predictions are shown by the dashed lines and the full cross section, including $b\bar{b}$ and gg channels, by the solid lines.

shown in figure 7.9, where we focus on parameters that allow for enhanced $\tilde{\tau}_1\tilde{\tau}_1^* h^0$ couplings. As discussed in section 7.1.2 and shown in section 2.3.2, this coupling is basically proportional to $\mu \tan\beta$. Indeed, in figure 7.9 (a) we consider $\mu = 800$ GeV and $\tan\beta = 50$ while the other parameters are fixed according to (7.22) and (7.23). Again, the contribution from the additional $b\bar{b}$ and gg channels can be sizeable. The enhancement amounts to a factor between two and three when considering very large values of $\tan\beta$ and maximal mixing $\theta_\tau \approx \pi/4$. However, here dominant contributions come mainly from off-shell h^0 exchange together with large stau-Higgs couplings. Thus, the relative importance between the gg channel and the $b\bar{b}$ channel can be different compared to situations with dominant contributions from on-shell H^0 exchange since the two Higgses couple differently to the quark and squark loops. Clearly, for a larger contribution of the loop-induced gg channel, a stronger dependence on the squark masses is introduced in our calculation. This does not only concern the overall mass scale but also the mass splitting between the squarks, as is well known for on-shell Higgs production via gluon fusion, see ref. [377] and references therein. For example, contributions from squark loops get small when squarks within one generation are almost degenerate. Additionally, slight enhancements in the gg channel can appear at thresholds where the resonance requirement $2m_{\tilde{q}} \approx m_{H^0}$ is fulfilled between squarks in the loops and the heavy Higgs H^0, as shown in ref. [180]. We want to note that, despite the large couplings, all parameter points considered here are in agreement with the CCB constraint (7.11).

We summarize the potential impact of the $b\bar{b}$ and gg channels for the SUSY scenario with parameters given in (7.22) and (7.23) in figure 7.10, where the Drell–Yan predictions (dashed lines) and the full cross sections (solid lines) are shown for $\tilde{\tau}_1\tilde{\tau}_1^*$ production at the LHC for $\sqrt{S} = 14$ TeV (top, red) and for 7 TeV (middle, blue). When going down from 14 TeV to 7 TeV, the cross section decreases by up to about a factor of 5. The relative importance of the $b\bar{b}$ and gg channels however are similarly important in the region where on-shell H^0 exchange contributes. Thus, for both $\sqrt{S} = 7$ TeV and 14 TeV, the $b\bar{b}$ and gg channels should not be neglected in a precise cross section prediction. We also show the direct $\tilde{\tau}_1\tilde{\tau}_1^*$ production cross section expected at the Tevatron with $\sqrt{S} = 1.96$ TeV (bottom, green). Due to the higher parton momentum fractions x needed at the Tevatron, the gluon and the $b\bar{b}$ luminosities are reduced compared to the LHC case. Thus, the respective gg and $b\bar{b}$ contributions to direct stau production are, as illustrated, also smaller.

Chapter 8

Phenomenology of long-lived staus

In this chapter we address aspects of LHC phenomenology of long-lived staus, i.e., $\tau_{\tilde{\tau}_1} \gtrsim 10^{-6}\ s$. We focus on parameter regions, where the additional production channels, $b\bar{b}$-annihilation and gluon-fusion, calculated in the previous chapter, become important.

First, in section 8.1 we investigate production cross sections including appropriate experimental cuts, associated prospects for SUSY parameter determination and stopping of staus. Second, in section 8.2 we consider, as an example, the CMSSM. Here we perform a scan in the relevant parameter space and study representative CMSSM benchmark scenarios to explore the relative importance of direct stau production with respect to the stau production in cascade decays. Third, in section 8.3 we explore ways to probe the viability of an exceptionally small relic stau abundance at colliders. As exemplary models we consider the CMSSM and a model with non-universal gaugino masses (NUGM) to illustrate our main points. Finally, in 8.5 we review the current experimental status and discuss future prospects.

8.1 Collider phenomenology with directly produced long-lived staus

At collider experiments, pair production of long-lived staus will give a clear CHAMP signal in the detectors if kinematical cuts are applied to discriminate between signal and muon background. Here, we study the impact of these kinematical cuts on the direct production cross section prediction and differential distributions. We show that experimental observation of direct stau production could provide important insights into the SUSY model realized in nature. For particularly well-motivated cosmological scenarios, we find that relatively large numbers of staus are expected to get stopped already in the main detectors at the LHC. Thereby, analyses of stau decays may become a viable crucial tool to identify the LSP and/or to probe high scales such as the Planck scale Λ_{Planck} or the Peccei–Quinn scale f_{PQ} in the laboratory.

8.1.1 Kinematical cuts

For a realistic experimental analysis, we need to include kinematical cuts on the phase space of the staus to reduce possible backgrounds to the CHAMP signal. At hadron colliders,

experimental CHAMP searches have been performed by the CDF [104] and the D0 [186] collaborations at the Tevatron and at the LHC by CMS [187] and ATLAS [378]. In accordance with those analyses, we apply the following kinematical cuts on the produced staus:

$$\begin{aligned} p^{\mathrm{T}} > 40 \text{ GeV}, \qquad & 0.4 < \beta < 0.9, \\ |\eta| < 0.7 \text{ (Tevatron)}, \qquad & |\eta| < 2.4 \text{ (LHC)}, \end{aligned} \tag{8.1}$$

where the cuts have to be fulfilled by at least one of the $\tilde{\tau}_1$'s. Here $\eta = -\ln(\tan\theta/2)$ is the pseudo-rapidity and $\beta = |\mathbf{p}|/E$ the stau velocity. This should reduce the background from very slow moving muons to a negligible level [187, 378–380].

For our theoretical predictions, we use the same inputs as in section 7.2.3. In particular, we include the inclusive NLO K-factors provided by `Prospino 2` for the Drell–Yan channel, also when cuts are applied. Since QCD and SUSY-QCD corrections only affect the hadronic part of the considered $\tilde{\tau}_1\tilde{\tau}_1^*$ production, the cut dependence of the K-factors is expected to be small. Note that here we furthermore assume direct $\tilde{\tau}_1\tilde{\tau}_1^*$ production to be the dominant $\tilde{\tau}_1$ production source and do not include $\tilde{\tau}_1$'s resulting from cascade decays in our signal definition. Otherwise, an additional jet and/or lepton veto can be used to separate directly produced staus from ones produced at the end of a decay chain. Limits for long-lived stau production from cascade decays of squarks and gluinos have been discussed in [381] in a simplified model approach. We briefly investigate the relative importance of these concurrent production mechanisms for representative CMSSM benchmark scenarios in section 8.2.2.

In figure 8.1 we compare the full direct production cross sections with (solid lines) and without (dashed lines) the kinematical cuts (8.1) applied as a function of $m_{\tilde{\tau}_1}$ for the LHC with $\sqrt{S} = 14$ TeV (top, red) and 7 TeV (middle, blue) and the Tevatron with $\sqrt{S} = 1.96$ TeV (bottom, green). At the LHC, the cuts shift the excess slightly away from the m_{H^0} threshold and towards smaller values of $m_{\tilde{\tau}_1}$ and reduce the overall cross section by some tens of percent. The reduction is stronger at the Tevatron, where in particular the $b\bar{b}$ and gg channel contributions get significantly cut , so that the Drell–Yan channel provides a good approximation for the full cross section.

Assuming the produced $\tilde{\tau}_1$'s to be stable on the scale of the detectors, our results for the Tevatron shown in figure 8.1 can directly be compared with the CHAMP-cross-section limit from the CDF collaboration [104] given in (3.16). This comparison does not allow to exclude any $m_{\tilde{\tau}_1} > 100$ GeV for the considered parameters. By now, dedicated studies have been performed by the experiments at the LHC [187, 378]. They already probe large parts of the small-$m_{\tilde{\tau}_1}$ parameter space, where the stau can be produced via on-shell H^0 exchange with only a relatively small amount of integrated luminosity. However, any robust exclusion would require a full simulation including detector effects, which we do not perform here. We would like to refer to a paper [380] on direct stau production at the LHC, where the authors focus on the Drell–Yan-production mechanism and study the LHC discovery potential by performing a Monte Carlo analysis including detector simulations of the signal and the main dimuon background.

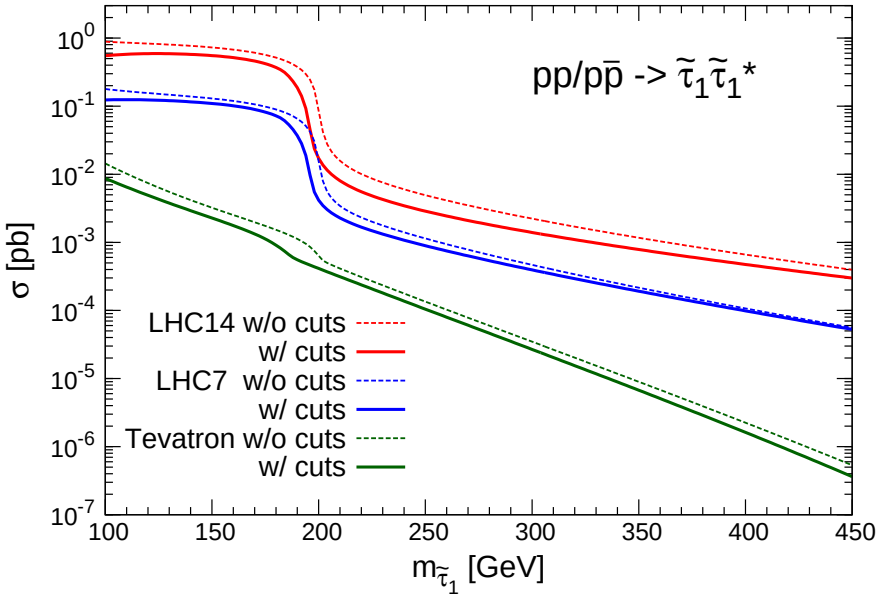

Figure 8.1: Direct $\tilde{\tau}_1\tilde{\tau}_1^*$-pair production cross sections before (dashed lines) and after (solid lines) application of the kinematical cuts (8.1) as a function of $m_{\tilde{\tau}_1}$ for the SUSY scenario with (7.22) and (7.23) at the LHC with $\sqrt{S} = 14$ TeV (top, red) and 7 TeV (middle, blue) and the Tevatron with $\sqrt{S} = 1.96$ TeV (bottom, green).

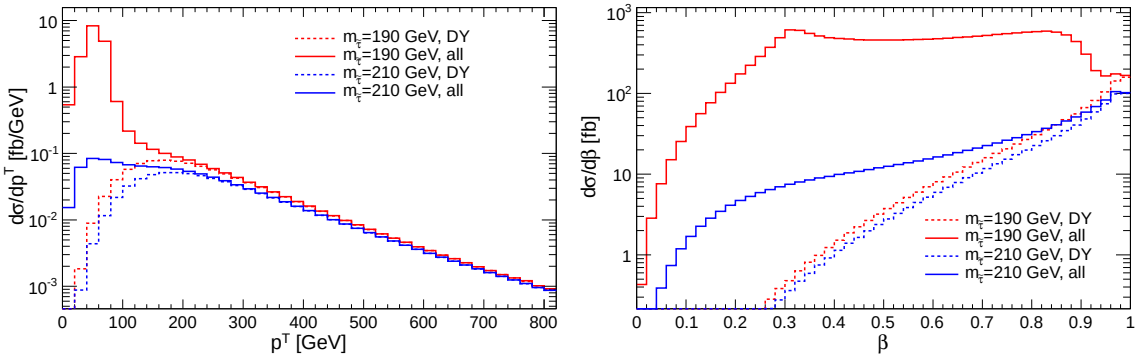

(a) (b)

Figure 8.2: (a) Transverse momentum p^T and (b) velocity $\beta = |\mathbf{p}|/E$ distributions of direct $\tilde{\tau}_1\tilde{\tau}_1^*$-pair production at the LHC with $\sqrt{S} = 14$ TeV. The Drell–Yan predictions are shown by dashed lines and the full cross sections, including $b\bar{b}$ and gg channels, by solid lines. We consider $m_{\tilde{\tau}_1} = 190$ GeV (red line) and $m_{\tilde{\tau}_1} = 210$ GeV (blue line), whereas the other SUSY input parameters are as given in (7.22) and (7.23).

So far we have concentrated on integrated cross sections. In order to further illustrate the importance of the $b\bar{b}$ and gg channel contributions and to investigate the impact of the cuts (8.1) on the different channels, we show in figure 8.2 the differential distributions with respect to the transverse momentum p^{T} and the velocity β of the directly produced staus. We give results for the LHC with $\sqrt{S} = 14$ TeV only, however, results for the LHC with $\sqrt{S} = 7$ TeV are qualitatively identical. We use the basic parameter inputs (7.22) and (7.23) and consider two distinct scenarios, $m_{\tilde{\tau}_1} = 190$ GeV (red line) and $m_{\tilde{\tau}_1} = 210$ GeV (blue line). Here $m_{H^0} = 400$ GeV, i.e., in the first scenario the intermediate H^0 boson can go on-shell while in the second scenario it can only be produced off-shell. We apply the cut $|\eta| < 2.4$ on the pseudo-rapidity of one of the staus to ensure that not both of the pair-produced staus leave the detector outside of the sensitive region. Cuts on p^{T} and β are not applied. We show the Drell–Yan-cross-section prediction (dashed lines) here without any K-factors and the full cross section including also the $b\bar{b}$ and gg channel contributions (solid lines). Clearly, in both scenarios, staus produced in $b\bar{b}$ and gg channels are softer and slower than their counterparts from the Drell–Yan-type production. The p^{T} distributions for the Drell–Yan channel peak at around $m_{\tilde{\tau}_1}$ and only few staus are produced with very low p^{T}. In contrast, the $b\bar{b}$ and gg channel contributions peak for low p^{T} and fall off rapidly. The velocity distributions for pure Drell–Yan production rise towards fast moving staus, $\beta \approx 1$, while adding the $b\bar{b}$ and gg channels results in a rather flat distribution for intermediate values of β. This behavior is more pronounced for scenarios in which an on-shell H^0 exchange is possible (red lines) since here the relative importance of the $b\bar{b}$ and gg channels with respect to the Drell–Yan channel is higher. In the case with $2m_{\tilde{\tau}_1} \gtrsim m_{H^0}$ with $2m_{\tilde{\tau}_1}$ still very close to m_{H^0} (blue lines), the $b\bar{b}$ and gg channels still contribute significantly and generate a large amount of events with very slow staus.

At this point we want to comment again on scenarios with a heavy, decoupled H^0 boson such as those considered in figure 7.9. The contributions from H^0-boson-mediated processes are suppressed in this case, and the same is true if the H^0 boson is far off-shell ($m_{H^0} \ll 2m_{\tilde{\tau}_1}$). Still, the $b\bar{b}$ and gg channels can be sizeable if h^0-mediated processes are important. For large $\tilde{\tau}_1\tilde{\tau}_1^* h^0$ couplings (large left-right mixing, large $|\mu| \tan\beta$ and/or large $|A_\tau|$), we find that the additional production mechanisms, and predominantly the gg-fusion channel, can give cross section contributions of the same order of magnitude as the Drell–Yan induced process. The shapes of the corresponding p^{T} and β distributions are found to be similar to those of the Drell–Yan prediction but have a slightly softer p^{T} spectrum.

To summarize, cuts on p^{T} or β affect the three production channels to a very different extent and thus change the relative importance of each of the contributions considerably. If the cuts (8.1) are applied, large parts of the additional $b\bar{b}$ and gg channel contributions can be lost. We therefore recommend to relax these cuts in future experimental searches to increase the sensitivity especially for cosmological motivated scenarios with $2m_{\tilde{\tau}_1} \approx m_{H^0}$, even when this implies that increased backgrounds have to be taken into account. A more detailed study of the interplay between different cut values and expected backgrounds would be required but is beyond the scope of this work.

8.1.2 Prospects for SUSY parameter determination

In this subsection we want to demonstrate how one can exploit the fact that the Drell–Yan production cross section depends only on the stau mass and mixing angle, whereas the $b\bar{b}$ and gg channels also depend on other SUSY parameters. In fact, the interplay of the Drell–Yan cross section and the additional channels might turn out to be helpful to determine SUSY parameters.

If signals of a quasi-stable stau are observed at the LHC, one of the first measurements will be the determination of the stau mass $m_{\tilde{\tau}_1}$ by using time-of-flight data from the muon chambers. The expected accuracy of such an $m_{\tilde{\tau}_1}$ measurement has been estimated to be $< 1\%$ [313, 382]. With such a precise knowledge of $m_{\tilde{\tau}_1}$, there are high hopes that further SUSY parameters can be extracted from the cross section and differential distributions by comparing experimental results and theoretical predictions. Clearly, such measurements are possible in the case of decay chains with several MSSM particles involved [313–322]. However, in the following we show, how such measurements could also be possible just from direct production. To disentangle those channels, appropriate jet and/or lepton vetoes are assumed. Moreover, such measurements require more integrated luminosity than needed for a potential stau discovery.

First of all, once the stau mass is known, the Drell–Yan production cross section can be given as a function of the stau mixing angle θ_τ alone. If also the direct stau production cross section can be identified experimentally, this will allow us to determine θ_τ in a scenario in which the stau pair production cross section is governed by the Drell–Yan channel. As shown in figures 7.8 (b) and 7.9 (a) and as already discussed, the Drell–Yan cross section is maximal in case of an almost purely left-handed $\tilde{\tau}_1$ and minimal for $\theta_\tau \approx \pi/2$. An excess of the experimentally obtained cross section over the Drell–Yan expectation at $\theta_\tau \approx \pi/2$ would thus point to $\theta_\tau < \pi/2$ and non-negligible mixing between the left-handed and right-handed eigenstates in Drell–Yan-channel-dominated scenarios. Furthermore, a sizeable deviation from $\theta_\tau \approx \pi/2$ may support also the hypothesis that the observed CHAMP is indeed a stau and not a quasi-stable dominantly right-handed selectron or smuon.

However, in general, an experimental cross section larger than the minimal Drell–Yan expectation for a certain mass could imply both $\theta_\tau < \pi/2$ or also sizeable contributions from $b\bar{b}$ annihilation and gg fusion; cf. figures 7.8 (b) and 7.9 (a). On the other hand, a significant excess of the measured cross section over the maximal Drell–Yan cross section prediction may provide a first hint for the importance of the $b\bar{b}$-annihilation and gg-fusion processes calculated in this chapter; see also section 8.3 below.

These possible ambiguities in the interpretation of experimental findings on the integrated cross section could be resolved by studying also the differential distributions. As we have seen above, the p^{T} and β distributions differ strongly from the Drell–Yan prediction when the $b\bar{b}$ and gg channels are important. Also the distribution with respect to the invariant mass of the produced stau pair, $m_{\tilde{\tau}_1\tilde{\tau}_1^*}$, can be helpful in this respect. In fact, the invariant mass distribution might allow even for the determination of the mass m_{H^0} and the width Γ_{H^0} of the H^0 boson: If $2m_{\tilde{\tau}_1} < m_{H^0}$, i.e., if the H^0 boson can go on-shell in the $b\bar{b}$ and gg channels, there is the possibility to see the resonance of the H^0 boson in the invariant mass distribution

Benchmark point		α	β	γ	ϵ
$m_{1/2}$	[GeV]	600	1050	600	440
m_0	[GeV]	800	30	600	20
$\tan\beta$		55	55	55	15
A_0	[GeV]	1600	60	1200	-250
$m_{\tilde{\tau}_1}$	[GeV]	193	136	148	153
θ_τ		81°	73°	77°	76°
m_{H^0}	[GeV]	402	763	413	613
Γ_{H^0}	[GeV]	15	26	16	2.2
$m_{\tilde{g}}$	[GeV]	1397	2276	1385	1028
avg. $m_{\tilde{q}}$	[GeV]	1370	1943	1287	894
μ	[GeV]	667	1166	648	562
A_τ	[GeV]	515	-143	351	-275
BR($b \to s\gamma$)	[10^{-4}]	3.08	3.03	2.94	3.00
BR($B_s^0 \to \mu^+\mu^-$)	[10^{-8}]	1.65	1.04	2.44	0.30
a_μ	[10^{-10}]	13.2	11.5	16.8	18.7
CCB [365]		✓	–	✓	✓
$Y_{\tilde{\tau}_1}$	[10^{-15}]	3.5	2.5	37.7	164

Table 8.1: Benchmark CMSSM scenarios α, β, γ, and ϵ defined by the given values of $m_{1/2}$, m_0, $\tan\beta$, and A_0. For all points, $\mu > 0$. Low-scale masses and parameters and quantities that are subject to the constraints discussed in section 7.1 are listed. The CCB constraint (7.11), as obtained in [365], is respected by the scenarios α, γ, and ϵ, whereas point β is in tension with this constraint.

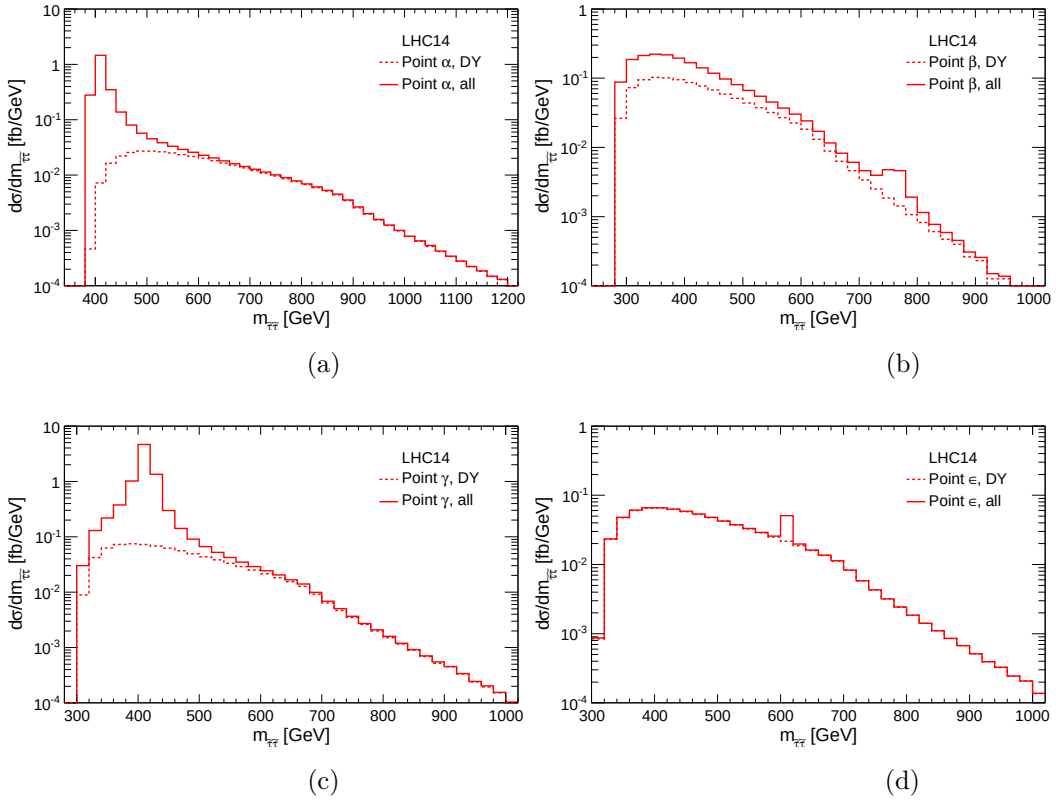

Figure 8.3: Invariant mass distributions of directly produced $\tilde{\tau}_1\tilde{\tau}_1^*$ pairs at the LHC with $\sqrt{S} = 14$ TeV for the benchmark points (a) α, (b) β, (c) γ, and (d) ϵ. Drell–Yan predictions are shown by the dashed lines and the full cross sections, including the $b\bar{b}$ and gg channels, by the solid lines.

of the staus at $m_{\tilde{\tau}_1\tilde{\tau}_1^*} \simeq m_{H^0}$ with a width given by Γ_{H^0}.

To illustrate this procedure, we consider four benchmark points, α, β, γ, and ϵ within the framework of the CMSSM with parameters listed in table 8.1. These benchmark points are in conflict with recent observations at the LHC (particularly they yield a too small Higgs mass and are excluded from direct searches). This will be discussed in detail in section 8.2. However, for the purpose of this section they are still useful. The low-energy SUSY spectrum is obtained using `SPheno` [82], while the Higgs sector is recalculated with `FeynHiggs`. We also refer to the constraints discussed in section 7.1, evaluated with `SuperISO` [383], and provide the thermal relic stau yield $Y_{\tilde{\tau}_1}$ as calculated with `micrOMEGAs` [354]. Benchmark points α and β are equivalent to points B and C of ref. [346], respectively, but we have adjusted m_0 for point α and $m_{1/2}$ for point β so that `SPheno` provides low-energy spectra that are similar to the ones of those points B and C. Point γ is very similar to point α but has a much larger stau yield. Point ϵ was already introduced in ref. [379]. Here, we are mainly interested in the ratio of $m_{\tilde{\tau}_1}$ and m_{H^0}. In all four benchmark scenarios, stau production via an on-shell H^0 exchange is possible. We have $2m_{\tilde{\tau}_1} \approx m_{H^0}$ for point α, $2m_{\tilde{\tau}_1} < m_{H^0}$ for point γ, and $2m_{\tilde{\tau}_1} \ll m_{H^0}$ for points β and ϵ. The stau-Higgs couplings are smallest for point ϵ, where $\tan\beta$ is relatively small.

In figure 8.3 we display the invariant mass distributions for the four benchmark points at the LHC with $\sqrt{S} = 14$ TeV. The kinematical cuts (8.1) are applied, with the requirement $|\eta| < 2.4$ for both staus. The invariant mass distributions show a resonance peak at the mass of the H^0 boson on top of the Drell–Yan continuum in all four considered scenarios. For point α considered in figure 8.3 (a), the peak is close to the threshold, $m_{\tilde{\tau}_1 \tilde{\tau}_1^*} \approx 2m_{\tilde{\tau}_1}$, and the distribution falls off steadily at higher invariant masses. Such a Higgs resonance at the beginning of the invariant mass distribution is a strong hint towards efficient stau annihilation in the early Universe, as further discussed in section 8.3 below. In the invariant mass distribution for point γ shown in figure 8.3 (c), the H^0 resonance lies on top of the maximum of the Drell–Yan contribution and the peak is very pronounced. For points β and ϵ, the Drell–Yan continuum is dominant and the resonance appears as a small bump at the tail of the distribution as can be seen in figures 8.3 (b) and (d). Note that although the $b\bar{b}$ and gg channels do not distort much the shape of the Drell–Yan curve in scenario β, they increase the differential cross section sizeably. This typically happens for large left-right mixing and large $\tan\beta$ even in the case of an heavy decoupled H^0 boson, see figure 7.9.

Both the α and γ scenarios would allow for a determination of the mass m_{H^0} and also the width Γ_{H^0} (especially in case of point γ) with a few fb^{-1} of data at the LHC with $\sqrt{S} = 14$ TeV. Nevertheless, also in scenarios with a rather heavy H^0 boson (such as point β) and in scenarios with small $\tan\beta$ (such as point ϵ), the LHC might eventually be able to determine the mass m_{H^0} from the invariant mass distribution of the directly produced long-lived $\tilde{\tau}_1\tilde{\tau}_1^*$ pairs. Such a procedure only requires $2m_{\tilde{\tau}_1} < m_{H^0}$ and is thus generic in large parts of the MSSM parameter space and within the CMSSM. Here a future study of theoretical and experimental uncertainties including detector effects and the possible contamination with SUSY backgrounds from cascade decays is necessary to allow for more precise predictions.

8.1.3 Prospects for the stopping of staus

Quasi-stable staus may allow for an intriguing non-standard collider phenomenology. Because of ionization energy loss, staus will be slowed down when traversing the detector material. In this way, staus that are produced with a relatively small initial velocity of

$$p_{\tilde{\tau}_1}/m_{\tilde{\tau}_1} = \beta\gamma \lesssim 0.45 \tag{8.2}$$

are expected to get trapped, e.g., in the calorimeters of the ATLAS detector [324] or in some additional dedicated stopping detector outside of the CMS detector [328]. This can allow for experimental studies of the stau decays. Measurements of $\tau_{\tilde{\tau}_1}$ could then probe the coupling strength that governs the stau decays and thereby $m_{\widetilde{G}}$ [311] or the Peccei–Quinn scale f_{PQ} [221, 229]. Moreover, one may be able to determine the mass of the EWIP LSP by analyzing the kinematics of the mentioned two-body decays [221, 229, 311, 323, 328]. In the gravitino LSP case, a kinematically determined $m_{\widetilde{G}}$ would allow us to test the Planck scale $\Lambda_{\mathrm{Planck}}$ microscopically [311] and to probe at colliders the reheating temperature T_{R} and thereby the viability of thermal leptogenesis [225]. Also studies of three-body stau decays, which could give further insights into the nature of the EWIP LSP are conceivable [221, 229, 311, 328]. The success of such studies will depend sensitively on the number of staus that can be stopped

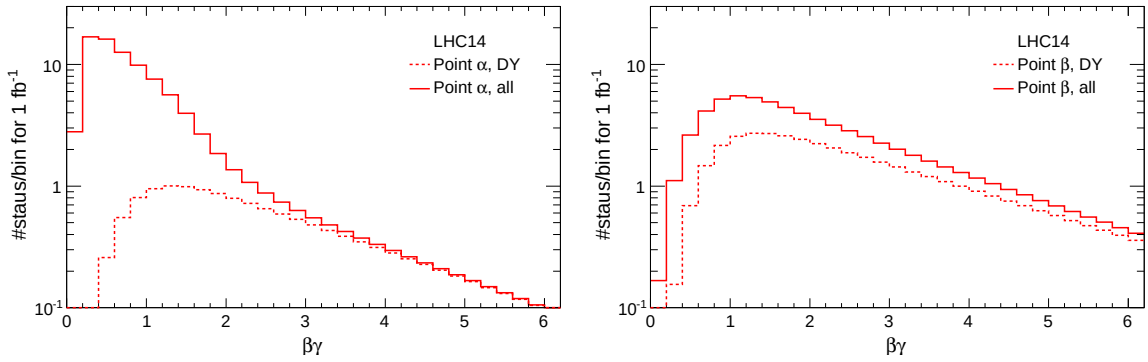

(a) (b)

Figure 8.4: Directly produced staus as a function of $\beta\gamma = |\mathbf{p}|/m$ at the LHC with $\sqrt{S} = 14$ TeV for an integrated luminosity of $L = 1$ fb^{-1}. The full results, including $b\bar{b}$ and gg channels, are shown by the solid lines and the Drell–Yan predictions by the dashed lines. Staus with $\beta\gamma \lesssim 0.45$ are expected to get stopped in the LHC detectors. Distributions are shown for the benchmark points (a) α and (b) γ, which are defined in table 8.1.

for the analysis of their decays and thereby on the initial velocity distribution.

In the following, we show that staus produced directly via the $b\bar{b}$ and gg channels provide a large additional source of potentially stopped objects, especially in the cosmologically motivated scenarios discussed in section 7.1.2.

In figure 8.4 we give the number of directly produced staus for an integrated luminosity of $L = 1$ fb^{-1} at the LHC with $\sqrt{S} = 14$ TeV as a function of $\beta\gamma = |\mathbf{p}|/m$ for the benchmark points α and β introduced above and defined in table 8.2. We only require the pseudo-rapidity of a stau to fulfill $|\eta| < 2.4$ to be included in the shown histograms. No other kinematical cuts are imposed as we are especially interested in very slow moving objects. We count each produced stau individually.

In both scenarios α and β, the number of potentially stopped staus, i.e., those with $\beta\gamma < 0.45$, is enlarged when the $b\bar{b}$ and gg channels are included in the cross section prediction. This enhancement is particularly substantial in scenario α where $2m_{\tilde{\tau}_1} \approx m_{H^0}$ and where the staus at the H^0 boson resonance are thus produced almost at rest in the center of mass frame. Indeed, from the Drell–Yan process alone, one would expect less than one stopped stau. For an account of the experimental prospects, it is thus crucial to consider also the $b\bar{b}$ and gg channels.

8.2 Direct stau production within the CMSSM

As a benchmark study, in this section we investigate the direct pair production cross section of light staus within the CMSSM. We are interested in parameter regions with a quasi-stable $\tilde{\tau}_1$ LOSP, where the $\tilde{\tau}_1\tilde{\tau}_1^*$ cross section is of particular importance. We consider the m_0-$m_{1/2}$ plane of the CMSSM with $A_0 = 2m_0$, $\tan\beta = 55$, and $\mu > 0$, which is cosmologically moti-

vated by the possible occurrence of exceptional small stau yields [346]. In this plane, $\tan\beta$ is large and the $\tilde{\tau}_1$ prefers to be right-handed, i.e., $\theta_\tau > \pi/4$; this is generic in the CMSSM due to the different running of the left-handed and right-handed soft masses. For the CMSSM benchmark scenarios introduced in section 8.1, we compare our results for direct stau production with indirect stau production mechanisms via the production and decay of other heavier SUSY particles. We find that direct stau production is often the dominant source of staus at colliders, in particular, at lower center-of-mass energies when the production of other SUSY particles is suppressed by their heavier masses.

The following CMSSM results are shown as an important benchmark example. However, the CMSSM parameter plane discussed here is mainly excluded due to the recent observation of a Higgs particle with $m_{h^0} \approx 125 - 126$ GeV, the observation of $\mathrm{BR}(B_s \to \mu^+\mu^-)$ found in agreement with SM predictions and partly due to the new limit, eq. (3.17). In general, within the CMSSM it became impossible to fulfill these constraints in regions where at the same time exceptional stau yields are realized. This has important consequences: for a standard cosmology the gravitino dark matter scenario within the CMSSM is excluded for SUSY masses allowing thermal leptogenesis or being accessible at the LHC. Nevertheless, this should rather be seen as a problem for the CMSSM where parameters are tightly related. In general, within the MSSM, m_{A^0} is essentially a free parameter and a heavy Higgs resonance together with large enough A_τ can allow for exceptional small relic stau abundances, while all other constraints are independently fulfilled. In section 8.3 we show examples how this can be achieved in generalizations of the CMSSM, namely in a model with non-universal gaugino masses.

8.2.1 CMSSM scans of the direct stau pair production cross section

In figure 8.5 we show in a m_0-$m_{1/2}$ plane of the CMSSM the direct stau production cross section at the LHC with $\sqrt{S} = 7$ TeV (top) and $\sqrt{S} = 14$ TeV (bottom), as well as mass contours and excluded/disfavored parameter regions. For $A_0 = 2m_0$, $\tan\beta = 55$ and $\mu > 0$, we consider the region in which the $\tilde{\tau}_1$ is the LOSP. Again, we compute the low-energy SUSY spectrum with `SPheno`, while the Higgs sector is reevaluated with `FeynHiggs`. Flavor constraints are evaluated using `SuperISO`. The cross section prediction includes the Drell–Yan channels with NLO K-factors, the $b\bar{b}$ annihilation and gg fusion contributions. The cuts (8.1), adequate for a long-lived stau, are applied. The white area in the lower left is excluded by a tachyonic spectrum, impossible electroweak symmetry breaking (EWSB), or a stau mass $m_{\tilde{\tau}_1} \leq 82$ GeV below the conservative LEP limit (3.15). In the upper left white area, the LOSP is the lightest neutralino $\tilde{\chi}_1^0$ (as indicated). In the gray area around $m_0 \sim m_{1/2} \sim 500$ GeV shown for $\sqrt{S} = 14$ TeV, $\mathrm{BR}(B_s^0 \to \mu^+\mu^-)$ exceeds the upper limit given in (3.22). The hatched area is disfavored by the CCB constraint (7.11). Contours for a constant Higgs mass of $m_{h^0} = 113$ GeV and 114 GeV are shown as thin solid black lines. The dashed black lines are $m_{\tilde{\tau}_1}$ contours and the solid white lines m_{H^0} contours, where the associated mass values are indicated on the respective contours in units of GeV.

The cross section depends mainly on $m_{\tilde{\tau}_1}$ and m_{H^0} and varies over several orders of magnitude in the given parameter ranges. At the LHC with $\sqrt{S} = 14$ TeV, it reaches 10^3 fb in the region with $m_0 \lesssim 700$ GeV and $m_{1/2} \lesssim 500$ GeV and drops to $\lesssim 2 \times 10^{-2}$ fb for, e.g.,

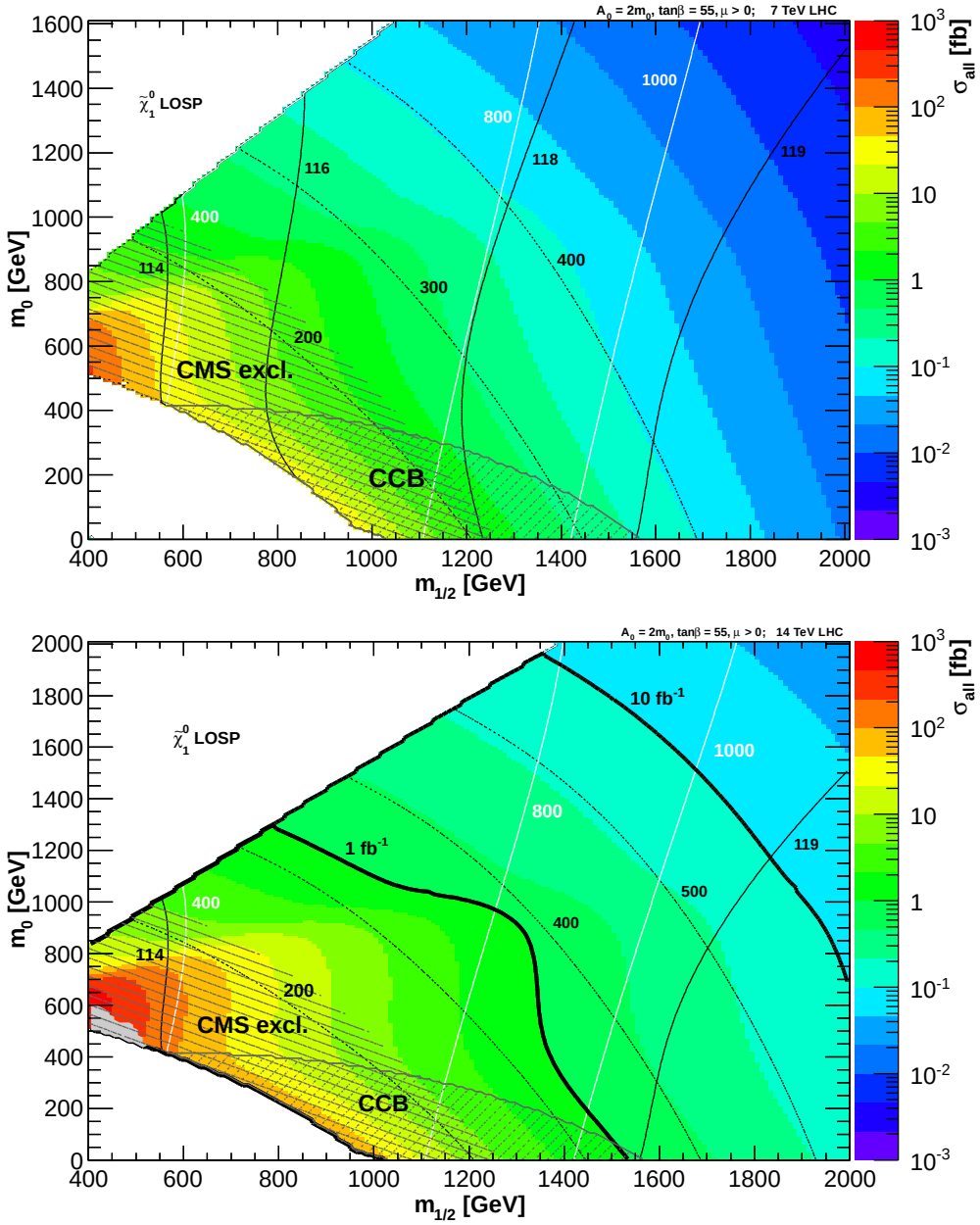

Figure 8.5: Contours of the total direct $\tilde{\tau}_1\tilde{\tau}_1^*$ production cross section (shaded, colored) at the LHC with $\sqrt{S} = 7$ TeV (top) and 14 TeV (bottom) after the cuts (8.1) in the CMSSM m_0-$m_{1/2}$ plane with $\tan\beta = 55$, $A_0 = 2m_0$, and $\mu > 0$. The white region in the lower left is excluded because of a tachyonic spectrum, impossible EWSB, or $m_{\tilde{\tau}_1} \leq 82$ GeV. In the upper white area, the lightest neutralino $\tilde{\chi}_1^0$ is the LOSP. Parameter points in the gray area around $m_0 \sim m_{1/2} \sim 500$ GeV do not respect the constraint $\mathrm{BR}(B_s^0 \to \mu^+\mu^-) < 4.3 \times 10^{-8}$. The lower hatched area is in tension with the CCB constraint (7.11). The thin solid black lines indicate m_{h^0}, the dashed black lines $m_{\tilde{\tau}_1}$, and the white lines m_{H^0}, where the mass values are given in units of GeV at the respective contour. For a naive estimate of the discovery potential at $\sqrt{S} = 14$ TeV, thick black lines show regions in which at least one $\tilde{\tau}_1\tilde{\tau}_1^*$-pair-production event is expected for integrated luminosities of $\mathcal{L} = 1$ fb^{-1} and 10 fb^{-1}. The striped area at small $\tilde{\tau}_1$ masses is excluded by CMS by searches at $\sqrt{S} = 7$ TeV.

$m_0 \sim m_{1/2} \sim 2$ TeV, as can be seen in the lower panel of figure 8.5. When going down from $\sqrt{S} = 14$ TeV to 7 TeV, considered in the upper panel of figure 8.5, we observe a decrease of the cross section by up to about a factor of 5 (see also figures 7.10 and 8.1). To give a naive estimate of the discovery potential, we also show contours (thick lines) on which one $\tilde{\tau}_1\tilde{\tau}_1^*$-pair-production event is expected for integrated luminosities of $\mathcal{L} = 1$ fb^{-1} and 5 fb^{-1} at $\sqrt{S} = 7$ TeV and $\mathcal{L} = 1$ fb^{-1} and 10 fb^{-1} at $\sqrt{S} = 14$ TeV. A more realistic determination of the discovery reach and/or the exclusion limits should be performed in the context of a detailed study including detector effects. Such a study has been performed in the case of direct Drell–Yan production [380].

The actual shape of the cross section and mass contours in the m_0-$m_{1/2}$ planes can easily be understood. We focus here on parameter regions with a $\tilde{\tau}_1$ LOSP, where typically $m_{1/2} > m_0$. For $\tan\beta > 20$, the A^0 mass can (neglecting Yukawa interactions) approximately be written as [384]

$$m_{A^0}^2 \approx m_0^2 + 2.5\ m_{1/2}^2 \tag{8.3}$$

and thus m_{A^0} is mainly determined by $m_{1/2}$. For $m_{1/2} \gg 0$, the Higgs sector is then typically in the decoupling limit, where $m_{H^0} \approx m_{A^0}$, and thus m_{H^0} also mainly determined by $m_{1/2}$. The dependence of $m_{\tilde{\tau}_1}$ on m_0 and $m_{1/2}$ is less intuitive in the considered parameter range ($\tilde{\tau}_1$ LOSP, large $\tan\beta$, sizeable Yukawa couplings), but the relation [384]

$$m_{\tilde{\tau}_1}^2 \propto m_0^2 + 0.15\ m_{1/2}^2 \tag{8.4}$$

still holds. Thus, one finds for $m_{1/2} \gg m_0$ that always $m_{H^0} > 2m_{\tilde{\tau}_1}$. For the stau production cross section, this means that there can be important contributions from the $b\bar{b}$ and gg channels in the region $m_{1/2} \gg m_0$, where the H^0 boson can go on-shell. Towards large m_0 and $m_{1/2}$ (as for example required for $m_{h^0} \approx 125$ GeV), however, the $\tilde{\tau}_1$ and (even faster) the H^0 become heavy. Then, contributions from the $b\bar{b}$ and gg channels become less important compared to the Drell–Yan channel. If the Drell–Yan contributions dominate, the overall production cross section is basically a function of the $\tilde{\tau}_1$ mass and decreases strongly for higher $m_{\tilde{\tau}_1}$.

Close to the boundary of the $\tilde{\chi}_1^0$ LOSP region, where $m_0 \approx m_{1/2}$, the $\tilde{\tau}_1$ gets heavier relative to the H^0 boson so that $2m_{\tilde{\tau}_1} > m_{H^0}$. This means that the direct stau production via an on-shell H^0 boson is no longer possible. However, the position of the transition at $2m_{\tilde{\tau}_1} = m_{H^0}$ depends strongly on $\tan\beta$. For large $\tan\beta$, bottom and tau Yukawa couplings can be sizable and drive down the masses of the heavy Higgses. For small $\tan\beta$, this transition lies mostly within the $\tilde{\chi}_1^0$ LOSP region and only for very large values of $m_{1/2}$ within the $\tilde{\tau}_1$ LOSP region. Thus, for smaller values of $\tan\beta$, contributions from on-shell H^0 exchange are a generic feature of the CMSSM, as one usually finds $2m_{\tilde{\tau}_1} < m_{H^0}$.

Let us emphasize that even if the $b\bar{b}$ and gg contributions are not necessarily large in parameter regions with $m_{H^0} > 2m_{\tilde{\tau}_1}$, i.e., when the H^0 boson is heavy, this configuration still opens the channels for stau production via on-shell H^0 exchange. As discussed in section 8.1.2, this could allow us to determine the H^0 boson width and mass by investigating the $\tilde{\tau}_1\tilde{\tau}_1^*$ invariant mass distribution.

Benchmark point		α	β	γ	ϵ
LHC 7 TeV					
$\sigma(\tilde{\tau}_1\tilde{\tau}_1^*)_{\rm DY}$	[fb]	3.2(2.3)	12.5 (7.3)	9.0 (5.6)	7.95 (5.00)
$\sigma(\tilde{\tau}_1\tilde{\tau}_1^*)_{b\bar{b}}$	[fb]	9.8 (5.1)	0.03 (0.02)	19.2 (16.5)	0.07 (0.06)
$\sigma(\tilde{\tau}_1\tilde{\tau}_1^*)_{\rm gg}$	[fb]	0.1 (0.1)	3.3 (2.4)	0.32 (0.25)	0.01 (0.01)
$\sigma(\tilde{\tau}_1\tilde{\tau}_1^*)_{\rm all}$	[fb]	13.1 (7.5)	15.8 (9.7)	28.5 (22.4)	8.03 (5.07)
$\sigma(\tilde{g}\tilde{g})$	[fb]	0.05	10^{-6}	0.06	2.57
$\sigma(\tilde{g}\tilde{q})$	[fb]	0.63	4×10^{-4}	0.99	37.36
$\sigma(\tilde{q}\tilde{q})$	[fb]	1.18	0.006	2.41	77.25
$\sigma(\tilde{\chi}\tilde{q})+\sigma(\tilde{\chi}\tilde{g})$	[fb]	0.481	0.007	0.72	12.77
$\sigma(\tilde{\chi}\tilde{\chi})$	[fb]	20.4	0.29	19.8	91.78
LHC 14 TeV					
$\sigma(\tilde{\tau}_1\tilde{\tau}_1^*)_{\rm DY}$	[fb]	11.2 (5.64)	37.5 (15.9)	28.0 (12.4)	24.7 (11.2)
$\sigma(\tilde{\tau}_1\tilde{\tau}_1^*)_{b\bar{b}}$	[fb]	58.4 (27.0)	0.7 (0.2)	113.3 (87.1)	0.5 (0.4)
$\sigma(\tilde{\tau}_1\tilde{\tau}_1^*)_{\rm gg}$	[fb]	0.7 (0.4)	17.4 (11.1)	1.8 (1.3)	0.07 (0.05)
$\sigma(\tilde{\tau}_1\tilde{\tau}_1^*)_{\rm all}$	[fb]	70.3 (33.1)	55.6 (27.2)	143.1 (100.8)	25.3 (11.6)
$\sigma(\tilde{g}\tilde{g})$	[fb]	20.2	0.12	20.8	232.19
$\sigma(\tilde{g}\tilde{q})$	[fb]	104.4	2.46	133.2	1328.4
$\sigma(\tilde{q}\tilde{q})$	[fb]	92.5	6.46	139.0	1301.1
$\sigma(\tilde{\chi}\tilde{q})+\sigma(\tilde{\chi}\tilde{g})$	[fb]	16.9	1.08	22.4	175.12
$\sigma(\tilde{\chi}\tilde{\chi})$	[fb]	134.5	6.40	131.1	422.2

Table 8.2: Hadronic cross sections for various SUSY pair production processes at the LHC with $\sqrt{S} = 7$ TeV and 14 TeV. For direct $\tilde{\tau}_1\tilde{\tau}_1^*$-pair production, we list our cross section results before and after applying the kinematical cuts (8.1), where the latter are given in parentheses. The other cross sections are inclusive NLO results obtained with `Prospino 2`, where no kinematical cuts have been considered.

8.2.2 Direct stau production vs. staus from cascade decays

So far we have focused on the analysis of direct stau production. But in a $\tilde{\tau}_1$ LOSP scenario, staus will also be generated in any process where heavier sparticles are produced. These cascade down to lighter sparticles and eventually into the LOSP, emitting SM particles. At hadron colliders, the largest contribution to the overall SUSY cross section is usually expected to originate from the production and subsequent decay of color-charged SUSY particles, i.e., squarks and gluinos. However, also direct production of neutralinos and charginos (e.g., $\tilde{\chi}_i^0\tilde{\chi}_j^\pm$) and associated production of a neutralino or chargino with a gluino or squark can give sizeable contributions in large parts of the allowed SUSY parameter space.

In table 8.2 we compare our predictions for the direct $\tilde{\tau}_1\tilde{\tau}_1^*$-pair production cross sections contributions from the Drell–Yan, $b\bar{b}$ annihilation, and gg fusion channels with the inclusive cross section for other SUSY particle production cross sections, calculated at NLO with `Prospino 2`, for the benchmark points defined in table 8.1. We sum over all possible combinations of squark, neutralino, and chargino eigenstates. For simplicity, we consider inclusive cross sections without any kinematical cuts. For the direct stau production channels we additionally give the cross sections after applying the cuts (8.1) in parentheses. Considering the LHC, each cross section is listed for $\sqrt{S} = 7$ TeV and 14 TeV.

From a comparison of the inclusive production cross sections, we can see that direct stau production is an important source of staus for the benchmark points α, β, and γ at the LHC with $\sqrt{S} = 7$ TeV. Only electroweak neutralino/chargino pair production ($\tilde{\chi}\tilde{\chi}$) can give comparable contributions. We even find that direct stau production can constitute the dominant part of the overall SUSY cross section together with $\tilde{\chi}\tilde{\chi}$ production. The other cross sections are suppressed at $\sqrt{S} = 7$ TeV by the heavier masses of squarks and gluinos. The situation changes for $\sqrt{S} = 14$ TeV, where the center-of-mass energy is high enough so that strongly interacting SUSY particles can be produced copiously. However, for point β, where $m_{1/2}$ is particularly large, the gluino is so heavy that direct stau production is always the dominant source for staus at colliders.

Benchmark point β is considered to illustrate the impact of a large $\tilde{\tau}_1\tilde{\tau}_1^* h^0$ coupling. However, such very large couplings are in strong conflict with CCB constraint (see eq. (7.11)). For this point, the H^0 boson is very massive and $b\bar{b}$ annihilation and gluon fusion into an intermediate H^0 boson is suppressed by the heavy particle's propagator. Stau production is thereby dominated by the Drell–Yan channel and gets sizeable contributions from the gluon fusion channel, where especially processes mediated by the h^0 boson are important.

Finally, benchmark scenario ϵ differs from the above scenarios by much smaller values of $m_{1/2}$ and $\tan\beta$. It could be considered a 'typical' $\tilde{\tau}_1$ LOSP scenario, without an exceptional stau yield. In this case, the direct stau production cross section is well described by the Drell–Yan process, whereas the $b\bar{b}$ and gg channels are basically negligible. Moreover, the indirect stau production mechanisms are much more efficient than the direct ones.

8.3 Collider tests of an exceptionally small relic stau abundance

In the preceding sections we have considered various aspects of stau production at hadron colliders with emphasis on parameter regions that allow for an exceptionally small yield of a long-lived stau (7.7). In the following we discuss the testability of such an exceptional yield

in collider experiments.

Excess of direct stau production cross sections over Drell–Yan predictions

Based on our results in sections 7.2.3 and 8.2, we already know that $b\bar{b}$-annihilation and gluon-fusion processes can lead to direct stau production cross sections that exceed the Drell–Yan predictions significantly, in particular, for $2m_{\tilde{\tau}_1} \lesssim m_{H^0}$ and/or enhanced stau-Higgs couplings. This motivates us to explore the ratio

$$R = \sigma(\tilde{\tau}_1\tilde{\tau}_1^*)_{\text{all}} \,/\, \sigma(\tilde{\tau}_1\tilde{\tau}_1^*)_{\text{DY}} \tag{8.5}$$

as a potential indicator for a cosmological scenario with an exceptionally small stau yield. Here the total direct stau production cross section, $\sigma(\tilde{\tau}_1\tilde{\tau}_1^*)_{\text{all}}$, and the Drell–Yan prediction, $\sigma(\tilde{\tau}_1\tilde{\tau}_1^*)_{\text{DY}}$, are considered after applying the cuts (8.1) for scenarios with a long-lived stau.

Before presenting and discussing our theoretical results for R, let us comment on its experimental determination, which has to rely on measurements of $m_{\tilde{\tau}_1}$ and $\sigma(\tilde{\tau}_1\tilde{\tau}_1^*)_{\text{all}}$. While an accuracy of $< 1\%$ is expected for a $m_{\tilde{\tau}_1}$ determination at the LHC [313, 382], $\sigma(\tilde{\tau}_1\tilde{\tau}_1^*)_{\text{all}}$ measurements may be more difficult, as mentioned in section 8.1. If indirect stau production is significant, they will require jet/lepton vetoes and/or additional kinematical cuts. With a precisely known $m_{\tilde{\tau}_1}$, $\sigma(\tilde{\tau}_1\tilde{\tau}_1^*)_{\text{DY}}$ can be calculated theoretically with an uncertainty of about a factor of 2 that is related to its dependence on θ_τ; see figures 7.8 (b) and 7.9 (a). To obtain a conservative estimate of R, one will then evaluate (8.5) with the maximum $\sigma(\tilde{\tau}_1\tilde{\tau}_1^*)_{\text{DY}}$ at $\theta_\tau = 0$. In fact, as already addressed in section 8.1.2, a measurement of θ_τ based on direct stau production is conceivable only if the Drell–Yan contribution dominates, i.e., for $R \simeq 1$. On the other hand, studies of staus produced in cascade decays may help to indirectly probe θ_τ [319] and thereby to determine R more precisely. Thus, we present in the following results for R that are not conservative estimates but theoretical predictions taking into account $\sigma(\tilde{\tau}_1\tilde{\tau}_1^*)_{\text{DY}}$ with its full θ_τ dependence. For an unknown θ_τ, $R > 2$ will then be a required indication for sizeable contributions of the $b\bar{b}$ and gg channels.

As an example we again turn to the CMSSM. In figure 8.6 the shaded (colored) contours indicate our theoretical predictions for R at the LHC with $\sqrt{S} = 7$ TeV (top panel) and 14 TeV (bottom panel) in the m_0-$m_{1/2}$ CMSSM plane with $A_0 = 2m_0$, $\tan\beta = 55$, and $\mu > 0$. The white lines show contours of $Y_{\tilde{\tau}_1} = 4 \times 10^{-15}$, 10^{-14}, 4×10^{-14} as obtained with `micrOMEGAs` [354]. The labeled (red) stars indicate the location of the benchmark points α, β, and γ, defined in table 8.1. The region disfavored by the CCB constraint (7.11) is now indicated by the gray hatched region.

The R contours show very explicitly that the Drell–Yan prediction can underestimate the direct $\tilde{\tau}_1\tilde{\tau}_1^*$ production cross section by up to a factor of 10 (20) for $\sqrt{S} = 7$ TeV (14 TeV). This demonstrates again the potential importance of the $b\bar{b}$ and gg channels included in our calculations.

In table 8.3 we list the R values at the LHC with $\sqrt{S} = 7$ TeV (R_{LHC7}) and 14 TeV (R_{LHC14}) and the stau yield $Y_{\tilde{\tau}_1}$ for the benchmark points α, β, γ, and ϵ. We see again that R increases when going from $\sqrt{S} = 7$ TeV to 14 TeV. This effect is most pronounced for the points α and γ for which $b\bar{b}$ annihilation dominates the direct stau production cross section. A

Benchmark point	α	β	γ	ϵ
R_{LHC7}	3.3	1.3	4.0	1.01
R_{LHC14}	5.8	1.7	8.1	1.04
$Y_{\tilde{\tau}_1}$ $[10^{-15}]$	3.5	2.5	37.7	164

Table 8.3: The stau yield $Y_{\tilde{\tau}_1}$ and $R = \sigma(\tilde{\tau}_1\tilde{\tau}_1^*)_{\text{all}}/\sigma(\tilde{\tau}_1\tilde{\tau}_1^*)_{\text{DY}}$ at the LHC with $\sqrt{S} = 7$ TeV (R_{LHC7}) and 14 TeV (R_{LHC14}) for the benchmark scenarios α, β, γ and ϵ, defined in table 8.1 and partially indicated in figure 8.6. The stau yield is obtained from `micrOMEGAs` and the R values from the respective cross sections after kinematical cuts (8.1) given in parentheses in table 8.2.

considerable 30% increase of R is predicted also for point β for which gluon fusion contributes up to about 40% of $\sigma(\tilde{\tau}_1\tilde{\tau}_1^*)_{\text{all}}$; cf. table 8.2.

Let us now turn to the main aspects of the $Y_{\tilde{\tau}_1}$ contours in figure 8.6; for additional details we refer to [346] in which those contours were studied in the same CMSSM plane. An exceptionally small yield (7.7) can be found in the two separate regions enclosed by the $Y_{\tilde{\tau}_1} = 4 \times 10^{-15}$ contour. The region, to which point α belongs, allows for primordial $\tilde{\tau}_1$ annihilation via the H^0 resonance, and the region, to which point β belongs, for efficient $\tilde{\tau}_1$ annihilation via enhanced stau-Higgs couplings. While the latter region is in conflict with the CCB constraint (7.11), we still include this point in our discussion of the testability of an exceptionally small $Y_{\tilde{\tau}_1}$ at colliders.

Comparing regions with $R \gtrsim 2$ to those with $Y_{\tilde{\tau}_1} < 4 \times 10^{-15}$, we find that there is no one-to-one link between a sizeable R value and an exceptionally small yield. For example, while the point β is associated with such an exceptional yield, we obtain $R < 2$, even at the LHC with $\sqrt{S} = 14$ TeV, as can be seen in table 8.3. Moreover, in figure 8.6, also moderate values of $R \simeq 2$–3 occur in the $2m_{\tilde{\tau}_1} \simeq m_{H^0}$ region enclosed by the $Y_{\tilde{\tau}_1} < 4 \times 10^{-15}$ contour. On the other hand, point γ is associated with $R \simeq 4$–8 while the yield at this point exceeds the limit (7.7) by more than one order of magnitude. Only for points such as α, one finds both an exceptionally large $R \simeq 3$–6 and an exceptionally small stau yield. Thus, a sizeable R could very well be a first hint for the possibility of efficient stau-annihilation in the early Universe but additional investigations will be crucial to clarify the situation.

8.4 Exceptional $Y_{\tilde{\tau}_1}$ and R in NUGM models

The resonance condition $2m_{\tilde{\tau}_1} \approx m_{H^0}$ is found in m_0–$m_{1/2}$ CMSSM planes only in a small horizontal region and for specific combinations of parameters. Furthermore, as mentioned above, within the CMSSM such regions are experimentally excluded by now. In less constrained models with non-universal gaugino masses (NUGM) or non-universal Higgs masses (NUHM) this mass pattern occurs in a more generic way and also in experimentally still viable parameter regions.

In figure 8.7 we consider a scenario in which the three gaugino soft masses are free parameters at the GUT scale, $M_1 \neq M_2 \neq M_3$, which is a framework denoted NUGM. We vary M_1 and set the other parameters to $m_0 = 400$ GeV, $M_2 = 1100$ GeV, $M_3 = 1100$ GeV,

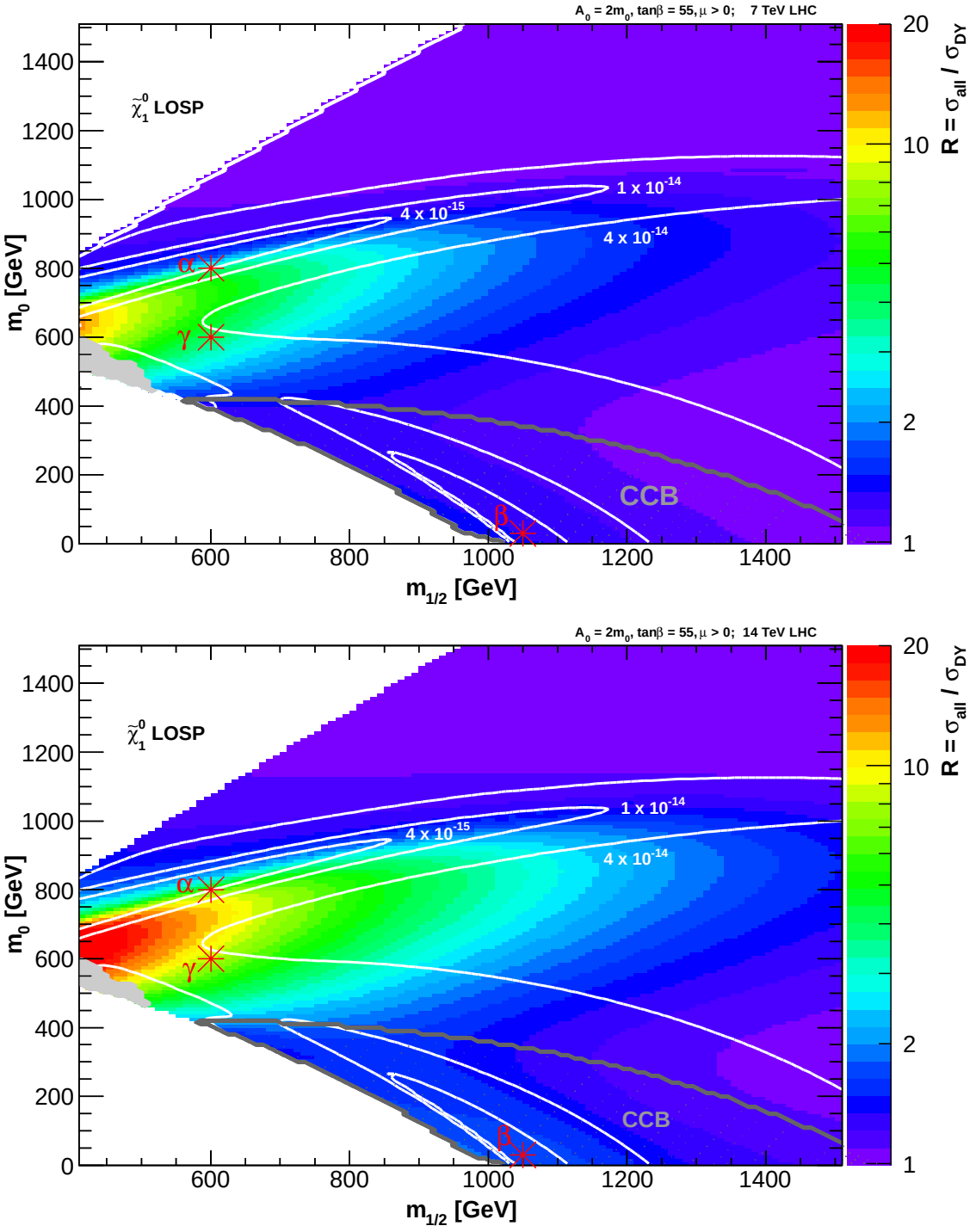

Figure 8.6: The ratio $R = \sigma(\tilde{\tau}_1\tilde{\tau}_1^*)_{\text{all}}/\sigma(\tilde{\tau}_1\tilde{\tau}_1^*)_{\text{DY}}$ (shaded contours, colored) for the LHC with $\sqrt{S} = 7$ TeV (top panel) and 14 TeV (bottom panel) and $Y_{\tilde{\tau}_1} = 4 \times 10^{-15}$, 10^{-14}, 4×10^{-14} (white lines) in the m_0-$m_{1/2}$ CMSSM plane with $A_0 = 2m_0$, $\tan\beta = 55$, and $\mu > 0$. The CCB constraint (gray hatched region) and excluded/unconsidered regions are as in figure 8.5. The labeled (red) stars indicate the location of the benchmark points α, β, and γ, defined in table 8.1.

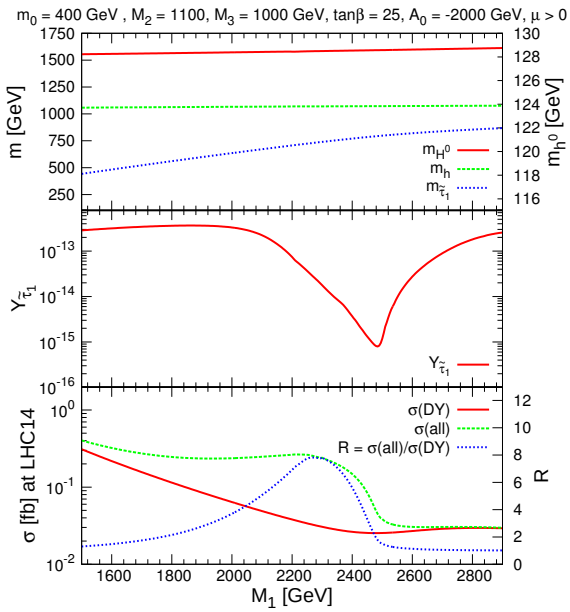

Figure 8.7: Masses $m_{\tilde{\tau}_1}$, m_{h^0}, and m_{H^0} (top panel), the stau yield $Y_{\tilde{\tau}_1}$ (middle panel), the cross sections $\sigma(\tilde{\tau}_1\tilde{\tau}_1^*)_{\text{all}}$ and $\sigma(\tilde{\tau}_1\tilde{\tau}_1^*)_{\text{DY}}$ and R at the LHC with $\sqrt{S} = 14$ TeV (bottom) in a NUGM model as a function of the bino soft mass parameter M_1, defined at the high scale together with $M_2 = 1100$ GeV, $M_3 = 1100$ GeV, $m_0 = 400$ GeV, $\tan\beta = 25$, $A_0 = -2000$ GeV.

$\tan\beta = 25$, $A_0 = -2000$ GeV, and $\mu > 0$. In the top panel, m_{H^0} is indicated by the solid (red) line, m_{h^0} by the dashed (green) line, and $m_{\tilde{\tau}_1}$ by the dotted (blue) line. The middle panel shows $Y_{\tilde{\tau}_1}$. In the bottom panel, $\sigma(\tilde{\tau}_1\tilde{\tau}_1^*)_{\text{DY}}$ is shown by the solid (red) line, $\sigma(\tilde{\tau}_1\tilde{\tau}_1^*)_{\text{all}}$ by the dashed (green) line, and R by the dotted (blue) line.

Considering the top panel, one sees that m_{H^0} only slightly increases with M_1 compared to the dependence of $m_{\tilde{\tau}_1}$ which is more sensitive to M_1. For $M_1 \simeq 2500$ GeV, one finds the resonance condition $2m_{\tilde{\tau}_1} = m_{H^0}$. In a region around this point, a significant depletion of the stau yield $Y_{\tilde{\tau}_1}$ by more than two orders of magnitude can be seen in the middle panel. At the resonance the light Higgs has a mass $m_{h^0} \approx 124$ GeV and is thus consistent with the recently observed state at the LHC. Furthermore, we want to note that the flavor constraints, eq. (3.23) and eq. (3.21) and the constraint from non-occurrence of CCBs are satisfied around the resonance region. To the left of this resonance point, i.e., for $M_1 < 2500$ GeV, $2m_{\tilde{\tau}_1} < m_{H^0}$ so on-shell H^0-boson exchange can contribute to direct stau production. Thereby, this leads to a significant contribution of the $b\bar{b}$ and gg channels to $\sigma(\tilde{\tau}_1\tilde{\tau}_1^*)_{\text{all}}$ and R increases significantly up to about $R \approx 8$. However, due to kinematical cuts (8.1) the maximum of $\sigma(\tilde{\tau}_1\tilde{\tau}_1^*)_{\text{all}}$ and of R is shifted away from the resonance point at which $Y_{\tilde{\tau}_1}$ approaches its minimum, and towards this resonance point, $\sigma(\tilde{\tau}_1\tilde{\tau}_1^*)_{\text{all}}$ and R decrease significantly.

At the resonance, $m_{\tilde{\tau}_1} \approx 760$ GeV and $\sigma(\tilde{\tau}_1\tilde{\tau}_1^*)_{\text{all}} \approx 0.05$ fb. Direct production of such a heavy stau will be testable at the LHC with 14 TeV and an integrated luminosity of about $\mathcal{L} = 200$ fb^{-1}.

8.5 Current status and future prospects

For a long-lived stau the best limit on direct production is set by CMS using 4.7 fb^{-1} at 7 TeV, see (3.17). With the currently available data from the 8 TeV run, exclusions for the production of a pair of staus produced via the Drell-Yan process up to $m_{\tilde{\tau}_1} \gtrsim 330$ GeV can be expected, assuming no significant excess in the data. A preliminary study yields the result given in (3.18).

Such an exclusion eliminates the possibility of exceptionally small stau yields from enhanced $\tilde{\tau}_1\tilde{\tau}_1 h^0$ couplings, as described in section 7.1.2. Due to CCB constraints the $\tilde{\tau}_1\tilde{\tau}_1 h^0$ coupling can not be large enough to allow $Y_{\tilde{\tau}_1} < 10^{-14}$ for $m_{\tilde{\tau}_1} \gtrsim 300$, as shown in [364].

This leaves the occurrence of the mass pattern $2m_{\tilde{\tau}_1} \simeq m_{H^0}$ together with moderate stau–stau–heavy-Higgs couplings, as only possibility to allow for exceptionally small stau yields. As discussed above, in such scenarios the direct stau production cross section can, but does not have to, be significantly enhanced compared to the pure DY prediction.

Within the CMSSM large values of $\tan\beta$ together with not too big $m_{1/2}$ is required to allow for $2m_{\tilde{\tau}_1} \simeq m_{H^0}$, as shown in section 8.2.1. Therefore, the possibility of a heavy-Higgs resonance is excluded due to a recent measurement of $\text{BR}(B_s \to \mu^+\mu^-)$, given in (3.21), and the observation of a SM-like Higgs at $m_{h^0} \approx 125$ GeV. However, within less constraint models this scenario remains viable.

On the other hand, in a $\tilde{\tau}_1$ NLSP and $\tilde{\chi}_1^0$ LSP scenario any direct stau production limits are still set by LEP, see (3.15). Using 20.7 fb^{-1} at $\sqrt{S} = 8$ TeV, ATLAS took a first look at direct stau production, where the staus directly decay into two neutralinos and two taus,

which both decay hadronically [385]. For a stau mass of $m_{\tilde{\tau}_1} = 140$ GeV they exclude cross sections larger than 0.17 pb, where the theoretical DY cross section for a purely left-handed stau is $\sigma_{\mathrm{DY}}^{\mathrm{NLO}}(m_{\tilde{\tau}_L} = 140) = 0.04$ pb.

Chapter 9

Conclusions

Supersymmetry remains one of the most appealing scenarios for physics beyond the Standard Model, which the ongoing experiments at the LHC are searching for. Most of the solutions to the shortcomings of the SM offered by SUSY require new particles around the TeV scale. Out of these predicted new states squarks and gluinos are strongly interacting and thus their production is expected to be dominant if they are not too heavy. But also electroweak production of sleptons, neutralinos and charginos can be sizable. The experiments at the LHC already performed many analyses exploiting various channels with the data collected during the first run, both for calored and electroweak production. They set impressive new limits, as until now no deviations from SM predictions have been observed. Nevertheless, there is a good chance that after the current energy upgrade there will be first hints for SUSY at the LHC.

In any case, a precise knowledge of SUSY particle production and decay processes including higher orders and detailed studies of motivated parameter regions and signatures are indispensable to exploit and guide current and future searches in the best way. This holds particularly for searches in difficult phase space regions and for future parameter determination. Both topics were covered in this work.

In this thesis we investigated how production of squarks can be combined with their decays including consistently NLO QCD corrections in all stages of the process. To this end we investigated different approximations at LO and NLO for processes with unstable intermediate particles. In particular, in the narrow-width approximation NLO corrections to production and decay factorize and can be calculated independently. Therefore, we provided calculations at NLO for squark–squark production and squark decays. These calculations have been implemented in a fully differential Monte Carlo program and soft and collinear divergences have been regularized via the phase-space slicing method. Different strategies to avoid a possible double-counting in the quark radiation contributions to the production have been investigated. Special care was given that integrated and differential results are independent of unphysical regulators. Additionally, we analytically calculated NLO corrections to the integrated total decay width of electroweakly decaying squarks. In this way we calculated all ingredients for the combined process in NWA at NLO.

As a first application of the explained procedure we presented a study of squark–squark

production and subsequent decays into lightest neutralinos at the LHC within the MSSM. In this way we provided fully differential predictions for the experimental signature $2j + \not{E}_T(+X)$ at NLO in QCD. The considered squark–squark channel should be understood as a first step for the calculation of all colored SUSY particle production channels. However, for heavy squarks and gluinos this is also the dominant channel. In contrast to previous calculations, we treat each flavour and chirality configuration of the squarks individually, allowing the combination of production cross sections and decay distributions in a consistent way. In any case, K-factors between different channels vary by up to almost 20%, which is not taken into account in studies performed until now. For the given signature we studied inclusive cross sections, differential distributions for jet observables, and experimental signatures with cuts, illustrating the effect of the NLO contributions. In general, the NLO corrections are important and, by our calculation the theoretical uncertainty on the level of differential distributions is reduced from about $\pm 30\%$ to $\pm 10\%$. Furthermore, fully differential NLO effects compared to a rescaling with a global NLO K-factor can differ by up to 40%, depending on the differential distribution and parameter point under consideration. Thus, such corrections should in general not be neglected for setting precise limits on the sparticle masses and model parameters. In model classes with compressed spectra such higher-order contributions become mandatory, as otherwise a reliable phenomenological prediction is not possible.

As a second application we provided an analysis at NLO of the contribution from squark–squark production and a subsequent "golden" decay chain to the experimental signature $2j + l^+l^- + \not{E}_T(+X)$, taking into account experimental cuts. We focused on the impact of NLO corrections on invariant mass distributions that can be used, in case of discovery of supersymmetric particles, for parameter determination. We observe that general shapes, besides smoothing of edges and kinks and a shift towards smaller invariant masses, are not strongly altered. This seems to be an universal behaviour despite the strong dependence of shapes on the parameter region.

We also analyzed the impact of NLO corrections including decays on the predictions for cut-and-count strategies used in discovery searches in the jets + $2l$(OS-SF) + $\not{E}_T$ channel. The impact of the corrections depend on the cuts applied and in general can be different from the result obtained rescaling LO predictions with flat K-factors obtained from the cross-section of just production without decays and cuts included. However, in particular cases, results obtained in this approximation can be in very good agreement with those from our calculation, provided that only the contributing chirality configurations are included in the calculation of the flat K-factor.

In our framework, results can be easily extended including off-shell effects in the electroweak decay chain. Also different kinds of experimental signatures emerging from different decay chains can be analyzed easily. In general an analogue calculation of such signatures from the other production channels of squarks and gluinos is desirable. Furthermore, also electroweak contributions of LO and NLO in production and decay should be merged in the calculation at some point. Additionally, off-shell effects in the strong part of the process and non-factorizable $\mathcal{O}(\alpha_s)$ corrections, which cannot be calculated in NWA, should be investigated.

Furthermore, we have studied the direct hadronic production of a pair of staus within the MSSM. In addition to the well-known Drell-Yan process, we considered production processes initiated by $b\bar{b}$ annihilation and gluon fusion, with all third-generation mixing effects taken into account. This allows us to provide reliable predictions of hadronic slepton production at $\mathcal{O}(\alpha_s^2\alpha^2)$. In parameter regions with non-negligible mixing these contributions can enhance the direct production cross section significantly and should always be included. This enhancement can be even larger than one order of magnitude. Particularly significant corrections are found when direct stau production can proceed via the exchange of an on-shell heavy CP-even Higgs boson H^0 and when the left-right-stau mixing is sizeable. Moreover, the contributions of the $b\bar{b}$ and gg channels are enhanced also in the case of large stau-Higgs couplings which are associated with large values of $\tan\beta$, $|\mu|$, and/or $|A_\tau|$ and thereby again with a sizeable left-right-stau mixing.

These predictions are independent of the stau lifetime and applicable in $\tilde{\chi}_1^0$ LSP scenarios as well as in settings in which the $\tilde{\tau}_1$ is long-lived, due to an EWIP LSP (for example a gravitino or axino). In long-lived stau scenarios sizeable left-right-stau mixing is motivated by exceptionally small relic stau yields, and in $\tilde{\chi}_1^0$ scenarios by a possible enhancement in the branching ratio $\mathrm{BR}(h^0 \to \gamma\gamma)$ compared to the SM prediction.

Assuming the $\tilde{\tau}_1$ being long-lived on the scale of colliders, we have provided cross section predictions for direct stau production at the LHC where necessary experimental cuts are applied. Once a deviation from SM backgrounds is observed, the parameters of the underlying theory have to be determined. We offered various ideas how, here, direct stau production can be of utter importance. For example, our results demonstrate that measurements of the distribution of direct stau production events as a function of the invariant stau-antistau mass can give $m_{\tilde{\tau}_1}$, independently of time-of-flight measurements, and, more importantly, the mass of the heavy CP-even Higgs boson m_{H^0}.

Also for a long-lived stau, we have provided cross section predictions for direct stau production at the LHC with $\sqrt{S} = 7$ TeV and 14 TeV within the CMSSM. Here, we compared direct production with production in cascade decays and interpreted recent exclusion limits from the experiments at the LHC. From this, at least within the CMSSM, the possibility of exceptionally small stau yields seems to be excluded. Finally, we have explored the testability of the conditions that allow for an exceptionally small stau yield at the LHC. Within the CMSSM and for a still viable NUGM scenario, we have studied whether an excess of the direct stau production cross section over the Drell–Yan prediction can be used as an indicator for the possibility of an exceptional yield. Although no one-to-one link is found, a large excess over the Drell–Yan prediction can very well be a first hint of efficient stau annihilation in the early Universe.

Appendix A

Squark production and decay

A.1 Renormalization constants and counter terms

Here, we list the counter terms for the renormalization of vertices and propagators in the NLO QCD one-loop amplitudes for squark–squark production and considered decays. These results follow [131]. We only consider squarks of the first two generations. Thus, L-R mixing can be neglected and the squark mixing matrix remains diagonal also at NLO. Feynman rules for the counter terms can be expressed in terms of field renormalization constants of squarks $Z_{\tilde{q}_{ia}}$, quarks $Z_{q_{ia}}$ and gluinos $Z_{\tilde{g}}$, which are defined by

$$q_{ia}^{\text{bare}} = q_{ia}^{\text{ren}} \left(1 + \frac{1}{2}\delta Z_{q_{ia}}\right), \qquad \tilde{q}_{ia}^{\text{bare}} = \tilde{q}_{ia}^{\text{ren}} \left(1 + \frac{1}{2}\delta Z_{\tilde{q}_{ia}}\right),$$
$$\tilde{g}^{\text{bare}} = \tilde{g}^{\text{ren}} \left(1 + \frac{1}{2}\delta Z_{\tilde{g}}\right), \tag{A.1}$$

together with renormalization constants for the strong coupling g_s, the strong Yukawa coupling $\hat{g}_s$, the squark masses and the gluino mass, defined by

$$g_s^{\text{bare}} = g_s^{\text{ren}}(1 + \delta Z_g), \qquad \hat{g}_s^{\text{bare}} = \hat{g}_s^{\text{ren}}(1 + \delta Z_{\hat{g}}), \tag{A.2}$$
$$m^{2\ \text{bare}}_{\tilde{q}_{ia}} = m^{2\ \text{ren}}_{\tilde{q}_{ia}} + \delta m^2_{\tilde{q}_{ia}}, \qquad m_{\tilde{g}}^{\text{bare}} = m_{\tilde{g}}^{\text{ren}} + \delta m_{\tilde{g}}, \tag{A.3}$$

where $i = \{u, d, c, s\}$ and $a = \{L, R\}$. These definitions relate bare and renormalized fields, masses and couplings.

All mass and field renormalization constants are determined according to the on-shell scheme. In the squark sector they read (see for example [386]),

$$\delta Z_{\tilde{q}_{ia}} = -\,\text{Re}\left\{\frac{\partial \Sigma_{\tilde{q}_{ia}}(p^2)}{\partial p^2}\right\}_{\big| p^2 = m^2_{\tilde{q}_{ia}}}, \qquad \delta m^2_{\tilde{q}_{ia}} = \text{Re}\left\{\Sigma_{\tilde{q}_{ia}}(m^2_{\tilde{q}_{ia}})\right\}, \tag{A.4}$$

for $\tilde{q}_{ia} = \{\tilde{q}_{uL}, \tilde{q}_{uR}, \tilde{q}_{dR}\}$ and $\Sigma_{\tilde{q}_{ia}}$ is the self energy of the squark $\tilde{q}_{ia}$. The renormalization constants for the left-handed down-type squarks are related (equal at order $\mathcal{O}(\alpha_s)$) to the up-type ones due to $SU(2)$ invariance:

$$\delta m^2_{\tilde{q}_{dL}} = \delta m^2_{\tilde{q}_{uL}}. \tag{A.5}$$

For the quarks the field renormalization constants are given by [252],

$$\delta Z_{q_{ia}} = -\,\mathrm{Re}\left\{\Sigma^a_{q_i}(m_q^2)\right\} - m_q^2\,\mathrm{Re}\left\{\frac{\partial}{\partial p^2}\Sigma^L_{q_i}(p^2) + \frac{\partial}{\partial p^2}\Sigma^R_{q_i}(p^2) + 2\frac{\partial}{\partial p^2}\Sigma^S_{q_i}(p^2)\right\}_{\Big|p^2=m_q^2}, \quad \text{(A.6)}$$

with $\Sigma^a_{q_i}$ being the self energy of the $a = \{L, R\}$ component of quark q_i in the general Lorentz decomposition of a fermion f, defined by

$$\Sigma_f(p^2) = \not{p} P_L \Sigma^L_f(p^2) + \not{p} P_R \Sigma^R_f(p^2) + m_f \Sigma^S_f(p^2)\,, \quad \text{(A.7)}$$

with the usual chiral projection operators $P_{L/R} = \frac{1}{2}(1 \mp \gamma_5)$. Here, the mass m_q^2 is not the actual mass of the quark (light-flavor quarks are considered massless), but the necessary regulator for collinear divergences.

Using again the decomposition defined in eq. (A.7), for the gluino, mass and field renormalization constants are fixed by

$$\begin{aligned} \delta m_{\tilde{g}} &= m_{\tilde{g}}\,\mathrm{Re}\left\{\Sigma^L_{\tilde{g}}(m_{\tilde{g}}^2) + \Sigma^S_{\tilde{g}}(m_{\tilde{g}}^2)\right\} \\ \delta Z_{\tilde{g}} &= -\,\mathrm{Re}\left\{\Sigma^L_{\tilde{g}}(m_{\tilde{g}}^2)\right\} - 2\; m_{\tilde{g}}^2\;\mathrm{Re}\left\{\frac{\partial}{\partial p^2}\left(\Sigma^L_{\tilde{g}}(p^2) + \Sigma^S_{\tilde{g}}(p^2)\right)\right\}_{\Big|p^2=m_{\tilde{g}}^2}, \end{aligned} \quad \text{(A.8)}$$

where due to the Majorana nature of the gluino $\Sigma_{\tilde{g}_L} = \Sigma_{\tilde{g}_R}$.

The renormalization constant for the strong coupling Z_g is defined in eq. (4.26) in the $\overline{\mathrm{MS}}$ scheme and $Z_{\hat{g}}$ in terms of Z_g in eq. (4.28).

The actual expressions of the counterterms relevant for squark–squark production and squark decay into neutralinos and charginos are given in the following.

- Self energy counter terms:

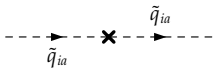

$$= \quad i[(p^2 - m^2_{\tilde{q}_{ia}})\delta Z_{\tilde{q}_{ia}} - \delta m^2_{\tilde{q}_{ia}}]$$

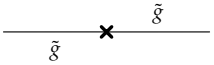

$$= \quad i[(\not{p} - m_{\tilde{g}})\delta Z_{\tilde{g}} - \delta m_{\tilde{g}}]$$

- Vertex counter terms:

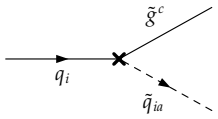

$$\begin{aligned} = \quad -i\tfrac{g_s}{\sqrt{2}}[\; &(\delta Z_{\tilde{q}_{iL}} + 2\delta Z_{\hat{g}_s} + \delta Z_{\tilde{g}} + \delta Z_{q_{iL}})\; P_L \\ &-(\delta Z_{\tilde{q}_{iR}} + 2\delta Z_{\hat{g}_s} + \delta Z_{\tilde{g}} + \delta Z_{q_{iR}})\; P_R\;]\; T^c \end{aligned}$$

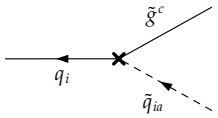

$$= \quad i\frac{g_s}{\sqrt{2}}[\ (\delta Z_{\tilde{q}_{iR}} + 2\delta Z_{\hat{g}_s} + \delta Z_{\tilde{g}} + \delta Z_{q_{iR}})\ P_R$$
$$-(\delta Z_{\tilde{q}_{iL}} + 2\delta Z_{\hat{g}_s} + \delta Z_{\tilde{g}} + \delta Z_{q_{iL}})\ P_L\ ]\ T^c$$

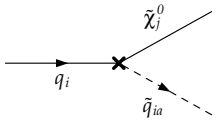

$$= \quad ie[A_{j-}(q_i)\ (\delta Z_{\tilde{q}_{iL}} + \delta Z_{q_{iL}})\ P_L$$
$$+A_{j+}(q_i)\ (\delta Z_{\tilde{q}_{iR}} + \delta Z_{q_{iR}})P_R]$$

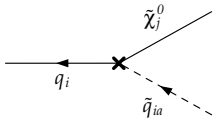

$$= \quad ie[A^*_{j+}(q_i)\ (\delta Z_{\tilde{q}_{iR}} + \delta Z_{q_{iR}})\ P_R$$
$$+A^*_{j-}(q_i)\ (\delta Z_{\tilde{q}_{iL}} + \delta Z_{q_{iL}})P_L]$$

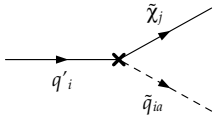

$$= \quad -ie\frac{B_j(q'_i)}{2s_W}(\delta Z_{\tilde{q}_{ia}} + \delta Z_{q'_{iL}})\ P_L$$

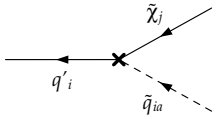

$$= \quad -ie\frac{B^*_j(q'_i)}{2s_W}(\delta Z_{\tilde{q}_{ia}} + \delta Z_{q'_{iL}})\ P_R$$

With,

$$A_{j+}(q_i) = \frac{1}{\sqrt{2}}\frac{e_q N_{j1}}{c_W}, \quad A_{j-}(q_i) = -\frac{1}{\sqrt{2}}\left(\frac{1}{6}\frac{N^*_{j1}}{c_W} + I^q_{3L}\frac{N^*_{j2}}{s_W}\right),$$
$$B_j(q_i) = U^*_{j1}, \quad B_j(q'_i) = V^*_{j1}\,.$$

A.2 Formulae for soft radiation

The soft-bremsstrahlung correction factor in eq. (4.33) involves the kinematical factors $C^{(tt,ut,uu)}_{\tilde{q}\tilde{q}'}$ from (4.34) and phase space integrals [135, 252]. We keep a finite quark mass m_q only in the mass-singular terms, which yields the following expressions for $\mathcal{I}_{ij}$ in the production process $qq' \to \tilde{q}\tilde{q}'$, where the labels i, j correspond to the assignment $q \to 1$, $q' \to 2$, $\tilde{q} \to 3$, and $\tilde{q}' \to 4$,

$$\begin{aligned}
\mathcal{I}_{ii} =& \frac{4}{3}\left[\ln\left(\frac{4(\Delta E)^2}{\lambda^2}\right) + \ln\left(\frac{m_i^2}{s_{12}}\right)\right] && \text{for } i = \{1,2\}, \quad \text{(A.9)}\\
\mathcal{I}_{ii} =& \frac{4}{3}\left[\ln\left(\frac{4(\Delta E)^2}{\lambda^2}\right) + \frac{1}{\beta_i}\ln\left(\frac{1-\beta_i}{1+\beta_i}\right)\right] && \text{for } i = \{3,4\},\\
\mathcal{I}_{12} =& \left(-\frac{1}{3}C^{(tt)}_{\tilde{q}\tilde{q}'} - \frac{1}{3}C^{(uu)}_{\tilde{q}\tilde{q}'} - \frac{5}{3}C^{(ut)}_{\tilde{q}\tilde{q}'}\right)\sum_{i=1,2}\left[\ln\left(\frac{s_{12}}{m_i^2}\right)\ln\left(\frac{4(\Delta E)^2}{\lambda^2}\right) - \frac{1}{2}\ln^2\left(\frac{s_{12}}{m_i^2}\right) - \frac{\pi^2}{3}\right],\\
\mathcal{I}_{34} =& \left(-\frac{1}{3}C^{(tt)}_{\tilde{q}\tilde{q}'} - \frac{1}{3}C^{(uu)}_{\tilde{q}\tilde{q}'} - \frac{5}{3}C^{(ut)}_{\tilde{q}\tilde{q}'}\right)\frac{1}{v_{34}}\sum_{i=3,4}\left[\ln\left(\frac{1+\beta_i}{1-\beta_i}\right)\ln\left(\frac{4(\Delta E)^2}{\lambda^2}\right) - 2\mathrm{Li}_2\left(\frac{2\beta_i}{1+\beta_i}\right)\right.\\
&\left. -\frac{1}{2}\ln^2\left(\frac{1-\beta_i}{1+\beta_i}\right)\right],\\
\mathcal{I}_{ij} =& \left(\frac{7}{6}C^{(tt)}_{\tilde{q}\tilde{q}'} - \frac{1}{6}C^{(uu)}_{\tilde{q}\tilde{q}'} - \frac{1}{6}C^{(ut)}_{\tilde{q}\tilde{q}'}\right)\left[\ln\left(\frac{s_{ij}^2}{m_i^2 m_j^2}\right)\ln\left(\frac{4(\Delta E)^2}{\lambda^2}\right) - \frac{1}{2}\ln^2\left(\frac{1-\beta_j}{1+\beta_j}\right) - \frac{\pi^2}{3}\right.\\
&\left. - \frac{1}{2}\ln^2\left(\frac{s_{12}}{m_i^2}\right) - 2\mathrm{Li}_2\left(1 - \frac{2p_i^0 p_j^0}{s_{ij}}(1+\beta_j)\right) - 2\mathrm{Li}_2\left(1 - \frac{2p_i^0 p_j^0}{s_{ij}}(1-\beta_j)\right)\right] \quad \text{for } i+j = 5,\\
\mathcal{I}_{ij} =& \left(-\frac{1}{6}C^{(tt)}_{\tilde{q}\tilde{q}'} + \frac{7}{6}C^{(uu)}_{\tilde{q}\tilde{q}'} - \frac{1}{6}C^{(ut)}_{\tilde{q}\tilde{q}'}\right)\left[\ln\left(\frac{s_{ij}^2}{m_i^2 m_j^2}\right)\ln\left(\frac{4(\Delta E)^2}{\lambda^2}\right) - \frac{1}{2}\ln^2\left(\frac{s_{12}}{m_i^2}\right)\right.\\
&\left. - \frac{1}{2}\ln^2\left(\frac{1-\beta_j}{1+\beta_j}\right) - \frac{\pi^2}{3} - 2\mathrm{Li}_2\left(1 - \frac{2p_i^0 p_j^0}{s_{ij}}(1+\beta_j)\right) - 2\mathrm{Li}_2\left(1 - \frac{2p_i^0 p_j^0}{s_{ij}}(1-\beta_j)\right)\right]\\
& \qquad \text{for } i+j = 4 \quad \text{or} \quad i+j = 6,
\end{aligned}$$

with $\quad s_{ij} = 2\,p_i{\cdot}p_j, \quad \beta_i = |\vec{p}_i|/p_i^0, \quad v_{ij} = \sqrt{1 - 4m_i^2 m_j^2/s_{ij}^2}\,.$

For the decay process $\tilde{q} \to q\,\tilde{\chi}^0$, the corresponding expressions for $\mathcal{I}_{ij}$ in the decay width eq. (4.59) read as follows (using the the label assignment $\tilde{q} \to 1$, $q \to 2$, $\tilde{\chi}^0 \to 3$),

$$\begin{aligned}
\mathcal{I}_{11} &= \ln\left(\frac{4(\Delta E)^2}{\lambda^2}\right) - 2\,,\\
\mathcal{I}_{12} &= \ln\left(\frac{4(p_2^0)^2}{m_q^2}\right)\ln\left(\frac{4(\Delta E)^2}{\lambda^2}\right) - \frac{1}{2}\ln^2\left(\frac{4(p_2^0)^2}{m_q^2}\right) - \frac{\pi^2}{3}\,, \qquad \text{(A.10)}\\
\mathcal{I}_{22} &= \ln\left(\frac{4(\Delta E)^2}{\lambda^2}\right) + \ln\left(\frac{m_q^2}{4(p_2^0)^2}\right)\,.
\end{aligned}$$

A.3 Diagrams of NLO corrections to squark–squark production

In the following we display all relevant virtual and real radiation diagrams used in our NLO calculation of squark–squark production. The contribution of some of them vanish under the assumption $m_q = 0$. For example, this is the case for the 5^{th} diagram on the first line when $a \neq b$, as any helicity state of the quark in the propagator can interact either with $\tilde{q}_{ia}$ or with $\tilde{q}_{jb}$, but not with both of them.

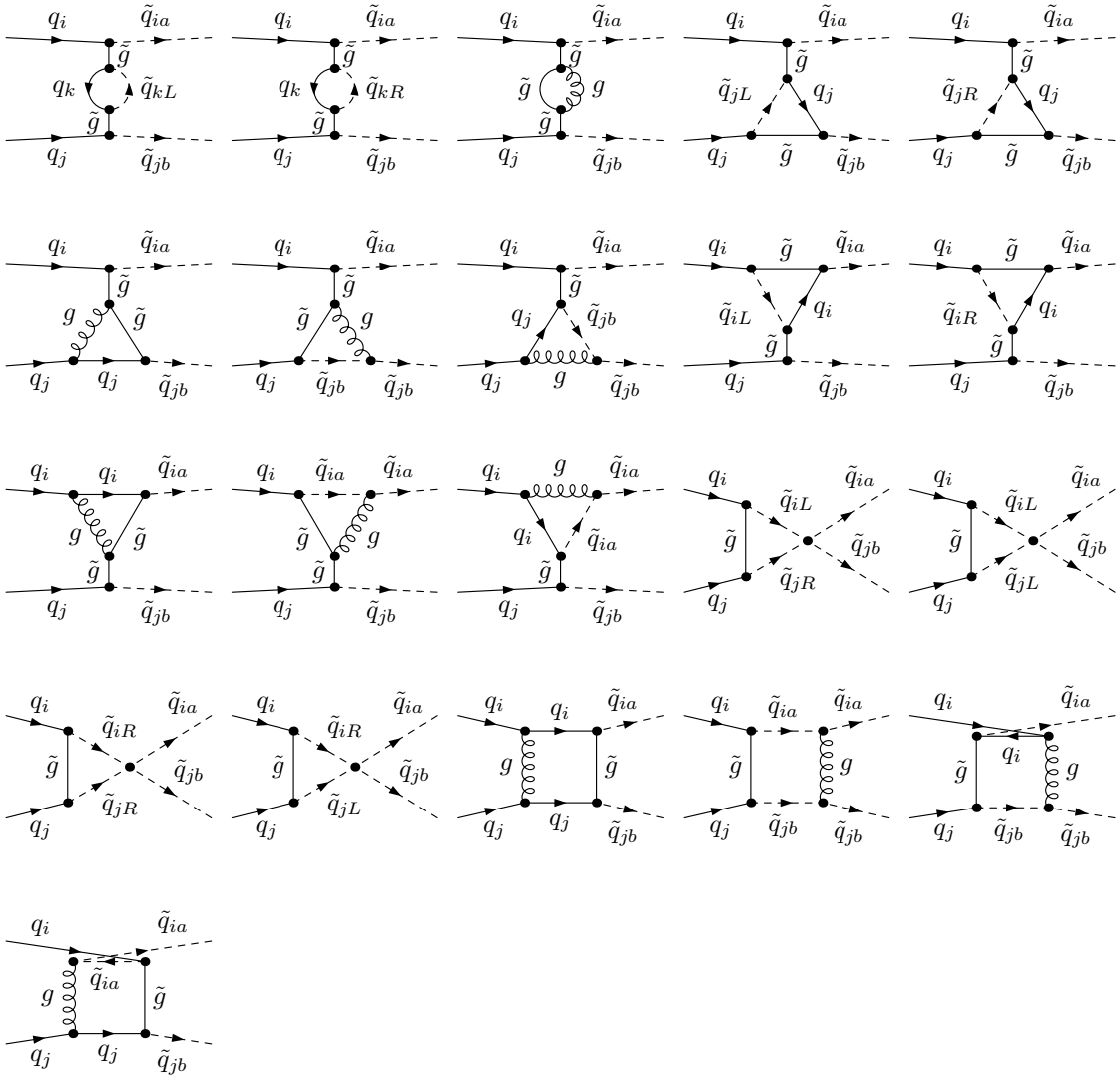

Figure A.1: Loop diagrams contributing to all flavor and chirality structures of squark–squark production.

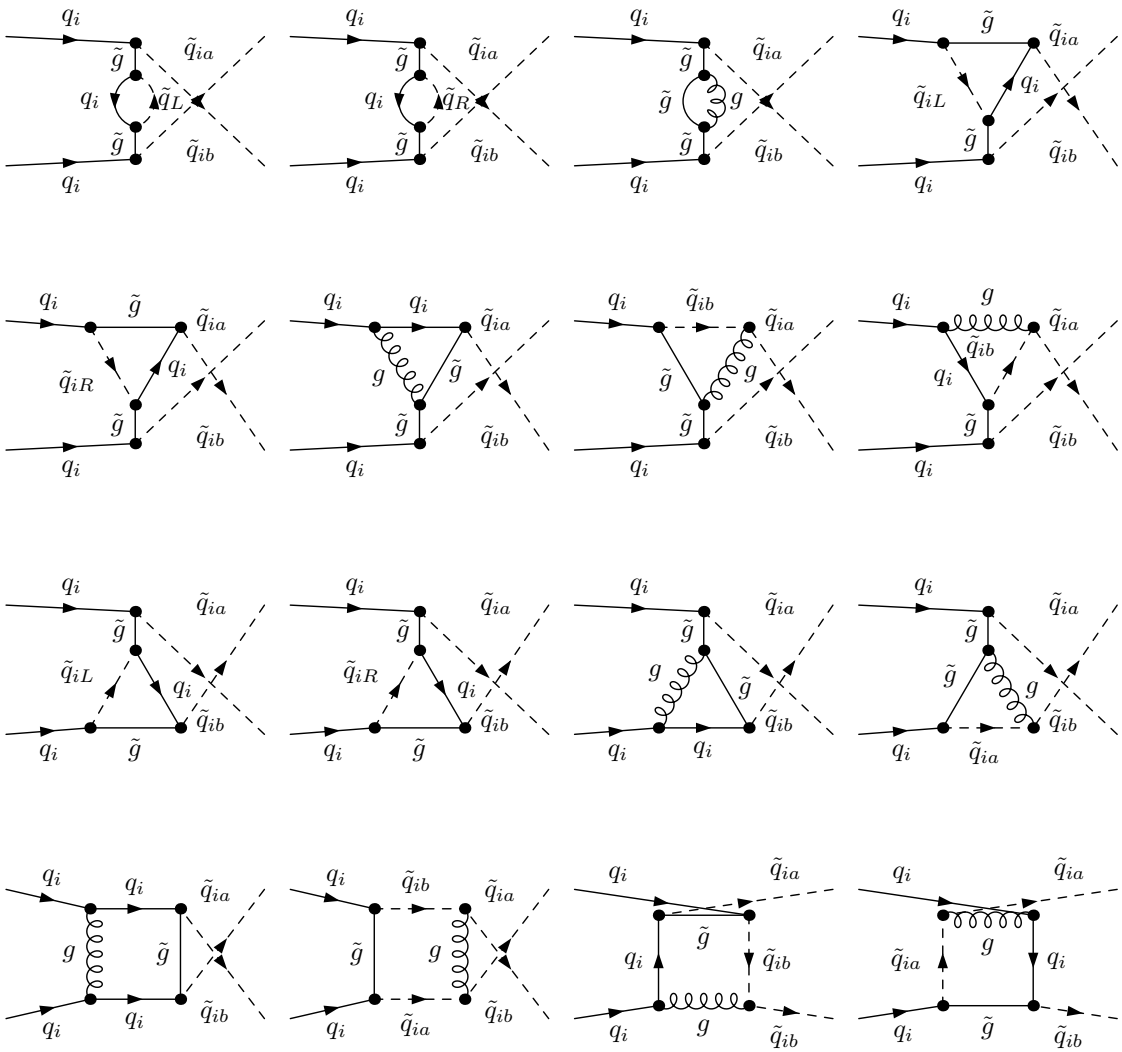

Figure A.2: Loop diagrams contributing only for squarks with equal flavor.

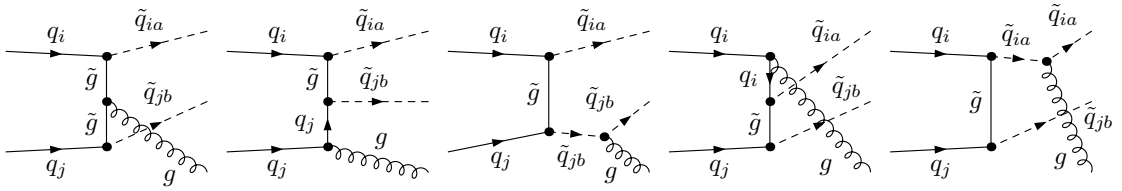

Figure A.3: Real gluon radiation diagrams contributing to all the flavor and chirality structures. Additional u-channel diagrams contributing only for equal flavor squarks are obtained from the above ones by a simple crossing of the initial state quarks.

A.4 Comparison between local and global diagram subtraction schemes

Here, expanding the discussion in section 4.3.2, we want to elucidate the differences between the implementations of the DS scheme in the global approach, as used in this paper, and in the local approach, as used e.g. in [38, 254, 255]. In the following discussion we consider the contribution from the resonant diagrams of figure 4.8(a). In a notation similar to the one of Appendix B.1 of [38], the contribution to the partonic cross section emerging from these diagrams can be written as

$$\hat{\sigma} = \int_{m^2_{\tilde{q}_{ia}}}^{q^2_{\max}} dq^2 \frac{f(q^2)}{(q^2 - m^2_{\tilde{g}})^2 + m^2_{\tilde{g}}\Gamma^2_{\tilde{g}}}\,, \tag{A.11}$$

where $f(q^2)$ is the differential cross section in q^2 (the squared invariant mass of $\tilde{q}_{ia}$ and q_i) without the squared gluino propagator. Given the squared total energy in the partonic center of mass s, the maximum allowed value for q^2 is $q^2_{\max} = (\sqrt{s} - m_{\tilde{q}_{jb}})^2$.

In the global approach the contribution from on-shell $\tilde{q}_{jb}\tilde{g}$ production is subtracted by substituting $\hat{\sigma}$ with

$$\Delta\hat{\sigma}_{\text{Global}} = \hat{\sigma} - \hat{\sigma}_{\tilde{q}_{jb}\tilde{g}} \frac{\Gamma_{\tilde{g}\to\tilde{q}_{ia}}}{\Gamma_{\tilde{g}}}\,, \tag{A.12}$$

i.e. subtracting exactly the total cross section for on-shell production of $\tilde{q}_{jb}\tilde{g}$ multiplied by the branching ratio of $\tilde{g} \to \tilde{q}_{ia}q_i$.

In the local approach, before phase-space integration, $f(q^2)$ evaluated in the on-shell gluino configuration

$$f(m^2_{\tilde{g}}) = \hat{\sigma}_{\tilde{q}_{jb}\tilde{g}} \frac{m_{\tilde{g}}\Gamma_{\tilde{g}}}{\pi} \frac{\Gamma_{\tilde{g}\to\tilde{q}_{ia}}}{\Gamma_{\tilde{g}}} \tag{A.13}$$

is subtracted in the numerator of the integrand of eq. (A.11),

$$\Delta\hat{\sigma}_{\text{Local}} = \int_{m^2_{\tilde{q}_{ia}}}^{q^2_{\max}} dq^2 \frac{f(q^2) - f(m^2_{\tilde{g}})}{(q^2 - m^2_{\tilde{g}})^2 + m^2_{\tilde{g}}\Gamma^2_{\tilde{g}}} := \hat{\sigma} - I\,, \quad \text{with} \quad I = \int_{m^2_{\tilde{q}_{ia}}}^{q^2_{\max}} dq^2 \frac{f(m^2_{\tilde{g}})}{(q^2 - m^2_{\tilde{g}})^2 + m^2_{\tilde{g}}\Gamma^2_{\tilde{g}}}\,. \tag{A.14}$$

In this parton level example the integral I can be calculated analytically. For $m_{\tilde{g}} > m_{\tilde{q}_{ia}}$ and $\sqrt{s} > m_{\tilde{g}} + m_{\tilde{q}_{jb}}$, i.e. in the region where subtraction is required, it yields

$$\begin{aligned} I &= \frac{f(m^2_{\tilde{g}})}{\Gamma_{\tilde{g}} m_{\tilde{g}}} \left[\arctan\left(\frac{q^2_{\max} - m^2_{\tilde{g}}}{\Gamma_{\tilde{g}} m_{\tilde{g}}} \right) - \arctan\left(\frac{m^2_{\tilde{q}_{ia}} - m^2_{\tilde{g}}}{\Gamma_{\tilde{g}} m_{\tilde{g}}} \right) \right] \\ &= \hat{\sigma}_{\tilde{q}_{jb}\tilde{g}} \frac{\Gamma_{\tilde{g}\to\tilde{q}_{ia}}}{\Gamma_{\tilde{g}}} \left[1 - \frac{\Gamma_{\tilde{g}} m_{\tilde{g}}}{\pi} \left(\frac{q^2_{\max} - m^2_{\tilde{q}_{ia}}}{(q^2_{\max} - m^2_{\tilde{g}})(m^2_{\tilde{g}} - m^2_{\tilde{q}_{ia}})} \right) \right] + \mathcal{O}(\Gamma_{\tilde{g}})\,. \end{aligned} \tag{A.15}$$

Comparing in this way the global and local approach for the DS subtraction we find

$$\Delta\hat{\sigma}_{\text{Global}} - \Delta\hat{\sigma}_{\text{Local}} = -\hat{\sigma}_{\tilde{q}_{jb}\tilde{g}} \Gamma_{\tilde{g}\to\tilde{q}_{ia}} \frac{m_{\tilde{g}}}{\pi} \left(\frac{q^2_{\max} - m^2_{\tilde{q}_{ia}}}{(q^2_{\max} - m^2_{\tilde{g}})(m^2_{\tilde{g}} - m^2_{\tilde{q}_{ia}})} \right) + \mathcal{O}(\Gamma_{\tilde{g}})\,. \tag{A.16}$$

Hence, even in the limit $\Gamma_{\tilde{g}} \to 0$, the two approaches differ by a finite term depending on the physical phase space boundaries, see also [387]. This can be understood from the fact that the approximation of the Breit-Wigner distribution $m_{\tilde{g}}\Gamma_{\tilde{g}}/[(q^2 - m_{\tilde{g}}^2)^2 + m_{\tilde{g}}^2\Gamma_{\tilde{g}}^2] \to \pi\delta(q^2 - m_{\tilde{g}}^2)$ in the integrand of I is strictly valid only for an integration over the entire real axis. Moreover, the result in eq. (A.16) can be altered if the mapping $q^2 \to m_{\tilde{g}}^2$ in the local subtraction is performed before the integration of the other phase space variables. This mapping is not uniquely defined and can lead to further differences. At the hadronic level the numerical differences between the two approaches can be of the order of a few per mill of the on-shell $\tilde{q}_{jb}\tilde{g}$ production. Thus, depending on the parameter region, few per-cent differences can appear for the $\tilde{q}_{ia}\tilde{q}_{jb}$ NLO relative corrections. For example, for SPS1a and $\sqrt{S} = 14$ TeV, corrections for the $\tilde{d}_R\tilde{d}_R$ cross section arising from eq. (A.16) amount to 0.08% of $\sigma^{(0)}_{\tilde{d}_R\tilde{g}}$ and to 1.9% of $\sigma^{(0)}_{\tilde{d}_R\tilde{d}_R}$, since $\sigma^{(0)}_{\tilde{d}_R\tilde{g}}/\sigma^{(0)}_{\tilde{d}_R\tilde{d}_R} \approx 23$. For different flavor and chirality configurations these corrections vary, they are, however, of the same order. Finally, we want to note that both the local and the global approach can be extended to a fully differential level.

A.5 NLO corrections to the integrated squark decay width

In eq. (4.14) and accordingly in section 4.4.3 we need the NLO corrections to the decay width $\Gamma(\tilde{q} \to q\,\tilde{\chi})$, where $\tilde{\chi}$ is either a neutralino or a chargino, and q a light quark. In this appendix we sketch the derivation of the NLO form factor F^{QCD}, following the steps of the former calculation [138], but keeping explicitly the dependence on the masses m_q for regularizing the collinear singularities and λ for the IR singularities. The NLO form factor F^{QCD}, eq. (4.64), receives four contributions,

$$F^{\mathrm{QCD}} = F_g + F_{\tilde{g}} + F_{\mathrm{ct}} + F_{\mathrm{real}}\,, \tag{A.17}$$

namely loop corrections involving gluons and gluinos, F_g and $F_{\tilde{g}}$, a counterterm contribution F_{ct}, and a contribution from real gluon emission F_{real}.

Keeping a quark mass m_q and a gluon mass λ as independent parameters regularizing the singular terms, in dimensional reduction F_g and F_{ct} can be written as,

$$\begin{aligned} F_g =& \frac{\Delta}{2} - \frac{1}{2}\log\left(\frac{m_{\tilde{q}}^2}{\mu^2}\right) + 1 - \log\left(\frac{m_q^2}{m_{\tilde{q}}^2}\right) + \frac{1}{4}\log^2\left(\frac{m_q^2}{m_{\tilde{q}}^2}\right) - \frac{1}{2}\log\left(\frac{\lambda^2}{m_{\tilde{q}}^2}\right)\log\left(\frac{m_q^2}{m_{\tilde{q}}^2}\right) \\ &+ \log\left(\frac{\lambda^2}{m_{\tilde{q}}^2}\right)\log(1-\kappa) - \log^2(1-\kappa) + \log(1-\kappa) - \mathrm{Li}_2\,(\kappa)\;, \end{aligned} \tag{A.18}$$

$$\begin{aligned} F_{\mathrm{ct}} =& -\frac{\Delta}{2} + \frac{1}{2}\log\left(\frac{m_{\tilde{q}}^2}{\mu^2}\right) - \log\left(\frac{\lambda^2}{m_{\tilde{q}}^2}\right) + \frac{3}{4}\log\left(\frac{m_q^2}{m_{\tilde{q}}^2}\right) + \frac{\gamma}{4\,(1-\gamma)} - \frac{\gamma}{2} - \frac{15}{8} \\ &- \frac{1}{2}(\gamma^2-1)\log\left(\frac{\gamma-1}{\gamma}\right) + \frac{1}{4}\left[\frac{2\,\gamma-1}{(1-\gamma)^2} + 3\right]\log(\gamma)\,, \end{aligned} \tag{A.19}$$

where $\kappa = m_{\tilde{\chi}}^2/m_{\tilde{q}}^2$, $\gamma = m_{\tilde{g}}^2/m_{\tilde{q}}^2$, and Δ denotes the UV divergence, cf. eq. (4.26).

$F_{\tilde{g}}$ is free of soft, collinear, and UV singularities, hence it is not affected by the choice of regulators; it is identical to the result in [138] and given by,

$$F_{\tilde{g}} = \sqrt{\kappa\gamma}\left[\frac{1}{\kappa}\ln(1-\kappa) + \frac{1}{1-\kappa}\left[\gamma\ln\gamma - (\gamma-1)\ln(\gamma-1)\right] + \frac{\kappa+\gamma-2}{(1-\kappa)^2}\,\hat{I}\right], \tag{A.20}$$

where for $\kappa\gamma < 1$ the function $\hat{I}$ is given by

$$\hat{I} = \mathrm{Li}_2\left(\frac{\gamma-1}{\gamma\kappa-1}\right) - \mathrm{Li}_2\left(\kappa\frac{\gamma-1}{\gamma\kappa-1}\right) - \mathrm{Li}_2\left(\frac{\gamma+\kappa-2}{\gamma\kappa-1}\right) + \mathrm{Li}_2\left(\kappa\frac{\gamma+\kappa-2}{\gamma\kappa-1}\right),$$

and for $\kappa\gamma > 1$ by

$$\begin{aligned}\hat{I} \;=\; & -\mathrm{Li}_2\left(\frac{\gamma\kappa-1}{\gamma-1}\right) + \mathrm{Li}_2\left(\frac{\gamma\kappa-1}{\gamma+\kappa-2}\right) + \mathrm{Li}_2\left(\frac{\gamma\kappa-1}{\kappa(\gamma-1)}\right) - \mathrm{Li}_2\left(\frac{\gamma\kappa-1}{\kappa(\gamma+\kappa-2)}\right) \\ & - \log(\kappa)\,\log\frac{\gamma+\kappa-2}{\gamma-1}\,.\end{aligned}$$

The real gluon emission F_{real}, integrated over the full phase space, can be expressed with the help of the bremsstrahlung integrals given in [252]. Evaluated in the limit $m_q = 0$, except for the mass-singular terms, the fully integrated decay width for $\tilde{q} \to q\tilde{\chi}g$ can be written as,

$$\Gamma_{\tilde{q}\to q\tilde{\chi}g} = \Gamma^{(0)}_{\tilde{q}\to q\tilde{\chi}} \cdot \frac{4}{3}\frac{\alpha_s}{\pi}\,F_{\mathrm{real}}\,, \tag{A.21}$$

$$F_{\mathrm{real}} = \frac{2}{m_{\tilde{q}}^2 - m_{\tilde{\chi}}^2}\left[2(m_{\tilde{\chi}}^2 - m_{\tilde{q}}^2)\,(m_{\tilde{q}}^2\,I_{00} + m_q^2\,I_{11} + I_0 + I_1) - 2(m_{\tilde{\chi}}^2 - m_{\tilde{q}}^2)^2\,I_{01} - I - I_1^0\right]$$

with $\Gamma^{(0)}$ from eq. (4.53) and (4.63). The phase space integrals $I \equiv I(m_{\tilde{q}}, m_q, m_{\tilde{\chi}})$, cf. [252], are given by

$$\begin{aligned}
I_{00} =& \frac{1}{4\,m_{\tilde{q}}^4}\left[m_{\tilde{\chi}}^2 - m_{\tilde{q}}^2 + m_{\tilde{q}}^2\log\left[\frac{m_{\tilde{q}}^2 - m_{\tilde{\chi}}^2}{\lambda m_{\tilde{q}}}\right] + m_{\tilde{\chi}}^2\log\left[\frac{\lambda m_{\tilde{\chi}}^2}{m_{\tilde{q}}^3 - m_{\tilde{q}}m_{\tilde{\chi}}^2}\right]\right], \\
I_{11} =& \frac{1}{4\,m_q^2\,m_{\tilde{q}}^2}\,(m_{\tilde{q}}^2 - m_{\tilde{\chi}}^2)\left[\log\left(\frac{m_q}{\lambda}\right) - 1\right], \\
I_{01} =& \frac{1}{4\,m_{\tilde{q}}^2}\left[\frac{\pi^2}{2} + \log^2\left(\frac{m_q}{\lambda}\right) - \log^2\left(\frac{m_{\tilde{q}}^2 - m_{\tilde{\chi}}^2}{\lambda m_{\tilde{q}}}\right) - \mathrm{Li}_2\left(1 - \frac{m_{\tilde{\chi}}^2}{m_{\tilde{q}}^2}\right)\right], \\
I =& \frac{1}{8\,m_{\tilde{q}}^2}\left[m_{\tilde{q}}^4 - m_{\tilde{\chi}}^4 + 4m_{\tilde{\chi}}^2 m_{\tilde{q}}^2\log\left(\frac{m_{\tilde{\chi}}}{m_{\tilde{q}}}\right)\right], \\
I_0 =& \frac{1}{4\,m_{\tilde{q}}^2}\left[m_{\tilde{\chi}}^2 - m_{\tilde{q}}^2 - 2m_{\tilde{\chi}}^2\,\log\left(\frac{m_{\tilde{\chi}}}{m_{\tilde{q}}}\right)\right], \\
I_1 =& \frac{1}{4\,m_{\tilde{q}}^2}\left[m_{\tilde{\chi}}^2 - m_{\tilde{q}}^2 + 2m_{\tilde{\chi}}^2\,\log\left(\frac{m_q m_{\tilde{\chi}}}{m_{\tilde{q}}^2 - m_{\tilde{\chi}}^2}\right) - 2m_{\tilde{q}}^2\,\log\left(\frac{m_q m_{\tilde{q}}}{m_{\tilde{q}}^2 - m_{\tilde{\chi}_j^0}^2}\right)\right], \\
I_1^0 =& \frac{1}{16\,m_{\tilde{q}}^2}\Bigg[5m_{\tilde{\chi}}^4 - 8m_{\tilde{\chi}}^2 m_{\tilde{q}}^2 + 3m_{\tilde{q}}^4 + 4(m_{\tilde{\chi}}^4 - 2m_{\tilde{\chi}}^2 m_{\tilde{q}}^2)\,\log\left(\frac{m_q m_{\tilde{\chi}}}{m_{\tilde{q}}^2 - m_{\tilde{\chi}}^2}\right) \\
& + 4m_{\tilde{q}}^4\,\log\left(\frac{m_q m_{\tilde{q}}}{m_{\tilde{q}}^2 - m_{\tilde{\chi}}^2}\right)\Bigg].
\end{aligned} \tag{A.22}$$

With these expressions, F_{real} in eq. (A.21) can be simplified to,

$$\begin{aligned} F_{\text{real}} = \quad & \frac{-5+8\kappa-3\kappa^2-8\kappa\log(\kappa)+6\kappa^2\log(\kappa)}{8(1-\kappa)^2} \\ & +4-\frac{\pi^2}{2}-\frac{5}{2}\log(1-\kappa)+\log(1-\kappa)^2-\log^2\left(\frac{m_q}{\lambda}\right)+2\log\left(\frac{m_{\tilde{q}}}{\lambda}\right) \\ & +\frac{1}{2}\log\left(\frac{m_q}{m_{\tilde{q}}}\right)+2\log(1-\kappa)\log\left(\frac{m_{\tilde{q}}}{\lambda}\right)+\log^2\left(\frac{m_{\tilde{q}}}{\lambda}\right)+\text{Li}_2\left(1-\kappa\right) . \end{aligned} \tag{A.23}$$

Combining all four contributions in eq. (A.17) we obtain a compact analytical expression for the form factor F^{QCD}, independent of m_q and λ, which agrees with the result in [138],

$$\begin{aligned} F^{\text{QCD}} = \quad & -\frac{1}{8}\left(\frac{4\,\gamma^2-27\,\gamma+25}{\gamma-1}+\frac{3\,\kappa-5}{\kappa-1}\right)-\frac{\pi^2}{3}-2\,\text{Li}_2(\kappa)-\frac{1}{2}\left(\gamma^2-1\right)\,\log\left(\frac{\gamma-1}{\gamma}\right) \\ & +\frac{3\,\gamma^2-4\,\gamma+2}{4\,(1-\gamma)^2}\,\log\left(\gamma\right)-\frac{3}{2}\,\log(1-\kappa)+\frac{1}{4}\cdot\frac{3\,\kappa^2-4\,\kappa}{(\kappa-1)^2}\,\log\left(\kappa\right)-\log\left(\kappa\right)\,\log(1-\kappa) \\ & +\sqrt{\kappa\gamma}\left[\frac{1}{\kappa}\log(1-\kappa)+\frac{1}{1-\kappa}\left[\gamma\log(\gamma)-(\gamma-1)\log(\gamma-1)\right]+\frac{\kappa+\gamma-2}{(1-\kappa)^2}\,\hat{I}\right], \end{aligned} \tag{A.24}$$

Appendix B

Invariant mass distribution endpoint relations

In this appendix we list relations for the endpoints of various invariant mass distributions built from the following decay chain [273, 275]:

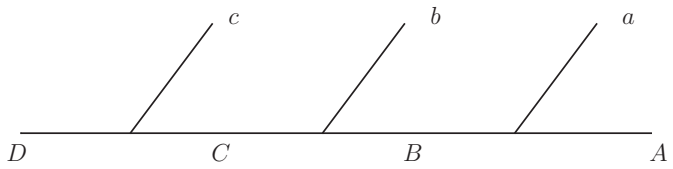

Here, massive particles are denoted with a capital letter and massless particles with a small letter. The particle A and all massless particles are assumed stable, the other massive particles are unstable and decay in two-body decays, where intermediate particles are treated on-shell. This decay chain corresponds to the "golden" decay chain (6.1), with $D = \tilde{q}_L, C = \tilde{\chi}_2^0, B = \tilde{l}_{L/R}, A = \tilde{\chi}_1^0$ and $c = q = j, b = l_n^{\pm}, a = l_f^{\mp}$.

Using the dimensionless squared mass ratios

$$R_{ij} \equiv \frac{m_i^2}{m_j^2}\,, \qquad i,j \in \{A,B,C,D\}\,. \tag{B.1}$$

the endpoints of the four primary invariant mass distributions are given by

$$(m_{ab}^{\max})^2 = (m_{ll}^{\max})^2 = m_D^2\, R_{CD}\,(1-R_{BC})\,(1-R_{AB}); \tag{B.2}$$

$$(m_{bc}^{\max})^2 = \left(m_{jl_n}^{\max}\right)^2 = m_D^2\,(1-R_{CD})\,(1-R_{BC})\,; \tag{B.3}$$

$$(m_{ac}^{\max})^2 = \left(m_{jl_f}^{\max}\right)^2 = m_D^2\,(1-R_{CD})\,(1-R_{AB})\,; \tag{B.4}$$

$$(m_{abc}^{\max})^2 = \left(m_{jll}^{\max}\right)^2 = \begin{cases} m_D^2(1-R_{CD})(1-R_{AC}), & \text{for } R_{CD} < R_{AC}, \\ m_D^2(1-R_{BC})(1-R_{AB}R_{CD}), & \text{for } R_{BC} < R_{AB}R_{CD}, \\ m_D^2(1-R_{AB})(1-R_{BD}), & \text{for } R_{AB} < R_{BD}, \\ m_D^2\left(1-\sqrt{R_{AD}}\right)^2, & \text{otherwise.} \end{cases}, \tag{B.5}$$

The two secondary invariant mass distribution endpoints are given by

$$\left(m^{\max}_{jl(lo)}\right)^2 = \begin{cases} \left(m^{\max}_{jl_n}\right)^2, & \text{for } (2-R_{AB})^{-1} < R_{BC} < 1, \quad (1) \\ \left(m^{\max}_{jl(eq)}\right)^2, & \text{for } R_{AB} < R_{BC} < (2-R_{AB})^{-1}, \quad (2) \\ \left(m^{\max}_{jl(eq)}\right)^2, & \text{for } 0 < R_{BC} < R_{AB}, \quad (3) \end{cases} \tag{B.6}$$

$$\left(m^{\max}_{jl(hi)}\right)^2 = \begin{cases} \left(m^{\max}_{jl_f}\right)^2, & \text{for } (2-R_{AB})^{-1} < R_{BC} < 1, \quad (1) \\ \left(m^{\max}_{jl_f}\right)^2, & \text{for } R_{AB} < R_{BC} < (2-R_{AB})^{-1}, \quad (2) \\ \left(m^{\max}_{jl_n}\right)^2, & \text{for } 0 < R_{BC} < R_{AB}, \quad (3) \end{cases} \tag{B.7}$$

where

$$\left(m^{\max}_{jl(eq)}\right)^2 = m_D^2\,(1-R_{CD})\,(1-R_{AB})\,(2-R_{AB})^{-1}. \tag{B.8}$$

The lower endpoint of the $m_{jll(\theta>\pi/2)}$ threshold distribution is given by

$$\left(m^{\min}_{jll(\theta>\frac{\pi}{2})}\right)^2 = \frac{1}{4}m_D^2\Big\{(1-R_{AB})(1-R_{BC})(1+R_{CD}) \tag{B.9}$$
$$+\,2\,(1-R_{AC})(1-R_{CD}) - (1-R_{CD})\sqrt{(1+R_{AB})^2(1+R_{BC})^2 - 16R_{AC}}\Big\}.$$

The endpoints of the distributions first introduced in [282] are given by

$$\left(M^{\max}_{jl(u)}\right)^2 = \max\left\{\left(m^{max}_{jl_n}\right)^2, \left(m^{max}_{jl_f}\right)^2\right\} \tag{B.10}$$

$$\left(m^{\max}_{jl(u)}\right)^2 = \min\left\{\left(m^{max}_{jl_n}\right)^2, \left(m^{max}_{jl_f}\right)^2\right\}, \tag{B.11}$$

$$\left(m^{\max}_{jl(d)}\right)^2 = \left(M^{\max}_{jl(u)}\right)^2, \tag{B.12}$$

$$\left(m^{\max}_{jl(s)}\right)^2 = m_D^2(1-R_{CD})(1-R_{AC}), \tag{B.13}$$

$$\left(m^{\max}_{jl(p)}\right)^2 = \begin{cases} \frac{1}{2}\,m_D^2(1-R_{CD})\sqrt{1-R_{AB}}, & \text{for } R_{BC} \le 0.5, \\ m_D^2(1-R_{CD})\sqrt{R_{BC}(1-R_{BC})(1-R_{AB})}, & \text{for } R_{BC} \ge 0.5. \end{cases} \tag{B.14}$$

Here, $\left(M^{max}_{jl(u)}\right)^2$ is the larger and $\left(m^{max}_{jl(u)}\right)^2$ the smaller upper endpoint of the distribution of the union, $m^2_{jl(u)}$; in the experimental reconstruction the larger endpoint (in the tail of the distribution) can be tagged via the endpoint of the $m^2_{jl(d)}$ distribition.

Appendix C

Constraints from CCBs for large stau left-right mixing

The occurrence of a charge or color breaking (CCB) vacuum in the scalar potential is not necessarily a problem, as long as the electroweak vacuum is metastable with a lifetime longer than the age of the Universe. This lifetime can be calculated using the semiclassical, so called, "bounce action" method [368, 388, 389], where the decay rate Γ of the false vacuum per unit spacetime volume V is given by

$$\Gamma/V = A\, e^{-S_E[\bar{\phi}]}\,. \tag{C.1}$$

Here, the "bounce" action $S_E[\phi]$ is the corresponding four-dimensional Euclidean action, which in terms of a radial coordinate r can be written as

$$S_E[\phi] = 2\pi \int dr\; r^3 \left[\sum_{i=1}^{N} \left(\frac{d\phi_i}{dr}\right)^2 + V(\phi)\right]\,. \tag{C.2}$$

$V(\phi)$ is the scalar potential of all N relevant scalar fields. The "bounce" action $S_E[\phi]$ has to be evaluated on the "bounce" solution $\bar{\phi}$, i.e. the solution connecting the two vacua. Often this solution is approximated by a straight line. However a full analysis can for example be achieved applying the computer code `CosmoTransitions` [390].

In eq. (C.1) the factor A can in principle be calculated. However, this is a difficult problem and its precise value is irrelevant for obtaining an approximate transition rate, as its value is expected to be of the order $A \approx (100\text{ GeV})^4$, 100 GeV being the electroweak scale. Asking the lifetime of the metastable electroweak vacuum to be longer than the age of the Universe, we must have

$$\Gamma/V \cdot \left(\frac{1}{H_0}\right)^4 \ll 1\,, \tag{C.3}$$

with the Hubble constant $H_0 \approx 1.5 \cdot 10^{-42}$ GeV. Therefore, the potential $V(\phi)$ must allow for

$$S_E[\bar{\phi}] \gtrsim 400\,. \tag{C.4}$$

This can be used to place upper limits on the parameters in the scalar potential $V(\phi)$.

In [365] a numerical study was performed concentrating on large $\tilde{\tau}_1\tilde{\tau}_1^* h^0$ couplings and thus large stau left-right mixing and large $\mu \tan\beta$. Using an effective one-loop scalar potential the authors of [365] state the approximate limit given in eq. (7.11). In [366] this limit was confirmed and additional corrections due to a resummed effective tau Yukawa coupling were found to be small.

Bibliography

[1] J. M. Lindert, F. D. Steffen, and M. K. Trenkel, "Direct stau production at hadron colliders in cosmologically motivated scenarios," *JHEP* **1108** (2011) 151, arXiv:1106.4005 [hep-ph].

[2] J. M. Lindert, F. D. Steffen, and M. K. Trenkel, "Direct stau production at the LHC," *PoS* **CORFU2011** (2011) 024, arXiv:1204.2379 [hep-ph].

[3] W. Hollik, J. M. Lindert, and D. Pagani, "NLO corrections to squark-squark production and decay at the LHC," *JHEP* **1303** (2013) 139, arXiv:1207.1071 [hep-ph].

[4] W. Hollik, J. M. Lindert, and D. Pagani, "On cascade decays of squarks at the LHC in NLO QCD," *Eur.Phys.J.* **C73** (2013) 2410, arXiv:1303.0186 [hep-ph].

[5] P. Ramond, "Dual Theory for Free Fermions," *Phys.Rev.* **D3** (1971) 2415–2418.

[6] J.-L. Gervais and B. Sakita, "Field Theory Interpretation Of Supergauges In Dual Models," *Nucl.Phys.* **B34** (1971) 632–639.

[7] A. Neveu and J. Schwarz, "Factorizable dual model of pions," *Nucl.Phys.* **B31** (1971) 86–112.

[8] Y. Golfand and E. Likhtman, "Extension of the Algebra of Poincare Group Generators and Violation of p Invariance," *JETP Lett.* **13** (1971) 323–326.

[9] D. Volkov and V. Akulov, "Is the Neutrino a Goldstone Particle?," *Phys.Lett.* **B46** (1973) 109–110.

[10] J. Wess and B. Zumino, "A Lagrangian Model Invariant Under Supergauge Transformations," *Phys.Lett.* **B49** (1974) 52.

[11] J. Wess and B. Zumino, "Supergauge Transformations in Four-Dimensions," *Nucl. Phys.* **B70** (1974) 39–50.

[12] R. Haag, J. T. Lopuszanski, and M. Sohnius, "All Possible Generators of Supersymmetries of the s Matrix," *Nucl.Phys.* **B88** (1975) 257.

[13] S. Glashow, "Partial Symmetries of Weak Interactions," *Nucl.Phys.* **22** (1961) 579–588.

[14] S. Weinberg, "A Model of Leptons," *Phys.Rev.Lett.* **19** (1967) 1264–1266.

[15] A. Salam, "Weak and Electromagnetic Interactions," *Conf.Proc.* **C680519** (1968) 367–377.

[16] H. Fritzsch, M. Gell-Mann, and H. Leutwyler, "Advantages of the Color Octet Gluon Picture," *Phys.Lett.* **B47** (1973) 365–368.

[17] D. Gross and F. Wilczek, "Asymptotically Free Gauge Theories. 1," *Phys.Rev.* **D8** (1973) 3633–3652.

[18] D. Gross and F. Wilczek, "Asymptotically Free Gauge Theories. 2," *Phys.Rev.* **D9** (1974) 980–993.

[19] H. D. Politzer, "Reliable Perturbative Results for Strong Interactions?," *Phys.Rev.Lett.* **30** (1973) 1346–1349.

[20] G. 't Hooft, "Renormalization of Massless Yang-Mills Fields," *Nucl.Phys.* **B33** (1971) 173–199.

[21] G. 't Hooft, "Renormalizable Lagrangians for Massive Yang-Mills Fields," *Nucl.Phys.* **B35** (1971) 167–188.

[22] C. Bouchiat, J. Iliopoulos, and P. Meyer, "An Anomaly Free Version of Weinberg's Model," *Phys.Lett.* **B38** (1972) 519–523.

[23] P. W. Higgs, "Broken Symmetries and the Masses of Gauge Bosons," *Phys.Rev.Lett.* **13** (1964) 508–509.

[24] P. W. Higgs, "Spontaneous Symmetry Breakdown without Massless Bosons," *Phys.Rev.* **145** (1966) 1156–1163.

[25] F. Englert and R. Brout, "Broken Symmetry and the Mass of Gauge Vector Mesons," *Phys.Rev.Lett.* **13** (1964) 321–323.

[26] G. Guralnik, C. Hagen, and T. Kibble, "Global Conservation Laws and Massless Particles," *Phys.Rev.Lett.* **13** (1964) 585–587.

[27] **ATLAS** Collaboration, G. Aad *et al.*, "Observation of a new particle in the search for the Standard Model Higgs boson with the ATLAS detector at the LHC," *Phys.Lett.* **B716** (2012) 1–29, `arXiv:1207.7214 [hep-ex]`.

[28] **CMS** Collaboration, S. Chatrchyan *et al.*, "Observation of a new boson at a mass of 125 GeV with the CMS experiment at the LHC," *Phys.Lett.* **B716** (2012) 30–61, `arXiv:1207.7235 [hep-ex]`.

[29] G. Degrassi, S. Di Vita, J. Elias-Miro, J. R. Espinosa, G. F. Giudice, *et al.*, "Higgs mass and vacuum stability in the Standard Model at NNLO," *JHEP* **1208** (2012) 098, `arXiv:1205.6497 [hep-ph]`.

[30] S. Weinberg, "Implications of Dynamical Symmetry Breaking: An Addendum," *Phys.Rev.* **D19** (1979) 1277–1280.

[31] H. P. Nilles, "Supersymmetry, Supergravity and Particle Physics," *Phys. Rept.* **110** (1984) 1–162.

[32] H. E. Haber and G. L. Kane, "The Search for Supersymmetry: Probing Physics Beyond the Standard Model," *Phys.Rept.* **117** (1985) 75–263.

[33] E. Witten, "Dynamical Breaking of Supersymmetry," *Nucl.Phys.* **B188** (1981) 513.

[34] R. K. Kaul and P. Majumdar, "Cancellation Of Quadratically Divergent Mass Corrections In Globally Supersymmetric Spontaneously Broken Gauge Theories ," *Nucl.Phys.* **B199** (1982) 36.

[35] G. Degrassi, S. Heinemeyer, W. Hollik, P. Slavich, and G. Weiglein, "Towards high precision predictions for the MSSM Higgs sector," *Eur.Phys.J.* **C28** (2003) 133–143, `arXiv:hep-ph/0212020 [hep-ph]`.

[36] L. E. Ibanez and G. G. Ross, "Low-Energy Predictions in Supersymmetric Grand Unified Theories," *Phys.Lett.* **B105** (1981) 439.

[37] S. Dimopoulos, S. Raby, and F. Wilczek, "Supersymmetry and the Scale of Unification," *Phys.Rev.* **D24** (1981) 1681–1683.

[38] W. Beenakker, R. Hopker, M. Spira, and P. M. Zerwas, "Squark and gluino production at hadron colliders," *Nucl. Phys.* **B492** (1997) 51–103, `arXiv:hep-ph/9610490`.

[39] **Particle Data Group** Collaboration, J. Beringer *et al.*, "Review of Particle Physics (RPP)," *Phys.Rev.* **D86** (2012) 010001.

[40] W. Hollik and G. Duckeck, "Electroweak precision tests at LEP," *Springer Tracts Mod.Phys.* **162** (2000) 1–161.

[41] S. Glashow, J. Iliopoulos, and L. Maiani, "Weak Interactions with Lepton-Hadron Symmetry," *Phys.Rev.* **D2** (1970) 1285–1292.

[42] L. Faddeev and V. Popov, "Feynman Diagrams for the Yang-Mills Field," *Phys.Lett.* **B25** (1967) 29–30.

[43] **UA1** Collaboration, G. Arnison *et al.*, "Experimental Observation of Isolated Large Transverse Energy Electrons with Associated Missing Energy at s**(1/2) = 540-GeV," *Phys.Lett.* **B122** (1983) 103–116.

[44] **UA1** Collaboration, G. Arnison *et al.*, "Experimental Observation of Lepton Pairs of Invariant Mass Around 95-GeV/c**2 at the CERN SPS Collider," *Phys.Lett.* **B126** (1983) 398–410.

[45] **UA2** Collaboration, M. Banner *et al.*, "Observation of Single Isolated Electrons of High Transverse Momentum in Events with Missing Transverse Energy at the CERN anti-p p Collider," *Phys.Lett.* **B122** (1983) 476–485.

[46] **UA2** Collaboration, P. Bagnaia *et al.*, "Evidence for Z0 –> e+ e- at the CERN anti-p p Collider," *Phys.Lett.* **B129** (1983) 130–140.

[47] **ALEPH, CDF, D0, DELPHI, L3, OPAL, SLD, LEP Electroweak Working Group, Tevatron Electroweak Working Group, SLD Electroweak and Heavy Flavour Groups** Collaboration, "Precision Electroweak Measurements and Constraints on the Standard Model," `arXiv:1012.2367 [hep-ex]`.

[48] **CDF** Collaboration, F. Abe *et al.*, "Observation of top quark production in $\bar{p}p$ collisions," *Phys.Rev.Lett.* **74** (1995) 2626–2631, `arXiv:hep-ex/9503002 [hep-ex]`.

[49] **D0** Collaboration, S. Abachi *et al.*, "Observation of the top quark," *Phys.Rev.Lett.* **74** (1995) 2632–2637, `arXiv:hep-ex/9503003 [hep-ex]`.

[50] J. Brodzicka, M. Corradi, I. Schienbein, and R. Schwienhorst, "Heavy Flavour Working Group Summary," `arXiv:1208.3379 [hep-ph]`.

[51] **Planck** Collaboration, P. Ade *et al.*, "Planck 2013 results. XVI. Cosmological parameters," `arXiv:1303.5076 [astro-ph.CO]`.

[52] R. Peccei and H. R. Quinn, "CP Conservation in the Presence of Instantons," *Phys.Rev.Lett.* **38** (1977) 1440–1443.

[53] A. Sakharov, "Violation of CP Invariance, c Asymmetry, and Baryon Asymmetry of the Universe," *Pisma Zh.Eksp.Teor.Fiz.* **5** (1967) 32–35.

[54] A. H. Guth, "The Inflationary Universe: A Possible Solution to the Horizon and Flatness Problems," *Phys.Rev.* **D23** (1981) 347–356.

[55] A. D. Linde, "A New Inflationary Universe Scenario: A Possible Solution of the Horizon, Flatness, Homogeneity, Isotropy and Primordial Monopole Problems," *Phys.Lett.* **B108** (1982) 389–393.

[56] R. Gwyn, M. Rummel, and A. Westphal, "Resonant non-Gaussianity with equilateral properties," `arXiv:1211.0070 [hep-th]`.

[57] S. Clesse, B. Garbrecht, and Y. Zhu, "Non-Gaussianities and Curvature Perturbations from Hybrid Inflation," `arXiv:1304.7042 [astro-ph.CO]`.

[58] **Muon g-2** Collaboration, G. Bennett *et al.*, "Measurement of the negative muon anomalous magnetic moment to 0.7 ppm," *Phys.Rev.Lett.* **92** (2004) 161802, `arXiv:hep-ex/0401008 [hep-ex]`.

[59] W. Hollik and D. Pagani, "The electroweak contribution to the top quark forward-backward asymmetry at the Tevatron," *Phys.Rev.* **D84** (2011) 093003, arXiv:1107.2606 [hep-ph].

[60] H. Georgi and S. Glashow, "Unity of All Elementary Particle Forces," *Phys.Rev.Lett.* **32** (1974) 438–441.

[61] H. Fritzsch and P. Minkowski, "Unified Interactions of Leptons and Hadrons," *Annals Phys.* **93** (1975) 193–266.

[62] S. P. Martin, "A Supersymmetry primer," arXiv:hep-ph/9709356 [hep-ph].

[63] M. Drees, R. Godbole, and P. Roy, "Theory and phenomenology of sparticles: An account of four-dimensional N=1 supersymmetry in high energy physics," *Hackensack, USA: World Scientific* (2004) .

[64] H. Baer and X. Tata, "Weak scale supersymmetry: From superfields to scattering events,".

[65] S. R. Coleman and J. Mandula, "All Possible Symmetries Of The S Matrix," *Phys.Rev.* **159** (1967) 1251–1256.

[66] J. Wess and B. Zumino, "Supergauge Invariant Extension of Quantum Electrodynamics," *Nucl.Phys.* **B78** (1974) 1.

[67] S. L. Adler, "Axial vector vertex in spinor electrodynamics," *Phys.Rev.* **177** (1969) 2426–2438.

[68] W. A. Bardeen, "Anomalous Ward identities in spinor field theories," *Phys.Rev.* **184** (1969) 1848–1857.

[69] A. Akeroyd, M. A. Diaz, J. Ferrandis, M. Garcia-Jareno, and J. Valle, "Charged Higgs boson and Stau phenomenology in the simplest R parity breaking model," *Nucl.Phys.* **B529** (1998) 3–22, arXiv:hep-ph/9707395 [hep-ph].

[70] B. Allanach, A. Dedes, and H. Dreiner, "R parity violating minimal supergravity model," *Phys.Rev.* **D69** (2004) 115002, arXiv:hep-ph/0309196 [hep-ph].

[71] W. Buchmüller, L. Covi, K. Hamaguchi, A. Ibarra, and T. Yanagida, "Gravitino dark matter in R-parity breaking vacua," *JHEP* **03** (2007) 037, hep-ph/0702184.

[72] H. K. Dreiner, S. Grab, and M. K. Trenkel, "Stau LSP Phenomenology: Two versus Four-Body Decay Modes. Example: Resonant Single Slepton Production at the LHC," *Phys. Rev.* **D79** (2009) 016002, arXiv:0808.3079 [hep-ph].

[73] K. Desch, S. Fleischmann, P. Wienemann, H. K. Dreiner, and S. Grab, "Stau as the Lightest Supersymmetric Particle in R-Parity Violating SUSY Models: Discovery Potential with Early LHC Data," *Phys. Rev.* **D83** (2011) 015013, arXiv:1008.1580 [hep-ph].

[74] L. Girardello and M. T. Grisaru, "Soft Breaking of Supersymmetry," *Nucl.Phys.* **B194** (1982) 65.

[75] S. Dimopoulos and H. Georgi, "Softly Broken Supersymmetry and SU(5)," *Nucl.Phys.* **B193** (1981) 150.

[76] H. E. Haber and R. Hempfling, "Can the mass of the lightest Higgs boson of the minimal supersymmetric model be larger than m(Z)?," *Phys.Rev.Lett.* **66** (1991) 1815–1818.

[77] S. Heinemeyer, W. Hollik, and G. Weiglein, "The Mass of the lightest MSSM Higgs boson: A Compact analytical expression at the two loop level," *Phys.Lett.* **B455** (1999) 179–191, arXiv:hep-ph/9903404 [hep-ph].

[78] H. E. Haber, "Higgs boson masses and couplings in the minimal supersymmetric model," arXiv:hep-ph/9707213 [hep-ph]. Perspectives on Higgs Physics II, Gordon L. Kane ed., World Scientific, Singapore, 1997.

[79] L. J. Hall, V. A. Kostelecky, and S. Raby, "New Flavor Violations in Supergravity Models," *Nucl.Phys.* **B267** (1986) 415.

[80] S. Dimopoulos and D. W. Sutter, "The Supersymmetric flavor problem," *Nucl.Phys.* **B452** (1995) 496–512, arXiv:hep-ph/9504415 [hep-ph].

[81] T. Ibrahim and P. Nath, "The Neutron and the lepton EDMs in MSSM, large CP violating phases, and the cancellation mechanism," *Phys.Rev.* **D58** (1998) 111301, arXiv:hep-ph/9807501 [hep-ph].

[82] W. Porod, "SPheno, a program for calculating supersymmetric spectra, SUSY particle decays and SUSY particle production at e+ e- colliders," *Comput.Phys.Commun.* **153** (2003) 275–315, arXiv:hep-ph/0301101 [hep-ph].

[83] B. C. Allanach, "SOFTSUSY: a program for calculating supersymmetric spectra," *Comput. Phys. Commun.* **143** (2002) 305–331, arXiv:hep-ph/0104145.

[84] A. Djouadi, M. M. Muhlleitner, and M. Spira, "Decays of Supersymmetric Particles: the program SUSY-HIT (SUspect-SdecaY-Hdecay-InTerface)," *Acta Phys. Polon.* **B38** (2007) 635–644, arXiv:hep-ph/0609292.

[85] A. H. Chamseddine, R. L. Arnowitt, and P. Nath, "Locally Supersymmetric Grand Unification," *Phys.Rev.Lett.* **49** (1982) 970.

[86] R. Barbieri, S. Ferrara, and C. A. Savoy, "Gauge Models with Spontaneously Broken Local Supersymmetry," *Phys.Lett.* **B119** (1982) 343.

[87] M. Dine and A. E. Nelson, "Dynamical supersymmetry breaking at low-energies," *Phys.Rev.* **D48** (1993) 1277–1287, arXiv:hep-ph/9303230 [hep-ph].

[88] M. Dine, A. E. Nelson, and Y. Shirman, "Low-energy dynamical supersymmetry breaking simplified," *Phys.Rev.* **D51** (1995) 1362–1370, arXiv:hep-ph/9408384 [hep-ph].

[89] M. Dine, A. E. Nelson, Y. Nir, and Y. Shirman, "New tools for low-energy dynamical supersymmetry breaking," *Phys.Rev.* **D53** (1996) 2658–2669, arXiv:hep-ph/9507378 [hep-ph].

[90] G. Giudice and R. Rattazzi, "Theories with gauge mediated supersymmetry breaking," *Phys.Rept.* **322** (1999) 419–499, arXiv:hep-ph/9801271 [hep-ph].

[91] P. Fayet and J. Iliopoulos, "Spontaneously Broken Supergauge Symmetries and Goldstone Spinors," *Phys.Lett.* **B51** (1974) 461–464.

[92] P. Fayet, "Spontaneously Broken Supersymmetric Theories of Weak, Electromagnetic and Strong Interactions," *Phys.Lett.* **B69** (1977) 489.

[93] L. O'Raifeartaigh, "Spontaneous Symmetry Breaking for Chiral Scalar Superfields," *Nucl.Phys.* **B96** (1975) 331.

[94] E. Cremmer, S. Ferrara, L. Girardello, and A. Van Proeyen, "Yang-Mills Theories with Local Supersymmetry: Lagrangian, Transformation Laws and SuperHiggs Effect," *Nucl.Phys.* **B212** (1983) 413.

[95] J. Wess and J. Bagger, "Supersymmetry and supergravity," *Princeton, USA: Univ. Pr.* (1992) .

[96] J. Bagger and J. Wess, "Supersymmetry and supergravity," *Princeton, USA: Univ. Pr.* (1990) .

[97] M. Drees and X. Tata, "Signals for heavy exotics at hadron colliders and supercolliders," *Phys.Lett.* **B252** (1990) 695–702.

[98] A. Nisati, S. Petrarca, and G. Salvini, "On the possible detection of massive stable exotic particles at the LHC," *Mod.Phys.Lett.* **A12** (1997) 2213–2222, arXiv:hep-ph/9707376 [hep-ph].

[99] S. Ambrosanio, G. D. Kribs, and S. P. Martin, "Signals for gauge-mediated supersymmetry breaking models at the CERN LEP2 collider," *Phys. Rev.* **D56** (1997) 1761–1777, arXiv:hep-ph/9703211.

[100] J. L. Feng and T. Moroi, "Tevatron Signatures of Long-lived Charged Sleptons in Gauge-Mediated Supersymmetry Breaking Models," *Phys. Rev.* **D58** (1998) 035001, arXiv:hep-ph/9712499.

[101] S. P. Martin and J. D. Wells, "Cornering gauge-mediated supersymmetry breaking with quasi-stable sleptons at the Tevatron," *Phys. Rev.* **D59** (1999) 035008, arXiv:hep-ph/9805289.

[102] M. Fairbairn, A. Kraan, D. Milstead, T. Sjostrand, P. Z. Skands, *et al.*, "Stable massive particles at colliders," *Phys.Rept.* **438** (2007) 1–63, arXiv:hep-ph/0611040 [hep-ph].

[103] A. R. Raklev, "Massive Metastable Charged (S)Particles at the LHC," *Mod.Phys.Lett.* **A24** (2009) 1955–1969, arXiv:0908.0315 [hep-ph].

[104] **CDF** Collaboration, T. Aaltonen *et al.*, "Search for Long-Lived Massive Charged Particles in 1.96 TeV $\bar{p}p$ Collisions," *Phys.Rev.Lett.* **103** (2009) 021802, arXiv:0902.1266 [hep-ex].

[105] J. L. Feng, M. Kamionkowski, and S. K. Lee, "Light Gravitinos at Colliders and Implications for Cosmology," *Phys.Rev.* **D82** (2010) 015012, arXiv:1004.4213 [hep-ph].

[106] G. L. Kane and J. P. Leveille, "Experimental Constraints on Gluino Masses and Supersymmetric Theories," *Phys. Lett.* **B112** (1982) 227.

[107] P. R. Harrison and C. H. Llewellyn Smith, "Hadroproduction of Supersymmetric Particles," *Nucl. Phys.* **B213** (1983) 223. [ERRATUM-ibid.B223:542,1983].

[108] E. Reya and D. P. Roy, "Supersymmetric particle production at p anti-p collider energies," *Phys. Rev.* **D32** (1985) 645.

[109] S. Dawson, E. Eichten, and C. Quigg, "Search for Supersymmetric Particles in Hadron - Hadron Collisions," *Phys. Rev.* **D31** (1985) 1581.

[110] H. Baer and X. Tata, "Component formulae for hadroproduction of left-handed and right-handed squarks," *Phys. Lett.* **B160** (1985) 159.

[111] A. Martin, W. Stirling, R. Thorne, and G. Watt, "Parton distributions for the LHC," *Eur.Phys.J.* **C63** (2009) 189–285, arXiv:0901.0002 [hep-ph].

[112] W. Beenakker, R. Hopker, M. Spira, and P. M. Zerwas, "Squark production at the Tevatron," *Phys. Rev. Lett.* **74** (1995) 2905–2908, arXiv:hep-ph/9412272.

[113] W. Beenakker, R. Hopker, M. Spira, and P. M. Zerwas, "Gluino pair production at the Tevatron," *Z. Phys.* **C69** (1995) 163–166, arXiv:hep-ph/9505416.

[114] W. Beenakker, M. Kramer, T. Plehn, M. Spira, and P. M. Zerwas, "Stop production at hadron colliders," *Nucl. Phys.* **B515** (1998) 3–14, arXiv:hep-ph/9710451.

[115] W. Beenakker, R. Hopker, and M. Spira, "PROSPINO: A program for the PROduction of Supersymmetric Particles In Next-to-leading Order QCD," arXiv:hep-ph/9611232.

[116] D. Goncalves-Netto, D. Lopez-Val, K. Mawatari, T. Plehn, and I. Wigmore, "Automated Squark and Gluino Production to Next-to-Leading Order," *Phys.Rev.* **D87** (2013) 014002, arXiv:1211.0286 [hep-ph].

[117] R. Gavin, C. Hangst, M. Krämer, M. Mühlleitner, M. Pellen, *et al.*, "Matching Squark Pair Production at NLO with Parton Showers," arXiv:1305.4061 [hep-ph].

[118] U. Langenfeld and S.-O. Moch, "Higher-order soft corrections to squark hadro- production," *Phys. Lett.* **B675** (2009) 210–221, arXiv:0901.0802 [hep-ph].

[119] A. Kulesza and L. Motyka, "Threshold resummation for squark-antisquark and gluino- pair production at the LHC," *Phys. Rev. Lett.* **102** (2009) 111802, arXiv:0807.2405 [hep-ph].

[120] A. Kulesza and L. Motyka, "Soft gluon resummation for the production of gluino-gluino and squark-antisquark pairs at the LHC," *Phys. Rev.* **D80** (2009) 095004, arXiv:0905.4749 [hep-ph].

[121] W. Beenakker *et al.*, "Soft-gluon resummation for squark and gluino hadroproduction," *JHEP* **12** (2009) 041, arXiv:0909.4418 [hep-ph].

[122] W. Beenakker *et al.*, "Supersymmetric top and bottom squark production at hadron colliders," *JHEP* **08** (2010) 098, arXiv:1006.4771 [hep-ph].

[123] M. Beneke, P. Falgari, and C. Schwinn, "Threshold resummation for pair production of coloured heavy (s)particles at hadron colliders," *Nucl. Phys.* **B842** (2011) 414–474, arXiv:1007.5414 [hep-ph].

[124] W. Beenakker *et al.*, "NNLL resummation for squark-antisquark pair production at the LHC," *JHEP* **01** (2012) 076, arXiv:1110.2446 [hep-ph].

[125] P. Falgari, C. Schwinn, and C. Wever, "NLL soft and Coulomb resummation for squark and gluino production at the LHC," *JHEP* **06** (2012) 052, arXiv:1202.2260 [hep-ph].

[126] W. Beenakker, T. Janssen, S. Lepoeter, M. Krämer, A. Kulesza, *et al.*, "Towards NNLL resummation: hard matching coefficients for squark and gluino hadroproduction," arXiv:1304.6354 [hep-ph].

[127] http://web.physik.rwth-aachen.de/service/wiki/bin/view/Kraemer/SquarksandGluinos.

[128] S. Bornhauser, M. Drees, H. K. Dreiner, and J. S. Kim, "Electroweak Contributions to Squark Pair Production at the LHC," *Phys. Rev.* **D76** (2007) 095020, arXiv:0709.2544 [hep-ph].

[129] A. Arhrib, R. Benbrik, K. Cheung, and T.-C. Yuan, "Higgs boson enhancement effects on squark-pair production at the LHC," *JHEP* **02** (2010) 048, arXiv:0911.1820 [hep-ph].

[130] W. Hollik, M. Kollar, and M. K. Trenkel, "Hadronic production of top-squark pairs with electroweak NLO contributions," *JHEP* **02** (2008) 018, arXiv:0712.0287 [hep-ph].

[131] W. Hollik and E. Mirabella, "Squark anti-squark pair production at the LHC: the electroweak contribution," *JHEP* **12** (2008) 087, arXiv:0806.1433 [hep-ph].

[132] W. Hollik, E. Mirabella, and M. K. Trenkel, "Electroweak contributions to squark–gluino production at the LHC," *JHEP* **02** (2009) 002, arXiv:0810.1044 [hep-ph].

[133] M. Beccaria, G. Macorini, L. Panizzi, F. M. Renard, and C. Verzegnassi, "Stop-antistop and sbottom-antisbottom production at LHC: a one-loop search for model parameters dependence," *Int. J. Mod. Phys.* **A23** (2008) 4779–4810, arXiv:0804.1252 [hep-ph].

[134] E. Mirabella, "NLO electroweak contributions to gluino pair production at hadron colliders," *JHEP* **12** (2009) 012, arXiv:0908.3318 [hep-ph].

[135] J. Germer, W. Hollik, E. Mirabella, and M. K. Trenkel, "Hadronic production of squark-squark pairs: The electroweak contributions," *JHEP* **08** (2010) 023, arXiv:1004.2621 [hep-ph].

[136] J. Germer, W. Hollik, and E. Mirabella, "Hadronic production of bottom-squark pairs with electroweak contributions," *JHEP* **05** (2011) 068, arXiv:1103.1258 [hep-ph].

[137] K.-i. Hikasa and Y. Nakamura, "Soft breaking correction to hard supersymmetric relations: QCD corrections to squark decay," *Z. Phys.* **C70** (1996) 139–144, arXiv:hep-ph/9501382. [ERRATUM-ibid.C71:356,1996].

[138] A. Djouadi, W. Hollik, and C. Junger, "QCD corrections to scalar quark decays," *Phys. Rev.* **D55** (1997) 6975–6985, arXiv:hep-ph/9609419.

[139] S. Kraml, H. Eberl, A. Bartl, W. Majerotto, and W. Porod, "SUSY-QCD corrections to scalar quark decays into charginos and neutralinos," *Phys. Lett.* **B386** (1996) 175–182, arXiv:hep-ph/9605412.

[140] A. Bartl, W. Majerotto, and W. Porod, "Squark and gluino decays for large tan beta," *Z. Phys.* **C64** (1994) 499–508. [ERRATUM-ibid.C68:518,1995].

[141] A. Bartl *et al.*, "Bosonic decays of stop(2) and sbottom(2)," *Phys. Lett.* **B435** (1998) 118–124, arXiv:hep-ph/9804265.

[142] A. Bartl *et al.*, "SUSY-QCD corrections to stop and sbottom decays into W+- and Z0 bosons," *Phys. Lett.* **B419** (1998) 243–252, arXiv:hep-ph/9710286.

[143] A. Arhrib, A. Djouadi, W. Hollik, and C. Junger, "SUSY Higgs boson decays into scalar quarks: QCD corrections," *Phys. Rev.* **D57** (1998) 5860–5870, arXiv:hep-ph/9702426.

[144] A. Bartl *et al.*, "SUSY - QCD corrections to top and bottom squark decays into Higgs bosons," *Phys. Rev.* **D59** (1999) 115007, arXiv:hep-ph/9806299.

[145] W. Beenakker, R. Hopker, and P. M. Zerwas, "SUSY QCD decays of squarks and gluinos," *Phys. Lett.* **B378** (1996) 159–166, arXiv:hep-ph/9602378.

[146] W. Beenakker, R. Hopker, T. Plehn, and P. M. Zerwas, "Stop decays in SUSY-QCD," *Z. Phys.* **C75** (1997) 349–356, arXiv:hep-ph/9610313.

[147] M. Muhlleitner, A. Djouadi, and Y. Mambrini, "SDECAY: A Fortran code for the decays of the supersymmetric particles in the MSSM," *Comput. Phys. Commun.* **168** (2005) 46–70, arXiv:hep-ph/0311167.

[148] J. Guasch, J. Sola, and W. Hollik, "Yukawa coupling corrections to scalar quark decays," *Phys. Lett.* **B437** (1998) 88–99, arXiv:hep-ph/9802329.

[149] J. Guasch, W. Hollik, and J. Sola, "Fermionic decays of sfermions: A complete discussion at one-loop order," *JHEP* **10** (2002) 040, arXiv:hep-ph/0207364.

[150] A. Arhrib and R. Benbrik, "Third generation sfermions decays into Z and W gauge bosons: Full one-loop analysis," *Phys. Rev.* **D71** (2005) 095001, arXiv:hep-ph/0412349.

[151] A. Arhrib and R. Benbrik, "Complete one-loop analysis to stop and sbottom decays into Z and W+- bosons," *Afr. J. Math. Phys.* **3** (2006) 85–91, arXiv:hep-ph/0511116.

[152] Q. Li, L. G. Jin, and C. S. Li, "Supersymmetric electroweak corrections to heavier top squark decay into lighter top squark and neutral Higgs boson," *Phys. Rev.* **D66** (2002) 115008, arXiv:hep-ph/0207363.

[153] C. Weber, K. Kovarik, H. Eberl, and W. Majerotto, "Complete one-loop corrections to decays of charged and CP- even neutral Higgs bosons into sfermions," *Nucl. Phys.* **B776** (2007) 138–169, arXiv:hep-ph/0701134.

[154] M. Drees, W. Hollik, and Q. Xu, "One-loop calculations of the decay of the next-to-lightest neutralino in the MSSM," *JHEP* **02** (2007) 032, arXiv:hep-ph/0610267.

[155] R. Horsky, M. Kramer, A. Muck, and P. M. Zerwas, "Squark Cascade Decays to Charginos/Neutralinos: Gluon Radiation," *Phys. Rev.* **D78** (2008) 035004, arXiv:0803.2603 [hep-ph].

[156] T. Plehn, D. Rainwater, and P. Z. Skands, "Squark and gluino production with jets," *Phys. Lett.* **B645** (2007) 217–221, arXiv:hep-ph/0510144.

[157] J. Alwall, S. de Visscher, and F. Maltoni, "QCD radiation in the production of heavy colored particles at the LHC," *JHEP* **02** (2009) 017, arXiv:0810.5350 [hep-ph].

[158] "Search for squarks and gluinos with the atlas detector in final states with jets and missing transverse momentum and 20.3 fb^{-1} of $\sqrt{s} = 8$ tev proton-proton collision data," Tech. Rep. ATLAS-CONF-2013-047, CERN, Geneva, May, 2013.

[159] **ATLAS** Collaboration, G. Aad *et al.*, "Search for squarks and gluinos using final states with jets and missing transverse momentum with the ATLAS detector in sqrt(s) = 7 TeV proton-proton collisions," *Phys.Lett.* **B710** (2012) 67–85, arXiv:1109.6572 [hep-ex].

[160] **ATLAS** Collaboration, G. Aad *et al.*, "Search for the neutral Higgs bosons of the Minimal Supersymmetric Standard Model in *pp* collisions at $\sqrt{s} = 7$ TeV with the ATLAS detector," *JHEP* **1302** (2013) 095, arXiv:1211.6956 [hep-ex].

[161] **CMS** Collaboration, S. Chatrchyan *et al.*, "Search for Supersymmetry at the LHC in Events with Jets and Missing Transverse Energy," *Phys.Rev.Lett.* **107** (2011) 221804, arXiv:1109.2352 [hep-ex].

[162] **CMS** Collaboration, S. Chatrchyan *et al.*, "Search for supersymmetry in hadronic final states with missing transverse energy using the variables α_T and b-quark multiplicity in pp collisions at $\sqrt{s} = 8$ TeV," arXiv:1303.2985 [hep-ex].

[163] **CMS** Collaboration, S. Chatrchyan *et al.*, "Interpretation of searches for supersymmetry with simplified models," arXiv:1301.2175 [hep-ex].

[164] N. Arkani-Hamed, G. L. Kane, J. Thaler, and L.-T. Wang, "Supersymmetry and the LHC inverse problem," *JHEP* **0608** (2006) 070, arXiv:hep-ph/0512190 [hep-ph].

[165] N. Bornhauser and M. Drees, "Mitigation of the LHC Inverse Problem," *Phys.Rev.* **D86** (2012) 015025, arXiv:1205.6080 [hep-ph].

[166] J. Hubisz, J. Lykken, M. Pierini, and M. Spiropulu, "Missing energy look-alikes with 100 pb^{-1} at the LHC," *Phys.Rev.* **D78** (2008) 075008, arXiv:0805.2398 [hep-ph].

[167] A. J. Barr and C. G. Lester, "A Review of the Mass Measurement Techniques proposed for the Large Hadron Collider," *J. Phys.* **G37** (2010) 123001, arXiv:1004.2732 [hep-ph].

[168] H. K. Dreiner, M. Kramer, J. M. Lindert, and B. O'Leary, "SUSY parameter determination at the LHC using cross sections and kinematic edges," *JHEP* **04** (2010) 109, arXiv:1003.2648 [hep-ph].

[169] W. Beenakker, M. Klasen, M. Kramer, T. Plehn, M. Spira, *et al.*, "The Production of charginos / neutralinos and sleptons at hadron colliders," *Phys.Rev.Lett.* **83** (1999) 3780–3783, arXiv:hep-ph/9906298 [hep-ph].

[170] E. Eichten, I. Hinchliffe, K. D. Lane, and C. Quigg, "Super Collider Physics," *Rev.Mod.Phys.* **56** (1984) 579–707.

[171] H. Baer, B. Harris, and M. H. Reno, "Next-to-leading order slepton pair production at hadron colliders," *Phys.Rev.* **D57** (1998) 5871–5874, arXiv:hep-ph/9712315 [hep-ph].

[172] G. Bozzi, B. Fuks, and M. Klasen, "Transverse-momentum resummation for slepton-pair production at the LHC," *Phys. Rev.* **D74** (2006) 015001, arXiv:hep-ph/0603074.

[173] G. Bozzi, B. Fuks, and M. Klasen, "Threshold Resummation for Slepton-Pair Production at Hadron Colliders," *Nucl. Phys.* **B777** (2007) 157–181, arXiv:hep-ph/0701202.

[174] G. Bozzi, B. Fuks, and M. Klasen, "Joint resummation for slepton pair production at hadron colliders," *Nucl. Phys.* **B794** (2008) 46–60, arXiv:0709.3057 [hep-ph].

[175] I. Fridman-Rojas and P. Richardson, "Next-to-Leading Order Simulation of Slepton Pair Production," arXiv:1208.0279 [hep-ph].

[176] B. Jager, A. von Manteuffel, and S. Thier, "Slepton pair production in the POWHEG BOX," *JHEP* **1210** (2012) 130, arXiv:1208.2953 [hep-ph].

[177] B. Fuks, M. Klasen, D. R. Lamprea, and M. Rothering, "Precision predictions for electroweak superpartner production at hadron colliders with Resummino," arXiv:1304.0790 [hep-ph].

[178] F. del Aguila and L. Ametller, "On the detectability of sleptons at large hadron colliders," *Phys.Lett.* **B261** (1991) 326–333.

[179] M. Bisset, S. Raychaudhuri, and P. Roy, "Higgs mediated slepton pair production at the large hadron collider," arXiv:hep-ph/9602430 [hep-ph].

[180] F. Borzumati and K. Hagiwara, "Testing supersymmetry at the LHC through gluon-fusion production of a slepton pair," *JHEP* **1103** (2011) 103, arXiv:0912.0454 [hep-ph].

[181] T. Sjostrand *et al.*, "High-energy physics event generation with PYTHIA 6.1," *Comput. Phys. Commun.* **135** (2001) 238–259, arXiv:hep-ph/0010017.

[182] G. Corcella *et al.*, "HERWIG 6.5: an event generator for Hadron Emission Reactions With Interfering Gluons (including supersymmetric processes)," *JHEP* **01** (2001) 010, arXiv:hep-ph/0011363.

[183] **CMS** Collaboration, S. Chatrchyan *et al.*, "Search for electroweak production of charginos and neutralinos using leptonic final states in pp collisions at $\sqrt{s} = 7$ TeV," *JHEP* **1211** (2012) 147, arXiv:1209.6620 [hep-ex].

[184] **ATLAS** Collaboration, G. Aad *et al.*, "Search for direct slepton and gaugino production in final states with two leptons and missing transverse momentum with the ATLAS detector in pp collisions at $\sqrt{s} = 7$ TeV," *Phys.Lett.* **B718** (2013) 879–901, arXiv:1208.2884 [hep-ex].

[185] **LEP2 SUSY Working Group** Collaboration, "Combined LEP GMSB Stau/Smuon/Selectron Results, 189-208 GeV,". http://lepsusy.web.cern.ch/lepsusy/www/gmsb_summer02/lepgmsb.html.

[186] **D0** Collaboration, V. Abazov *et al.*, "Search for Long-Lived Charged Massive Particles with the D0 Detector," *Phys.Rev.Lett.* **102** (2009) 161802, arXiv:0809.4472 [hep-ex].

[187] **CMS** Collaboration, S. Chatrchyan *et al.*, "Search for heavy long-lived charged particles in pp collisions at $\sqrt{s} = 7$ TeV," *Phys.Lett.* **B713** (2012) 408–433, arXiv:1205.0272 [hep-ex].

[188] **CMS** Collaboration, S. Chatrchyan *et al.*, "Searches for long-lived charged particles in pp collisions at sqrt(s)=7 and 8 TeV," arXiv:1305.0491 [hep-ex].

[189] **LHC Higgs Cross Section Working Group** Collaboration, S. Dittmaier *et al.*, "Handbook of LHC Higgs Cross Sections: 1. Inclusive Observables," arXiv:1101.0593 [hep-ph].

[190] S. Dittmaier *et al.*, "Handbook of LHC Higgs Cross Sections: 2. Differential Distributions," arXiv:1201.3084 [hep-ph].

[191] "Combined measurements of the mass and signal strength of the Higgs-like boson with the ATLAS detector using up to 25 fb^{-1} of proton-proton collision data," Tech. Rep. ATLAS-CONF-2013-014, CERN, Geneva, Mar, 2013.

[192] "Combination of standard model Higgs boson searches and measurements of the properties of the new boson with a mass near 125 GeV," Tech. Rep. CMS-PAS-HIG-13-005, CERN, Geneva, 2013.

[193] P. Bechtle, S. Heinemeyer, O. Stal, T. Stefaniak, G. Weiglein, *et al.*, "MSSM Interpretations of the LHC Discovery: Light or Heavy Higgs?," arXiv:1211.1955 [hep-ph].

[194] "Higgs to tau tau (MSSM) (HCP)," Tech. Rep. CMS-PAS-HIG-12-050, CERN, Geneva, 2012.

[195] M. Frank, T. Hahn, S. Heinemeyer, W. Hollik, H. Rzehak, *et al.*, "The Higgs Boson Masses and Mixings of the Complex MSSM in the Feynman-Diagrammatic Approach," *JHEP* **0702** (2007) 047, arXiv:hep-ph/0611326 [hep-ph].

[196] M. S. Carena, S. Heinemeyer, C. Wagner, and G. Weiglein, "Suggestions for benchmark scenarios for MSSM Higgs boson searches at hadron colliders," *Eur.Phys.J.* **C26** (2003) 601–607, arXiv:hep-ph/0202167 [hep-ph].

[197] M. S. Carena, S. Heinemeyer, C. Wagner, and G. Weiglein, "MSSM Higgs boson searches at the Tevatron and the LHC: Impact of different benchmark scenarios," *Eur.Phys.J.* **C45** (2006) 797–814, arXiv:hep-ph/0511023 [hep-ph].

[198] **LHCb** Collaboration, R. Aaij *et al.*, "First evidence for the decay Bs -> mu+ mu-," *Phys.Rev.Lett.* **110** (2013) 021801, arXiv:1211.2674 [Unknown].

[199] A. J. Buras, J. Girrbach, D. Guadagnoli, and G. Isidori, "On the Standard Model prediction for BR(Bs,d to mu+ mu-)," *Eur.Phys.J.* **C72** (2012) 2172, arXiv:1208.0934 [hep-ph].

[200] **Heavy Flavor Averaging Group** Collaboration, D. Asner *et al.*, "Averages of b-hadron, c-hadron, and tau-lepton Properties," arXiv:1010.1589 [hep-ex].

[201] A. J. Buras, R. Fleischer, S. Recksiegel, and F. Schwab, "Anatomy of prominent B and K decays and signatures of CP violating new physics in the electroweak penguin sector," *Nucl.Phys.* **B697** (2004) 133–206, arXiv:hep-ph/0402112 [hep-ph].

[202] S. Antusch, J. P. Baumann, V. F. Domcke, and P. M. Kostka, "Sneutrino Hybrid Inflation and Nonthermal Leptogenesis," *JCAP* **1010** (2010) 006, arXiv:1007.0708 [hep-ph].

[203] S. Clesse and B. Garbrecht, "Slow Roll during the Waterfall Regime: The Small Coupling Window for SUSY Hybrid Inflation," *Phys.Rev.* **D86** (2012) 023525, arXiv:1204.3540 [hep-ph].

[204] T. Asaka, K. Hamaguchi, M. Kawasaki, and T. Yanagida, "Leptogenesis in inflationary universe," *Phys.Rev.* **D61** (2000) 083512, arXiv:hep-ph/9907559 [hep-ph].

[205] T. Falk, K. A. Olive, and M. Srednicki, "Heavy sneutrinos as dark matter," *Phys.Lett.* **B339** (1994) 248–251, arXiv:hep-ph/9409270 [hep-ph].

[206] H.-S. Lee, K. T. Matchev, and S. Nasri, "Revival of the thermal sneutrino dark matter," *Phys.Rev.* **D76** (2007) 041302, arXiv:hep-ph/0702223 [HEP-PH].

[207] G. Bertone, D. Hooper, and J. Silk, "Particle dark matter: Evidence, candidates and constraints," *Phys.Rept.* **405** (2005) 279–390, arXiv:hep-ph/0404175 [hep-ph].

[208] **XENON100** Collaboration, E. Aprile *et al.*, "Dark Matter Results from 100 Live Days of XENON100 Data," *Phys.Rev.Lett.* **107** (2011) 131302, arXiv:1104.2549 [astro-ph.CO].

[209] M. Garny, A. Ibarra, M. Pato, and S. Vogl, "On the spin-dependent sensitivity of XENON100," *Phys.Rev.* **D87** (2013) 056002, arXiv:1211.4573 [hep-ph].

[210] T. Bringmann, L. Bergstrom, and J. Edsjo, "New Gamma-Ray Contributions to Supersymmetric Dark Matter Annihilation," *JHEP* **0801** (2008) 049, arXiv:0710.3169 [hep-ph].

[211] **Fermi-LAT** Collaboration, M. Ackermann *et al.*, "Constraining Dark Matter Models from a Combined Analysis of Milky Way Satellites with the Fermi Large Area Telescope," *Phys.Rev.Lett.* **107** (2011) 241302, arXiv:1108.3546 [astro-ph.HE].

[212] T. Bringmann, X. Huang, A. Ibarra, S. Vogl, and C. Weniger, "Fermi LAT Search for Internal Bremsstrahlung Signatures from Dark Matter Annihilation," *JCAP* **1207** (2012) 054, arXiv:1203.1312 [hep-ph].

[213] V. D. Barger, F. Halzen, D. Hooper, and C. Kao, "Indirect search for neutralino dark matter with high-energy neutrinos," *Phys.Rev.* **D65** (2002) 075022, arXiv:hep-ph/0105182 [hep-ph].

[214] **ICECUBE** Collaboration, R. Abbasi *et al.*, "Limits on a muon flux from neutralino annihilations in the Sun with the IceCube 22-string detector," *Phys.Rev.Lett.* **102** (2009) 201302, arXiv:0902.2460 [astro-ph.CO].

[215] S. Galli, F. Iocco, G. Bertone, and A. Melchiorri, "CMB constraints on Dark Matter models with large annihilation cross-section," *Phys.Rev.* **D80** (2009) 023505, arXiv:0905.0003 [astro-ph.CO].

[216] K. Jedamzik, "Neutralinos and Big Bang nucleosynthesis," *Phys.Rev.* **D70** (2004) 083510, arXiv:astro-ph/0405583 [astro-ph].

[217] G. G. Raffelt, "Astrophysical axion bounds," *Lect. Notes Phys.* **741** (2008) 51–71, arXiv:hep-ph/0611350.

[218] N. Tajuddin, "Axinos in the Sky and on Earth," *PhD Thesis, University of Zürich* (2010) .

[219] H. Baer, S. Kraml, A. Lessa, and S. Sekmen, "Thermal leptogenesis and the gravitino problem in the Asaka-Yanagida axion/axino dark matter scenario," *JCAP* **1104** (2011) 039, arXiv:1012.3769 [hep-ph].

[220] C. Cheung, G. Elor, and L. J. Hall, "The Cosmological Axino Problem," arXiv:1104.0692 [hep-ph].

[221] A. Freitas, F. D. Steffen, N. Tajuddin, and D. Wyler, "Axinos in Cosmology and at Colliders," *JHEP* **1106** (2011) 036, arXiv:1105.1113 [hep-ph].

[222] P. Graf and F. D. Steffen, "Dark radiation and dark matter in supersymmetric axion models with high reheating temperature," arXiv:1302.2143 [hep-ph].

[223] M. Bolz, A. Brandenburg, and W. Buchmüller, "Thermal production of gravitinos," *Nucl.Phys.* **B606** (2001) 518–544, arXiv:hep-ph/0012052 [hep-ph]. [Erratum-ibid. B **790**, 336 (2008)].

[224] A. Brandenburg and F. D. Steffen, "Axino dark matter from thermal production," *JCAP* **0408** (2004) 008, arXiv:hep-ph/0405158 [hep-ph].

[225] J. Pradler and F. D. Steffen, "Thermal gravitino production and collider tests of leptogenesis," *Phys.Rev.* **D75** (2007) 023509, arXiv:hep-ph/0608344 [hep-ph].

[226] J. Pradler and F. D. Steffen, "Constraints on the reheating temperature in gravitino dark matter scenarios," *Phys. Lett.* **B648** (2007) 224–235, arXiv:hep-ph/0612291.

[227] V. S. Rychkov and A. Strumia, "Thermal production of gravitinos," *Phys.Rev.* **D75** (2007) 075011, arXiv:hep-ph/0701104 [hep-ph].

[228] L. Covi, L. Roszkowski, R. Ruiz de Austri, and M. Small, "Axino dark matter and the CMSSM," *JHEP* **06** (2004) 003, arXiv:hep-ph/0402240.

[229] A. Brandenburg, L. Covi, K. Hamaguchi, L. Roszkowski, and F. D. Steffen, "Signatures of axinos and gravitinos at colliders," *Phys. Lett.* **B617** (2005) 99–111, arXiv:hep-ph/0501287.

[230] A. Strumia, "Thermal production of Axino Dark Matter," *JHEP* **06** (2010) 036, arXiv:1003.5847 [hep-ph].

[231] K. J. Bae, K. Choi, and S. H. Im, "Effective interactions of axion supermultiplet and thermal production of axino dark matter," arXiv:1106.2452 [hep-ph].

[232] R. H. Cyburt, J. R. Ellis, B. D. Fields, and K. A. Olive, "Updated nucleosynthesis constraints on unstable relic particles," *Phys.Rev.* **D67** (2003) 103521, arXiv:astro-ph/0211258 [astro-ph].

[233] M. Kawasaki, K. Kohri, and T. Moroi, "Big-Bang nucleosynthesis and hadronic decay of long-lived massive particles," *Phys.Rev.* **D71** (2005) 083502, arXiv:astro-ph/0408426 [astro-ph].

[234] K. Jedamzik, "Big bang nucleosynthesis constraints on hadronically and electromagnetically decaying relic neutral particles," *Phys.Rev.* **D74** (2006) 103509, arXiv:hep-ph/0604251 [hep-ph].

[235] M. Kawasaki, K. Kohri, T. Moroi, and A. Yotsuyanagi, "Big-Bang Nucleosynthesis and Gravitino," *Phys.Rev.* **D78** (2008) 065011, arXiv:0804.3745 [hep-ph].

[236] M. W. Grunewald, G. Passarino, E. Accomando, A. Ballestrero, P. Bambade, *et al.*, "Reports of the Working Groups on Precision Calculations for LEP2 Physics: Proceedings. Four fermion production in electron positron collisions," arXiv:hep-ph/0005309 [hep-ph].

[237] A. Denner, S. Dittmaier, M. Roth, and D. Wackeroth, "Predictions for all processes e+ e- –>gt; 4 fermions + gamma," *Nucl.Phys.* **B560** (1999) 33–65, arXiv:hep-ph/9904472 [hep-ph].

[238] K. Melnikov and M. Schulze, "NLO QCD corrections to top quark pair production and decay at hadron colliders," *JHEP* **08** (2009) 049, arXiv:0907.3090 [hep-ph].

[239] J. M. Campbell and R. K. Ellis, "Top-quark processes at NLO in production and decay," arXiv:1204.1513 [hep-ph].

[240] R. Boughezal and M. Schulze, "Precise predictions for top quark plus missing energy signatures at the LHC," arXiv:1212.0898 [hep-ph].

[241] D. Wackeroth and W. Hollik, "Electroweak radiative corrections to resonant charged gauge boson production," *Phys.Rev.* **D55** (1997) 6788–6818, arXiv:hep-ph/9606398 [hep-ph].

[242] W. Beenakker, F. A. Berends, and A. Chapovsky, "Radiative corrections to pair production of unstable particles: results for e+ e- –> four fermions," *Nucl.Phys.* **B548** (1999) 3–59, arXiv:hep-ph/9811481 [hep-ph].

[243] A. Denner, S. Dittmaier, and M. Roth, "Nonfactorizable photonic corrections to e+ e- –> W W –> four fermions," *Nucl.Phys.* **B519** (1998) 39–84, arXiv:hep-ph/9710521 [hep-ph].

[244] T. Hahn, "Generating Feynman diagrams and amplitudes with FeynArts 3," *Comput. Phys. Commun.* **140** (2001) 418–431, arXiv:hep-ph/0012260.

[245] T. Hahn and M. Perez-Victoria, "Automatized one-loop calculations in four and D dimensions," *Comput. Phys. Commun.* **118** (1999) 153–165, arXiv:hep-ph/9807565.

[246] T. Hahn and C. Schappacher, "The implementation of the minimal supersymmetric standard model in FeynArts and FormCalc," *Comput. Phys. Commun.* **143** (2002) 54–68, arXiv:hep-ph/0105349.

[247] W. Hollik and D. Stockinger, "Regularization and supersymmetry-restoring counterterms in supersymmetric QCD," *Eur. Phys. J.* **C20** (2001) 105–119, arXiv:hep-ph/0103009.

[248] H. D. Abarbanel and C. Itzykson, "Relativistic eikonal expansion," *Phys.Rev.Lett.* **23** (1969) 53.

[249] M. Levy and J. Sucher, "Eikonal approximation in quantum field theory," *Phys.Rev.* **186** (1969) 1656–1670.

[250] S. Catani and M. Seymour, "A General algorithm for calculating jet cross-sections in NLO QCD," *Nucl.Phys.* **B485** (1997) 291–419, arXiv:hep-ph/9605323 [hep-ph].

[251] G. 't Hooft and M. Veltman, "Scalar One Loop Integrals," *Nucl.Phys.* **B153** (1979) 365–401.

[252] A. Denner, "Techniques for calculation of electroweak radiative corrections at the one loop level and results for W physics at LEP-200," *Fortschr. Phys.* **41** (1993) 307–420, arXiv:0709.1075 [hep-ph].

[253] U. Baur, S. Keller, and D. Wackeroth, "Electroweak radiative corrections to W boson production in hadronic collisions," *Phys. Rev.* **D59** (1999) 013002, arXiv:hep-ph/9807417.

[254] S. Frixione, E. Laenen, P. Motylinski, B. R. Webber, and C. D. White, "Single-top hadroproduction in association with a W boson," *JHEP* **0807** (2008) 029, arXiv:0805.3067 [hep-ph].

[255] T. Binoth *et al.*, "Automized Squark-Neutralino Production to Next-to-Leading Order," *Phys. Rev.* **D84** (2011) 075005, arXiv:1108.1250 [hep-ph].

[256] **Particle Data Group** Collaboration, K. Nakamura *et al.*, "Review of particle physics," *J. Phys.* **G37** (2010) 075021.

[257] P. M. Nadolsky, H.-L. Lai, Q.-H. Cao, J. Huston, J. Pumplin, *et al.*, "Implications of CTEQ global analysis for collider observables," *Phys.Rev.* **D78** (2008) 013004, arXiv:0802.0007 [hep-ph].

[258] M. R. Whalley, D. Bourilkov, and R. C. Group, "The Les Houches Accord PDFs (LHAPDF) and Lhaglue," arXiv:hep-ph/0508110.

[259] B. C. Allanach *et al.*, "The Snowmass points and slopes: Benchmarks for SUSY searches," *Eur. Phys. J.* **C25** (2002) 113–123, arXiv:hep-ph/0202233.

[260] M. J. Dolan, D. Grellscheid, J. Jaeckel, V. V. Khoze, and P. Richardson, "New Constraints on Gauge Mediation and Beyond from LHC SUSY Searches at 7 TeV," *JHEP* **1106** (2011) 095, arXiv:1104.0585 [hep-ph].

[261] S. AbdusSalam, B. Allanach, H. Dreiner, J. Ellis, U. Ellwanger, *et al.*, "Benchmark Models, Planes, Lines and Points for Future SUSY Searches at the LHC," *Eur.Phys.J.* **C71** (2011) 1835, arXiv:1109.3859 [hep-ph].

[262] M. Cacciari and G. P. Salam, "Dispelling the N^3 myth for the k_t jet-finder," *Phys.Lett.* **B641** (2006) 57–61, arXiv:hep-ph/0512210 [hep-ph].

[263] M. Cacciari, G. P. Salam, and G. Soyez, "FastJet user manual," *Eur. Phys. J.* **C72** (2012) 1896, arXiv:1111.6097 [hep-ph].

[264] G. Hallenbeck, M. Perelstein, C. Spethmann, J. Thom, and J. Vaughan, "Model Discrimination with the CMS Detector: a Case Study," *Phys. Rev.* **D79** (2009) 075024, arXiv:0812.3135 [hep-ph].

[265] G. Moortgat-Pick, K. Rolbiecki, and J. Tattersall, "Early spin determination at the LHC?," *Phys. Lett.* **B699** (2011) 158–163, arXiv:1102.0293 [hep-ph].

[266] L. Randall and D. Tucker-Smith, "Dijet Searches for Supersymmetry at the LHC," *Phys. Rev. Lett.* **101** (2008) 221803, arXiv:0806.1049 [hep-ph].

[267] **CMS** Collaboration, V. Khachatryan *et al.*, "Search for Supersymmetry in pp Collisions at 7 TeV in Events with Jets and Missing Transverse Energy," *Phys. Lett.* **B698** (2011) 196–218, arXiv:1101.1628 [hep-ex].

[268] B. C. Allanach, "Impact of CMS Multi-jets and Missing Energy Search on CMSSM Fits," *Phys. Rev.* **D83** (2011) 095019, arXiv:1102.3149 [hep-ph].

[269] J. Alwall, M. Herquet, F. Maltoni, O. Mattelaer, and T. Stelzer, "MadGraph 5 : Going Beyond," *JHEP* **1106** (2011) 128, arXiv:1106.0522 [hep-ph].

[270] Z. Usubov, "Looking for Squark Pair Production in the Early LHC Data," arXiv:1005.5062 [hep-ph].

[271] I. Hinchliffe, F. Paige, M. Shapiro, J. Soderqvist, and W. Yao, "Precision SUSY measurements at CERN LHC," *Phys.Rev.* **D55** (1997) 5520–5540, arXiv:hep-ph/9610544 [hep-ph].

[272] H. Bachacou, I. Hinchliffe, and F. E. Paige, "Measurements of masses in SUGRA models at CERN LHC," *Phys.Rev.* **D62** (2000) 015009, arXiv:hep-ph/9907518 [hep-ph].

[273] B. Allanach, C. Lester, M. A. Parker, and B. Webber, "Measuring sparticle masses in nonuniversal string inspired models at the LHC," *JHEP* **0009** (2000) 004, arXiv:hep-ph/0007009 [hep-ph].

[274] **LHC/LC Study Group** Collaboration, G. Weiglein *et al.*, "Physics interplay of the LHC and the ILC," *Phys.Rept.* **426** (2006) 47–358, arXiv:hep-ph/0410364 [hep-ph].

[275] B. K. Gjelsten, D. J. Miller, and P. Osland, "Measurement of SUSY masses via cascade decays for SPS 1a," *JHEP* **0412** (2004) 003, arXiv:hep-ph/0410303 [hep-ph].

[276] D. J. Miller, P. Osland, and A. R. Raklev, "Invariant mass distributions in cascade decays," *JHEP* **0603** (2006) 034, arXiv:hep-ph/0510356 [hep-ph].

[277] C. G. Lester, "Constrained invariant mass distributions in cascade decays: The Shape of the 'm(qll)-threshold' and similar distributions," *Phys.Lett.* **B655** (2007) 39–44, arXiv:hep-ph/0603171 [hep-ph].

[278] M. Bisset, R. Lu, and N. Kersting, "Improving SUSY Spectrum Determinations at the LHC with Wedgebox Technique," *JHEP* **1105** (2011) 095, arXiv:0806.2492 [hep-ph].

[279] D. Costanzo and D. R. Tovey, "Supersymmetric particle mass measurement with invariant mass correlations," *JHEP* **0904** (2009) 084, arXiv:0902.2331 [hep-ph].

[280] G. Polesello and D. R. Tovey, "Supersymmetric particle mass measurement with the boost-corrected contransverse mass," *JHEP* **1003** (2010) 030, arXiv:0910.0174 [hep-ph].

[281] K. T. Matchev and M. Park, "A General method for determining the masses of semi-invisibly decaying particles at hadron colliders," *Phys.Rev.Lett.* **107** (2011) 061801, arXiv:0910.1584 [hep-ph].

[282] K. T. Matchev, F. Moortgat, L. Pape, and M. Park, "Precise reconstruction of sparticle masses without ambiguities," *JHEP* **0908** (2009) 104, arXiv:0906.2417 [hep-ph].

[283] H.-C. Cheng, J. F. Gunion, Z. Han, and B. McElrath, "Accurate Mass Determinations in Decay Chains with Missing Energy. II," *Phys.Rev.* **D80** (2009) 035020, arXiv:0905.1344 [hep-ph].

[284] L. Edelhauser, W. Porod, and R. K. Singh, "Spin Discrimination in Three-Body Decays," *JHEP* **1008** (2010) 053, arXiv:1005.3720 [hep-ph].

[285] K. Agashe, D. Kim, M. Toharia, and D. G. Walker, "Distinguishing Dark Matter Stabilization Symmetries Using Multiple Kinematic Edges and Cusps," *Phys.Rev.* **D82** (2010) 015007, arXiv:1003.0899 [hep-ph].

[286] M. M. Nojiri and K. Sakurai, "Controlling ISR in sparticle mass reconstruction," *Phys.Rev.* **D82** (2010) 115026, arXiv:1008.1813 [hep-ph].

[287] A. Barr, T. Khoo, P. Konar, K. Kong, C. Lester, *et al.*, "Guide to transverse projections and mass-constraining variables," *Phys.Rev.* **D84** (2011) 095031, arXiv:1105.2977 [hep-ph].

[288] C.-Y. Chen and A. Freitas, "General analysis of decay chains with three-body decays involving missing energy," *JHEP* **1201** (2012) 124, arXiv:1110.6192 [hep-ph].

[289] K. Choi, D. Guadagnoli, and C. B. Park, "Reducing combinatorial uncertainties: A new technique based on MT2 variables," *JHEP* **1111** (2011) 117, arXiv:1109.2201 [hep-ph].

[290] B. K. Gjelsten, D. J. Miller, P. Osland, and A. R. Raklev, "Mass Determination in Cascade Decays Using Shape Formulas," *AIP Conf.Proc.* **903** (2007) 257–260, arXiv:hep-ph/0611259 [hep-ph].

[291] A. Barr, "Determining the spin of supersymmetric particles at the LHC using lepton charge asymmetry," *Phys.Lett.* **B596** (2004) 205–212, arXiv:hep-ph/0405052 [hep-ph].

[292] J. M. Smillie and B. R. Webber, "Distinguishing Spins in Supersymmetric and Universal Extra Dimension Models at the Large Hadron Collider," *JHEP* **10** (2005) 069, arXiv:hep-ph/0507170.

[293] C. Athanasiou, C. G. Lester, J. M. Smillie, and B. R. Webber, "Distinguishing Spins in Decay Chains at the Large Hadron Collider," *JHEP* **0608** (2006) 055, arXiv:hep-ph/0605286 [hep-ph].

[294] M. Battaglia, A. K. Datta, A. De Roeck, K. Kong, and K. T. Matchev, "Contrasting supersymmetry and universal extra dimensions at colliders," *eConf* **C050318** (2005) 0302, arXiv:hep-ph/0507284 [hep-ph].

[295] A. Datta, K. Kong, and K. T. Matchev, "Discrimination of supersymmetry and universal extra dimensions at hadron colliders," *Phys.Rev.* **D72** (2005) 096006, arXiv:hep-ph/0509246 [hep-ph].

[296] L.-T. Wang and I. Yavin, "Spin measurements in cascade decays at the LHC," *JHEP* **0704** (2007) 032, arXiv:hep-ph/0605296 [hep-ph].

[297] S. Choi, K. Hagiwara, H.-U. Martyn, K. Mawatari, and P. Zerwas, "Spin Analysis of Supersymmetric Particles," *Eur.Phys.J.* **C51** (2007) 753–774, arXiv:hep-ph/0612301 [hep-ph].

[298] C. Kilic, L.-T. Wang, and I. Yavin, "On the existence of angular correlations in decays with heavy matter partners," *JHEP* **0705** (2007) 052, arXiv:hep-ph/0703085 [hep-ph].

[299] L.-T. Wang and I. Yavin, "A Review of Spin Determination at the LHC," *Int.J.Mod.Phys.* **A23** (2008) 4647–4668, arXiv:0802.2726 [hep-ph].

[300] S. Choi, M. Drees, A. Freitas, and P. Zerwas, "Testing the Majorana Nature of Gluinos and Neutralinos," *Phys.Rev.* **D78** (2008) 095007, arXiv:0808.2410 [hep-ph].

[301] M. Burns, K. Kong, K. T. Matchev, and M. Park, "A General Method for Model-Independent Measurements of Particle Spins, Couplings and Mixing Angles in Cascade Decays with Missing Energy at Hadron Colliders," *JHEP* **0810** (2008) 081, arXiv:0808.2472 [hep-ph].

[302] O. Gedalia, S. J. Lee, and G. Perez, "Spin Determination via Third Generation Cascade Decays," *Phys.Rev.* **D80** (2009) 035012, arXiv:0901.4438 [hep-ph].

[303] W. Ehrenfeld, A. Freitas, A. Landwehr, and D. Wyler, "Distinguishing spins in decay chains with photons at the Large Hadron Collider," *JHEP* **0907** (2009) 056, arXiv:0904.1293 [hep-ph].

[304] N. Srimanobhas and B. Asavapibhop, "A review of the spin determination of supersymmetric decay chain via neutralino at the LHC," *J.Phys.* **G38** (2011) 075001.

[305] **CMS** Collaboration, S. Chatrchyan *et al.*, "Search for new physics in events with opposite-sign leptons, jets, and missing transverse energy in pp collisions at $\sqrt{s} = 7$ TeV," *Phys.Lett.* **B718** (2013) 815–840, arXiv:1206.3949 [hep-ex].

[306] **ATLAS** Collaboration, G. Aad *et al.*, "Search for an excess of events with an identical flavour lepton pair and significant missing transverse momentum in $\sqrt{s} = 7$ TeV proton-proton collisions with the ATLAS detector," *Eur.Phys.J.* **C71** (2011) 1647, arXiv:1103.6208 [hep-ex].

[307] H.-C. Cheng, J. F. Gunion, Z. Han, G. Marandella, and B. McElrath, "Mass determination in SUSY-like events with missing energy," *JHEP* **0712** (2007) 076, arXiv:0707.0030 [hep-ph].

[308] H. Baer, C.-h. Chen, F. Paige, and X. Tata, "Signals for minimal supergravity at the CERN large hadron collider: Multi - jet plus missing energy channel," *Phys.Rev.* **D52** (1995) 2746–2759, arXiv:hep-ph/9503271 [hep-ph].

[309] **CMS** Collaboration, G. Bayatian *et al.*, "CMS technical design report, volume II: Physics performance," *J.Phys.* **G34** (2007) 995–1579.

[310] M. M. Nojiri, Y. Shimizu, S. Okada, and K. Kawagoe, "Inclusive transverse mass analysis for squark and gluino mass determination," *JHEP* **0806** (2008) 035, arXiv:0802.2412 [hep-ph].

[311] W. Buchmüller, K. Hamaguchi, M. Ratz, and T. Yanagida, "Supergravity at colliders," *Phys. Lett.* **B588** (2004) 90–98, arXiv:hep-ph/0402179.

[312] K. Hamaguchi, Y. Kuno, T. Nakaya, and M. M. Nojiri, "A Study of late decaying charged particles at future colliders," *Phys.Rev.* **D70** (2004) 115007, arXiv:hep-ph/0409248 [hep-ph].

[313] J. R. Ellis, A. R. Raklev, and O. K. Oye, "Gravitino dark matter scenarios with massive metastable charged sparticles at the LHC," *JHEP* **0610** (2006) 061, arXiv:hep-ph/0607261 [hep-ph].

[314] K. Ishiwata, T. Ito, and T. Moroi, "Long-Lived Unstable Superparticles at the LHC," *Phys.Lett.* **B669** (2008) 28–33, arXiv:0807.0975 [hep-ph].

[315] S. Biswas and B. Mukhopadhyaya, "Chargino reconstruction in supersymmetry with long-lived staus," *Phys.Rev.* **D81** (2010) 015003, arXiv:0910.3446 [hep-ph].

[316] J. L. Feng, S. T. French, I. Galon, C. G. Lester, Y. Nir, *et al.*, "Measuring Slepton Masses and Mixings at the LHC," *JHEP* **1001** (2010) 047, arXiv:0910.1618 [hep-ph].

[317] T. Ito, R. Kitano, and T. Moroi, "Measurement of the Superparticle Mass Spectrum in the Long-Lived Stau Scenario at the LHC," *JHEP* **1004** (2010) 017, arXiv:0910.5853 [hep-ph].

[318] J. J. Heckman, J. Shao, and C. Vafa, "F-theory and the LHC: Stau Search," *JHEP* **1009** (2010) 020, arXiv:1001.4084 [hep-ph].

[319] R. Kitano and M. Nakamura, "Tau polarization measurements at the LHC in supersymmetric models with a long-lived stau," *Phys.Rev.* **D82** (2010) 035007, arXiv:1006.2904 [hep-ph].

[320] T. Ito and T. Moroi, "Spin and Chirality Determination of Superparticles with Long-Lived Stau at the LHC," *Phys.Lett.* **B694** (2011) 349–354, arXiv:1007.3060 [hep-ph].

[321] T. Ito, "Squark Mass Measurement in the Long-lived Stau Scenario at the LHC," *Phys.Lett.* **B699** (2011) 151–157, arXiv:1012.1318 [hep-ph].

[322] S. Asai, Y. Azuma, M. Endo, K. Hamaguchi, and S. Iwamoto, "Stau Kinks at the LHC," arXiv:1103.1881 [hep-ph].

[323] H.-U. Martyn, "Detecting metastable staus and gravitinos at the ILC," *Eur.Phys.J.* **C48** (2006) 15–24, arXiv:hep-ph/0605257 [hep-ph].

[324] S. Asai, K. Hamaguchi, and S. Shirai, "Measuring lifetimes of long-lived charged massive particles stopped in LHC detectors," *Phys.Rev.Lett.* **103** (2009) 141803, arXiv:0902.3754 [hep-ph].

[325] J. Pinfold and L. Sibley, "Measuring the Lifetime of Trapped Sleptons Using the General Purpose LHC Detectors," *Phys.Rev.* **D83** (2011) 035021, arXiv:1006.3293 [hep-ph].

[326] J. Goity, W. Kossler, and M. Sher, "Production, collection and utilization of very longlived heavy charged leptons," *Phys.Rev.* **D48** (1993) 5437–5439, arXiv:hep-ph/9305244 [hep-ph].

[327] J. L. Feng and B. T. Smith, "Slepton trapping at the Large Hadron and International Linear Colliders," *Phys. Rev.* **D71** (2005) 015004, arXiv:hep-ph/0409278.

[328] K. Hamaguchi, M. M. Nojiri, and A. de Roeck, "Prospects to study a long-lived charged next lightest supersymmetric particle at the LHC," *JHEP* **0703** (2007) 046, arXiv:hep-ph/0612060 [hep-ph].

[329] M. Pospelov, "Particle physics catalysis of thermal big bang nucleosynthesis," *Phys. Rev. Lett.* **98** (2007) 231301, hep-ph/0605215.

[330] R. H. Cyburt, J. R. Ellis, B. D. Fields, K. A. Olive, and V. C. Spanos, "Bound-State Effects on Light-Element Abundances in Gravitino Dark Matter Scenarios," *JCAP* **0611** (2006) 014, arXiv:astro-ph/0608562 [astro-ph].

[331] K. Hamaguchi, T. Hatsuda, M. Kamimura, Y. Kino, and T. Yanagida, "Stau-catalyzed Li-6 Production in Big-Bang Nucleosynthesis," *Phys.Lett.* **B650** (2007) 268–274, arXiv:hep-ph/0702274 [HEP-PH].

[332] J. Pradler and F. D. Steffen, "Implications of Catalyzed BBN in the CMSSM with Gravitino Dark Matter," *Phys. Lett.* **B666** (2008) 181–184, arXiv:0710.2213 [hep-ph].

[333] M. Pospelov, "Bridging the primordial A=8 divide with Catalyzed Big Bang Nucleosynthesis," arXiv:0712.0647 [hep-ph].

[334] M. Pospelov, J. Pradler, and F. D. Steffen, "Constraints on Supersymmetric Models from Catalytic Primordial Nucleosynthesis of Beryllium," *JCAP* **0811** (2008) 020, arXiv:0807.4287 [hep-ph].

[335] F. D. Steffen, "Constraints on Gravitino Dark Matter Scenarios with Long-Lived Charged Sleptons," *AIP Conf. Proc.* **903** (2007) 595–598, arXiv:hep-ph/0611027.

[336] J. Kersten and K. Schmidt-Hoberg, "The Gravitino-Stau Scenario after Catalyzed BBN," *JCAP* **0801** (2008) 011, arXiv:0710.4528 [hep-ph].

[337] J. Pradler and F. D. Steffen, "CBBN in the CMSSM," *Eur. Phys. J.* **C56** (2008) 287–291, arXiv:0710.4548 [hep-ph].

[338] S. Bailly, K. Jedamzik, and G. Moultaka, "Gravitino Dark Matter and the Cosmic Lithium Abundances," *Phys. Rev.* **D80** (2009) 063509, arXiv:0812.0788 [hep-ph].

[339] A. Freitas, F. D. Steffen, N. Tajuddin, and D. Wyler, "Upper Limits on the Peccei-Quinn Scale and on the Reheating Temperature in Axino Dark Matter Scenarios," *Phys. Lett.* **B679** (2009) 270–277, arXiv:0904.3218 [hep-ph].

[340] M. Fukugita and T. Yanagida, "Baryogenesis without Grand Unification," *Phys.Lett.* **B174** (1986) 45.

[341] S. Davidson and A. Ibarra, "A Lower bound on the right-handed neutrino mass from leptogenesis," *Phys.Lett.* **B535** (2002) 25–32, arXiv:hep-ph/0202239 [hep-ph].

[342] W. Buchmüller, P. Di Bari, and M. Plümacher, "Leptogenesis for pedestrians," *Annals Phys.* **315** (2005) 305–351, arXiv:hep-ph/0401240 [hep-ph].

[343] S. Blanchet and P. Di Bari, "Flavor effects on leptogenesis predictions," *JCAP* **0703** (2007) 018, arXiv:hep-ph/0607330 [hep-ph].

[344] S. Antusch and A. Teixeira, "Towards constraints on the SUSY seesaw from flavour-dependent leptogenesis," *JCAP* **0702** (2007) 024, arXiv:hep-ph/0611232 [hep-ph].

[345] M. Ratz, K. Schmidt-Hoberg, and M. W. Winkler, "A Note on the primordial abundance of stau NLSPs," *JCAP* **0810** (2008) 026, arXiv:0808.0829 [hep-ph].

[346] J. Pradler and F. D. Steffen, "Thermal relic abundances of long-lived staus," *Nucl.Phys.* **B809** (2009) 318–346, arXiv:0808.2462 [hep-ph].

[347] G. Jungman, M. Kamionkowski, and K. Griest, "Supersymmetric dark matter," *Phys. Rept.* **267** (1996) 195–373, hep-ph/9506380.

[348] J. R. Ellis, T. Falk, K. A. Olive, and M. Srednicki, "Calculations of neutralino-stau coannihilation channels and the cosmologically relevant region of MSSM parameter space," *Astropart.Phys.* **13** (2000) 181–213, arXiv:hep-ph/9905481 [hep-ph].

[349] E. A. Baltz, M. Battaglia, M. E. Peskin, and T. Wizansky, "Determination of dark matter properties at high-energy colliders," *Phys. Rev.* **D74** (2006) 103521, hep-ph/0602187.

[350] F. D. Steffen, "Dark Matter Candidates - Axions, Neutralinos, Gravitinos, and Axinos," *Eur. Phys. J.* **C59** (2009) 557–588, arXiv:0811.3347.

[351] M. Carena, S. Gori, N. R. Shah, and C. E. Wagner, "A 125 GeV SM-like Higgs in the MSSM and the $\gamma\gamma$ rate," *JHEP* **1203** (2012) 014, arXiv:1112.3336 [hep-ph].

[352] M. Carena, S. Gori, N. R. Shah, C. E. Wagner, and L.-T. Wang, "Light Stau Phenomenology and the Higgs $\gamma\gamma$ Rate," *JHEP* **1207** (2012) 175, arXiv:1205.5842 [hep-ph].

[353] G. Belanger, F. Boudjema, A. Pukhov, and A. Semenov, "micrOMEGAs: A program for calculating the relic density in the MSSM," *Comput. Phys. Commun.* **149** (2002) 103–120, arXiv:hep-ph/0112278.

[354] G. Belanger, F. Boudjema, P. Brun, A. Pukhov, S. Rosier-Lees, *et al.*, "Indirect search for dark matter with micrOMEGAs2.4," *Comput.Phys.Commun.* **182** (2011) 842–856, arXiv:1004.1092 [hep-ph].

[355] T. Asaka, K. Hamaguchi, and K. Suzuki, "Cosmological gravitino problem in gauge mediated supersymmetry breaking models," *Phys. Lett.* **B490** (2000) 136–146, arXiv:hep-ph/0005136.

[356] M. Fujii, M. Ibe, and T. Yanagida, "Upper bound on gluino mass from thermal leptogenesis," *Phys. Lett.* **B579** (2004) 6–12, arXiv:hep-ph/0310142.

[357] C. F. Berger, L. Covi, S. Kraml, and F. Palorini, "The number density of a charged relic," *JCAP* **0810** (2008) 005, arXiv:0807.0211 [hep-ph].

[358] A. Freitas, F. D. Steffen, N. Tajuddin, and D. Wyler, "Late Energy Injection and Cosmological Constraints in Axino Dark Matter Scenarios," *Phys. Lett.* **B682** (2009) 193–199, arXiv:0909.3293 [Unknown].

[359] J. Hasenkamp and J. Kersten, "Leptogenesis, Gravitino Dark Matter and Entropy Production," *Phys.Rev.* **D82** (2010) 115029, arXiv:1008.1740 [hep-ph].

[360] J. F. Gunion and H. E. Haber, "The CP conserving two Higgs doublet model: The Approach to the decoupling limit," *Phys.Rev.* **D67** (2003) 075019, arXiv:hep-ph/0207010 [hep-ph].

[361] M. Klute, R. Lafaye, T. Plehn, M. Rauch, and D. Zerwas, "Measuring Higgs Couplings at a Linear Collider," *Europhys.Lett.* **101** (2013) 51001, arXiv:1301.1322 [hep-ph].

[362] R. Benbrik, M. Gomez Bock, S. Heinemeyer, O. Stal, G. Weiglein, *et al.*, "Confronting the MSSM and the NMSSM with the Discovery of a Signal in the two Photon Channel at the LHC," *Eur.Phys.J.* **C72** (2012) 2171, arXiv:1207.1096 [hep-ph].

[363] **CMS** Collaboration, "Updated measurements of the Higgs boson at 125 GeV in the two photon decay channel,".

[364] M. Endo, K. Hamaguchi, and K. Nakaji, "Probing High Reheating Temperature Scenarios at the LHC with Long-Lived Staus," *JHEP* **1011** (2010) 004, arXiv:1008.2307 [hep-ph].

[365] J. Hisano and S. Sugiyama, "Charge-breaking constraints on left-right mixing of stau's," *Phys.Lett.* **B696** (2011) 92–96, arXiv:1011.0260 [hep-ph].

[366] M. Carena, S. Gori, I. Low, N. R. Shah, and C. E. Wagner, "Vacuum Stability and Higgs Diphoton Decays in the MSSM," *JHEP* **1302** (2013) 114, arXiv:1211.6136 [hep-ph].

[367] T. Kitahara, "Vacuum Stability Constraints on the Enhancement of the h –> gamma gamma rate in the MSSm," *JHEP* **1211** (2012) 021, arXiv:1208.4792 [hep-ph].

[368] A. D. Linde, "Decay of the False Vacuum at Finite Temperature," *Nucl.Phys.* **B216** (1983) 421.

[369] J. Espinosa, "Dominant two loop corrections to the MSSM finite temperature effective potential," *Nucl.Phys.* **B475** (1996) 273–292, arXiv:hep-ph/9604320 [hep-ph].

[370] M. Endo, K. Hamaguchi, and K. Nakaji, "LHC signature with long-lived stau in high reheating temperature scenario," arXiv:1105.3823 [hep-ph].

[371] L. J. Hall, R. Rattazzi, and U. Sarid, "The Top quark mass in supersymmetric SO(10) unification," *Phys.Rev.* **D50** (1994) 7048–7065, arXiv:hep-ph/9306309 [hep-ph].

[372] R. Hempfling, "Yukawa coupling unification with supersymmetric threshold corrections," *Phys.Rev.* **D49** (1994) 6168–6172.

[373] M. S. Carena, M. Olechowski, S. Pokorski, and C. Wagner, "Electroweak Symmetry Breaking and Bottom-Top Yukawa Unification," *Nucl.Phys.* **B426** (1994) 269–300, arXiv:hep-ph/9402253 [hep-ph].

[374] D. M. Pierce, J. A. Bagger, K. T. Matchev, and R.-j. Zhang, "Precision corrections in the minimal supersymmetric standard model," *Nucl.Phys.* **B491** (1997) 3–67, arXiv:hep-ph/9606211 [hep-ph].

[375] M. S. Carena, D. Garcia, U. Nierste, and C. E. Wagner, "Effective Lagrangian for the $\bar{t}bH^+$ interaction in the MSSM and charged Higgs phenomenology," *Nucl.Phys.* **B577** (2000) 88–120, arXiv:hep-ph/9912516 [hep-ph].

[376] S. Heinemeyer, W. Hollik, H. Rzehak, and G. Weiglein, "High-Precision Predictions for the MSSM Higgs Sector at $O(\alpha_b\alpha_s)$," *Eur.Phys.J.* **C39** (2005) 465–481, arXiv:hep-ph/0411114 [hep-ph].

[377] A. Djouadi, "The Anatomy of electro-weak symmetry breaking. II. The Higgs bosons in the minimal supersymmetric model," *Phys.Rept.* **459** (2008) 1–241, arXiv:hep-ph/0503173 [hep-ph].

[378] **ATLAS** Collaboration, G. Aad *et al.*, "Searches for heavy long-lived sleptons and R-Hadrons with the ATLAS detector in pp collisions at $\sqrt{s} = 7$ TeV," *Phys.Lett.B* **720** (2013) 277–308, arXiv:1211.1597 [hep-ex].

[379] A. De Roeck, J. R. Ellis, F. Gianotti, F. Moortgat, K. Olive, *et al.*, "Supersymmetric benchmarks with non-universal scalar masses or gravitino dark matter," *Eur.Phys.J.* **C49** (2007) 1041–1066, arXiv:hep-ph/0508198 [hep-ph].

[380] J. Heisig and J. Kersten, "Production of long-lived staus in the Drell-Yan process," *Phys.Rev.* **D84** (2011) 115009, arXiv:1106.0764 [hep-ph].

[381] J. Heisig and J. Kersten, "Long-lived staus from strong production in a simplified model approach," *Phys.Rev.* **D86** (2012) 055020, arXiv:1203.1581 [hep-ph].

[382] S. Ambrosanio, B. Mele, S. Petrarca, G. Polesello, and A. Rimoldi, "Measuring the SUSY breaking scale at the LHC in the slepton NLSP scenario of GMSB models," *JHEP* **01** (2001) 014, arXiv:hep-ph/0010081.

[383] A. Arbey and F. Mahmoudi, "SuperIso Relic v3.0: A program for calculating relic density and flavour physics observables: Extension to NMSSM," *Comput.Phys.Commun.* **182** (2011) 1582–1583.

[384] M. Drees and S. P. Martin, "Implications of SUSY model building," arXiv:hep-ph/9504324 [hep-ph]. Report of Subgroup 2 of the DPF Working Group on 'Electroweak Symmetry Breaking and Beyond the Standard Model'.

[385] **ATLAS** Collaboration, "Search for electroweak production of supersymmetric particles in final states with at least two hadronically decaying taus and missing transverse momentum with the ATLAS detector in proton-proton collisions at $\sqrt{s} = 8$ TeV," *ATLAS-CONF-2013-028, ATLAS-COM-CONF-2013-026* (2013) .

[386] W. Hollik and H. Rzehak, "The Sfermion mass spectrum of the MSSM at the one loop level," *Eur.Phys.J.* **C32** (2003) 127–133, arXiv:hep-ph/0305328 [hep-ph].

[387] D. Berdine, N. Kauer, and D. Rainwater, "Breakdown of the Narrow Width Approximation for New Physics," *Phys.Rev.Lett.* **99** (2007) 111601, arXiv:hep-ph/0703058 [hep-ph].

[388] S. R. Coleman, "The Fate of the False Vacuum. 1. Semiclassical Theory," *Phys.Rev.* **D15** (1977) 2929–2936.

[389] J. Callan, Curtis G. and S. R. Coleman, "The Fate of the False Vacuum. 2. First Quantum Corrections," *Phys.Rev.* **D16** (1977) 1762–1768.

[390] C. L. Wainwright, "CosmoTransitions: Computing Cosmological Phase Transition Temperatures and Bubble Profiles with Multiple Fields," *Comput.Phys.Commun.* **183** (2012) 2006–2013, arXiv:1109.4189 [hep-ph].

Acknowledgments

First and foremost, I would like to thank my supervisor Prof. Wolfgang Hollik for his guidance, advice and support over the last years. His encouragement but also his confidence made this work possible.

Second, I would like to thank Prof. Björn Garbrecht for agreeing on acting as a second referee for this thesis.

Next, sincere thanks are given to Frank Steffen for guidance, supervision, collaboration, and continuous valuable support.

I would like to thank Davide Pagani to whom I am indebted for fruitful and inspiring collaboration, help and countless discussions.

Also I gratefully acknowledge collaboration with Maike Trenkel, Lorenzo Calibbi, Toshihiko Ota and Yasutaka Takanishi.

I would like to thank all current and former colleagues of the theory group at the Max-Planck-Institute for Physics for such an enjoyable, helpful and productive atmosphere; in particular I want to thank my (former) office mates Ananda Landwehr, Jochen Baumann, Peter Graf, Davide Cadamuro and Hendrik Vogel. Special thanks are given to Thomas Hahn for answers to many technical questions, and to Peter Graf, Davide Pagani and Hendrik Vogel for proofreading (parts of) this thesis.

For various discussions, help and support I would like to thank Markus Rummel, Malte Nuhn and Tobias Schlüter. The last-mentioned I also very much thank for proofreading parts of this thesis.

Last but not least I would like to express my deepest gratitude to my parents Jutta and Jan, my sisters Judith and Johanna, my grandmothers and to Juli for giving me all the support they could give.